Towards Sustainable Halide Perovskite Nanocrystals: Doping and Solvent Engineering

A Thesis Submitted

In Partial Fulfilment of the Requirements

for the Degree of

DOCTOR OF PHILOSOPHY

by

SHOVON CHATTERJEE

Roll No. 16107290

to the

Department of Chemistry
Indian Institute of Technology Kanpur
Kanpur, India

January, 2023

CERTIFICATE

It is certified that the work reported in the thesis entitled "**Towards Sustainable Halide Perovskite Nanocrystals: Doping and Solvent Engineering**" has been carried out by Mr. Shovon Chatterjee under my supervision and has not been submitted elsewhere for a degree.

January 2023
IIT Kanpur

(Prof. Pratik Sen)
Thesis supervisor
Department of Chemistry
Indian Institute of Technology Kanpur
Kanpur, U.P, India- 208016

DECLARATION

This is to certify that the thesis titled "**Mechanistic Investigation on Photostability of Colloidal 2D Perovskite Nanoplate against UV Irradiation and Potential Remedies**" has been authored by me. It presents the research conducted by me under the supervision of **Prof. Pratik Sen**.

To the best of my knowledge, it is an original work, both in terms of research content and narrative, and has not been submitted elsewhere, in part or in full, for a degree. Further, due credit has been attributed to the relevant state-of-the-art and collaborations (if any) with appropriate citations and acknowledgements, in line with established norms and practice.

(Signature)
Name: SHOVON CHATTERJEE
Programme: PhD
Department: CHEMISTRY
Indian Institute of Technology Kanpur
Kanpur 208016

Dedicated to
My Dadu
(My Grandfather)

Acknowledgements

When I joined IIT Kanpur as a Ph.D. student, with the hope to see the science beyond the textbook stories, I found myself in the mid of the ocean with thousands of possibilities. Luckily, I found my supervisor, Prof. Pratik Sen, who remained with me like a sailor in the ocean of science. Discussing ideas with an open mind whether it is unique or absurd with the supervisor is the most important thing, I feel, during Ph.D. research. His lessons taught me how spectroscopy serves as a gateway to the elusive molecular world, which greatly aided my investigation of the spectroscopy of the nanoworld. Discussions with him on this subject helped me to build a clear and comprehensible understanding which later became beneficial during my research. The main research focus of our lab was to gain physical insight into how and why dynamics in various lengths and timescale control chemistry, mainly in biological systems and organic molecules. I also started my research by studying the Photophysics of dyes. I still remember the day when he came to me and said, "Let us do something else. There is a new system called perovskite, I have heard. Let's find something in it!" After this, we together started to explore this new perovskite world. We were new, and he always tried to understand everything with logic which gave me the opportunity to understand this new field from the very basics. He was always humble and down to earth. Every discussion with him was a real pleasure. He always gave me endless freedom in the lab for which I will be always grateful. I really enjoyed working under him. I wish all the good fortunes for him and his family in the future.

It is my pleasure to express my sincere gratitude to Dr. Tanmay Maity of the Department of Material Science and Engineering, Indian Institute of Technology Kanpur. He is the person with whom in collaboration, I started to work on the

perovskite system. In my early Ph.D. days, we often had long discussions which helped me a lot to develop the idea in materials science.

It's my sincere gratitude to acknowledge Dr. T. G. Gopakumar for helping me in understanding the physics of semiconductor materials. He was always available with a smiling face whenever I had any doubts regarding any basic problem.

I want to take this opportunity to express my gratitude to Prof. A. Chandra, Prof. S. Monogaran, Dr. M. Ranganathan, and Dr. M. Chandra for their insightful teaching during coursework. I would like to thank again Prof. Pratik Sen, and Dr. M. Ranganathan for their constant encouragement during my time as their teaching assistant.

I express my overwhelming acknowledgement to the Department of Chemistry, IIT Kanpur for making a part of it and providing all the facilities. My sincere gratitude is due to the respected head of the departments Prof. S. Verma (former), Prof. A. Chandra (former), and Prof. J. K. Bera (current). Special thanks are due to Sudha mam and Geeta mam for their constant cooperation and generous help.

I want to sincerely thank Dr. Arnab Halder of Presidency University, Kolkata. His lectures and discussions inspired my interest in physical chemistry. Throughout the duration of my Ph.D., he remained a steady source of encouragement for me. He is more than just an older brother in my personal life, encouraging me in every circumstance. I will always remember the hours-long phone calls we used to have during the Corona Lockdown to discuss various issues involving the graphene oxide system, which eventually led to a few publications.

I also want to acknowledge all my teachers from childhood to college. Specifically, I would like like to thank Dr. Amrit Mitra, Dr. Nabakumar Bera, Prof. Suman Das, and Mr. Sailen Karmaker for their inspired teaching.

A special thank you to Puspal Da, my lab senior, who constantly helped me to understand the fundamental concepts of spectroscopy. He continued to be in touch with me even after he left this lab and helped me in every way he could in my journey of Ph.D. I would like to thank Vijaykant Da, who actually introduced the perovskite system in our lab. Pritam Da from the Department of Materials Science and Engineering has my sincere gratitude. He really aided me in the synthesis of perovskite systems during the early stages of my Ph.D. Also, my appreciation goes out to Khushubo Di, Rahul, and Pratip for their assistance with the TEM and PXRD analyses. I want to thank Bhaswati Di and Navin Da for making me feel welcome in the lab and for our enjoyable time spent together. Also, the help from Navin Da in every difficult situation that I will never forget. No words are sufficient to express my thanks to Nilimesh. We were batchmates in our M.Sc. that continued in our Ph.D. with so many eventful memories. Thanks are due to my seniors Ejaj Da, Vaisakh Da, Vipin Da, Faizi da, and Gulab da. I would like to acknowledge all my juniors Abhijit, Kuldeep, Sandeep, Suman, Tanmoy, Subhendu, Arnab, Bhupendra, Patralekha, and Bishal for their unwavering support and for keeping the lab environment cozy. I would like to thank Arghya, my junior with whom I spent a lot of time in the lab working together. His eagerness for dispelling every scientific scepticism was a great assistance to me in clarifying my own thoughts. Throughout my experiments, he was always there anytime I needed the assistance of any type. I have also enjoyed the moments that I have shared with all M.Sc. project students Nishit, Sukanta, Mainak, Pushpakant, and Shakil in the lab. I also give a special thanks to Dinesh Da of Presidency University for always encouraging me. His astonishing questions also helped me to understand basic physical chemistry.

I had been lucky enough to have three persons in my life, Aritra, Pratyush (Gudum), and Kanyashree, whom I cannot just mention as batchmates or labmates or friends. They were my family here. Their significance in my life cannot be adequately expressed in words. Aritra has been my batchmate since my M.Sc. days, and I am lucky to have him in my Ph.D. life too. From morning to night, from lab to

hostel he was the person with whom I spent most of my time. Our friendship was so heartful that we could even read each other minds in every situation. Whenever I planned any trip or any other plan, he was always the constant one. Pratyush came into our lab as an M.Sc. student and in time became a younger brother to me. His ever-smiling face with always funny demands was like a gift to me. I can recall very few nights when he hadn't said, "Shovon da, mangsho khabo!" or "cholo ludo kheli!". Kanya and I had the same taste in humor which brought us close. The funny memory of making memes with her on current affairs that I will never forget. Her excellent ability to cook delicious foods was what made the four of us together. I will cherish every moment we four spent together.

Hostel life always remains very close to every student and I am also no exception. It is always some people who make this life beautiful and memorable. It is impossible to imagine this hostel life without 'Saturday Party', 'late night tea adda', 'lunch and dinner time adda', 'emotional fanboy quarreling on Brazil-Argentina-Germany', 'Funny leg-pulling, 'nightlong discussions on hostel election', 'Saraswati Puja arrangements', and so on. I cherish all these moments shared with all crazy partners like Vuut Da, Puspal Da, Susanta Da (Unnoyon), How Da, Sanjay Jana, Tarak Da, Amit Da, Suman Da, Chiru Da, Bappa Da, Saikat Da, Tathagata Da (Huri), Arindam, Partha Da, Aritra (Khat), Nilimesh, Joydev, Tutu, Anubrata (Panu), Nripajyoti, Biplab, Manik Da, Debarun Da, Sabyasachi (Bishmal), Shila Da, Subha Da (Tumpa), Debarghya (Bong guy), Santanu (Guria), Sunanda (Mota), Ramranjan Da, Sayantan, Shaswata, Kaushik Da (Gadai), and Payra Da.

I was also lucky enough to have Sayantani (Mayabati) as my friend during my Ph.D. time. She was always there for me, supporting me in every circumstance. I would like to mention especially Samarpita Di and Susanta Da (Unnoyon) for loving me like a younger brother. I would also like to thank Rajib, Pranali, Razia, Monika, Krishnakant for making this Ph.D. journey memorable. I would like to

acknowledge Bidisha for being in this journey as a very good friend. I was also fortunate to have Dolphin (Deepannita) who was always like a cute sister to me.

Our hostel life had never been easy without the contribution of some people. I take this opportunity to acknowledge all the mess staff and sweepers of hall-4 and hall-11 for making our IIT Kanpur life so beautiful and trouble-free. I also thank all the canteen staff, especially Binoy bhaiya and Anup bhaiya for providing delicious food late at night. I would also like to mention about all the security staff who have made our campus life safe.

Travelling is always very close to my heart. Exploring new places was just like meditation to me. On my trips from IIT Kanpur, I was accompanied by Aritra, Susanta Da, Samarpita Di, Sabyasachi, Shila Da, Puspal Da, Tutu, Joydev, Nripajyoti, Subha Da, Payra Da, Kanyashree, Ramranjan Da, Abhijit, Suman, Subhendu. Thank you all for making these vacation times so enjoyable. I also thank Rahul bhaiya who remained an almost constant driver on each of my trips.

There are usually numerous ups and downs during a lengthy Ph.D. journey, both professionally and personally. I had the good fortune to have Vuut Da and Madhusree Di with me on this journey, who constantly supported me and helped me solve issues like family. There are simply not enough words to express how essential they are to me. In our hostel days, Vuut Da and I experienced many priceless memories that I will always remember. He was to me a sort of mentor during this journey. In this regard, I also acknowledge How Da, Sanjay Jana, Anubrata, and Joydev for their presence during my hard time.

I want to take this opportunity to thank Angana for being there for me. She always waited for me without any complaint. She is the one who is to bear all my frustrations and anger but always remained calm and cool. Thank you for your time and support.

I want to express my gratitude to my friends in my hometown for their unfailing support. Avantika, Nabamita, Sayantani, Mainak, Saheb, Srabani, Rekha, Koushik, and Subhajit, I love you all.

I am grateful to the IIT Kanpur for providing the fellowship. I also acknowledge IIT Kanpur for infrastructures and facilities. I also want to acknowledge ACMS, and Advance Imaging Centre for characterization support. Especially I would like to thank Ashish Ji, Jai Sir, Mitesh Ji, DD pal sir, and Sivakumar sir for their constant help.

The most important part of my life is my parents. They are the ones who will fight to the last end for me. It is their endless efforts, unconditional love, huge patience, and a lot of sacrifices are what that made me today. My maa Aparna Chatterjee and baba Prosanta Chatterjee, you both have given up everything in your life to put a smile on my face. 800 miles away from me, it was the same tough journey for you too. You own this Ph.D. more than I do. I love you, Maa. I love you, Baba. My dadu was the strongest pillar of my life who brought me up with his endless affection. He was the one who loved me more than anything else. Nobody would be much happier seeing me getting a Ph.D. degree if he was alive. I know you are always with me with all your blessings. Still, I miss you at each and every moment. I dedicate this milestone in my career to you, Dadu.

- ***Shovon Chatterjee***

Synopsis

Name of the Student	Shovon Chatterjee
Roll Number:	16107290
Degree for which Thesis is Submitted:	Ph. D.
Department:	Chemistry
Supervisor:	Prof. Pratik Sen
Thesis Title:	Towards Sustainable Halide Perovskite Nanocrystals: Doping and Solvent Engineering
Month and Year of Submission:	January, 2023

Halide perovskite is a class of semiconductors and is one of the most flourishing scientific fields in the last decade due to its highly promising characteristics in optoelectronics, solar cell, photocatalysis, and so on. Lead halide perovskites (LHP) in the halide perovskite family remain at the field's forefront as it has high photoluminescence quantum yield (PLQY), narrow PL bandwidth, easy PL tunability, and highly defect-tolerant nature. Although the LHP research started with its potential use as a solar cell, the nanocrystalline form of this material has already shown its immense potential in light-emitting diodes (LED). Using these extremely important and interesting properties of the LHPs, the potential use of these systems has already reached beyond solar cells and LEDs. So far, the LHP nanocrystals (NCs)/thin films have been studied in different applications like X-ray detectors, lasers, and in photocatalysis.

Despite the significant advancements made in LHP materials, several technical and scientific barriers still prevent their widespread commercial use. Among these, employing LHP has a severe flaw: lead toxicity. Also, the inherent instability of the LHP structure in an open atmosphere restricts its commercialization. Another important but overlooked aspect of this research field is solvent-related toxicity. In

perovskite NC synthesis we often use organic precursor solvents which may cause severe problems to the human body, which indicates the essence of looking for a new alternative green medium for perovskite NC synthesis. In the first part of this thesis, I focused on the optical property modulation and on the stability boosting of the LHP NCs upon heterovalent Bi^{3+} doping. The second part of the thesis deals with solvent-related toxicity. In this part, I have tried to discard conventionally used organic precursor solvents with environment-friendly so-called green solvents to synthesize the LHP NC systems. In the final part of this thesis, an environment-friendly green solvent is used lead-free copper halide perovskite NCs to discard lead related as well as solvent-related toxicity to achieve environmental sustainability. Also, the evidence of the presence of a high-energy emissive state in copper halide perovskite remains in focus. In the journey, we will also see the suppression of the nonradiative processes to achieve high PLQY.

Summary of the work done

(1) Reversible Ultra-Slow Crystal Growth of Mixed Lead Bismuth Perovskite Nanocrystal – Presence of Dynamic Capping

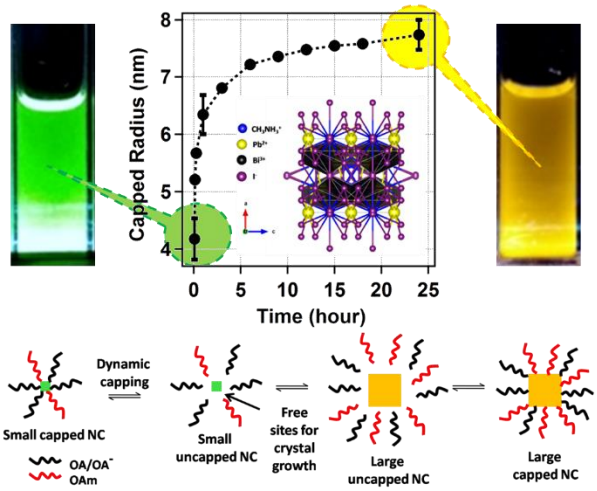

In this work, I have synthesized Bi^{3+} doped $CH_3NH_3PbI_3$ (MPBI) NCs via ligand assisted method, which crystallizes in phase pure tetragonal structure. XPS analysis of MPBI confirms the presence of both lead and bismuth in the NC. Stable MPBI NC shows broad absorption and a strong emission cantered at 579 nm with photoluminescence quantum yield of 15%. The interesting feature of this study is the time dependent red shift in the emission maximum by 37 nm starting from 542

nm at 25ºC in toluene. As the absorption spectra are found very broad, we have taken the time-dependent excitation spectra where also a clear red shift of 45 nm in excitation band edge maxima starting from 509 nm was be observed. The red shift in both excitation band edges as well as in emission maxima is proposed to be due to the change in the size of the NC. The average fluorescence lifetime of MPBI also shows a similar trend as a function of time. The lifetime is found to be 5.3 ns at 1 hr, which become 6.4 ns at 24 hr and remain unaltered henceforth. In a similar line, we propose that the increase in the average lifetime is due to the increase in the size of the MPBI NC with time. From the FCS measurement, I have calculated the capped radius of the NC with time. The capped radius value is found to increase from 4.2 nm at 1 min to 7.7 nm at 24 hr. The trend of the increase in size is found to correlate well with the shift in emission maxima and average lifetime indicating clearly that the size modulation is the reason for the observed change in the steady state and time-resolved emission measurements. The size increment is attributed to the individual crystal growth and the possibility of stacking of NCs is ruled out as FCS is done in nanomolar concentration. To confirm more we have taken TEM images of the NC suspension at three different times (1 min, 1 hr and 24 hr). Here also we have seen a clear increment in size distribution starting from 3 nm to ultimately 9.5 nm after 24 hr. The increment in the size of NC even after being capped with organic ligands may be due to the presence of dynamic capping. To confirm this, we have done the temperature-dependent emission and FCS studies, which shows high reversibility, confirming the presence of the equilibrium in the medium.

(2) Potassium-Induced Passivation of Deep Traps in Bismuth-Doped Hybrid Lead Bromide Perovskite Nanocrystal: Massive Amplification of Photoluminescence Quantum Yield

Pure LHP NCs exhibit very high PLQY due to their defect-tolerant nature. However, it suffers from quick degradation under the atmospheric condition that restricts its

use in practical life. Bi^{3+} doping into the LHP NCs has been found to be beneficial to boost its stability to a certain extent. But the incorporation of heterovalent Bi^{3+} into the LHP lattice modulates its electronic properties to a large extent and quenches the PLQY by introducing additional trap states. In this work, I have studied the nature of these Bi^{3+}-induced trap states and their probable energy position through time-resolved photoluminescence spectroscopic study. I have prepared $CH_3NH_3PbBr_3$ NCs (MPBr) and Bi^{3+} doped $CH_3NH_3PbBr_3$ NCs (MPBBr) through the facile ligand-assisted reprecipitation method. MPBBr NCs show a huge red-shifted PL centred at 510 nm from MPBr NCs (PL maxima 451 nm) along with the drop of PLQY from 72% to 9% which may be the result of electronic state modulation. The PL transient of MPBr NCs exhibits bi-exponential decay kinetics arising from excitonic recombination (2.3 ns) and surface trap-assisted recombination (~12 ns). Interestingly, the PL transient of MPBBr NCs exhibits a four-component decay kinetics. Apart from excitonic recombination (~4.4 ns) and surface trap-assisted recombination (~14 ns), the presence of two short-lived states having a lifetime of 0.1 ns and ~0.8 ns were observed. The 0.1 ns decay is proposed as the recombination of charge carriers through the deep trap state induced by Bi^{3+}. The PL transient at different wavelengths of the PL spectrum further reveals that this short-lived state (0.1 ns) density is higher in the red edge of the PL spectrum. The contribution of these short-lived trap states remained unaltered upon surface ligand modulation, further confirming that the origin of these trap states is not related to the surface. Analyzing these results, it is proposed that the short-lived state is originating from the deep traps within the lattice induced by uncoordinated bromine 4p orbitals. These bromine 4p orbitals could not have a proper bonding interaction with bismuth 6s

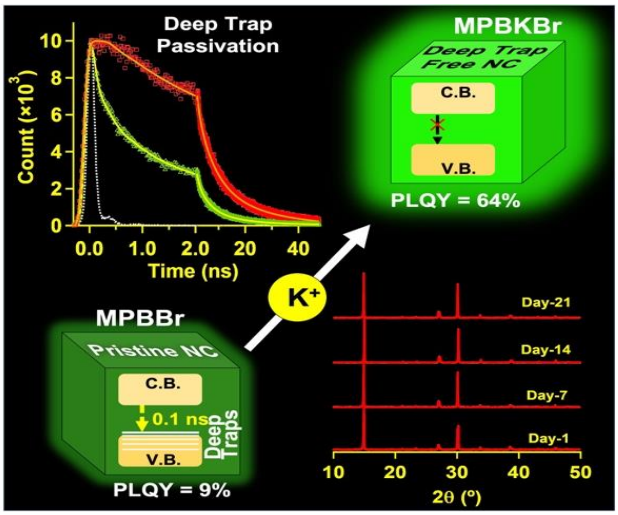

orbitals which remain inert due to higher spin-orbit coupling. Besides this, another reason for the formation of deep traps may be charge mismatch that leads to the formation of vacant sites in the NCs. Further, monovalent potassium was co-doped into the MPBBr NCs to passivate the deep traps as K^+ ions have a similar size with Pb^{2+} and Bi^{3+}. Upon co-doping, the PLQY of the system (MPBKBr NCs) showed a massive seven-fold amplification from 9% to 64%. The passivation of deep traps was further verified through the suppression of the short lifetime component in the PL transient. The atmospheric stability of the developed MPBKBr NCs was found to be much higher than MPBr and MPBBr NCs (observed up to 21 days). MPBKBr NC also sustained its PL and its phase stability up to 100 ºC.

(3) Massive Amplification of Photoluminescence and Exceptional Water Stability of $MAPbBr_3$ Nanocrystals through Core-Shell Nanostructure formation in a Self-Defense Mechanism

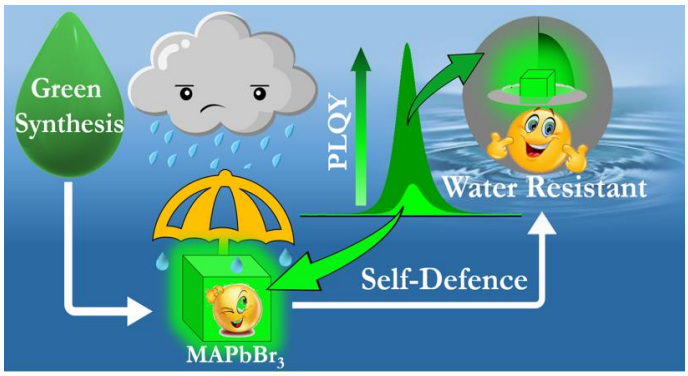

Vulnerability to the atmospheric condition and associated lead-related toxicity limit perovskite's practical/industrial use despite its tremendous promises in optoelectronics. Although the discarding of lead toxicity through the synthesis of lead-free perovskite NCs remains at the forefront in this aspect, the organic precursor solvent-related toxicity is mostly overlooked in this research field. In perovskite NC synthesis we often use toxic organic solvents like dimethylformamide (DMF), skin-penetrating dimethyl sulphoxide (DMSO), and octadecene, which may cause severe problems to the human body upon exposure. Also, the co-ordinating ability of these solvents to the perovskite NC surface was found to be detrimental to the long-term colloidal stability. So, the search for a new

alternative noncoordinating green medium is necessary for perovskite NC synthesis. I used an ionic liquid like so-called green solvent composed of methylamine and hydrophobic lauric acid to synthesize methylammonium lead bromide ($MAPbBr_3$) nanocrystals (NCs). The NCs were synthesized by direct addition of solid lead bromide salt into the ionic liquid medium. The synthesized NC shows moderate photoluminescence quantum yield (PLQY) (~19%) and high environmental stability (at least six months). Further, the entire visible range was tuned through the anion exchange method. More interestingly, the synthesized NC forms a core-shell structure in a unique self-defense mechanism in presence of water, which is proposed to be $MAPbBr_3$@lead laurate. This core-shell structure is found to be beneficial in (a) preventing further degradation of the NC, and it becomes highly water stable (at least for two months), (b) surface modification to induce a massive five-fold amplification of PLQY (to near unity), and (c) restricting the anion exchange reaction. Moreover, these unique properties are achieved without any special control. Also, the successful synthesis of other $MAPbX_3$ (X=Cl, I) demonstrates its potential universality as a green medium for the first time.

(4) Green Synthesis of 3D Cesium Lead Halide Perovskite Nanocrystals and 2D Ruddlesden-Popper Nanoplatelets in Menthol-based Deep Eutectic Solvents

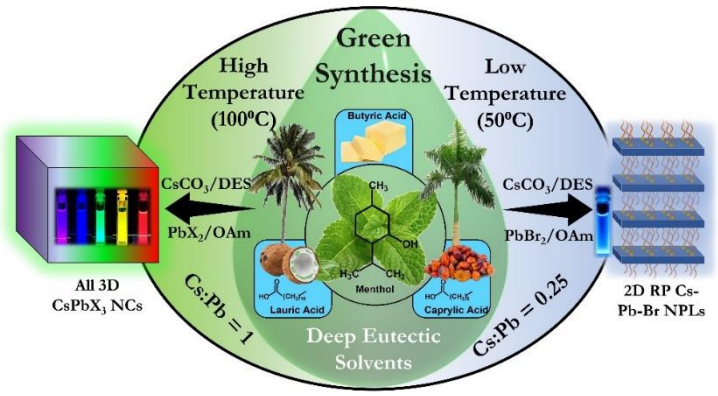

In previous work, I have used an ionic liquid like green medium to synthesize $MAPbBr_3$ NCs, which largely reduces the solvent-related toxicity. But the use of such methylamine-based ionic liquids in perovskite synthesis has some limitations such as, (i) It is only selective

towards methylammonium-based perovskite NC synthesis. (ii) The perovskite NCs have been synthesized by direct addition of lead halide salts into the ionic liquid medium which limits its control over size and morphology. (iii) And most importantly, as NCs are formed by the direct addition of solid lead halide salts to the ionic liquid medium, direct synthesis of mixed halide perovskite NCs and doped lead halide perovskite NCs are not possible in this medium. To overcome these issues, we need a green medium with a high solubilizing ability of precursor salts that will remain inert in the synthesis process. Addressing these problems, I have introduced three different menthol-based deep eutectic solvents (DESs), c.a. 1:2 lauric acid/menthol (LAMe), 1:1 caprylic acid/menthol (CAMe), and 1:1 butyric acid/menthol (BAMe), for the synthesis of cesium lead halide perovskite NCs. The NCs have been synthesized using two precursor approach using oleylamine as a ligand. The NCs show a uniform particle size distribution with an average size of ~12 nm. The NCs exhibit strong PL centered at 513 nm with PLQY of 78%, 67%, and 65% for $CsPbBr_3$ NCs prepared in LAMe, CAMe, and BAMe, respectively. PL decay kinetics of the NCs reveals the presence of three different recombination sites in the NCs. The short lifetime component of ~1.2 ns is attributed to the recombination of charge carriers through bromide vacancy-induced trapping sites and further passivated by oleylammonium bromide treatment to achieve near unity PLQY. The ultrafast carrier dynamics of $CsPbBr_3$ NCs prepared in LAMe was further investigated and compared with pristine $CsPbBr_3$ NCs prepared through normal hot-injection procedure where both NCs show similar carrier dynamics. The reaction temperature and added cesium to lead precursor ratio in the DES medium were found to be the key factor in controlling the dimensionality of the NCs. Lower temperature and lower cesium-to-lead ratio favored the formation of lower-order Ruddlesden-Popper (RP) 2D nanoplatelets (NPLs) where oleylammonium cation from oleylamine ligand act as spacer cation. With precise control over temperature and precursor ratio, I was able to synthesize pure $(OAm)_2Cs_2Pb_3Br_{10}$ RP NPLs (n=3) with PL maxima centered at 460 nm. To check the universality of the DES medium

all other lead halide/ mixed lead halide perovskite NCs were synthesized using the similar procedure which also show very high PLQY. This study presents a novel approach to the environmentally friendly synthesis of lead halide perovskite NCs and NPLs, which holds great potential for the practical large-scale synthesis of perovskites in industrial scale.

(5) Evidence of Short-Lived High Energy Emissive State in Lead-Free $Cs_3Cu_2I_5$ Nanocrystals Synthesized in Lauric Acid- Menthol Deep Eutectic Solvent

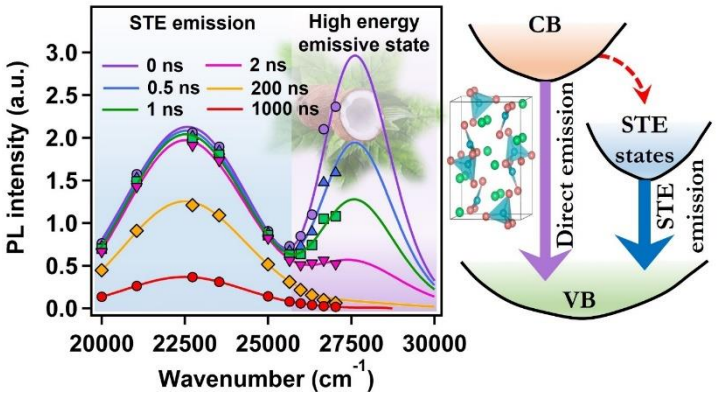

In the last two works, I have introduced two new types of green solvent media for LHP NC synthesis, which largely reduces the solvent-related toxicity in LHP NC synthesis. The menthol-based DES media was found to be highly promising for the synthesis of all types of LHP NCs and NPLs. In this work, I have used LAMe DES medium to synthesize lead-free $Cs_3Cu_2I_5$ NCs through which both solvent-related toxicity and lead toxicity can be eliminated. The synthesized NCs show a uniform size distribution with an average size of 22 nm. The synthesized NCs exhibit a highly Stoke-shifted strong broad steady-state PL band centered at 445 nm originating from the self-trapped excitonic (STE) emission. The STE emission in $Cs_3Cu_2I_5$ originates from the Jahn-Teller effect in the excited state, which is already discussed in detail in the literature. Because of this excited state Jahn-Teller distortion, the excited state modulates its energy immediately after photoexcitation and the charge carriers get trapped in it forming STE states. However, free excitons are always in a competitive relation with STE. So, it is abnormal that free exciton emission is not observed in steady-state PL spectra of $Cs_3Cu_2X_5$ perovskites. In this work, the PL decay kinetics of the $Cs_3Cu_2I_5$

NCs reveals the presence of a short-lived state in the higher energy. Further time-resolved emission spectra (TRES) analysis confirms that the high energy emissive state in the ~350 nm region is the origin of the short lifetime decay component. The high emission intensity in the early time of this ~350 nm emission band further nullifies the possible origin to be trap states and proposed to be originating from band-to-band free exciton recombination. The very short lifetime of this high-energy emissive state compared to the long-lived STE emission is the main culprit behind its absence in the steady-state PL spectrum. The evidence of the presence of a highly emissive energy state or free excitonic recombination is unique in copper halide perovskites and the evidence of its presence is presented for the first time to the best of our knowledge. This study will help to understand the photophysics of copper-based perovskites from a new perspective.

Table of Contents

Chapter-1

Introduction

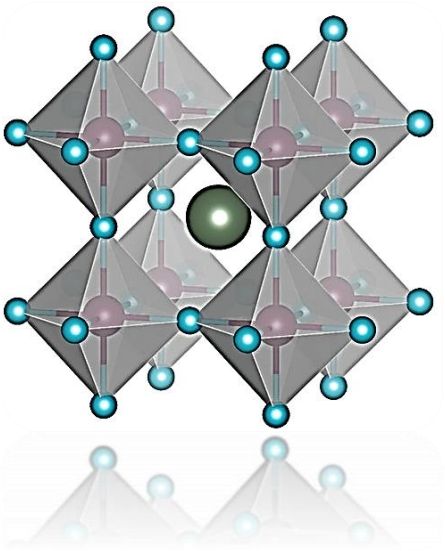

This chapter provides a very brief elementary idea about the semiconducting nanoparticles, particularly of a certain type, Lead halide perovskites (LHP). The band structure, quantum confinement effect, emission color tunability is subsequently discussed. This chapter also focused on the very brief idea about some very important characteristic features like crystal structure, basic charge carrier dynamics, surface properties, the importance of the trapping sites etc, which are the key knowledge to improve the system to make forward for the practical use. The effect of heterovalent doping, mainly Bi^{3+} doping on charge carrier dynamics and on stability is also well discussed. The final part of this chapter deals with the problems of using the environmentally hazardous solvents and discussion on green synthesis of perovskites which is a way of hope for the commercialization.

1.1 Motivation and thesis goal

"Oh Hi! So, what is your research area?"

"Hi! I am working in perovskite."

"Perovskite? What is this?"

"This is a class of materials having unique structure and properties."

"Like? Can you explain a little more?"

"The term perovskite refers to crystals with a very specific structure of the form ABX_3. In 1839 Gustav Rose discovered the mineral $CaTiO_3$ in the Ural Mountain of Russia. Latter its crystal was named perovskite after the Russian mineralogist Lev Perovski. Different atoms or molecules can form this ABX_3-type structure. For example, most of the Earth's mantle consists of $MgSiO_3$ which is also a perovskite. In general, you can say that the crystals having a structure of ABX_3 can be termed as perovskite."

"Oh, that means you are working on these minerals?"

"Actually, I am working on a particular nanocrystalline form of a particular perovskite naming lead halide perovskite."

"Is this a very new field? I haven't heard about this. I guess very few people are doing research on it!"

"You'd be shocked! Just go through Google Scholar or Scopus. Up until 2008, there were no more than 500 articles on this subject; after that, the number surged. More than 10000 publications have been published in the last ten years or so. Do you want to know what happened in 2009 that was so magical?"

During my early PhD years, I frequently engaged in this type of dialogue while discussing my research work with the people outside of my research community. To begin with, it is important to understand the reason behind the significant surge in the interest on lead halide perovskites (LHPs) have been observed over the last decade.[1] The journey of LHPs started with potential implementation as solar cell material by Myasaka research group back in 2009[2], paving the way for a whole new research field- the development of LHP- based photovoltaics. Recently, the efficiency have touched a new record of 29% of a LHP based solar cell.[3] Despite these remarkable developments, there has been very little widespread public awareness.

Now the question is why common people should be aware of this? LHPs are semiconductors and a promising material for optical purposes. Without computers, smartphones, and other electrical devices- all of which are made of semiconductors- we cannot imagine spending daily life. On top of that, solar cells can also use semiconductor materials. Promoting the usage of renewable energy is a top concern due to the current energy crisis. Energy demand is anticipated to skyrocket in the foreseeable future, particularly in India, given our constantly expanding population. In light of the limited supply of non-renewable energy, one must search for alternative renewable energy sources, such as sunshine, wind, water, etc. Utilizing solar energy may be beneficial due to India's geological location and year-round access to a lot of sun radiation. Despite being widely available, silicon solar cells are still relatively expensive for usage and large-scale manufacturing. On the other hand, perovskite solar cells are anticipated to be inexpensive in this context.[4] Among all perovskite materials, LHPs is particularly important due to their direct bandgap nature.[1, 4, 5] The remarkable improvements in LHPs' photovoltaic efficiency have been witnessed in thin films of these materials. This thesis will focus on LHP nanocrystals (NCs), a different form of LHP instead of bulk films. In contrast to the bulk films, NCs of LHPs usually exhibit strong visible photoluminescence (PL) proofs its eligibility as a potential material for light emitting diodes (LEDs). Such

NCs can be synthesised quickly and consistently utilising colloidal chemistry. Notably, the LHP's optical properties modulates dramatically when length scale is reduced to these extreme levels- a few nanometers or even smaller, as quantum confinement starts playing a role.[6, 7] Using these extremely important and interesting properties of the LHPs, the potential use of these system has already reached beyond solar cell and LEDs. So far, the LHP thin films/ NCs have been studied in different applications like X-ray detector, lasers and in photo catalysis.[8-10]

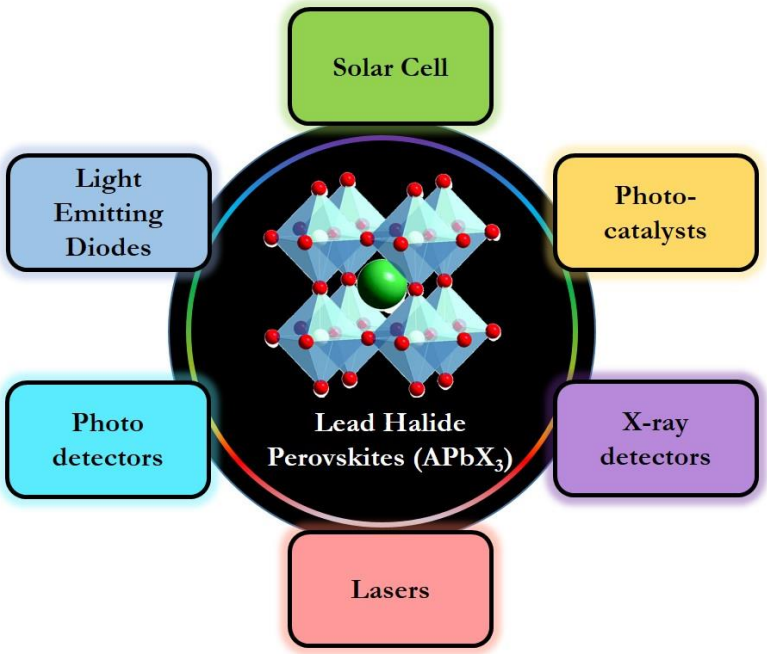

Figure 1.1. Schematic overview of the applications of the LHPs.

Despite these tremendous advancements of the LHP NCs, its practical use is still way off because of its poor environmental stability. The fundamental LHP NC research is mainly roaming around three different directions. Firstly, to increase its environmental and water stability. In general, researchers are trying to develop the environmentally stable LHP NCs through doping of metal ions, ligand engineering and core-shell nanostructure formation.[11, 12] The second direction focuses on the amplification of the photoluminescence quantum yield (PLQY) of the NCs to near unity to maximize LED efficiency. This field also involves surface ligand

engineering and doping to reduce the nonradiative deactivation channels.[11] The third part mainly related to the toxicity. Lead is highly toxic in nature, which arises an inevitable question mark on the environmental acceptability of these LHP NCs.[13] This can be tackled through partial substitution of lead by other metal ions (B-site doping) to minimize the lead content and the ultimate goal of this field is to reach lead free perovskite NCs with high PLQY. However, overcoming solvent-related toxicity is one of the most crucial but overlooked aspects of this research subject. Toxic solvents including dimethylformamide (DMF) and NMP are typically used in perovskite synthesis. Hazardous organic solvents, such as octadecene and skin penetrating DMSO, are also commonly used. Another major worry is that these precursor solvents have a high propensity to coordinate with the perovskite surface, allowing the perovskite structure to degrade.[14, 15]

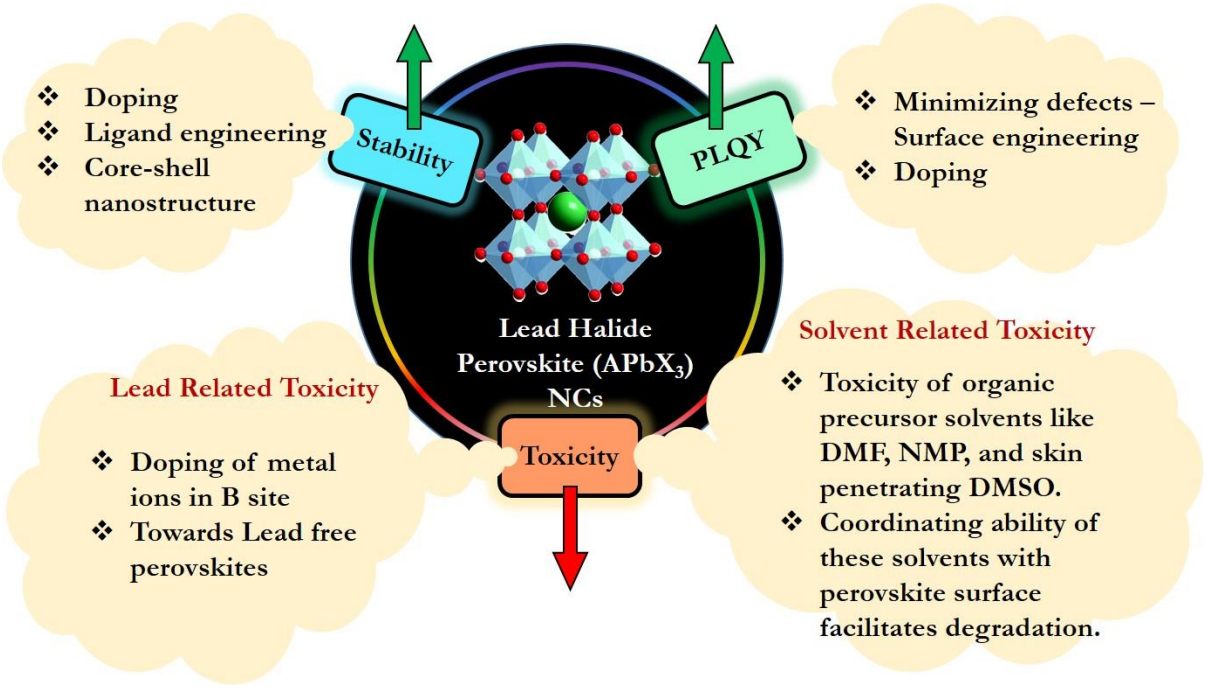

Figure 1.2. Schematic representation of the fundamental research areas on the LHP NCs.

The first part of this thesis focuses on the modulation in optical properties and on the increment of the stability of the LHP NCs upon heterovalent Bi^{3+} doping. The

second part of the thesis deals with the solvent related toxicity. In this part, I have tried to discard conventionally used organic precursor solvents with environment friendly so-called green solvents to synthesize the LHP NC systems. In the final part of this thesis, environment friendly green solvent is used lead-free $Cs_3Cu_2I_5$ perovskite NCs to discard lead related as well as solvent related toxicity to achieve environmental sustainability. Also, the evidence of the presence of high energy emissive state in coper halide perovskite remain in focus. In the journey, we will also see the suppression of the nonradiative processes to achieve high PLQY.

1.2. Band structure and semiconductor basics

1.2.1. Free electron in space

For a free electron propagating in one dimension without any potential, the Schrödinger equation is expressed as,

$$\frac{d^2\Psi}{dx^2} + \frac{2m}{\hbar^2}E\Psi = 0 \qquad (1.2.1)$$

In general, this differential equation's solution can be written as,

$$\Psi(x) = Aexp(ikx) + Bexp(-ikx) \qquad (1.2.2)$$

Where A and B are constants and,

$$k = (\frac{2m_eE}{\hbar^2})^{\frac{1}{2}} \qquad (1.2.3)$$

The first term in the equation 1.2.2 corresponds to the propagation of wave in the positive *x*-direction, and the second term corresponds to the propagation of wave in the negative *x*-direction. From equation 1.2.3 we can write,

$$E = \frac{\hbar^2k^2}{2m_e} \qquad (1.2.4)$$

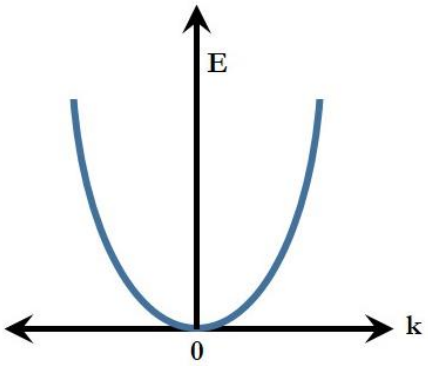

Figure 1.3. Plot of electron energy *E* vs *k* for free electron.

This shows that all energy values are allowed for free electrons.

Since $E = \frac{p^2}{2m_e}$, the momentum $p = \hbar k$. And we know that $p = \frac{h}{\lambda}$ or, $p = \frac{2\pi\hbar}{\lambda}$. Thus, we can say that $k = \frac{2\pi}{\lambda}$, where k is the electrons's wave vector. The *E*(k) relation i.e., relation of electron energy with the momentum, is shown in figure 1.3.

1.2.2. The Kronig-Penney model: Electron in a periodic crystal potential

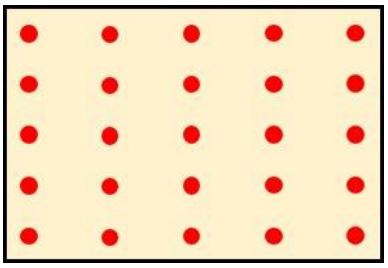

Figure 1.4. Simplified form of a crystal showing periodic arrangements of atoms.

The crystal is an ordered and periodic arrangement of atoms (figure 1.4). When an electron moves through a crystal lattice, it will experience a periodic potential induced by the atoms in a particular direction.[16, 17] For one dimensional case periodic potential is expressed as $V(x) = V(x + a)$, where 'a' is the distance between two successive atoms in the *x*-direction (for one dimensional case).

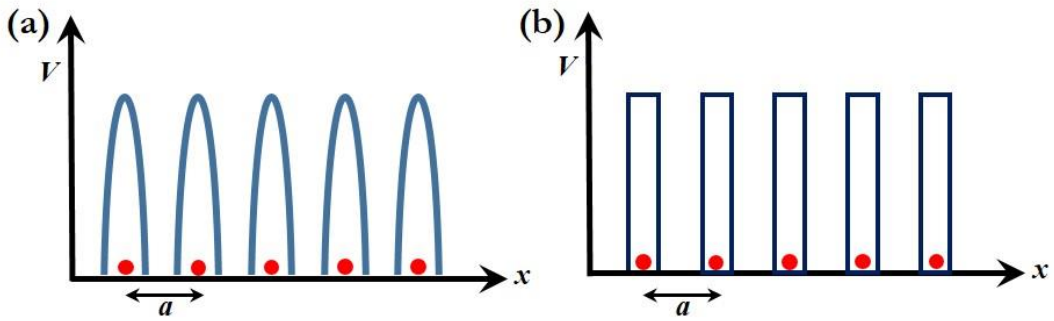

Figure 1.5. (a) Scheme representing the potential energy variation of electrons in a one-dimensional crystal lattice where '*a*' is the lattice constant i.e., distance between two successive atoms in that direction. (b) An approximation of the realistic potential energy, as shown in (a), according to the Kronig-Penney model.

The Schrödinger wave equation's solution for this case can be written using periodic Bloch functions[17]

$$\Psi(x) = u(x)\exp(ikx) \qquad (1.2.5)$$

Where $u(x) = u(x + a)$, is called a Bloch function. This is a periodic function which is periodic with the crystal structure or lattice constant 'a', which is k value dependent. The analysis of the realistic potential in a crystal lattice (figure 1.5a) would be very complex. And thus, a simplified model can be considered as shown in figure 1.5b.

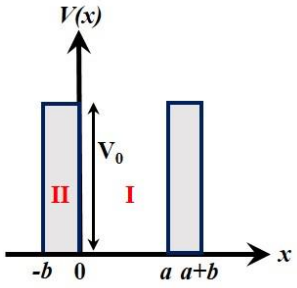

Figure 1.6. One-dimensional periodic potential diagram according to Kronig-penny model.

In the Kronig-Penny model, the electronic motion is considered for a one-dimensional array of square potential barriers of width 'a' (area I in figure 1.6),

which are separated by potential barriers V_0 having width '*b*' (area II in figure 1.6). These parameters i.e., '*a*', '*b*', and V_0 are very much dependent on the crystal structure of the material as well as on the elements of the crystals.[16]

The boundary condition for the solution of this one-dimensional case depends on the following equation,[16]

$$\frac{P \sin \alpha a}{\alpha a} + \cos \alpha a = \cos k\alpha \qquad (1.2.6)$$

In this equation 1.2.6,

$$\alpha = \frac{(2m_e E)^{\frac{1}{2}}}{\hbar} \qquad (1.2.7)$$

'P' is the measure of strength of the potential barrier. And,

$$P = \frac{m_e V_0 b a}{\hbar^2} \qquad (1.2.8)$$

Thus, the energy E relates to *k* (through α) by the equation 1.2.6. This implies that E are allowed for certain α values for electrons in this periodic potential.[18] This can be further visualized by plotting $\frac{P \sin \alpha a}{\alpha a} + \cos \alpha a$ as a function of αa, as depicted in figure 1.7.

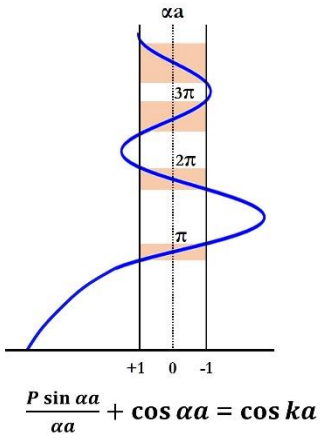

Figure 1.7. Plot of $\frac{P \sin \alpha a}{\alpha a} + \cos \alpha a$ as a function of αa.

The cos *k*α values are only acceptable if it lies between +1 and -1, implying that, energies will be in the same limit, as α is a function to E.[16, 19] This effectively indicates that the allowed energies of the electrons will be within specific energy band depicted inside the shaded areas in figure 1.7, when travelling in a periodically fluctuating potential field. These permitted energy bands are divided into zones that correspond to forbidden energy ranges when cos ka is greater than +1 or less than -1. Thus, summarizing these observations, (i) The energy has allowed and forbidden regions for movement of electron in crystal potential., (ii) the width of these bands is a function of P, i.e., $V_0 b$ and (iii) The forbidden bands become narrower with increasing E. Furthermore, the curve is steeper with larger P, which causes shrinkage of allowed bands and broadening of forbidden bands. It is important to note that at the boundary of an allowed band $\cos k\alpha = \pm 1$; and hence $k = \frac{n\pi}{a}$; demonstrating the energy become discontinuous at these *k* values. These circumstances also match the Bragg reflection rule, indicating that standing waves can be used to describe the electron states with $k = \frac{n\pi}{a}$, i.e., These electrons are unable travel within lattice, which reveals the existence of an energy gap in that specific *k*.

1.2.3. Energy bands in crystals

The presence of the energy gaps, and other related properties, can be thought of in terms of how much energy is needed to free an electron from a material and allow the free movement through it (under the applied field).[16, 17, 20] The explication of key aspects of the electronic properties of semiconductors is made easier by the formulation of the E(k) relationship, which calls for a more detailed ellaboration of the energy bands in crystals. For free electrons, according to equation 1.2.4 this relationship is, $E = \frac{\hbar^2 k^2}{2m_e}$.

And for one-dimensional case,

$$k_x = \left(\frac{2m_e}{\hbar^2}\right)^{\frac{1}{2}} E^{\frac{1}{2}} \qquad (1.2.9)$$

Which is a parabolic function as shown in figure 1.3.

According to Kronig-Penney model (equation 1.2.6),

$$\frac{P \sin \alpha a}{\alpha a} + \cos \alpha a = \cos k\alpha$$

For the free electron system, P is 0. Thus,

$$\cos \alpha a = \cos k\alpha \qquad (1.2.10)$$

As the cosine function is periodic in 2π; so,

$$\cos \alpha a = \cos k\alpha = \cos(k\alpha + n2\pi) \qquad (1.2.11)$$

where $n = 0, \pm 1, \pm 2, \pm 3, \ldots \ldots \ldots$

And thus, $\alpha a = ka + n2\pi$ (1.2.12)

So, combining equation 1.2.7 and equation 1.2.12,

$$\frac{(2m_e E)^{\frac{1}{2}}}{\hbar} = k + \frac{n2\pi}{a} \qquad (1.2.13)$$

This shows that iteratively repetition of the parabola with a factor $\frac{n2\pi}{a}$. Which means, the energy and *k* is in periodic relation with the periodicity $\frac{2\pi}{a}$. As discussed earlier, the discontinuity in E(*k*) diagram occurs at $\cos k\alpha = \pm 1$ in a periodic crystal potential; that means at the allowed band's bounday, $k = \frac{n\pi}{a}$ $(n = 0, \pm 1, \pm 2, \pm 3, \ldots \ldots \ldots)$. This indicates that except for $k = \frac{n\pi}{a}$, in a periodic lattice the electron behaves like a free particle. This is depicted in figure 1.8, the E(*k*) dependence in extended zone representation.[16, 21]

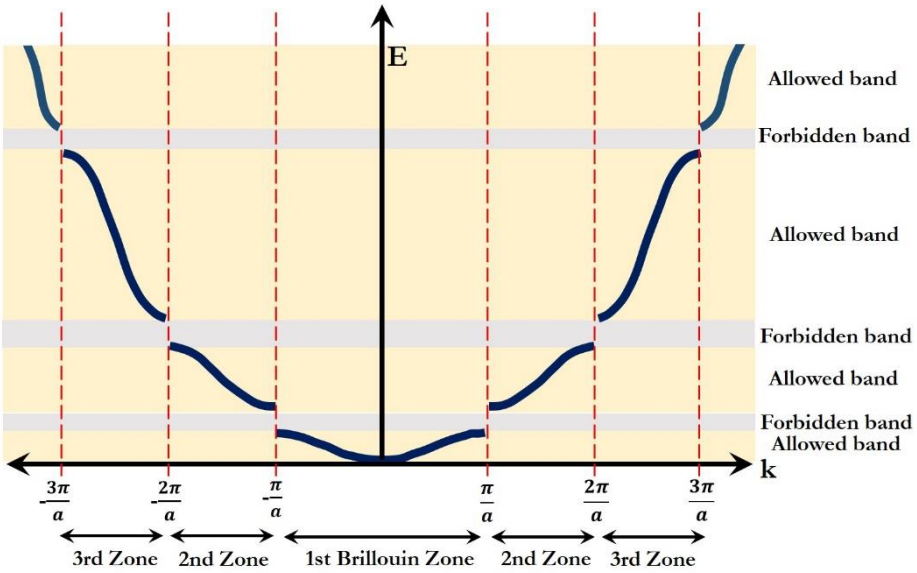

Figure 1.8. Extended-zone depiction demonstrating E(k) deviation for free electrons at band edges with $k = \frac{n\pi}{a}$. First three Brillouin zones are also indicated.

Figure 1.8 shows the Brillouin zones, i.e., the k values for each energy band. (These are labelled as the 1st zone, 2nd zone, 3rd zone, etc. in the illustration).

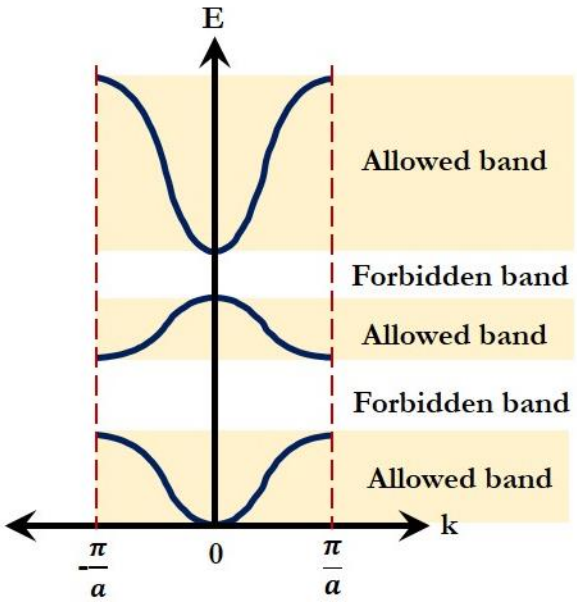

Figure 1.9. The reduced-zone representation

The reduced zone representation derives from folding the bands back into the first (Brillouin) zone. (see figure 1.9).[16, 17] For discussing various semiconductor properties, this reduced zone model is very important as it contains almost every information related to the transport and optical properties of the semiconductor.[22]

1.2.4. Electronic band in real space

So far, we have seen the energy bands in the reciprocal space, i.e., in *k* space. This $\vec{k}$ vector has a dimension inverse to the length ($\vec{a}$) for which it is called as reciprocal space. All the electron band calculations are generally done in reciprocal space as it is directly related to the Schrödinger wave equation of the system. Now to visualize this electronic bands in real space (*r*), we must start again with free electron model. Now for a electron, moving in a zero potential (free electron) in real space (*r*) can have every possible energy as there is no restriction. In other term, we can say that the free electron energy is continuous (see figure 1.10).[16, 17]

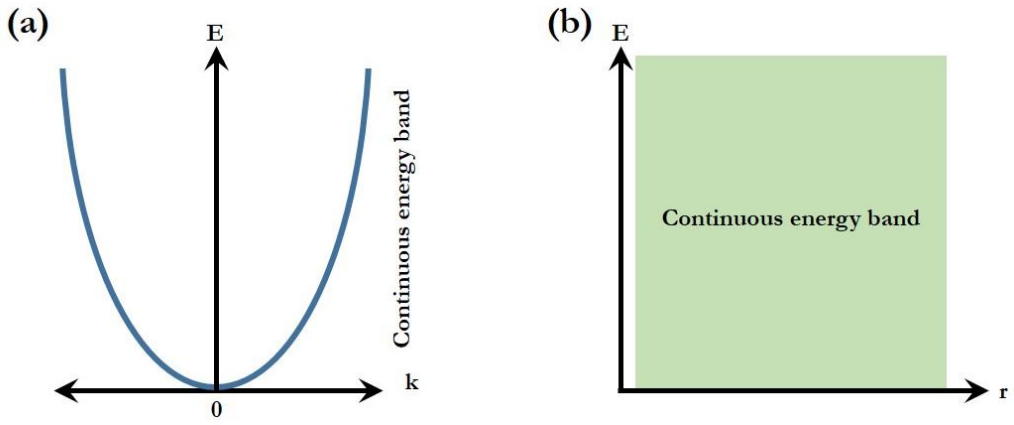

Figure 1.10. Electronic energy band for a free electron system in (a) reciprocal space and (b) in real space.

Now electron in a periodic crystal potential according to Kronig-Penny model, from equation 1.2.6,

$$\frac{P \sin \alpha a}{\alpha a} + \cos \alpha a = \cos k\alpha$$

For free electron P is 0 as discussed earlier and energy of the system will be

$$E = \frac{\hbar^2 k^2}{2m_e}$$

In case, $P \to \infty$, $\sin \alpha a = 0$ and thus $\alpha a = n\pi$, or $\alpha^2 = \frac{n^2\pi^2}{a^2}$. From this using equation 1.2.7, we get

$$E_n = \frac{\hbar^2 \pi^2}{2m_e a^2} n^2 \qquad (1.2.14)$$

where $n = 0, \pm 1, \pm 2, \pm 3, \ldots\ldots\ldots$

At these values of n, the electron will behave like a standing wave and a deviation in $E(k)$ diagram from the free electron occurs. In k space it is already shown in figure 1.8. In real space thus discontinuity in energy takes place at $E = 0$, $\frac{\hbar^2\pi^2}{2m_e a^2}, 4\frac{\hbar^2\pi^2}{2m_e a^2}, 9\frac{\hbar^2\pi^2}{2m_e a^2}, \ldots\ldots$ so on. Here for one-dimensional case, the space coordinate r is equivalent to a. This can be visualized by figure 1.11 as follows.

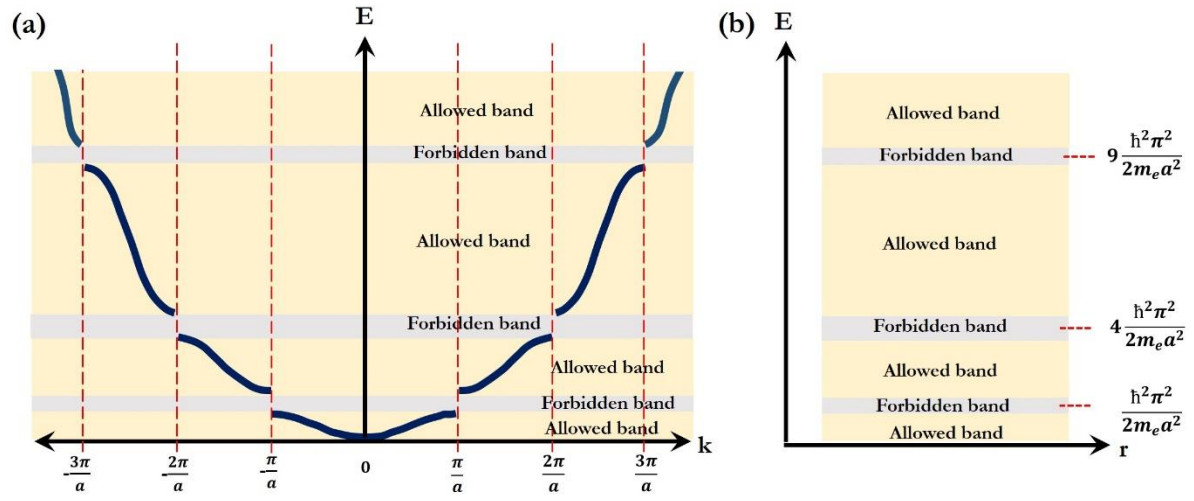

Figure 1.11. Extended-zone representation in (a) reciprocal space and (b) its visualization in real space.

In reduced-zone representation also this can be visualized as figure 1.12.

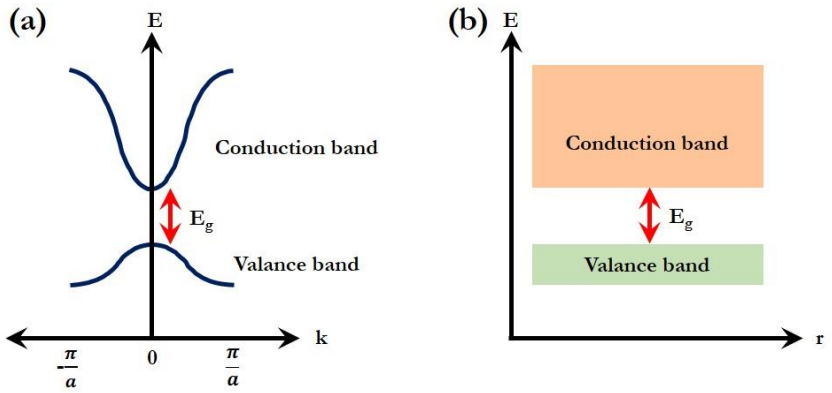

Figure 1.12. Reduced-zone representation in (a) reciprocal space and (b) its visualization in real space.

1.2.5. Concept of effective mass and its importance

In semiconductor crystal for periodic potential the property of electron modifies, resulting the electron mass different than free electron mass.[16, 17, 23] The actual experimental mass of the electron in this periodic potential that is within the electronic band here is the effective mass (m^*).[23] All the calculations with electron mass that we have done so far in the previous sections is actually the effective mass of electron.

Recalling the equation 1.2.4. now can be written as,

$$E = \frac{\hbar^2 k^2}{2m^*} \tag{1.2.15}$$

$$\text{or } \frac{dE}{dk} = \frac{2\hbar^2 k}{2m^*} \tag{1.2.16}$$

$$\text{or } \frac{d^2E}{dk^2} = \frac{\hbar^2}{m^*} \tag{1.2.17}$$

Rearranging the equation 1.2.17, we get

$$m^* = \hbar^2 \left(\frac{d^2E}{dk^2}\right)^{-1} \tag{1.2.18}$$

This means the effective mass of the electron is related to the curvature of the $E(k)$ diagram in a inverse proportional relation. This means, higher the curvature of the band, lesser the effective mass of the electron. This concept is very much important to understand the carrier transport i.e., current flow in a semiconducting material.[16] Lighter electrons can travel through the lattice in a much faster rate than heavier electrons, suggesting materials having higher curved bands are much promising as device material.[24] Also, from the reduced-zone representation of E(k) diagram (figure 1.9), we can say that (i) the effective mass is positive in conduction band (as $\frac{d^2E}{dk^2} = +ve$) and the effective mass is negative in the valance band (as $\frac{d^2E}{dk^2} = -ve$), except near the top and bottom of the valance and conduction band. (ii) Near the top of the valence band and bottom of the conduction band, the effective mass is not dependent on which means at these points energy is constant. In the valance band, the electron having a negative mass is termed as an "electron hole".[16] A negative charge with a negative mass is equivalent to a positive mass with a positive charge in the presence of an electric field. As a result, holes are defined as carriers with positive charge and positive mass. This suggests that in an electric field, hole in the valence band and electron in the conduction band moves in opposite direction in real space. After photoexcitation in semiconducting system, an electron goes to the conduction band and a corresponding hole is left behind in the valance band which is commonly referred to a photoexcited state.[25, 26] After photoexcitation the effective mass of an electron can be different than its corresponding hole if the excitation takes place at k value not equal to zero, as the curvature of the valance band and conduction band may be different. But their momentum will be conserved as their motion will be guided by the band structure.[16]

1.2.6. Direct and indirect bandgap semiconductor

During an electronic transition (absorption or emission) in a semiconductor the momentum and energy ($\hbar k$) must be conserved. When the conduction band minima and valence band maxima occur at same *k* value then the semiconductor is termed

as direct bandgap semiconductor (figure 1.13a). Whereas, if conduction band minima and valence band maxima occur at different *k* values then the semiconductor is termed as indirect bandgap semiconductor (figure 1.13b).

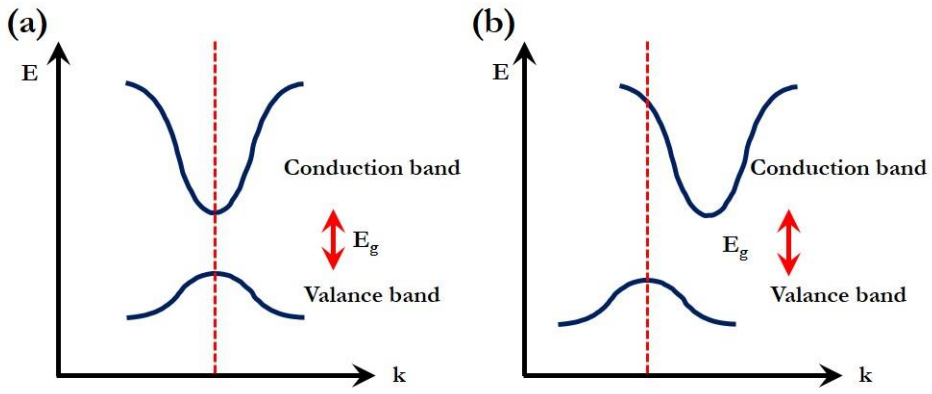

Figure 1.13. Schematic representation of E-k diagram of (a) direct bandgap semiconductor and (b) indirect bandgap semiconductor.

The electron after photoexcitation goes to the conduction band from the valence band which is the fundamental absorption process. In this process, momentum and energy must both be conserved. In the absorption process the electron momentum is conserved because the crystal momentum is far larger compared to photon momentum. In direct bandgap semiconductor the optical transitions across the bandgap are direct as both valance band maxima and conduction band minima are situated at same *k* values. For indirect band gap semiconductor, the transition across the bandgap cannot be possible directly as *k* values are different at valance bond maxima and conduction band minima. In this type of materials, for optical transitions involvement of phonon is required. For this reason, in indirect bandgap semiconductor optical transitions are very weak.

Silicon (Si) have the indirect bandgap and for this the light absorbing ability of commercially available Si-based solar cells are very weak. For an efficient amount of absorption, the thickness of the Si-layer in Si-based solar cells is usually around 500 μm which makes these systems very costly. However, unlike silicon,

perovskites have direct bandgap and making ~200 nm thick perovskite solar cell sufficient for practical use. This makes perovskite system much more superior than silicon in solar cell.

1.2.7. Semiconductor- bulk to nano level: Lower dimensional semiconductors

So far, we have discussed the band structure of the bulk semiconducting system. When the size of the semiconductor reduced to nano level (~1-30 nm), we often see change in its properties like absorption band edge position, PL and so on. This effect is termed as quantum confinement effect in semiconductor. This can be well explained using density of states (DOS).

The number of states available per unit energy per unit volume of a semiconductor is known as DOS. This DOS is a function of energy and can be expressed as,[16]

$$g(E) = \frac{4\pi}{h^3}(2m^*)^{\frac{3}{2}}\sqrt{E} \qquad (1.2.19)$$

This means that the DOS is energy's parabolic function and as energy increases the number of available states also increases. In semiconductor if the conduction band minima energy is E_c, then bellow this E_c the DOS will be zero. Thus, the equation 1.2.19 can be modified as,

$$g(E) = \frac{4\pi}{h^3}(2m^*)^{\frac{3}{2}}\sqrt{(E - E_c)} \qquad (1.2.20)$$

For valence band, the DOS expression can be written as,

$$g(E) = \frac{4\pi}{h^3}(2m^*)^{\frac{3}{2}}\sqrt{(E_v - E)} \qquad (1.2.21)$$

E_v is the energy of valence band maxima. This can be better visualized in figure 1.14.

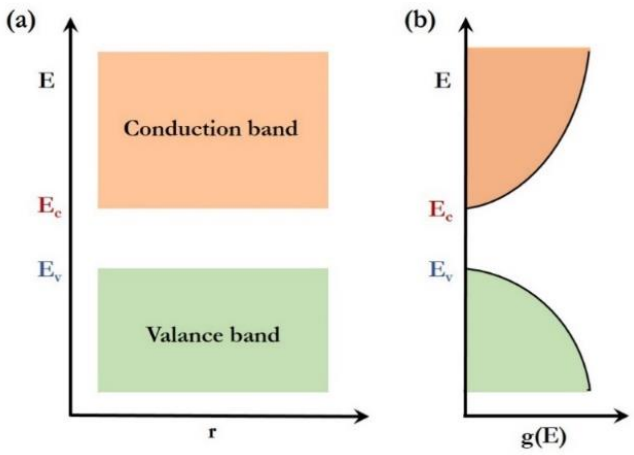

Figure 1.14. (a) Conduction and valence band energies and (b) corresponding DOS of a bulk 3D semiconductor.

For two-dimensional (2D) quantum well (QW) semiconducting system, the carrier movement are confined in one direction (height of the well), and free to move to other two direction (in plane). In the plane the semiconductor will behave like a bulk. In 2D QW the energy level of electron can be obtained from solving the Schrödinger equation in an infinitely deep potential well, which can be expressed as,[16]

$$E_n = \frac{\hbar^2\pi^2}{2m_e^* L^2} n^2; (n = 1,2,3, \ldots\ldots) \quad (1.2.22)$$

The $\frac{1}{L^2}$ term is the energy dependence with the width (or height) of the QW and is known as quantum size effect. For conduction band this relation can be expressed as (given in the confinement direction the finite motion corresponding to the *x*-axis and the infinite motion in the *y*-*z* plane),

$$E(k) = E_c + E_{n_x} + \frac{\hbar^2(k_y^2+k_z^2)}{2m_e^*} \quad (1.2.23)$$

where, E_{n_x} is given by equation 1.2.22,

$$E_{n_x} = \frac{\hbar^2\pi^2}{2m_e^* L_x^2} n^2 \quad (1.2.24)$$

In a two-dimensional system (i.e., QW) the DOS per unit area for one sub-band for the conduction band can be represented as (when the energy greater than $E_c + E_{n_x}$)

$$g(E) = \frac{m_e^*}{\pi \hbar^2} \tag{1.2.25}$$

As a result, in this scenario, the DOS is constant for each quantum number n_x (i.e., it is independent of energy), and the total DOS can be expressed as the sum of these for all values of n_x, resulting in a staircase-type distribution, with a step height determined by equation 1.2.25.

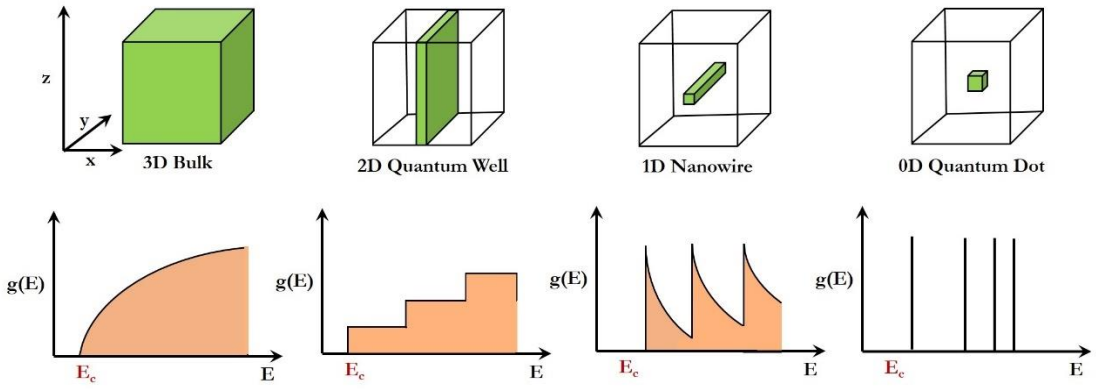

Figure 1.15. Scheme representing lower dimensional structures and corresponding DOS.

Quantum wire confines carriers like a potential well. (both electrons and holes) in two directions. The E(k) relation is for the conduction band is,

$$E(k) = E_c + E_{n_x} + E_{n_z} + \frac{\hbar^2 k_y^2}{2m_e^*} \tag{1.2.26}$$

In this instance, $\sqrt{E}$ dependence can be used to define the DOS in each of the sub-bands as a function of energy (see figure 1.15).

For quantum dots, the carriers are confined from all direction and energy can be expressed as,

$$E(k) = E_c + E_{n_x} + E_{n_y} + E_{n_z} \tag{1.2.27}$$

In this case, a set of discrete δ functions can describe the DOS (figure 1.15).

1.2.8. Concept of quantum confinement

According to Heisenberg uncertainty principle, if a moving particle with a mass *m* is confined to a region (Δx) in *x*-direction, then the uncertainty in its momentum (ΔP_x) is given by,

$$\Delta P_x \approx \frac{\hbar}{\Delta x} \tag{1.2.28}$$

The particle gains additional kinetic energy from this confinement along the *x*-direction, also referred to as confinement energy. This can be expressed as,[27]

$$E_{confinement} = \frac{(\Delta P_x)^2}{2m^*} \approx \frac{\hbar^2}{2m^*(\Delta x)^2} \tag{1.2.29}$$

This confinement energy become substantial when kinetic energy of the charged carriers ($E_{x(T)}$) is comparable because of its thermal motion in the x-direction. In this condition,

$$E_{confinement} = E_{x(T)} \approx \frac{1}{2} k_B T \tag{1.2.30}$$

Using equation 1.2.29 and 1.2.30 we get,

$$\frac{\hbar^2}{2m^*(\Delta x)^2} \approx \frac{1}{2} k_B T \tag{1.2.31}$$

From this we get,

$$\Delta x \approx \sqrt{\frac{\hbar^2}{m k_B T}} \tag{1.2.32}$$

Now, the de Broglie wavelength related to thermal motion of the carriers along *x*-direction is given by,

$$\lambda_{DB}^{c} \approx \frac{\hbar}{P_{x(T)}} = \frac{\hbar}{2m^* E_{x(T)}} = \frac{\hbar}{\sqrt{m k_B T}} \tag{1.2.33}$$

Using equation 1.2.32 and equation 1.2.33 we get,

$$\lambda_{DB}^{c} \approx \Delta x \qquad (1.2.34)$$

So, from equation 1.2.34 we can say that for quantum confinement, the de Broglie wavelength related to the thermal motion of the carriers must be comparable with the length of the system (in a particular direction, or in all direction).

In general, we can say that a nanomaterial is within quantum confinement when its size is comparable with the de Broglie's wavelength of its charge carriers (electron or hole). With increase in size, the confinement energy will decrease, and the system's properties will be closer to the bulk system. For this, within quantum confinement regime if we increase the size of the NCs, the bandgap changes to lower values and we can tune the PL position by this fine tuning of size (figure 1.16).

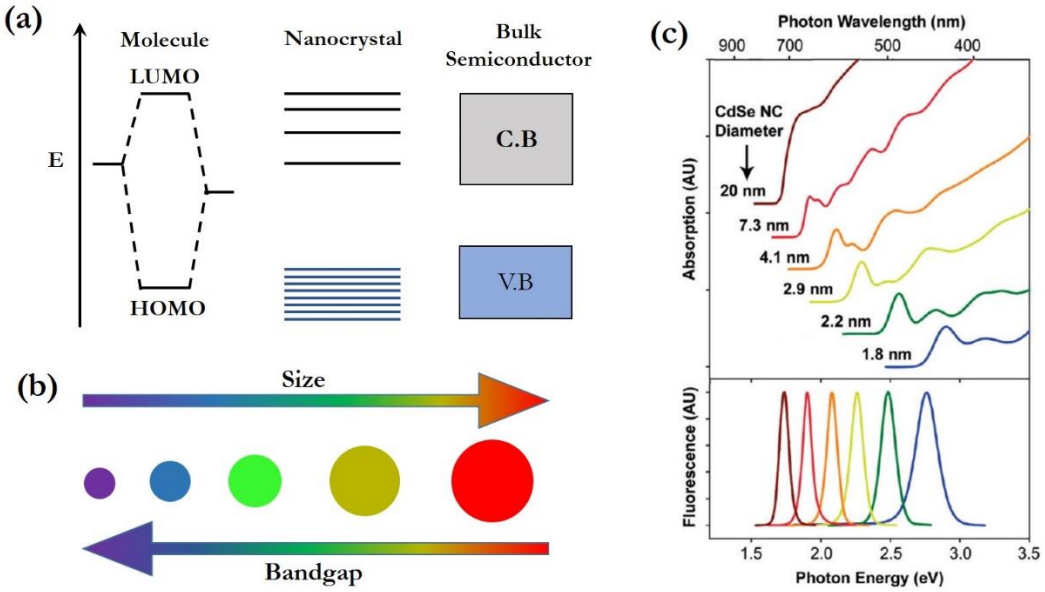

Figure 1.16. Quantum confinement effect. (a) Schematic representation of molecular orbital energy levels from molecule, nanocrystal to bulk semiconductor. (b) Schematic representation of size-bandgap relationship. (c) Size dependent bandgap variation and PL tunability of CdSe QDs of varying diameters. Reproduced from Ref. 40.

These confinement size effects now differ from one material to another. As the motion of the carrier is governed by the band curvature of the material, the de Broglie's wavelength associated with it will also vary; this effectively alter the size of the quantum confinement regime in different materials.

These effects are shown for quasi-spherical nanocrystals in Figure 1.16c, demonstrating how nanocrystal size can be used to control the wavelengths of absorption and fluorescence. CdSe nanocrystals (Eg=1.76 eV) can be regulated through quantum confinement to emit in whole visible region, making them valuable for both imaging study in biological systems and optoelectronic devices of many types.

1.2.9. Exciton and exciton Bohr radius

Absorbing a photon electron is excited from valence band to conduction band leaving behind a positively charged hole in valance band. This electron-hole pair (electron in conduction band and hole in valance band) is called an exciton (see figure 1.17). The exciton in a semiconductor is known as a quasi-particle in which electron and hole are bound in a coulombic attraction. In Wannier-Mott model, the electron and hole are considered to form a hydrogen like atom in solid state in which hole in valence band replaces the nucleus and electron in the conduction band replaces the hydrogen electron.

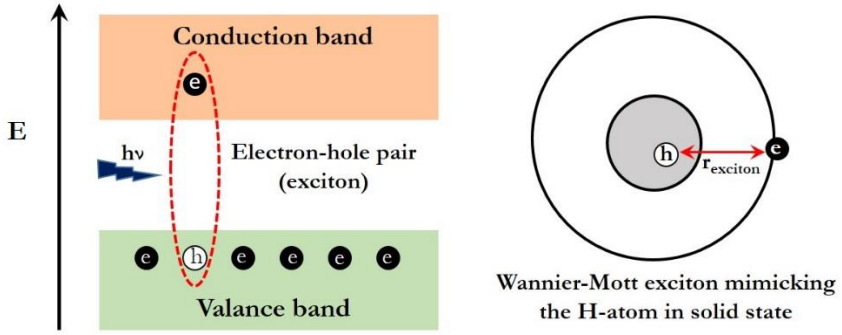

Figure 1.17. Schematic representation of exciton formation after light absorption in semiconductor.

The effective mass approximation allows to consider electrons and holes as free particles in respective conduction band and valence band by neglecting the periodic crystal potential of a medium having dielectric constant ε. By resolving a Schrödinger equation which is similar to the electron state in a hydrogen atom, one can get the wave functions and energy values. The exciton's energy values are solution to the particle in a box problem when reduced mass is used in place of the original mass.[27, 28]

$$|E_{exciton}| = E_{confinement} = E_e + E_h \tag{1.2.35}$$

$$\text{Now, } E_e + E_h = \frac{n^2h^2}{8m_e^*R^2} + \frac{n^2h^2}{8m_h^*R^2} = \frac{n^2h^2}{8R^2}\left(\frac{1}{m_e^*} + \frac{1}{m_h^*}\right) \tag{1.2.36}$$

$$\text{As reduced mass of electron-hole system } \frac{1}{\mu} = \frac{1}{m_e^*} + \frac{1}{m_h^*} \tag{1.2.37}$$

$$|E_{exciton}| = E_e + E_h = \frac{n^2h^2}{8\mu R^2} = \frac{\hbar^2\pi^2}{2\mu R^2} \ (taking\ n = 1) \tag{1.2.38}$$

Where, R is the radius of a spherical particle (exciton here); m* is the corresponding effective mass; and μ is the reduced mass of electron-hole system as stated in equation 1.2.37.

The radius of the exciton can be stated from the Coulombic attraction between electron and hole as,[29]

$$r_{exciton} = -\frac{\varepsilon_r\hbar^2}{\mu e^2} \tag{1.2.39}$$

The exciton binding energy ($E_{exciton}$) using equation 1.2.38 thus can be given by,

$$E_{exciton} = -\frac{\mu e^4}{2\hbar^2\varepsilon_r^2} = -\frac{\hbar^2}{2\mu r_{exciton}^2} \tag{1.2.40}$$

Using this 1.2.40 equation, we get

$$r_{exciton} = \frac{\hbar^2 \varepsilon_r}{e^2}\left(\frac{1}{m_e^*} + \frac{1}{m_h^*}\right) \quad (1.2.41)$$

The exciton Bohr radius is determined by the effective masses of the electron and hole and the material's dielectric constant (ε_r). It is a crucial factor in determining how much confinement a material possesses.

1.2.10. Effect of confinement on bandgap

Due to their distinctive characteristics from their bulk equivalent, the nanocrystalline forms of semiconductor materials are particularly fascinating. These qualities result from the excitons' "quantum confined" nature. From now on, "confinement" refers to the confinement of the excitonic wavefunction. The size of the system and the exciton Bohr radius are used to determine whether or not a system is quantum confined. As a result, quantum confinement is a size dependent feature, where a change in the diameter of the NCs causes changes in the electrical and optical properties. A system's band structure directly depends on how big and how many dimensions it has. Figure 1.15 depicts a schematic illustration of a bulk three-dimensional (3D), two-dimensional (2D), one-dimensional (1D), and zero-dimensional (0D) nanostructure. The system's bandgaps increase as confinement increases. The following generic statement defines the bandgap energy of such a quantum confined system:[28]

$$E_g^{QD} = E_b^{bulk} + \frac{\hbar^2 \pi^2}{2\mu R^2} - 1.786\frac{e^2}{\varepsilon R} - 0.248E_{Ry}^* \quad (1.2.42)$$

$$\text{Where } E_{Ry}^* = 13605.8\frac{1}{\varepsilon}\left(\frac{m_0}{m_e^*} + \frac{m_0}{m_h^*}\right)^{-1} \quad (1.2.43)$$

The bandgaps of the confined and bulk systems are represented, respectively, by E_g^{QD} and E_b^{bulk}. The second term arises due to the confinement energy associated with electron and hole. The energy of Coulombic attraction between the electron and hole is represented by the third term. The final term corresponds to exciton Rydberg

energy, which arises due to spatial correlation between electron and hole. For materials with very low dielectric constants, the last term, which is typically ignored, becomes crucial. Here, the electron and hole are both described by spherical effective masses using the effective-mass approximation. When the system is viewed as spherical dots, attractive Coulomb interaction is also present in addition to spherically symmetric confining potentials. There are two limiting scenarios depending on the ratio between the radius of the quantum dot, R, and the effective Bohr radius of the bulk exciton, $r_{exciton}$. For R/$r_{exciton}$ » 1, the exciton can be considered as a bound quasi-particle with negligible confinement energy. Such systems are considered as weak confinement regime. Whereas, for R/$r_{exciton}$ « 1, the confinement energy dominates, therefore there is very little spatial corelation between the electron and the hole, which are both thought of as separate entities. Such systems fall within the strongly confined regime. Importantly, the strong-confinement regime threshold is still holds up to roughly $R = 2r_{exciton}$.

1.3. Perovskite Nanocrystals

1.3.1. Basic background and difference with conventional quantum dots

Colloidal semiconductor nanocrystals, which range in size from 2 to 20 nm,[30] have emerged as intriguing and attractive prospects for studies on optoelectronic emissions properties and associated applications.[30-32] Although the history of colloidal nanocrystals dates back to the 19th century, Michael Grätzel's research team developed the synthesis of CdS in order to circumvent the problem of photo corrosion of semiconductors.[33] The scientific community has recently become interested in perovskite semiconductors. Due to how easily their properties may be tailored, perovskite quantum dots have attracted a lot of interest for usage in solar cells,[34] LEDs,[35] laser diodes,[36] electronics,[35, 37] and also as photocatalyst.[38]

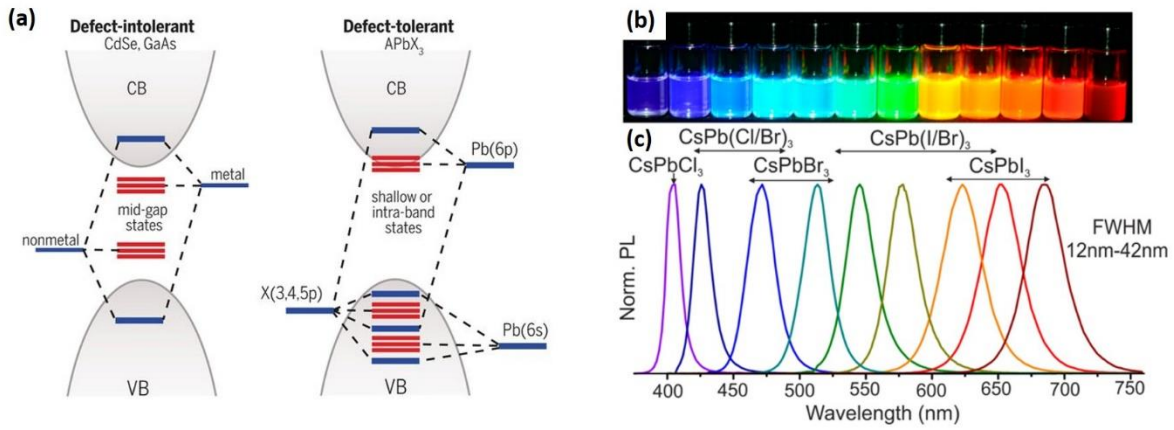

Figure 1.18. (a) Electronic structure of typical III−V, II−VI, or group IV semiconductors (left) and LHPs (right). Reproduced from Ref. 41. (b) Composition tuned $CsPbX_3$ NCs under UV light. (c) Photoluminescence spectra of halide tuned $CsPbX_3$ NCs. Reproduced from Ref. 44.

But before the discovery of perovskite nanocrystal by the Pérez-Prieto's group in 2014,[39] the most celebrated colloidal nanocrystals for the optoelectronic world were II−VI semiconductor QDs (e.g., CdSe and GaAs QDs). For these QDs the photoluminescence properties can be tuned from violet to red by fine tuning their size (see figure 1.16).[40] But these NCs suffers from its inherent defect intolerant nature.[41, 42] If we consider the basic molecular orbital energy levels of II−VI semiconductor QDs, we can see that the presence of mid-bandgap states originating from the non-bonding levels of metal as well as nonmetals which acts as a deep trap states.[41] The existence of these mid-bandgap states affects the PLQY of the system by trapping the charge carriers (electron and hole). In contrast, these kinds of mid-bandgap states are not present in perovskite systems, which renders these perovskite NCs defect tolerant (see figure 1.18a).[41] Even so, there present intraband defects in the perovskite system that can be easily passivated using surface ligands. These perovskite systems are perfect for optoelectronics due to high PLQY and defect-tolerant nature.[43] Also, in II−VI semiconductor QDs, the only way to change its photoluminescence is by fine tuning the size of the QDs.[40] However, for perovskite NCs the photoluminescence properties can easily be tuned through facile anion exchange (figure 1.18b and figure 1.18c).[44, 45]

1.3.2. Crystal Structure

LHP NCs: The crystal structure of LHPs is similar to the oxide perovskites. The [PbX_6] octahedra that share corners and are connected in three dimensions forms the backbone of cubic lattice (figure 1.19.a).[46, 47] One large cation [e.g.,$CH_3NH_3^+$,$CH(NH_2)^{2+}$, or Cs^+] fills the vast space between the octahedra (the A-site), resulting in an overall composition of $APbX_3$.[42, 47] The Goldschmidt tolerance factor (t), which depends on the ionic radii of A^+, Pb^{2+}, and X^-, is what controls the stabilization of perovskite structure.[48, 49] Its formula is as follows,[48]

$$t = \frac{R_A + R_X}{\sqrt{2}(R_B + R_X)} \qquad (1.3.1)$$

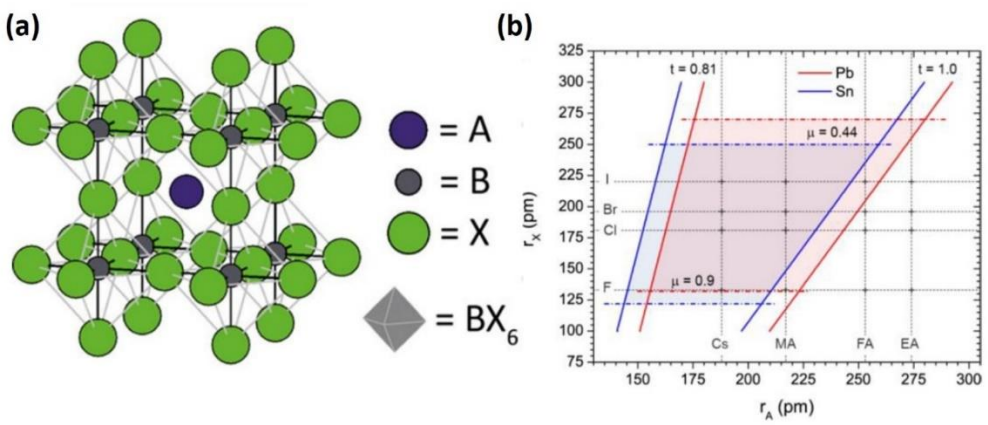

Figure 1.19. (a) Schematic representation of a cubic perovskite structure. Reproduced from Ref. 46. (b) Formability of 3D halide perovskites as a function radii of halide anion and A-site cation. The boundaries for tolerance and octahedral factors are marked with solid and dashed lines, respectively. Reproduced from Ref. 49.

In general, Group 14 elements including Pb^{2+} or Sn^{2+} having ionic radii of 1.19[50], 1.18 Å[51], respectively, are ideal for B-site cations halide perovskite NCs.[47] The A-site cations mentioned above have acceptable ionic radii and meet the Goldschmidt tolerance factor, namely organic $CH_3NH_3^+$ (MA, 2.17 Å), and $HC(NH_2)_2^+$ (FA, 2.53 Å), and inorganic Cs^+ (1.88 Å), [50, 52] The ionic radii of halide anions are 1.18 of Cl, 1.96 of Br, and 2.20 Å of I.[47, 8] Even though the calculated *t* values based on the

aforementioned ionic radii differ for various perovskite polymorphs, they fall within the general range of 0.8 to 1.1 for a stable 3D perovskite structure.[53], The crystal structures are more likely high-symmetric cubic at a range of $0.89 < t < 1$, but if the t value is small or large, then less symmetric perovskite structures or non-perovskite structures are formed.[47] For example, because of small t, $CsPbI_3$ tend to stabilize in yellow δ phases.[54]

The highest amount of electronic delocalization inside the lead-halide framework is only achievable if the perovskite structure is crystallizes in its 3D polymorphs. This may be either cubic (figure 1.20a) or may be slightly distorted versions of it, which also have the associated desired semiconducting characteristics.[42, 55] Orthorhombic $CsPbBr_3$ is one of the fifteen potential octahedral tilings of the cubic perovskite structure that preserves three-dimensional connectivity (figure 1.20b).[42] On the contrary, 1D polymorphs of $APbX_3$compounds (figure 1.20c and figure 1.20d) are not appealing semiconductors because of their poor electronic transport and much larger bandgaps.[56]

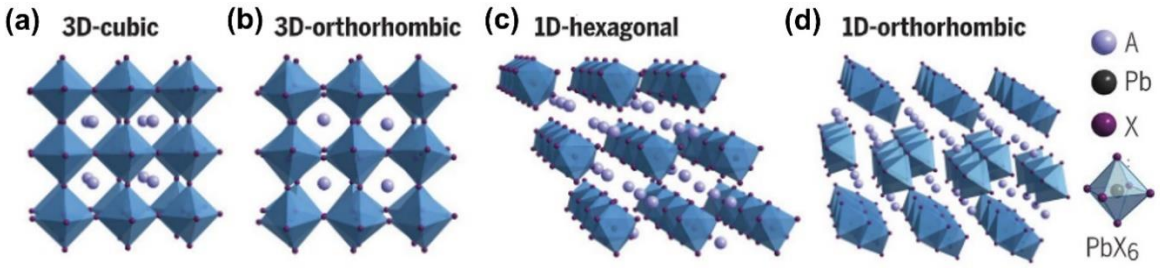

Figure 1.20. (a) Cubic structure $APbX_3$, space group Pm3m and (b) Orthorombic $CsPbBr_3$, (space group Pnma). 1D polymorphs which are nonperovskite, formed by the (c) face- or (d) edge-sharing of octahedra. Reproduced from Ref. 42.

Three 3D polymorphs, in decreasing order of symmetry, are generally seen in bulk LHPs: cubic, tetragonal, and orthorhombic.[42] The phase transitions have well-defined temperatures, and at high temperature cubic phase is most stable.[42] Surface effects can modify the relative stabilities of NC polymorphs, which is poorly

understood. All as-synthesized LHP NCs crystallise into the following 3D phases at ambient temperature: $MAPbBr_3$, $FAPbBr_3$, and $FAPbI_3$ NCs are pseudocubic, tetragonal, $CsPbI_3$ and $CsPbBr_3$ NCs are orthorhombic. The 3D polymorphs of $CsPbI_3$, and $FAPbI_3$ NCs have band gaps at 710 nm and 840 nm, respectively, that are primarily interesting for near-infrared emission, are metastable at ambient temperature.[57] Bulk forms of these compounds crystallise into 1D orthorhombic and 1D hexagonal structures, respectively, since size sof A-site ions are not ideal for 3D polymorphs of $FAPbI_3$ and $CsPbI_3$ (FA^+ being too large and Cs^+ being too tiny) (figure 1.20.c and figure 1.20d).

Lead free Copper halide perovskite: The copper halide perovskite system have recently have shown immence potential as light emitting material with two forms with nice optical properties: $Cs_3Cu_2X_5$ and $CsCu_2X_3$ (X=Cl, Br, I).[58] The crystal $Cs_3Cu_2X_5$ is orthogonal (space group *Pnma*).[59] In $Cs_3Cu_2X_5$ copper has four different chemical environments: two different spatial orientation of tetrahedral CuX_4 with four I atoms in the surroundings and two diiferent spatial orientation of trangular planer CuI_3 unit with surrunding three I atoms. This is depicted in figure 1.21a. This two units share an edge and forms $[Cu_2X_5]^{3-}$ dimer which are speparated by cesium atoms in the crystal. This each $[Cu_2X_5]^{3-}$ dimer units seperated by cesium atoms form induvudual charge centre, resulting a 0D electronic structure.[60, 61]

The only known $CsCu_2X_3$ perovskite is $CsCu_2I_5$ so far in literature.[58, 60] The $CsCu_2I_5$ is from the *Cmcm* orthogonal space group family. In $CsCu_2I_5$, Cu has two chemical environments. The both environment consist of different spatial orientation of $[CuI_4]^{3-}$ tetrahedral units which form 1D $[Cu_2I_6]^{4-}$ tetradedral chain units through alternate connectivity separated by cesium atom forming a 1D electronic structure (figure 1.21b).[60, 62] The seventh chapter of this thesis deals with the synthesis of the copper halide perovskite systems.

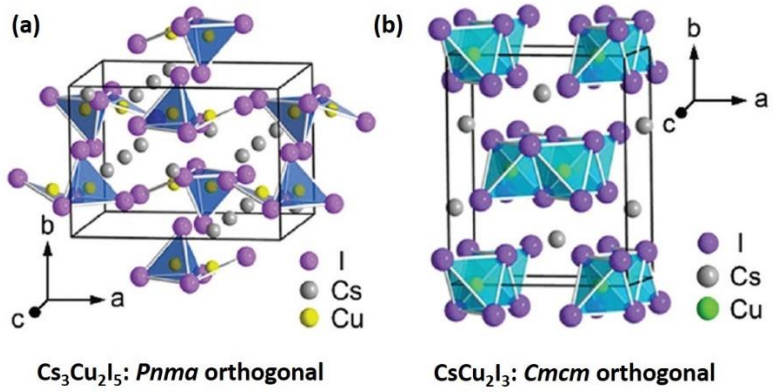

Figure 1.21. (a) Crystal structure of $Cs_3Cu_2I_5$. (b) Crystal structure of $CsCu_2I_3$. Reproduced from ref. 60.

1.3.3. Methods for halide NCs preparations

An intriguing feature of NCs is synthesis process can control the optical properties to a large extent and this optical properties can be modulated by changing preparation technique parameters.[32, 63] Furthermore, the shape, surface defects, and composition of the materials all affect their optoelectronic capabilities. Perovskite NC synthesis approaches and surface engineering have been employed in order to learn more about the mechanisms at work and to provide simpler, more reliable, and less expensive ways to synthesize NCs with certain properties.[64]

Several synthetic colloidal techniques, such as anion exchange, hot injection, room temperature reprecipitation, and ultrasound, are used to synthesize the majority of NCs.[65, 66] Perovskite NC synthesis has made significant strides, but there are still numerous obstacles to overcome. For instance, in various methods, the size distribution and photophysical characteristics differ greatly, which makes these perovskite NCs less suitable for real-world use.[65, 67] Additionally, these procedures frequently include hazardous solvents, which are typically unwelcome by environment and also in industry, making them complex, difficult to manage, and frequently resulting in NCs with degrading issues.[65] The hot injection method and the ligand-assisted reprecipitation (LARP) method are the two most popular

synthesis techniques. Additionally, attempts have been made to create synthetic processes that have fewer negative effects on the environment, such as the use of solvents that are more eco-friendly and alternative, which may be more appealing for use in practical and industrial operations. More information on a few of the popular methods for obtaining perovskite NCs is provided below.

1.3.3.1. Ligand assisted reprecipitation (LARP) technique: The LARP method is one of the most popular room temperature synthesis processes for perovskite NCs.[65] The precursor salts are dissolved in a solvent, typically dimethyl sulfoxide (DMSO) or, dimethylformamide (DMF) what is thought to be a straightforward and scalable technique, as shown in figure 1.22.[68] The precursor salt solution is then injected into a solvent-miscible solution where the perovskite's component ions are less soluble, resulting in a supersaturated state, leading to the perovskite crystallization, as shown in figure 1.22. Prior to nucleation, organic surface ligands are added to one of the solvent which controls the crystal growth and make colloidal dispersion of NCs stable.[68] In the first part of this thesis, we have used this LARP methods for the preparation of hybrid LHP NCs and their Bi^{3+} doped analogs.

Figure 1.22. Schematic representation of LARP method.

1.3.3.2. Hot injection method: The quantum dot (QD) synthesis using hot injection procedure was developed by Murray *et al.* in 1993 and is frequently used to synthesize NCs.[69] Organometallic reagents are quickly injected into a hot coordinating solvent in this technique to have a homogenous nucleation process. By modifying the method, perovskite colloidal NCs are often prepared by quickly

injecting the right precursors at a high temperature. The procedure entails in an inert atmosphere by heating precursors to a specific temperature before injecting a different solution.[70] Immediately after injection process, the phase of nucleation process starts, followed by the phase of NC growth, which enables the narrow particle size distribution.[68] High temperatures are also used to improve the materials' phase purity and morphological control.[70] Earlier conventional semiconductors including CdSe were also synthesized through same approach.[71] The all-inorganic halide perovskite NCs are preferably synthesized in this method.[68, 72]

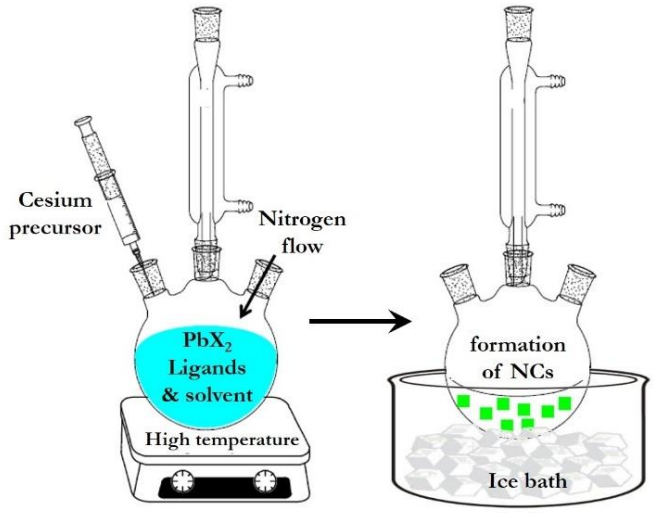

Figure 1.23. Schematic representation of hot injection procedure.

The inorganic LHP synthesis in hot injection method involves two basic steps. Firstly, lead halide salt is dissolved in octadecene solvent at inert atmosphere at high temperature in presence of long chain surface passivating ligands (in general oleic acid (OA) and oleylamine (OAm)). After solubilizing, a cesium precursor (Cesium oleate) is injected in the reaction mixture at a particular high temperature to synthesize the NCs.[72] The process is schematically shown in figure 1.23. However, the formation mechanism of the NCs in this process is still under debate.[73] Over the time, after the first synthesis of $CsPbBr_3$ NCs, this hot injection method is being modified to certain extent by different groups to achieve high PLQY and better colloidal stability of the synthesized NCs.[68]

In this hot-injection method, temperature plays the most crucial role to determine the morphology and size of the synthesized NCs.[74, 75] In general, higher temperature favours the formation of larger NCs and this temperature tuning is one of the key factors to synthesize the perovskite NCs of different size and shape.[75, 76]

1.3.3.4. Mechanochemical methods: This process combines mechanical engineering with chemistry to break down the building blocks at the molecular level and carry out the reaction between the precursors to produce the final product. As an illustration, when synthesizing $MAPbX_3$ (X=Cl, Br, I) PNCs, we grind the respective metal salts in the presence of surface passivating long chain organic ligands for a short period of time to produce luminous $MAPbX_3$. This process uses solvent-free synthesis, a green methodology.[77]

1.3.4. Trap state in Perovskite Nanocrystals:

Trap state of defect state in a material generally originates from the dislocation of atoms from its original position or absence of an atom in crystal lattice. These disorders affect the lattice bonding and have detrimental effect on charge carrier movement through the lattice.[78] This imperfection in lattice creates localised states in the band and the photogenerated carriers can fall into it and get trapped. This is illustrated in figure 1.24.

Now, depending on the energy difference of the trap states from the conduction band (electron trapping centre) or valence band (hole trapping centre) these trap states generally classified into deep trap states and shallow trap states. [78] For deep trap states in nanocrystals, the energy difference of the confined trap state with conduction level is too high that thermal energy (k_BT) cannot turn the carriers back to conduction level.[78-80] Thus, the only way of recombination of the charged carriers trapped in a deep trap state is the non-radiative recombination, resulting very low PLQY of the system.[81] On the other hand, for shallow trap states, trapped charged

carriers can easily escape back to the conduction band or valance band absorbing thermal energy.[78, 81]

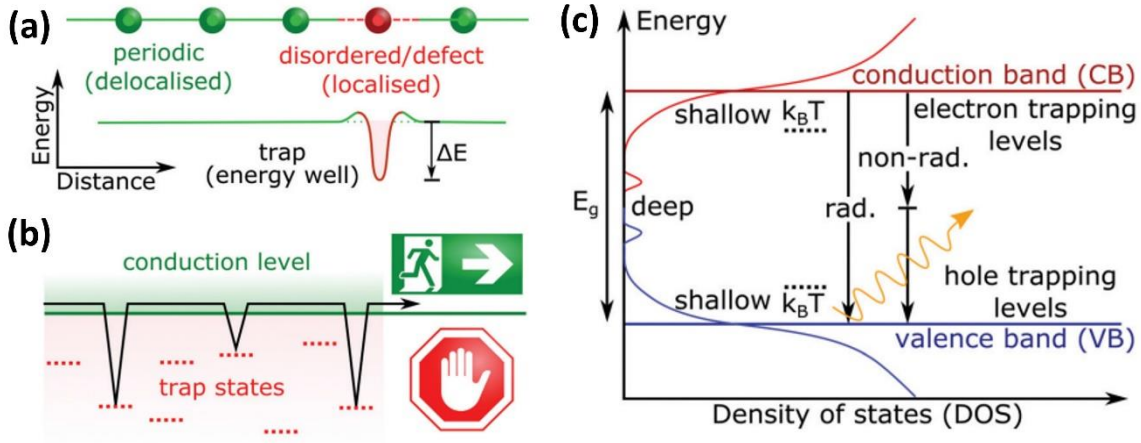

Figure 1.24. (a) Schematic of a charge localization brought on by a defect in a semiconductor lattice and non-periodic disorder (top), which results in the introduction of new energy levels (bottom).(b) Diagram of charge trapping kinetics, which shows how traps use events called trapping and detrapping to slow down the transport of charge carriers. (c) Schematic representation of how disordered in semiconductor modulate the state density, whereby both radiative (rad.) and non-radiative (non-rad.) recombination (vertical arrows) can occur. All three figures reproduced from Ref. 78.

In perovskite NCs the most common defects are shallow in nature, enabling these materials to have very high PLQY despite having defects.[81, 82] The defect tolerance nature of these LHP family can be rationalized through the electronic structure. Figure 1.18a shows the electronic structure of $MAPbI_3$ where the Pb 6s orbital hybridized with I 5p orbital to form a pair of bonding and antibonding states. The valence band of the $MAPbI_3$ system is composed of these antibonding set of orbitals originating from this hybridization.[42] Whereas, the conduction band of the system is composed of a new set of antibonding orbitals, which originates from the hybridization of Pb 6p orbital with the I 5p orbitals. Due to this, the original atomic orbitals's energy remain very close to the energy of the band edge position. The defect states in perovskites are generally surface defects which are formed by the

non-bonding atomic orbitals.[81, 83] As, the atomic orbitals energy levels are very close to the band edges in $MAPbI_3$, makes these defects as shallow trap states. In addition to this, the strong spin-orbit coupling in $MAPbI_3$ system due to presence of heavy atom iodine reduces the band gap resulting these defects shallower.[41, 81] The high polarizability of Pb^{2+} also leading to high dielectric constant which resists the capture of charged carrier in the trapping site and consequently resulting low trap assisted recombination rates.[84]

Crystal structure also plays a pivotal role in defect formation in addition to the electronic structure.[85] As an example, $CsPbI_3$ can form three polymorphs: cubic α-phase, or orthorhombic δ- and γ-phases.[85] The electronic structure for cubic α-phase is qualitatively same with $MAPbI_3$ resulting defect tolerant nature of $CsPbI_3$. However, going from α-phase (I-Pb-I bond angle 180º) to γ-phase and δ-phase, the I-Pb-I bond angle reduces to 155º and 95º, respectively. This results in reduction of overlaps between orbitals of lead and iodine leading to formation of deep trap states.[85]

The lattice parameter also plays a decisive role to control the energetics of the defect states. Going from iodide to bromide to chloride in $MAPbX_3$ (X=Cl, Br, and I), the lattice parameter decreases. When halide vacancies form, Pb^{2+} dangling bonds interact more, resulting in deeper trap levels for the halide vacancy. So, $MAPbCl_3$ forms deep traps, whereas $MAPbI_3$ and $MAPbBr_3$ mostly form shallow traps (figure 1.25).[86]

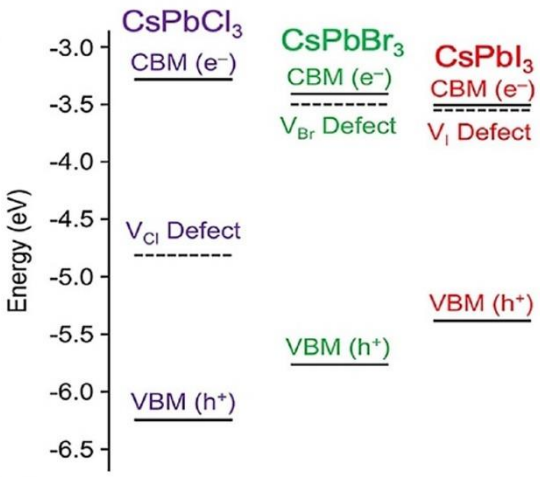

Figure 1.25. Energy level of halide vacancy related defect sites within the band gap of LHP materials. Reproduced from Ref. 86.

1.3.5. Surface properties and colloidal stability- importance of surface ligands:

Surface chemistry of the NCs play an essential role in stability and its optoelectronic properties. Although, the surface properties of LHP nanocrystals have been extensively studied but still it is not fully understood. In the LHP NC synthesis, the most common ligand pair is oleic acid and oleylamine which are being used for the surface defect passivation of the NCs as well as to maintain the colloidal stability.[81] To have an idea about the choice of the ligands it is important to get knowledge about the surface terminations of the NCs. During crystallization process, the NC surface can be terminated by PbX_2 or AX or both which depends largely on the synthetic condition. Figure 1.26 represents the surface stoichiometry of $CsPbX_3$ NCs. There are two possibilities of the surface termination: [CsX] or [PbX_2]. However, as the NCs are capped with ligands, in realistic model the [PbX_2] terminated surfaces of the $CsPbX_3$ are represented as [$CsPbX_3$](PbX_2)(AX′), where the capping ligand is represented by AX′.[87]

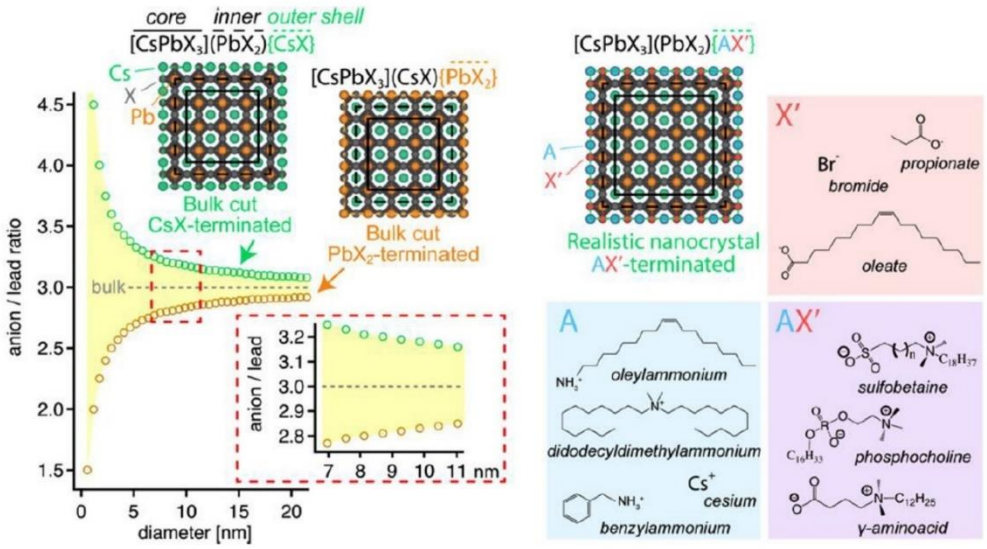

Figure 1.26. Models describing surface stoichiometry of typical $CsPbX_3$ type perovskite NCs. Adapted from Ref. 87.

In the acid-amine pair ligand system alkylammonium cation ($R\text{-}NH_4^+$) is formed by a proton exchange between acid and amine. This alkylammonium cation then binds to the NC surface by replacing some A-site cations on the NC surface.[88] It is also believed that the $R\text{-}NH_3^+$ also binds to the bromide surface through the H-bonding.[81, 88] However, the role of long chain carboxylic acid (eg. oleic acid) or carboxylate anion ($RCOO^-$, eg. oleate) as a ligand is still under debate. Earlier it was argued that $RCOO^-$ do not have direct binding with NC surface but provide colloidal stability by remaining in the solution.[88] Later, it was shown that both oleic acid and oleylamine bind to the surface of the NC.[89, 90] Another argument is that oleate anion replaces some halide ions from the NC surface to coordinate with the NC.[91] However, these ligand binding is highly dynamic in nature which is detrimental for NC stability as well as high PLQY.[90] To overcome this difficulties, various ligands such as zwitterionic molecules, phosphonic acid, quaternary ammonium salts have been introduced to the NC surface in place of oleic acid/oleylamine pair.[81, 91, 92] The desorption of surface ligands from the NC surface is highly dependent on how strongly they bind to the surface.[81, 91] The above-mentioned ligand molecules have

been proved as better capping ligand due to their strong affinity to the NC surface than oleic acid/oleylamine pair, thus come up with superior colloidal stability and maintain high PL stability. [81, 91] The year wise progress in ligand chemistry in LHP NCs is shown in figure 1.27a. The binding modes of all these ligand systems is pictorially shown in figure 1.27b.

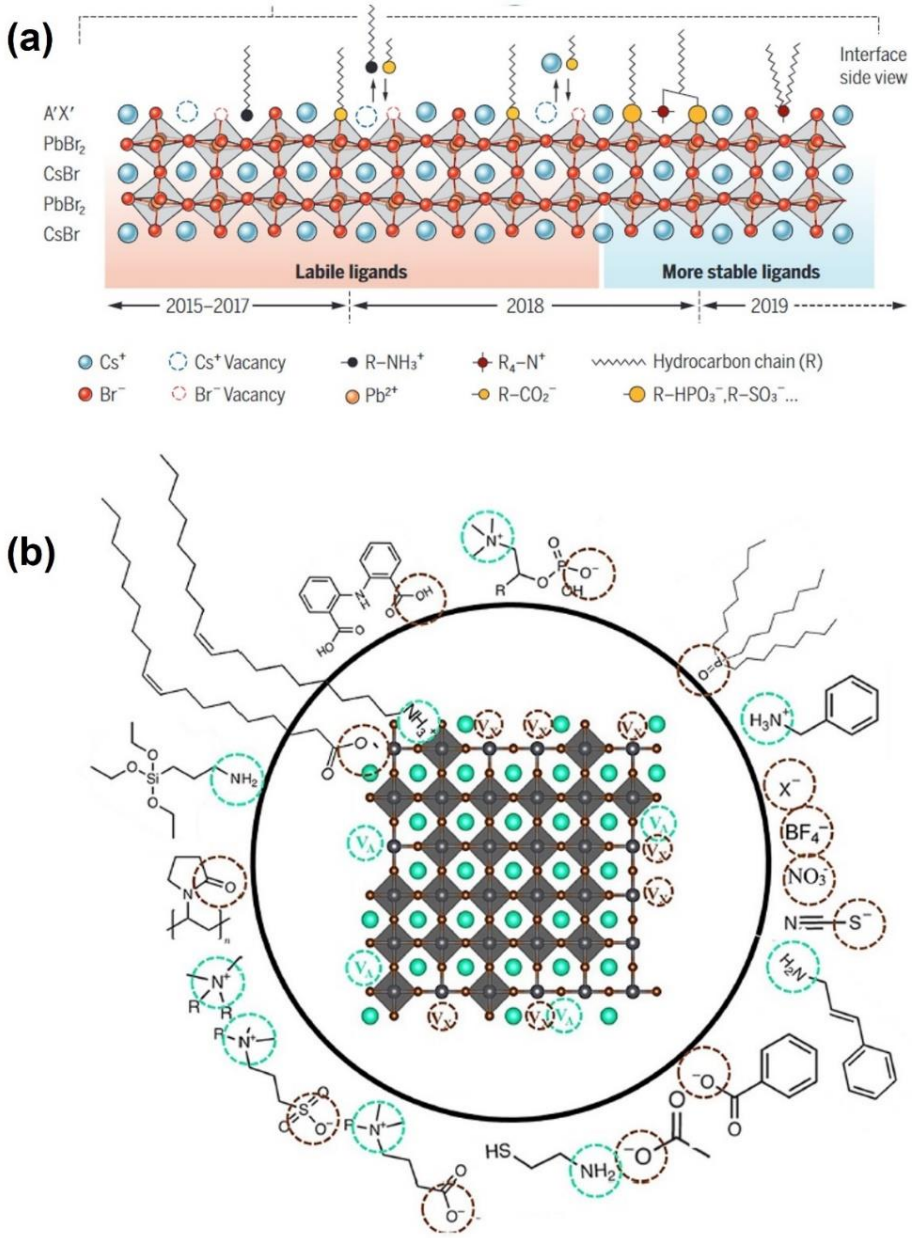

Figure 1.27. (a) Ligand development for LHP NCs over time. Reproduced from Ref. 91. (b) Types of ligands which are used for surface passivation of perovskite nanocrystal systems. Reproducd from Ref. 81.

1.3.6. Charge carrier dynamics in perovskite nanocrystals

Study of charge carrier dynamics in light emitting material is one of the most crucial aspects of this research. Understanding the photo-induced carrier dynamics in NCs is crucial for optoelectronics application. In NC, after photoexcitation an electron goes to the conduction band leaving behind a corresponding hole in the valence band. This electron and hole are generally bound through coulombic attraction force which we call an exciton.[93] Now after formation of electron and hole this will again recombine through radiative or non-radiative processes depending on the nature of the NCs. A complete charge carrier dynamics give us the idea of the fate of these photo induced carries in the NCs. These photo-induced carriers can recombine in several processes, with timescale spanning from few picoseconds to hundreds of nanoseconds.[94] To look into the charge carrier dynamics, we use time resolved studies. Here, we will discuss these different carrier dynamic processes that is observed after photoexcitation in perovskite NCs.

1.3.6.1. Hot carrier cooling: If the perovskite NCs is photo excited with the energy higher than band gap energy then electrons and holes goes to the higher excited states which are termed as hot electrons and hot holes, respectively.[94-96] After formation, these hot electrons and holes dissipates its excess energy through carrier-phonon interaction to reach their equilibrium position at band edge.[97] This excess energy dissipation process of hot carriers to reach at band edges is termed as hot carrier cooling. As this process is highly dependent on carrier phonon coupling, the timescale of hot carrier cooling process differs from NC to NC.[97] The hot carrier lifetime is strongly influenced by the excitation energy as well as excitation fluence.[98] The hot carrier lifetime is found to increase with higher excitation energy. At high excitation fluence, auger heating become predominant which also slows down the hot carrier cooling.[98] The movement of carriers within a band is highly dependent on the effective mass of the carrier. From hot carrier cooling dynamics it

is often very difficult to determine the identity of the carriers as in perovskite NCs, both electron and hole have similar effective mass. [94]

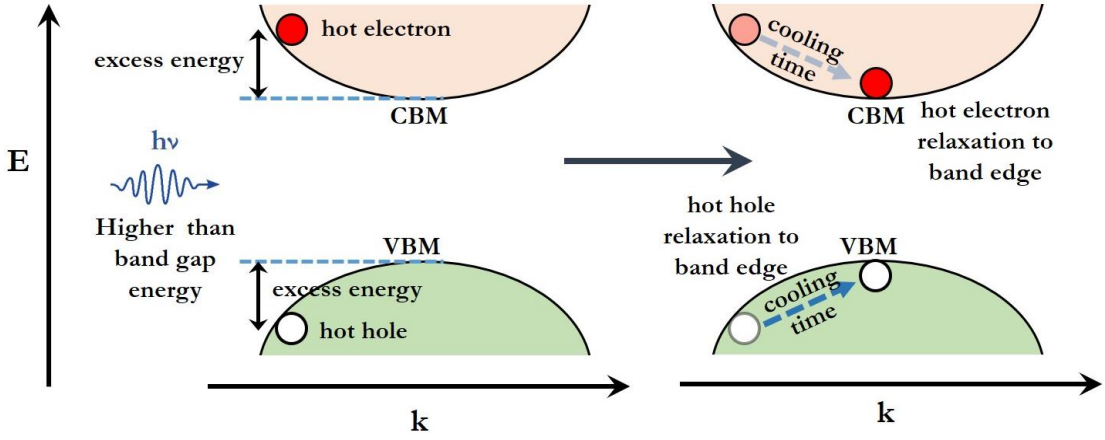

Figure 1.28. Schematic representation of hot carrier cooling process.

Till date, many studies have been done to elucidate the mechanism of different parameters that can modulate the hot carrier lifetime. In general, the hot carrier cooling process takes place in timescale of sub-picosecond level due to strong interaction between longitudinal optical phonons in perovskite NCs and hot carriers.[99] The size of the NCs are also a very important factor that influences the hot carrier cooling rate to a certain extent.[100] The lifetimes of hot carriers is prolonged in nanocrystals due to the quantum confinement. in perovskite system [100, 101] In a recent study it has been shown that the lifetime of hot carrier increases from ~400 fs to ~800 fs when the size of the $CsPbI_3$ NCs reduced to 4.6 nm from 8.2 nm.[100] The hot carrier cooling is shown schematically in figure 1.28.

1.3.6.2. Exciton Recombination: After photoexcitation the hot carriers are formed in NC which eventually relax to the band edge within hundreds of femtoseconds. In NC, due to confinement, these electron and hole remain bound to each other through strong coulombic attraction force which increases with decrease in size and dimensionality of the system.[102] After cooling, the hot electron and hole reach their equilibrium position in the band edge, forming band edge exciton. This electron at conduction band minima (CBM) and hole at valence band maxima (VBM) then

recombine in radiative process, producing photoluminescence which is schematically depicted in figure 1.29.[94] The LHP NC have direct band gap for which the PLQY of the system is very high.[103] The timescale of this exciton recombination process is in the order of few nanoseconds to tens of nanosecond, depending on the system and surroundings.[104] The lifetime of these band edge exciton strongly influenced by the trapping sites within the NCs.[104, 105] The presence of trapping sites below the CBM of VBM in the system effectively reduce the carrier density in the band edge, resulting shortening of the lifetime of the exciton recombination process.[105] The presence of any electron or hole acceptor molecule on the surface of the NCs can also reduce the lifetime of the system by effective capturing electron or hole, respectively.[106, 107]

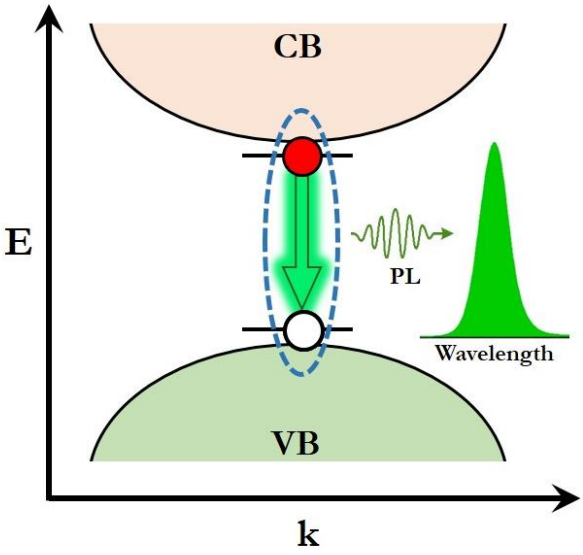

Figure 1.29. Schematic representation of exciton recombination**.**

1.3.6.3. Trapping of charge carrier and trap assisted recombination: In the section 1.3.4 of this chapter, we have already discussed about the trap states in perovskite NCs. In LHP NCs, surface unsaturated orbitals cause the formation of most trap states. Energetically these trap states a shallow in nature (figure 1.30). [81, 82] But these trap states can also trap the charge carrier from the band edge and promote the non-radiative recombination, which quenches the PLQY of the

system.[81] In presence of this charge trapping (electron or hole trapping) from the band edge to the trap states can effectively depopulate the band edge population which eventually leads to lowering the exciton lifetime.[108] An effective passivation of these shallow trap states reduces the charge carrier trapping and also amplifies the PLQY of the system. [108, 109]

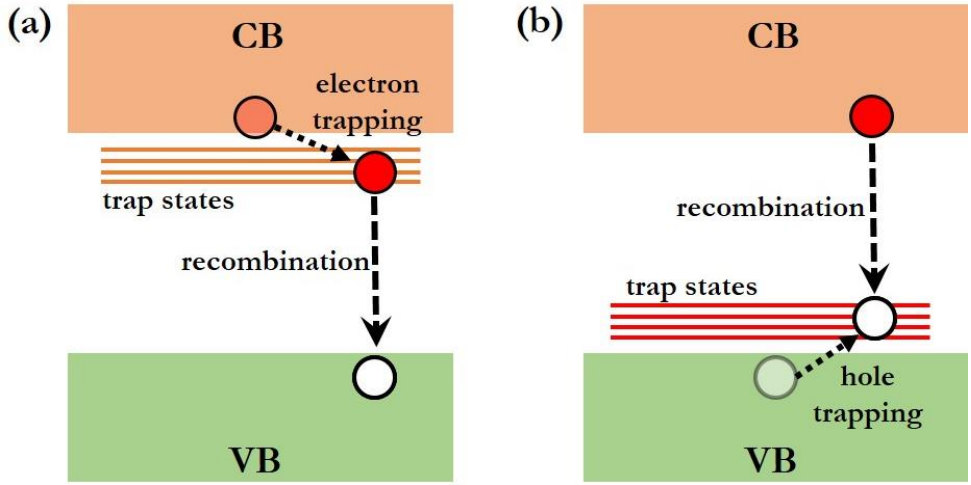

Figure 1.30. Schematic representation of the charge carrier trapping and trap assisted recombination through shallow trap states.

To have an idea about nature of the trapped carrier (electron or hole), monitoring PLQY using some post-synthetic treatment is a good option. As an example, electron traps can originate from excess lead on the surface of the LHP NC. Treating the NCs with NH_4SCN amplifies the PLQY by removing the excess lead from the surface.[110] Another good way to determine the nature of the charge carrier is to use some electron or hole accepting molecules which are commonly known as scavengers. For example, the faster lifetime of $CsPbBr_3$ NCs in the presence of a viologen derivative indicates that electron is the carrier which is being trapped.[94]

However, as the trap states in LHP NCs are shallow in nature (except chloride based LHP system), the trapped carriers can again easily repopulate the band edge through detrapping process absorbing some heat energy (k_BT).[86] These detrapped carriers in the band edge can recombine in radiative way.[111] This process, however, shows a

longer lifetime component in PL decay dynamics because of the involvement of this carrier recycling process through trap states.[112] This process is schematically shown in figure 1.31. However, in chloride based LHP NCs, the trap states are generally energetically deep, leading to the detrapping process inaccessible. This is the reason of low PLQY of the chloride based LHP NCs.

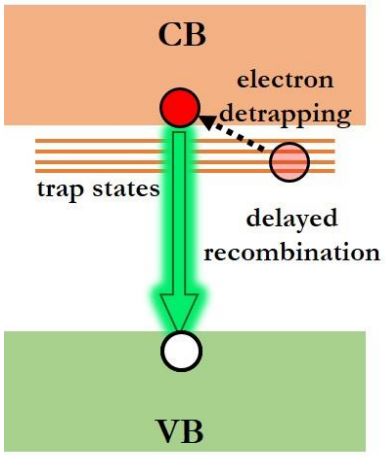

Figure 1.31. Schematic representation of the delayed radiative recombination mediated through carrier trapping-detrapping process.

1.3.6.4. Formation of biexciton and trion: The charge carrier dynamics is highly dependent on excitation fluence in perovskite NCs. At high excitation fluence, the formation of multiple excitons is favoured because of the large absorption cross section of the NCs. The formation of these multi exciton species largely control the carrier dynamics under this strong excitation fluence.[97, 113]

The biexcitons are formed with two electrons in the conduction band coulombically attracted with two holes in the valence band.[114] These two excitons have a repulsive interaction between them which results in increased band gap after biexciton formation, evident from many recent studies.[115, 116] The biexcitons can decay in two possible pathways. After formation of biexciton it can emit a photon to come to excitonic state. Another common pathway is to decay via Auger recombination in which it can give energy in nonradiative way to an electron which goes to the higher

excitonic state.[114] These two processes of biexiton relaxation are depicted in figure 1.32. The biexciton relaxation occurs in perovskite NCs in the order of 10-100 ps timescale.[113]

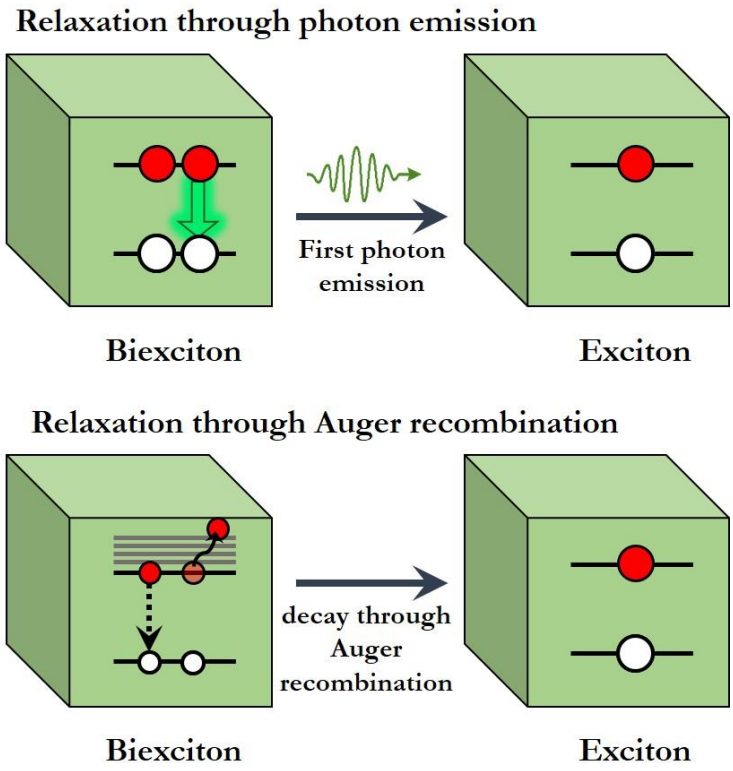

Figure 1.32. Schematic representation biexciton relaxation.

Another species, trion can be formed under strong fluence which can also to govern the PL properties of the NCs to a large extent. The trion is a charged three particle system which can have two forms, positive trion (an exciton with a free hole) and a negative trion (an exciton with a free electron) (see figure 1.33).[114, 117] As trion is charged species, its formation is related to the ionization of the NCs. The NCs can be ionized through chemical treatment on the NC surface by electron or hole extraction.[114] Also, Auger recombination of a biexciton can produce a trion after subsequent photoexcitation.

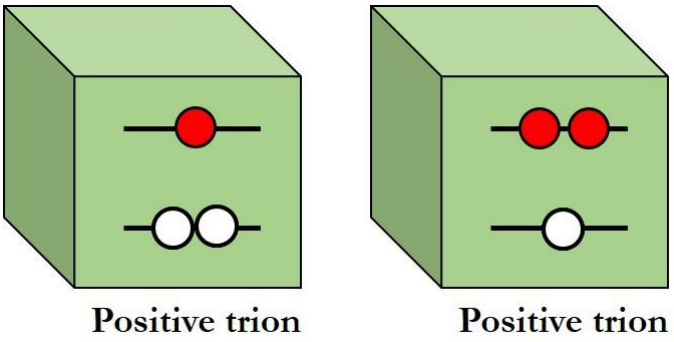

Figure 1.33. Schematic representation positive and negative trion.

The trion formation in the NC is always remain in focus of interest as it is directly controlled by the ionization of the NCs. The trap states in NCs plays a pivotal role to control the trion formation.[117] This further conclude that trion formation in NCs also directly related to the process through which NCs have been prepared. The surface treatment has been found to be beneficial to suppress the generation of trion through minimizing the defects on the NCs.[117] The trion relaxation also found to be very much dependent on excitation fluence as well as size of a particular NCs. In general, the relaxation time of trion is in the order of 150-500 ps depending on the experimental condition.[114]

1.3.6.5. Effect of doping on charge carrier dynamics: Doping is intentional incorporation of impurity or foreign element in pure material. The metal ion doping in LHP NCs have large impact on the stability and optical properties of the NCs. The charge carrier dynamics of doped NCs gives us the insight of the modulation of optical properties. Many metal ions have been reported as B-site dopant in different LHP NCs to improve its stability and PLQY. This thesis also deals with heterovalent Bi^{3+} doping in the B-site of the LHP NCs. Bi^{3+} doping in the B-site of the LHP NC reduces the PLQY of the system to a large extent (figure 1.34c).[118, 119] Earlier few reports have come up, addressing the reason of decrease in PLQY after Bi^{3+} doping, which clearly indicate the formation of deep trapping sites in the NCs (figure 1.34a).[118-120] As, the deep trapping sites effectively trap the charge carriers, the

lifetime of the system is the system is found to be shorter after Bi^{3+} doping (figure 1.34b and figure 1.34d). In the fourth chapter of this thesis, we have discussed on the origin of these Bi^{3+} induced trap states in Bi^{3+} doped $MAPbBr_3$ QDs.

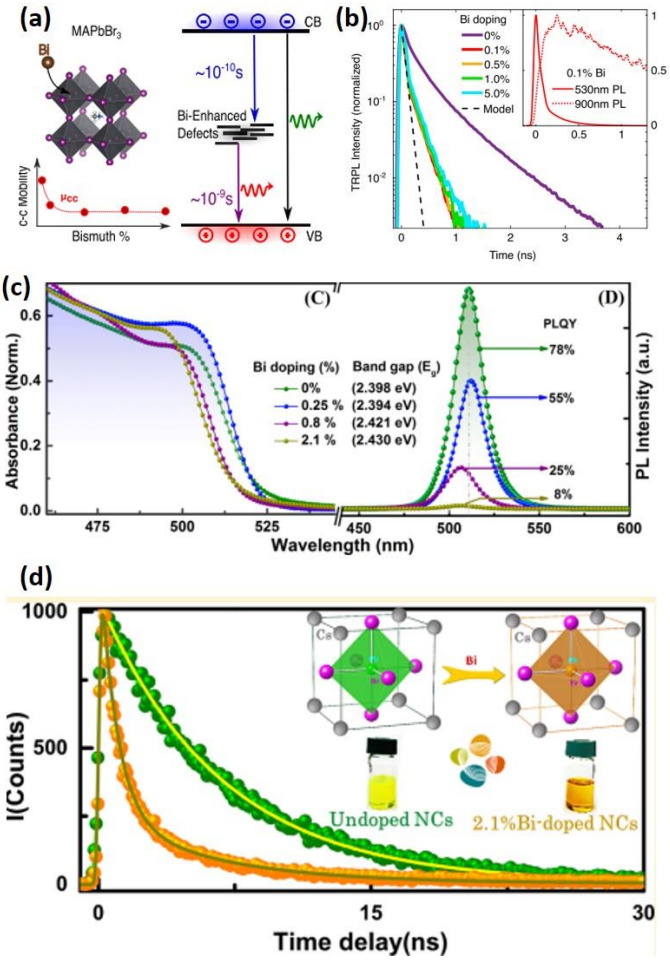

Figure 1.34. (a) Schematic representation of Bi^{3+} induced trap states in $MAPbBr_3$. (b) Effect of Bi^{3+} doping on lifetime of the system. Reproduced from Ref. 118. (c) Effect of Bi^{3+} doping on absorption and PL of the $CsPbBr_3$ NCs and (d) Effect of Bi^{3+} doping on lifetime of $CsPbBr_3$ NCs. Reproduced from Ref. 119.

1.3.6.6. Self-trapped excitons: The self-trapped exciton (STE) is often found in the soft crystals.[121-124] Carrier-phonon interactions are strong enough in these crystals to allow excited electrons and holes to deform the lattice around them in an elastic way.[123] As a result, electrons and holes will rapidly self-trap after being photogenerated since this state is more stable than the one in which they would

move, causing the lattice to deform.[123, 125] As these STE states originates well below the conduction band, the emission from these states is highly stoke shifted (see figure 1.35).[125] This type of STE emission is reported in 2D LHPs.[125-127] The lead-free copper halide perovskite emission is also governed by STE.[128] The materials showing STE emission is in high demand due to absence of self-absorption because of the large stoke shift. These STE emissions shows very long lifetime ranging from hundreds of nanoseconds to microsecond timescale.[128]

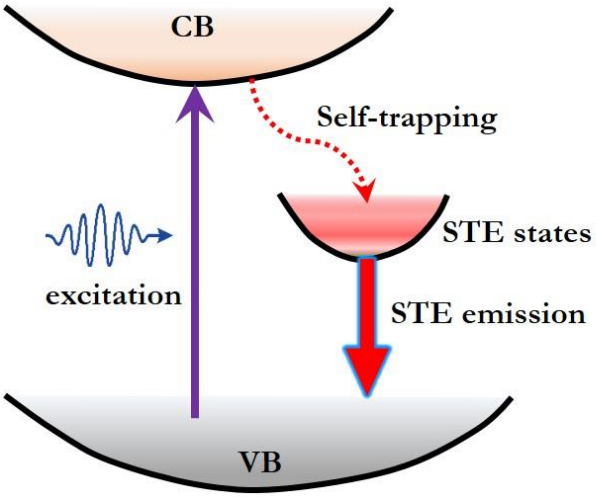

Figure 1.35. Schematic representation of STE emission.

1.3.7. Challenges with LHP NCs and possible way out

LHP NCs have rapidly advanced in terms of simple synthetic techniques with adjustable size, shape and tunable optical properties, but we have yet to successfully navigate the significant challenges posed by these crystal structures. In comparison to optical, electrical, and photovoltaic applications, these PNCs' major challenges still include structural stability and lead toxicity.

1.3.7.1. Stability: The stability of LHP in various working environments is a problem from a scientific standpoint. Even after decade of tireless research, the LHP still suffers from degradations and PL quenching under adverse conditions, such as high temperatures, residual precursor solvents, high levels of humidity, oxygen, and

light which is schematically represented in figure 1.36. In order to a significant extent insulate from air, solvents, and water, photovoltaic materials are protected by packaging technology. However, due to their low crystal lattice energy, and ionic bonding nature the residues will nonetheless disintegrate their structure. Furthermore, in real-world applications, the LHP will invariably degrade when exposed to the heat and light of the environment and operating chips. As a result, improving the stability is a problem that must be solved for their commercial uses, particularly for the stability under light and the moisture stability.

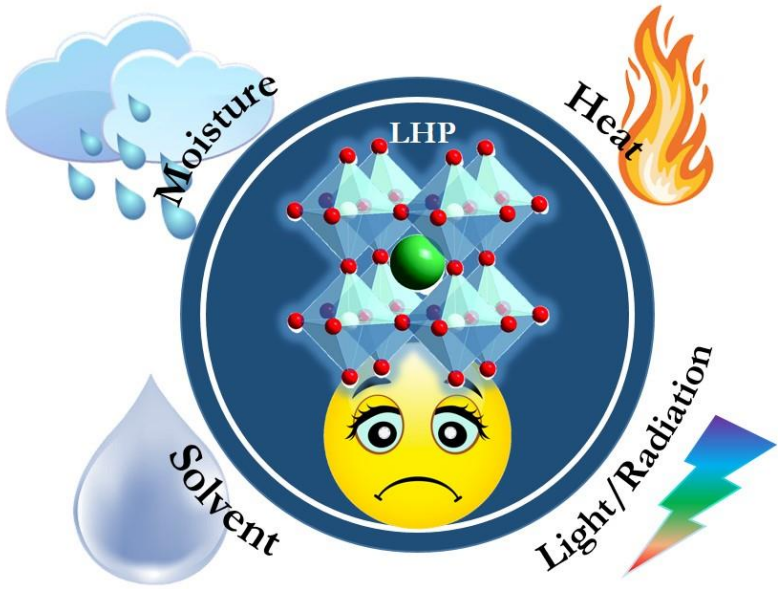

Figure 1.36. Factors that control the stability of LHP.

Because the organic component of organic-inorganic hybrid perovskites is thermally unstable and hygroscopic, humidity plays a significant role in the long-term operation or preservation of LHP.[129-133] The water molecules effectively interact with $[PbX_6]^{4-}$ octahedral units of the perovskite structure resulting rapture of the chemical bond between the A-site cation and $[PbX_6]^{4-}$ octahedral units. The units will completely convert to PbX_2 as the water content rises. In the meanwhile, in all polar organic solvents LHP are soluble and destroyed because of the ionic bonding nature.[134] Residual precursor solvents also plays a significant role in degradation of

LHP NC structure. Most of the precursor solvents (e.g., DMSO, DMF) that are used in perovskite NC synthesis have coordinating ability.[14] The residual precursor solvents in the colloidal NC suspension can adhere to the surface of the NC, which promotes NC degradation.[135]

The light irradiation is one of the most important factors that large affect the stability of the NCs. For using NCs in LED devices, it is very important to be stable under continuous irradiation. Continuous UV radiation can change the morphology of the NCs.[136] Lower dimensional NPLs have been reported to transform to their 3D counterpart in presence of UV light.[137, 138] The morphological change in LHP NCs/NPLs under light irradiation is mostly governed by the ligand desorption process. The light irradiation in presence of oxygen is even more fatal and promote the full degradation of the NCs.[139, 140] These photoinduced transformations or degradation of LHP NCs is a serious concern which can limits its practical applicability.

Temperature or heat is another factor that can damage the crystal structure of the LHPs. However, the cesium lead halide perovskites show much more heat tolerance than the organic-inorganic hybrid perovskites. Whereas the thermal stability of $MAPbBr_3$ and $MAPbI_3$ are 220°C[141] and 250°C, [142] respectively, the decomposition temperature of $CsPbX_3$ is ~500°C.[141] This heat induced degradation of perovskite crystal even accelerate in presence of moisture and light.[70] The PL stability of the NCs not only depends on the crystal structure decomposition, but also on the ligand desororption from the NC surface. Heat induced desorption of ligand from the NC surface can originate trapping sites, resulting decrease in the PL intensity of the NCs.[143]

1.3.7.2. Toxicity: The lead atom in the LHP plays a vital role in the properties as well as in the electronic structure.[144, 145] The electronic configuration $6s^26p^0$ of Pb^{2+} allows the filled 6s orbital of lead to couple with halide np orbitals (n=3,4, and 5 for Cl, Br, I, respectively) to form the valence band.[146] The strong coupling between

lead 6s orbital with halide np orbitals effectively increases the valence band level, resulting defect states shallower.[147, 148]

However, reducing toxicity of LHPs is inevitable to achieve environmental sustainability. Lead has an adverse effect on the environment and as its soluble salts are poisonous to people.[149] Prolonged exposure to lead can have negative health effects, including harm to the central nervous system, disorders of the liver, blood, lungs, and kidneys even an increased risk of cancer.[150] This toxicity is because of the bond affinity of lead with thiol of various enzymes, proteins, and cell membranes and with cellular phosphate groups. In addition, release into the environment can affect the ecology which limits the possible applications of these materials.[151] Li *et al.* discovered lately that plants are around ten times more capable of absorbing lead as a result of the perovskite structure than other sources of lead contamination that are already present in the soil.[152]

A proper encapsulation of these NCs can prolong the stability in the device application. However, this encapsulation does not ensure that it will be fully effective for the duration of the device's functioning life.[153] So, the risk of lead contamination from the LHP NC devices always remains a key concern in commercial use.

The precursor solvent related toxicity is one of most important but underestimated topic in the perovskite research. In common synthesis methods (LARP or hot injection), we generally use toxic or hazardous organic solvents like skin-penetrating dimethyl sulfoxide (DMSO), dimethylformamide (DMF) along with its homologous dimethylacetamide (DMAC), N-methyl-2-pyrrolidone (NMP), and octadecene to dissolve the lead halide salts. These all-organic solvents and also have adverse effect on human body.

1.3.7.3. Possible way out:

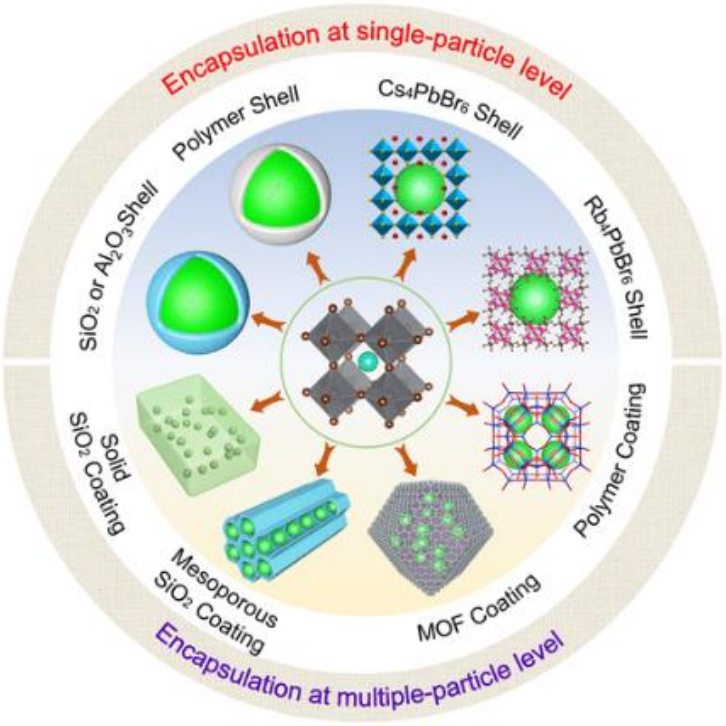

Figure 1.37. Overview of the various shell materials used to encapsulate perovskite NCs in a schematic fashion for increasing their stability against water, moisture, heat, and other environmental pressures. Reproduced from Ref. 11.

Researchers around the globe have been trying to solve these key issues of stability and toxicity from very beginning for LHP research. Stability of the LHP NCs vastly depends on how these NCs interact with moisture, light or any other external perturbation. So, to minimize these interactions the most used technique is proper encapsulation of these NCs. Ligand engineering takes the leading role in this area.[81] Uses of many innovative ligands in place of conventional OA and OAm pair have been reported in recent times which can effectively increase the stability of the NCs which is shown in figure 1.27. Another strategy is to make core-shell type of NCs where a shell is grown on the LHP NC surface which gives superior stability. Over last few years, many reports have come up with varies coating materials which is illustrated in figure 1.35.[11] It has been demonstrated that encapsulation by inert materials is a workable and successful method to stop the degradation and improve

stability, allowing them to endure under water, light, and heat treatment.[11, 154-160] Many of these reports also suggests the suppression of nonradiative channels by minimizing the surface defects through proper encapsulation, resulting amplification of the PLQY.[11] The possible methods and materials used for encapsulation of LHP NCs are schematically shown in figure 1.37.

Doping of metal ions in B-site of LHP NCs also have been found to be effective for improving the phase and air stability of the LHP NCs.[161] Monovalent Ag^{+}, divalent Cu^{2+}, Zn^{2+}, Mn^{2+}, Sr^{2+}, Cd^{2+}, Sn^{2+} doping in LHP NCs have successfully been introduced to boost the stability.[162-166] Doping of trivalent Ce^{3+}, Sb^{3+}, and Bi^{3+} also been reported for introducing better stability of LHP structure.[165-168]

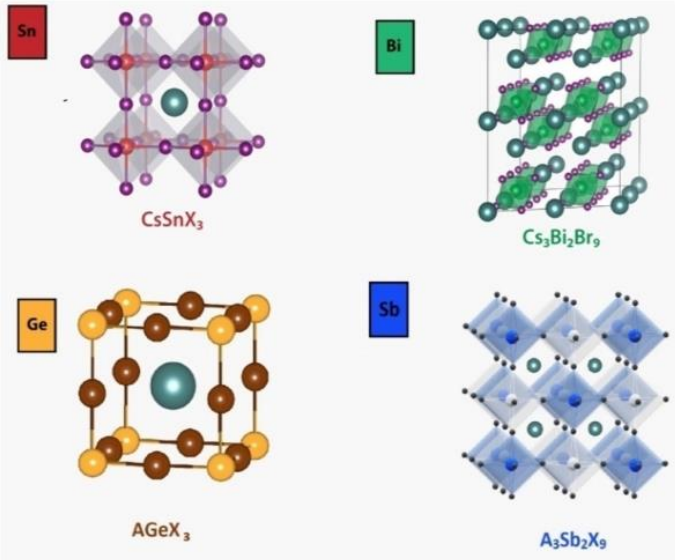

Figure 1.38. Structures of cesium tin halide perovskite, cesium bismuth halide perovskite, cesium germanium halide perovskite, and cesium antimony halide perovskite. Reproduced from Ref. 63.

The only possible way to tackle the toxicity issue is to replace lead with other metal ions. Recent years have witnessed the development of several novel "lead-free" materials.[169] Substituents need to have similar electronic structures with lead-based perovskites in order to achieve exceptional optoelectronic characteristics. Recent studies have replaced lead with a number of less toxic cations that belong to the same

group as the element or are close to it. These include ions from the IVA group, such Sn^{2+} and Ge^{2+}, ions from group VA with a similar structure, like Bi^{3+} and Sb^{3+}, and others.[170] Lead free perovskites shows PL over a wide spectral range, from blue to near IR region, due to the variety of chemical compositions they can have. However, still date the lead-free perovskite have not achieved the extraordinary properties like LHPs. Most of lead-free perovskite NCs suffers from very low PLQY which restricts their practical applicability.[170] Tin based perovskite NCs on the contrary shows very nice PL properties but suffers from arial oxidation to Sn^{4+}.[171, 172] The germanium based perovskites have been explored theoretically but again their high probability of arial oxidation from Ge^{2+} to Ge^{4+} limits its applicability.[173] Antimony (Sb) can be used as a replacement for lead because of its superior optoelectronic qualities and ability to form in a variety of structural dimensions, from 0D to 3D.[174] Trivalent metals, like Sb, can produce perovskites that are arranged according to vacancy. A stoichiometric $A_3Sb_2X_9$ is produced in this instance because of the 2:1 occupation of the B sites.[46] These perovskites often display low conductivity due to the high trap density, which again limits their use.[175] Bismuth is another intriguing option for a lead substitute (Bi). The Bi^{3+} ion is less hazardous than lead and resembles the Pb^{2+} ion in terms of its ionic radius and electron configuration.[176] Due to their proximity in the periodic table (same period), the two elements have comparable energy levels and electronic characteristics. Bi-based perovskites display an $A_3Bi_2X_9$ configuration, which differs from the Pb-based perovskite stoichiometry.[177] Bi^{3+} transforms the crystal from 3D to 2D as just two-thirds of the octahedral sites fully occupied.[148] Shen et al. recently synthesised $FA_3Bi_2Br_9$ quantum dots with emission at 437 nm and a PLQY of 52%, displaying high stability in air and outstanding stability in ethanol.[178] An anion exchange reaction was demonstrated by Lou *et al.* in the synthesis of $Cs_3Bi_2X_9$, which showed an emission band in the range of 380–526 nm with a PLQY of 62% for the $Cs_3Bi_2Cl_9$ composition.[179] The majority of bismuth compounds are readily available on the market, affordable, manageable, and non-toxic, making them excellent replacements for lead. But still the bismuth-based

perovskite NCs mostly appears with very low PLQY due to the high trap density which needs to overcome. The structures for lead-free Sn-based, Ge-based, Bi-based, and Sb-based perovskites are shown in figure 1.38.

In the last few years, Manganese (Mn) and Copper (Cu) based perovskite materials have emerged with great possibilities. Several stoichiometries of Mn-based perovskite system have been reported recently. Recent research by Kwon *et al.* has synthesized Mn- based green light emitting NCs, Cs_3MnI_5 and Cs_3MnBr_5 with high PLQY.[180] Almutlaq *et al.* reported the monodispersed red emitting $CsMnBr_3$ NCs with high PLQY.[181] Jalali *et al.* reported the phase selective synthesis of Cs_3MnBr_5 and $CsMnBr_3$ NCs with green and red emission, respectively.[182] These reports of lead-free Mn based perovskites NCs shows very nice PL properties with good environmental stabilities which may make them a desirable candidate in the lead-free perovskite optoelectronics family.

Copper-based halide perovskite materials on the other hand is becoming the most popular in lead-free perovskite family due to its unique stoke shifted emission properties.[58] Blue emissive $Cs_3Cu_2I_5$ perovskite have been successfully synthesized with 100% PLQY. The emission of these Cu-based perovskites originates from the self-trapped excitonic state. The photoexcitation of Cu (I) based perovskites leading to the formation of Cu (II) in the excited state, resulting photoinduced Jahn-Teller distortion in the lattice.[183] This lattice distortion effectively traps the exciton to form STE in lower energy. The formation of this lower energy self-trapped excitonic state is the origin of large stoke shift in copper halide perovskites. The stoke shift is even higher in $Cs_3Cu_2Br_5$ and $Cs_3Cu_2Cl_5$, because of the higher carrier phonon coupling, resulting blue-green and green emissions, respectively.[59, 184] This STE emission in $Cs_3Cu_2X_5$ (X=Cl, Br, and I) is schematically shown in figure 1.39. Another phase of copper halide perovskite is $CsCu_2I_3$, which shows yellow emission, again governed by the self-trapped excitons.[128] The zero probability of self-absorption in these materials because of the highly stoke shifted emission makes them ideal for practical

applications. Because of the unique properties, these copper-based halide perovskites have already successfully introduced in photodetectors,[185-187] LED[187, 188], and X-ray scintillators.[189, 190]

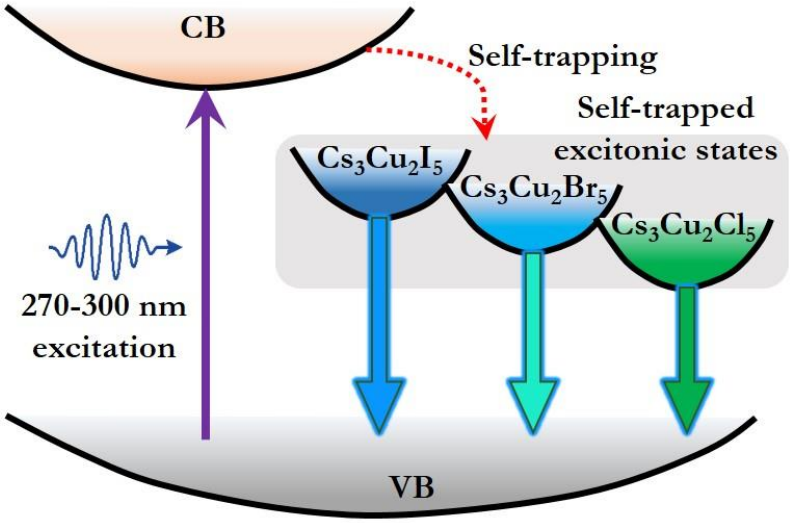

Figure 1.39. Schematic representation of self-trapped emission in $Cs_3Cu_2X_5$ perovskite (X=Cl, Br, and I).

The solvent related toxicity is also one of the key concerns that is rarely talked about in the perovskite community. In very recent time this field of research is gaining its interest because of the obvious sustainable issues.[191, 192] The use of hazardous organic precursor solvents also can affect human body which in the previous section (section 1.3.7.2) we have already discussed. Also, the coordinating ability of many of these solvents which remains in the NC suspension as residual, allows them to interact with the perovskite NC surface and facilitates degradation.[14, 15] For these reasons search of new green solvents is necessary for perovskite NC synthesis. The first report of synthesizing bulk $MAPbI_3$ thin film using ionic liquid (IL)came up in 2015 from Estroff's research group.[193] In this report, they have used methylammonium formate as IL for synthesizing the perovskite. Although, the quality of the material was not good enough, but this process shed a light of hope on the possibilities to perovskite synthesis in green alternative medium. After this report, various methylammonium and formamidinium carboxylate ILs have been

used for the synthesis of various methylammonium and formamidinium based LHPs.[191, 194-197] ILs have also been introduced as additives to improve the efficiency, interface modification, and stability of the LHP solar cells.[198] Although significant improvements have been done related to synthesis as well as properties of LHPs using ILs, but still this field is roaming mainly around thin film solar cells. However, recently in 2020 Hoang *et al.* reported the first green synthesis of $MAPbBr_3$ NCs with ~50% PLQY in three different IL medium composed of methylamine and three short chain carboxylic acids (formic acid, acetic acid, and butyric acid).[199] Even after this report, still the synthesis of LHP NCs in alternative medium is rare in literature and development is necessary in this research field.

1.3.8. Focus of this thesis

From all the discussion so far, it is evident that LHP NCs suffer from severe problems which are mainly related to the stability and toxicity. The focus of this thesis is on improving stability through metal ion doping, reducing toxicity by using green solvents in LHP NC synthesis and synthesizing lead-free copper halide perovskite NCs in these environment friendly green solvents for ultimate non-toxicity. The thesis is divided into eight chapters. Apart from introduction (chapter 1) and experimental part (chapter 2), the working chapter starts with chapter 3. In chapter 3, the properties of Bi^{3+} doped $MAPbI_3$ NCs (MPBI NCs) have been investigated. The MPBI NCs shows a very slow reversible crystal growth in toluene medium which is proposed to be mediated through dynamic ligand binding. Chapter 4 deals with the low PLQY of Bi^{3+} doped LHP NCs. In this chapter, the reason of PL quenching is investigated through charge carrier dynamics and PLQY is amplified through K^+ co-doping. In these first two working chapters (chapter 3 and chapter 4) we will also see that introducing bismuth in the LHP NCs can boost the environmental stability to a certain extent than their pure lead analogues, and K^+ co-doping can boost it further. Chapter 5 and chapter 6 are mainly focused on the solvent related toxicity in LHP NC synthesis. In chapter 5, an IL medium composed

of methylamine and lauric acid (LA) is introduced to synthesize the $MAPbX_3$ (X=Cl, Br, and I) NCs. The high hydrophobicity of LA is then put into use to synthesize $MAPbBr_3$@lead laurate core-shell structure which increases the water stability of the system to a far extent. However, despite having better stability, this methylamine based ILs are very selective towards methylammonium based perovskite NCs. Also, solid lead halide salts immediately form perovskite coming in contact to this medium restricts its use in synthesizing mixed halide perovskites and doped lead halide perovskites. To address these issues, I employed menthol based deep eutectic solvents (DES) as a green medium in chapter 6 to synthesize all inorganic cesium lead halide perovskite NCs. The variation in synthesis temperature and lead to cesium precursor ratio in these DES media have been found to be a key factor in preparation of lower dimension LHP NPLs. In the final chapter (chapter 7) these menthol-based DES is used to synthesize lead-free $Cs_3Cu_2I_5$ and $Cs_3Cu_2Br_5$ NCs which eventually eliminate both lead related toxicity as well as solvent related toxicity. Apart from the synthesis the role of trap state in the photo physics of the copper halide perovskite NCs is discussed in this chapter. In the end, the general conclusions and future aspects of this thesis work is discussed in chapter 8.

References

1. Yoo, J. J.; Shin, S. S.; Seo, J., Toward Efficient Perovskite Solar Cells: Progress, Strategies, and Perspectives. *ACS Energy Letters* **2022,** *7*, 2084-2091.
2. Kojima, A.; Teshima, K.; Shirai, Y.; Miyasaka, T., Organometal Halide Perovskites as Visible-Light Sensitizers for Photovoltaic Cells. *Journal of the American Chemical Society* **2009,** *131* (17), 6050-6051.
3. Liu, J.; De Bastiani, M.; Aydin, E.; Harrison, G. T.; Gao, Y.; Pradhan, R. R.; Eswaran, M. K.; Mandal, M.; Yan, W.; Seitkhan, A., Efficient and stable perovskite-silicon tandem solar cells through contact displacement by MgF_x. *Science* **2022,** *377* (6603), 302-306.
4. Shi, Z.; Jayatissa, A. H., Perovskites-based solar cells: A review of recent progress, materials and processing methods. *Materials* **2018,** *11* (5), 729.
5. Ono, L. K.; Qi, Y.; Liu, S. F., Progress toward stable lead halide perovskite solar cells. *Joule* **2018,** *2* (10), 1961-1990.
6. Qiao, T.; Son, D. H., Synthesis and Properties of Strongly Quantum-Confined Cesium Lead Halide Perovskite Nanocrystals. *Accounts of Chemical Research* **2021,** *54* (6), 1399-1408.
7. Malgras, V.; Tominaka, S.; Ryan, J. W.; Henzie, J.; Takei, T.; Ohara, K.; Yamauchi, Y., Observation of Quantum Confinement in Monodisperse Methylammonium Lead Halide Perovskite Nanocrystals Embedded in Mesoporous Silica. *Journal of the American Chemical Society* **2016,** *138* (42), 13874-13881.
8. Chen, Q.; Wu, J.; Ou, X.; Huang, B.; Almutlaq, J.; Zhumekenov, A. A.; Guan, X.; Han, S.; Liang, L.; Yi, Z.; Li, J.; Xie, X.; Wang, Y.; Li, Y.; Fan, D.; Teh, D. B. L.; All, A. H.; Mohammed, O. F.; Bakr, O. M.; Wu, T.; Bettinelli, M.; Yang, H.; Huang, W.; Liu, X., All-inorganic perovskite nanocrystal scintillators. *Nature* **2018,** *561* (7721), 88-93.
9. Xu, Y.; Chen, Q.; Zhang, C.; Wang, R.; Wu, H.; Zhang, X.; Xing, G.; Yu, W. W.; Wang, X.; Zhang, Y.; Xiao, M., Two-Photon-Pumped Perovskite

Semiconductor Nanocrystal Lasers. *Journal of the American Chemical Society* **2016,** *138* (11), 3761-3768.

10. Ketavath, R.; Mohan, L.; Sumukam, R. R.; Alsulami, Q. A.; Premalatha, A.; Murali, B., Can perovskites be efficient photocatalysts in organic transformations? *Journal of Materials Chemistry A* **2022,** *10* (23), 12317-12333.
11. Dey, A.; Ye, J.; De, A.; Debroye, E.; Ha, S. K.; Bladt, E.; Kshirsagar, A. S.; Wang, Z.; Yin, J.; Wang, Y.; Quan, L. N.; Yan, F.; Gao, M.; Li, X.; Shamsi, J.; Debnath, T.; Cao, M.; Scheel, M. A.; Kumar, S.; Steele, J. A.; Gerhard, M.; Chouhan, L.; Xu, K.; Wu, X.-g.; Li, Y.; Zhang, Y.; Dutta, A.; Han, C.; Vincon, I.; Rogach, A. L.; Nag, A.; Samanta, A.; Korgel, B. A.; Shih, C.-J.; Gamelin, D. R.; Son, D. H.; Zeng, H.; Zhong, H.; Sun, H.; Demir, H. V.; Scheblykin, I. G.; Mora-Seró, I.; Stolarczyk, J. K.; Zhang, J. Z.; Feldmann, J.; Hofkens, J.; Luther, J. M.; Pérez-Prieto, J.; Li, L.; Manna, L.; Bodnarchuk, M. I.; Kovalenko, M. V.; Roeffaers, M. B. J.; Pradhan, N.; Mohammed, O. F.; Bakr, O. M.; Yang, P.; Müller-Buschbaum, P.; Kamat, P. V.; Bao, Q.; Zhang, Q.; Krahne, R.; Galian, R. E.; Stranks, S. D.; Bals, S.; Biju, V.; Tisdale, W. A.; Yan, Y.; Hoye, R. L. Z.; Polavarapu, L., State of the Art and Prospects for Halide Perovskite Nanocrystals. *ACS Nano* **2021,** *15* (7), 10775-10981.
12. Shankar, H.; Ghosh, S.; Kar, P., Boosting the stability of lead halide perovskite nanocrystals by metal–organic frameworks and their applications. *Journal of Materials Chemistry C* **2022,** *10* (32), 11532-11554.
13. Ravi, V. K.; Mondal, B.; Nawale, V. V.; Nag, A., Don't Let the Lead Out: New Material Chemistry Approaches for Sustainable Lead Halide Perovskite Solar Cells. *ACS Omega* **2020,** *5* (46), 29631-29641.
14. Zhang, F.; Huang, S.; Wang, P.; Chen, X.; Zhao, S.; Dong, Y.; Zhong, H., Colloidal synthesis of air-stable $CH_3NH_3PbI_3$ quantum dots by gaining

chemical insight into the solvent effects. *Chemistry of Materials* **2017,** *29* (8), 3793-3799.

15. Stevenson, J.; Sorenson, B.; Subramaniam, V. H.; Raiford, J.; Khlyabich, P. P.; Loo, Y.-L.; Clancy, P., Mayer bond order as a metric of complexation effectiveness in lead halide perovskite solutions. *Chemistry of Materials* **2017,** *29* (6), 2435-2444.
16. Yacobi, B. G., *Semiconductor materials: an introduction to basic principles*. Springer Science & Business Media, Springer New York: New York, NY: **2003**.
17. Neamen, D. A., *Semiconductor physics and devices: basic principles*. McGraw-hill, Hoboken, New Jersey, U.S.: **2003**.
18. Kerner, E. H., Periodic impurities in a periodic lattice. *Physical Review* **1954,** *95* (3), 687.
19. Ginzbarg, A. S. Electronic Band Structure of Mixed Crystals. Purdue University, United States, **1949**.
20. Singleton, J., *Band theory and electronic properties of solids*. Oxford University Press, London, UK: **2001**; Vol. 2.
21. Colinge, J.-P.; Colinge, C. A., *Physics of semiconductor devices*. Springer Science & Business Media, New York, NY: **2005**.
22. Bouckaert, L. P.; Smoluchowski, R.; Wigner, E., Theory of Brillouin zones and symmetry properties of wave functions in crystals. *Physical Review* **1936,** *50* (1), 58.
23. Fowler, R. H., An elementary theory of electronic semi-conductors, and some of their possible properties. *Proceedings of the Royal Society of London. Series A, Containing Papers of a Mathematical and Physical Character* **1933,** *140* (842), 505-522.
24. Lax, B., Experimental investigations of the electronic band structure of solids. *Reviews of Modern Physics* **1958,** *30* (1), 122.

25. Burstein, E.; Egli, P. H., The physics of semiconductor materials. In *Advances in Electronics and Electron Physics*, Elsevier: 1955; Vol. 7, pp 1-84.
26. Smith, R., Physics of semiconductors. Nature Publishing Group UK London, London, UK: **1960**.
27. Das, A. K.; Das, M., An Introduction to Nanomaterial and Nanoscience. CBS Publishers and Distributors Pvt Ltd: Delhi, India: **2005**.
28. Gaponenko, S. V., *Introduction to nanophotonics*. Cambridge University Press, Cambridge, UK: **2010**.
29. Henderson, B., G. F. Imbusch, Optical Spectroscopy of Inorganic Solids. Clarendon Press, Oxford, London, UK: **1989**.
30. Xia, Y.; Xiong, Y.; Lim, B.; Skrabalak, S. E., Shape-controlled synthesis of metal nanocrystals: simple chemistry meets complex physics? *Angewandte Chemie International Edition* **2009,** *48* (1), 60-103.
31. Owen, J.; Brus, L., Chemical synthesis and luminescence applications of colloidal semiconductor quantum dots. *Journal of the American Chemical Society* **2017,** *139* (32), 10939-10943.
32. Yin, Y.; Alivisatos, A. P., Colloidal nanocrystal synthesis and the organic–inorganic interface. *Nature* **2005,** *437* (7059), 664-670.
33. Duonghong, D.; Ramsden, J.; Grätzel, M., Dynamics of interfacial electron-transfer processes in colloidal semiconductor systems. *J. Am. Chem. Soc* **1982,** *104* (11), 2977-2985.
34. Que, M.; Zhu, L.; Guo, Y.; Que, W.; Yun, S., Toward perovskite nanocrystalline solar cells: progress and potential. *Journal of Materials Chemistry C* **2020,** *8* (16), 5321-5334.
35. Dey, A.; Ye, J.; De, A.; Debroye, E.; Ha, S. K.; Bladt, E.; Kshirsagar, A. S.; Wang, Z.; Yin, J.; Wang, Y., State of the art and prospects for halide perovskite nanocrystals. *ACS nano* **2021,** *15* (7), 10775-10981.
36. Gao, W.; Yu, S. F., Reality or fantasy—Perovskite semiconductor laser diodes. *EcoMat* **2021,** *3* (1), e12077.

37. Liu, D.; Guo, Y.; Que, M.; Yin, X.; Liu, J.; Xie, H.; Zhang, C.; Que, W., Metal halide perovskite nanocrystals: application in high-performance photodetectors. *Materials Advances* **2021,** *2* (3), 856-879.
38. Ketavath, R.; Lakavath, M.; Sumukam, R. R.; Alsulami, Q. A.; Premalatha, A.; Banavoth, M., Can perovskites be efficient photocatalysts in organic transformations? *Journal of Materials Chemistry A* **2022**.
39. Schmidt, L. C.; Pertegás, A.; González-Carrero, S.; Malinkiewicz, O.; Agouram, S.; Minguez Espallargas, G.; Bolink, H. J.; Galian, R. E.; Pérez-Prieto, J., Nontemplate synthesis of $CH_3NH_3PbBr_3$ perovskite nanoparticles. *Journal of the American Chemical Society* **2014,** *136* (3), 850-853.
40. Smith, A. M.; Nie, S., Semiconductor nanocrystals: structure, properties, and band gap engineering. *Accounts of chemical research* **2010,** *43* (2), 190-200.
41. Brandt, R. E.; Poindexter, J. R.; Gorai, P.; Kurchin, R. C.; Hoye, R. L.; Nienhaus, L.; Wilson, M. W.; Polizzotti, J. A.; Sereika, R.; Zaltauskas, R., Searching for "defect-tolerant" photovoltaic materials: combined theoretical and experimental screening. *Chemistry of Materials* **2017,** *29* (11), 4667-4674.
42. Kovalenko, M. V.; Protesescu, L.; Bodnarchuk, M. I., Properties and potential optoelectronic applications of lead halide perovskite nanocrystals. *Science* **2017,** *358* (6364), 745-750.
43. Huang, H.; Bodnarchuk, M. I.; Kershaw, S. V.; Kovalenko, M. V.; Rogach, A. L., Lead halide perovskite nanocrystals in the research spotlight: stability and defect tolerance. *ACS energy letters* **2017,** *2* (9), 2071-2083.
44. Nedelcu, G.; Protesescu, L.; Yakunin, S.; Bodnarchuk, M. I.; Grotevent, M. J.; Kovalenko, M. V., Fast anion-exchange in highly luminescent nanocrystals of cesium lead halide perovskites ($CsPbX_3$, X= Cl, Br, I). *Nano letters* **2015,** *15* (8), 5635-5640.
45. Creutz, S. E.; Crites, E. N.; De Siena, M. C.; Gamelin, D. R., Anion exchange in cesium lead halide perovskite nanocrystals and thin films using

trimethylsilyl halide reagents. *Chemistry of Materials* **2018,** *30* (15), 4887-4891.

46. Akkerman, Q. A.; Manna, L., What defines a halide perovskite? *ACS Energy Letters* **2020,** *5* (2), 604-610.
47. Chen, J.-K.; Zhao, Q.; Shirahata, N.; Yin, J.; Bakr, O. M.; Mohammed, O. F.; Sun, H.-T., Shining Light on the Structure of Lead Halide Perovskite Nanocrystals. *ACS Materials Letters* **2021,** *3* (6), 845-861.
48. Goldschmidt, V. M., Die gesetze der krystallochemie. *Naturwissenschaften* **1926,** *14* (21), 477-485.
49. Manser, J. S.; Christians, J. A.; Kamat, P. V., Intriguing Optoelectronic Properties of Metal Halide Perovskites. *Chemical Reviews* **2016,** *116* (21), 12956-13008.
50. Shannon, R. D., Revised effective ionic radii and systematic studies of interatomic distances in halides and chalcogenides. *Acta crystallographica section A: crystal physics, diffraction, theoretical and general crystallography* **1976,** *32* (5), 751-767.
51. Van der Stam, W.; Geuchies, J. J.; Altantzis, T.; Van Den Bos, K. H.; Meeldijk, J. D.; Van Aert, S.; Bals, S.; Vanmaekelbergh, D.; de Mello Donega, C., Highly emissive divalent-ion-doped colloidal $CsPb_{1-x}M_xBr_3$ perovskite nanocrystals through cation exchange. *Journal of the American Chemical Society* **2017,** *139* (11), 4087-4097.
52. Kieslich, G.; Sun, S.; Cheetham, A. K., Solid-state principles applied to organic–inorganic perovskites: new tricks for an old dog. *Chemical Science* **2014,** *5* (12), 4712-4715.
53. Green, M. A.; Ho-Baillie, A.; Snaith, H. J., The emergence of perovskite solar cells. *Nature photonics* **2014,** *8* (7), 506-514.
54. Aharon, S.; Etgar, L., Two Dimensional Organometal Halide Perovskite Nanorods with Tunable Optical Properties. *Nano Letters* **2016,** *16* (5), 3230-3235.

55. Howard, C. J.; Stokes, H. T., Group-theoretical analysis of octahedral tilting in perovskites. *Acta Crystallographica Section B: Structural Science* **1998,** *54* (6), 782-789.
56. Fonseca, A. F. V. d.; Vale, B. R. C.; Carvalho, T. A. d. S.; Bettini, J.; Pereira, A. C.; Schiavon, M. A., Charge Transfer Improvement after Solvent-Induced Phase Change in Type-I Cs_4PbBr_6@$CsPbBr_3$ Core–Shell Perovskites. *The Journal of Physical Chemistry C* **2021,** *125* (49), 27363-27371.
57. Protesescu, L.; Yakunin, S.; Kumar, S.; Bär, J.; Bertolotti, F.; Masciocchi, N.; Guagliardi, A.; Grotevent, M.; Shorubalko, I.; Bodnarchuk, M. I., Dismantling the "red wall" of colloidal perovskites: highly luminescent formamidinium and formamidinium–cesium lead iodide nanocrystals. *ACS nano* **2017,** *11* (3), 3119-3134.
58. Li, Y.; Zhou, Z.; Tewari, N.; Ng, M.; Geng, P.; Chen, D.; Ko, P. K.; Qammar, M.; Guo, L.; Halpert, J. E., Progress in copper metal halides for optoelectronic applications. *Materials Chemistry Frontiers* **2021,** *5* (13), 4796-4820.
59. Sebastia-Luna, P.; Navarro-Alapont, J.; Sessolo, M.; Palazon, F.; Bolink, H. J., Solvent-Free Synthesis and Thin-Film Deposition of Cesium Copper Halides with Bright Blue Photoluminescence. *Chemistry of Materials* **2019,** *31* (24), 10205-10210.
60. Hui, Y.; Chen, S.; Lin, R.; Zheng, W.; Huang, F., Photophysics in $Cs_3Cu_2I_5$ and $CsCu_2I_3$. *Materials Chemistry Frontiers* **2021,** *5* (19), 7088-7107.
61. Cheng, S.; Beitlerova, A.; Kucerkova, R.; Nikl, M.; Ren, G.; Wu, Y., Zero-Dimensional $Cs_3Cu_2I_5$ Perovskite Single Crystal as Sensitive X-Ray and γ-Ray Scintillator. *physica status solidi (RRL) – Rapid Research Letters* **2020,** *14* (11), 2000374.
62. Li, Z.; Li, Z.; Shi, Z.; Fang, X., Facet-Dependent, Fast Response, and Broadband Photodetector Based on Highly Stable All-Inorganic $CsCu_2I_3$

Single Crystal with 1D Electronic Structure. *Advanced Functional Materials* **2020,** *30* (28), 2002634.

63. Souza Carvalho, T. A.; Magalhães, L. F.; Santos, C. I. d. L.; Freitas, T. A. Z.; de Carvalho Vale, B. R.; Vale da Fonseca, A. F.; Schiavon, M. A., Lead-Free Metal Halide Perovskite Nanocrystals: From Fundamentals to Applications. *Chemistry–A European Journal*.
64. Yang, D.; Cao, M.; Zhong, Q.; Li, P.; Zhang, X.; Zhang, Q., All-inorganic cesium lead halide perovskite nanocrystals: synthesis, surface engineering and applications. *Journal of Materials Chemistry C* **2019,** *7* (4), 757-789.
65. Huang, H.; Polavarapu, L.; Sichert, J. A.; Susha, A. S.; Urban, A. S.; Rogach, A. L., Colloidal lead halide perovskite nanocrystals: synthesis, optical properties and applications. *NPG Asia Materials* **2016,** *8* (11), e328-e328.
66. de Souza Carvalho, T. A.; Magalhaes, L. F.; do Livramento Santos, C. I.; de Freitas, T. A. Z.; Carvalho Vale, B. R.; Vale da Fonseca, A. F.; Schiavon, M. A., Lead-Free Metal Halide Perovskite Nanocrystals: From Fundamentals to Applications. *Chemistry – A European Journal n/a* (n/a), e202202518.
67. Chen, M.; Zou, Y.; Wu, L.; Pan, Q.; Yang, D.; Hu, H.; Tan, Y.; Zhong, Q.; Xu, Y.; Liu, H., Solvothermal synthesis of high-quality all-inorganic cesium lead halide perovskite nanocrystals: from nanocube to ultrathin nanowire. *Advanced Functional Materials* **2017,** *27* (23), 1701121.
68. Shamsi, J.; Urban, A. S.; Imran, M.; De Trizio, L.; Manna, L., Metal halide perovskite nanocrystals: synthesis, post-synthesis modifications, and their optical properties. *Chemical reviews* **2019,** *119* (5), 3296-3348.
69. Murray, C.; Norris, D. J.; Bawendi, M. G., Synthesis and characterization of nearly monodisperse CdE (E= sulfur, selenium, tellurium) semiconductor nanocrystallites. *Journal of the American Chemical Society* **1993,** *115* (19), 8706-8715.

70. Wang, S.; Yousefi Amin, A. A.; Wu, L.; Cao, M.; Zhang, Q.; Ameri, T., Perovskite nanocrystals: Synthesis, stability, and optoelectronic applications. *Small Structures* **2021,** *2* (3), 2000124.
71. Mahajan, S.; Rani, M.; Dubey, R.; Mahajan, J., Synthesis of CdSe crystal using hot injection method. *Int. J. Lat. Reas. Sci. Nanotechnol* **2013,** *1*, 518-521.
72. Protesescu, L.; Yakunin, S.; Bodnarchuk, M. I.; Krieg, F.; Caputo, R.; Hendon, C. H.; Yang, R. X.; Walsh, A.; Kovalenko, M. V., Nanocrystals of cesium lead halide perovskites ($CsPbX_3$, X= Cl, Br, and I): novel optoelectronic materials showing bright emission with wide color gamut. *Nano letters* **2015,** *15* (6), 3692-3696.
73. Pradhan, N., Growth of Lead Halide Perovskite Nanocrystals: Still in Mystery. *ACS Physical Chemistry Au* **2022**.
74. Dutta, S. K.; Peng, L.; Hudait, B.; Xie, R.; Pradhan, N., Halide Perovskite Cluster Precursors: A Paradigm for Obtaining Structure-and Color-Tunable Light-Emitting Nanocrystals. *ACS Energy Letters* **2022,** *7* (9), 3177-3186.
75. Otero-Martínez, C.; García-Lojo, D.; Pastoriza-Santos, I.; Pérez-Juste, J.; Polavarapu, L., Dimensionality Control of Inorganic and Hybrid Perovskite Nanocrystals by Reaction Temperature: From No-Confinement to 3D and 1D Quantum Confinement. *Angewandte Chemie* **2021,** *133* (51), 26881-26888.
76. Otero-Martínez, C.; Ye, J.; Sung, J.; Pastoriza-Santos, I.; Pérez-Juste, J.; Xia, Z.; Rao, A.; Hoye, R. L.; Polavarapu, L., Colloidal Metal-Halide Perovskite Nanoplatelets: Thickness-Controlled Synthesis, Properties, and Application in Light-Emitting Diodes. *Advanced Materials* **2022,** *34* (10), 2107105.
77. Nim, G. K.; Bansal, P.; Kar, P., Nitrate ion-incorporated stable perovskite nanocrystals by a solvent-free mechanochemical reaction. *ACS omega* **2019,** *4* (13), 15678-15683.

78. Jin, H.; Debroye, E.; Keshavarz, M.; Scheblykin, I. G.; Roeffaers, M. B. J.; Hofkens, J.; Steele, J. A., It's a trap! On the nature of localised states and charge trapping in lead halide perovskites. *Materials Horizons* **2020,** *7* (2), 397-410.
79. Mandal, S.; Mukherjee, S.; De, C. K.; Roy, D.; Ghosh, S.; Mandal, P. K., Extent of Shallow/Deep Trap States beyond the Conduction Band Minimum in Defect-Tolerant $CsPbBr_3$ Perovskite Quantum Dot: Control over the Degree of Charge Carrier Recombination. *The Journal of Physical Chemistry Letters* **2020,** *11* (5), 1702-1707.
80. Wu, X.; Trinh, M. T.; Niesner, D.; Zhu, H.; Norman, Z.; Owen, J. S.; Yaffe, O.; Kudisch, B. J.; Zhu, X. Y., Trap States in Lead Iodide Perovskites. *Journal of the American Chemical Society* **2015,** *137* (5), 2089-2096.
81. Ye, J.; Byranvand, M. M.; Martínez, C. O.; Hoye, R. L.; Saliba, M.; Polavarapu, L., Defect passivation in lead-halide perovskite nanocrystals and thin films: toward efficient LEDs and solar cells. *Angewandte Chemie* **2021,** *133* (40), 21804-21828.
82. du Fossé, I.; Mulder, J. T.; Almeida, G.; Spruit, A. G. M.; Infante, I.; Grozema, F. C.; Houtepen, A. J., Limits of Defect Tolerance in Perovskite Nanocrystals: Effect of Local Electrostatic Potential on Trap States. *Journal of the American Chemical Society* **2022,** *144* (25), 11059-11063.
83. ten Brinck, S.; Zaccaria, F.; Infante, I., Defects in Lead Halide Perovskite Nanocrystals: Analogies and (Many) Differences with the Bulk. *ACS Energy Letters* **2019,** *4* (11), 2739-2747.
84. Huang, Y.-T.; Kavanagh, S. R.; Scanlon, D. O.; Walsh, A.; Hoye, R. L., Perovskite-inspired materials for photovoltaics and beyond—from design to devices. *Nanotechnology* **2021,** *32* (13), 132004.
85. Huang, Y.; Yin, W.-J.; He, Y., Intrinsic point defects in inorganic cesium lead iodide perovskite $CsPbI_3$. *The Journal of Physical Chemistry C* **2018,** *122* (2), 1345-1350.

86. Nenon, D. P.; Pressler, K.; Kang, J.; Koscher, B. A.; Olshansky, J. H.; Osowiecki, W. T.; Koc, M. A.; Wang, L.-W.; Alivisatos, A. P., Design principles for trap-free $CsPbX_3$ nanocrystals: enumerating and eliminating surface halide vacancies with softer Lewis bases. *Journal of the American Chemical Society* **2018,** *140* (50), 17760-17772.
87. Bodnarchuk, M. I.; Boehme, S. C.; ten Brinck, S.; Bernasconi, C.; Shynkarenko, Y.; Krieg, F.; Widmer, R.; Aeschlimann, B.; Günther, D.; Kovalenko, M. V.; Infante, I., Rationalizing and Controlling the Surface Structure and Electronic Passivation of Cesium Lead Halide Nanocrystals. *ACS Energy Letters* **2019,** *4* (1), 63-74.
88. Ravi, V. K.; Santra, P. K.; Joshi, N.; Chugh, J.; Singh, S. K.; Rensmo, H.; Ghosh, P.; Nag, A., Origin of the substitution mechanism for the binding of organic ligands on the surface of $CsPbBr_3$ perovskite nanocubes. *The Journal of Physical Chemistry Letters* **2017,** *8* (20), 4988-4994.
89. Smock, S. R.; Williams, T. J.; Brutchey, R. L., Quantifying the thermodynamics of ligand binding to $CsPbBr_3$ quantum dots. *Angewandte Chemie International Edition* **2018,** *57* (36), 11711-11715.
90. De Roo, J.; Ibáñez, M.; Geiregat, P.; Nedelcu, G.; Walravens, W.; Maes, J.; Martins, J. C.; Van Driessche, I.; Kovalenko, M. V.; Hens, Z., Highly dynamic ligand binding and light absorption coefficient of cesium lead bromide perovskite nanocrystals. *ACS nano* **2016,** *10* (2), 2071-2081.
91. Almeida, G.; Infante, I.; Manna, L., Resurfacing halide perovskite nanocrystals. *Science* **2019,** *364* (6443), 833-834.
92. Hills-Kimball, K.; Yang, H.; Cai, T.; Wang, J.; Chen, O., Recent Advances in Ligand Design and Engineering in Lead Halide Perovskite Nanocrystals. *Advanced Science* **2021,** *8* (12), 2100214.
93. Bohn, B. J., *Exciton Dynamics in Lead Halide Perovskite Nanocrystals: Recombination, Dephasing and Diffusion*. Springer Nature, New York, NY: **2021**.

94. Mondal, N.; Samanta, A., Complete ultrafast charge carrier dynamics in photo-excited all-inorganic perovskite nanocrystals ($CsPbX_3$). *Nanoscale* **2017,** *9* (5), 1878-1885.
95. Shen, Q.; Ripolles, T. S.; Even, J.; Ogomi, Y.; Nishinaka, K.; Izuishi, T.; Nakazawa, N.; Zhang, Y.; Ding, C.; Liu, F.; Toyoda, T.; Yoshino, K.; Minemoto, T.; Katayama, K.; Hayase, S., Slow hot carrier cooling in cesium lead iodide perovskites. *Applied Physics Letters* **2017,** *111* (15), 153903.
96. Chung, H.; Jung, S. I.; Kim, H. J.; Cha, W.; Sim, E.; Kim, D.; Koh, W.-K.; Kim, J., Composition-Dependent Hot Carrier Relaxation Dynamics in Cesium Lead Halide ($CsPbX_3$, X=Br and I) Perovskite Nanocrystals. *Angewandte Chemie International Edition* **2017,** *56* (15), 4160-4164.
97. Mondal, N.; De, A.; Das, S.; Paul, S.; Samanta, A., Ultrafast carrier dynamics of metal halide perovskite nanocrystals and perovskite-composites. *Nanoscale* **2019,** *11* (20), 9796-9818.
98. Li, M.; Bhaumik, S.; Goh, T. W.; Kumar, M. S.; Yantara, N.; Grätzel, M.; Mhaisalkar, S.; Mathews, N.; Sum, T. C., Slow cooling and highly efficient extraction of hot carriers in colloidal perovskite nanocrystals. *Nature communications* **2017,** *8* (1), 1-10.
99. Li, M.; Bhaumik, S.; Goh, T. W.; Kumar, M. S.; Yantara, N.; Grätzel, M.; Mhaisalkar, S.; Mathews, N.; Sum, T. C., Slow cooling and highly efficient extraction of hot carriers in colloidal perovskite nanocrystals. *Nature Communications* **2017,** *8* (1), 14350.
100. Yu, B.; Chen, L.; Qu, Z.; Zhang, C.; Qin, Z.; Wang, X.; Xiao, M., Size-Dependent Hot Carrier Dynamics in Perovskite Nanocrystals Revealed by Two-Dimensional Electronic Spectroscopy. *The Journal of Physical Chemistry Letters* **2021,** *12* (1), 238-244.
101. Hintermayr, V. A.; Polavarapu, L.; Urban, A. S.; Feldmann, J., Accelerated Carrier Relaxation through Reduced Coulomb Screening in Two-Dimensional Halide Perovskite Nanoplatelets. *ACS Nano* **2018,** *12* (10), 10151-10158.

102. Wang, Q.; Liu, X.-D.; Qiu, Y.-H.; Chen, K.; Zhou, L.; Wang, Q.-Q., Quantum confinement effect and exciton binding energy of layered perovskite nanoplatelets. *AIP Advances* **2018,** *8* (2), 025108.
103. Wang, T.; Daiber, B.; Frost, J. M.; Mann, S. A.; Garnett, E. C.; Walsh, A.; Ehrler, B., Indirect to direct bandgap transition in methylammonium lead halide perovskite. *Energy & Environmental Science* **2017,** *10* (2), 509-515.
104. Gautam, R. K.; Das, S.; Samanta, A., Can Sulfur-Containing Small Systems Enhance the Photoluminescence and Stability of the Blue-, Green- and Yellow-Emitting Perovskite Nanocrystals? A Case Study with Sodium Thiosulfate. *The Journal of Physical Chemistry C* **2021,** *125* (43), 24170-24179.
105. Behera, R. K.; Das Adhikari, S.; Dutta, S. K.; Dutta, A.; Pradhan, N., Blue-Emitting $CsPbCl_3$ Nanocrystals: Impact of Surface Passivation for Unprecedented Enhancement and Loss of Optical Emission. *The Journal of Physical Chemistry Letters* **2018,** *9* (23), 6884-6891.
106. Wu, K.; Liang, G.; Shang, Q.; Ren, Y.; Kong, D.; Lian, T., Ultrafast Interfacial Electron and Hole Transfer from $CsPbBr_3$ Perovskite Quantum Dots. *Journal of the American Chemical Society* **2015,** *137* (40), 12792-12795.
107. DuBose, J. T.; Kamat, P. V., Energy Versus Electron Transfer: Managing Excited-State Interactions in Perovskite Nanocrystal–Molecular Hybrids. *Chemical Reviews* **2022,** *122* (15), 12475-12494.
108. Bohn, B. J.; Tong, Y.; Gramlich, M.; Lai, M. L.; Döblinger, M.; Wang, K.; Hoye, R. L.; Müller-Buschbaum, P.; Stranks, S. D.; Urban, A. S., Boosting tunable blue luminescence of halide perovskite nanoplatelets through postsynthetic surface trap repair. *Nano letters* **2018,** *18* (8), 5231-5238.
109. Malinoski, A.; Hu, G.; Wang, C., Strong Bidentate Coordination for Surface Passivation and Ligand-Shell Engineering of Lead Halide Perovskite Nanocrystals in the Strongly Quantum-Confined Regime. *The Journal of Physical Chemistry C* **2021,** *125* (44), 24521-24530.

110. Koscher, B. A.; Swabeck, J. K.; Bronstein, N. D.; Alivisatos, A. P., Essentially Trap-Free $CsPbBr_3$ Colloidal Nanocrystals by Postsynthetic Thiocyanate Surface Treatment. *Journal of the American Chemical Society* **2017,** *139* (19), 6566-6569.
111. Vonk, S. J. W.; Fridriksson, M. B.; Hinterding, S. O. M.; Mangnus, M. J. J.; van Swieten, T. P.; Grozema, F. C.; Rabouw, F. T.; van der Stam, W., Trapping and Detrapping in Colloidal Perovskite Nanoplatelets: Elucidation and Prevention of Nonradiative Processes through Chemical Treatment. *The Journal of Physical Chemistry C* **2020,** *124* (14), 8047-8054.
112. Becker, M. A.; Bernasconi, C.; Bodnarchuk, M. I.; Rainò, G.; Kovalenko, M. V.; Norris, D. J.; Mahrt, R. F.; Stöferle, T., Unraveling the Origin of the Long Fluorescence Decay Component of Cesium Lead Halide Perovskite Nanocrystals. *ACS Nano* **2020,** *14* (11), 14939-14946.
113. Vale, B. R. C.; Socie, E.; Burgos-Caminal, A.; Bettini, J.; Schiavon, M. A.; Moser, J.-E., Exciton, Biexciton, and Hot Exciton Dynamics in $CsPbBr_3$ Colloidal Nanoplatelets. *The Journal of Physical Chemistry Letters* **2020,** *11* (2), 387-394.
114. Kanemitsu, Y., Trion dynamics in lead halide perovskite nanocrystals. *The Journal of Chemical Physics* **2019,** *151* (17), 170902.
115. Yumoto, G.; Tahara, H.; Kawawaki, T.; Saruyama, M.; Sato, R.; Teranishi, T.; Kanemitsu, Y., Hot Biexciton Effect on Optical Gain in $CsPbI_3$ Perovskite Nanocrystals. *The Journal of Physical Chemistry Letters* **2018,** *9* (9), 2222-2228.
116. Shen, X.; Wang, S.; Geng, C.; Li, L.; Zhao, E.; Sun, J.; Wu, W.; An, L.; Pan, K., Red Shift of Bleaching Signals in Femtosecond Transient Absorption Spectra of $CsPbX_3$ (X = Cl/Br, Br, Br/I) Nanocrystals Induced by the Biexciton Effect. *The Journal of Physical Chemistry C* **2021,** *125* (9), 5278-5287.
117. Nakahara, S.; Tahara, H.; Yumoto, G.; Kawawaki, T.; Saruyama, M.; Sato, R.; Teranishi, T.; Kanemitsu, Y., Suppression of Trion Formation in $CsPbBr_3$

Perovskite Nanocrystals by Postsynthetic Surface Modification. *The Journal of Physical Chemistry C* **2018,** *122* (38), 22188-22193.

118. Ulatowski, A. M.; Wright, A. D.; Wenger, B.; Buizza, L. R. V.; Motti, S. G.; Eggimann, H. J.; Savill, K. J.; Borchert, J.; Snaith, H. J.; Johnston, M. B.; Herz, L. M., Charge-Carrier Trapping Dynamics in Bismuth-Doped Thin Films of $MAPbBr_3$ Perovskite. *The Journal of Physical Chemistry Letters* **2020,** *11* (9), 3681-3688.
119. Begum, R.; Parida, M. R.; Abdelhady, A. L.; Murali, B.; Alyami, N. M.; Ahmed, G. H.; Hedhili, M. N.; Bakr, O. M.; Mohammed, O. F., Engineering Interfacial Charge Transfer in $CsPbBr_3$ Perovskite Nanocrystals by Heterovalent Doping. *Journal of the American Chemical Society* **2017,** *139* (2), 731-737.
120. Yin, J.; Ahmed, G. H.; Bakr, O. M.; Brédas, J.-L.; Mohammed, O. F., Unlocking the Effect of Trivalent Metal Doping in All-Inorganic $CsPbBr_3$ Perovskite. *ACS Energy Letters* **2019,** *4* (3), 789-795.
121. Vij, D., *Luminescence of solids*. Springer Science & Business Media, New York, NY: **2012**.
122. Song, K.; Williams, R. T., Self-trapped excitons, Springer, New York, NY: **2013**.
123. Williams, R.; Song, K., The self-trapped exciton. *Journal of Physics and Chemistry of Solids* **1990,** *51* (7), 679-716.
124. Tan, J.; Li, D.; Zhu, J.; Han, N.; Gong, Y.; Zhang, Y., Self-trapped excitons in soft semiconductors. *Nanoscale* **2022,** *14* (44), 16394-16414.
125. Li, S.; Luo, J.; Liu, J.; Tang, J., Self-Trapped Excitons in All-Inorganic Halide Perovskites: Fundamentals, Status, and Potential Applications. *The Journal of Physical Chemistry Letters* **2019,** *10* (8), 1999-2007.
126. Li, J.; Wang, H.; Li, D., Self-trapped excitons in two-dimensional perovskites. *Frontiers of Optoelectronics* **2020,** *13* (3), 225-234.

127. Tao, W.; Zhang, C.; Zhou, Q.; Zhao, Y.; Zhu, H., Momentarily trapped exciton polaron in two-dimensional lead halide perovskites. *Nature Communications* **2021,** *12* (1), 1400.
128. Hui, Y.; Chen, S.; Lin, R.; Zheng, W.; Huang, F., Photophysics in Cs 3 Cu 2 I 5 and CsCu 2 I 3. *Materials Chemistry Frontiers* **2021,** *5* (19), 7088-7107.
129. Peng, C.; Chen, J.; Wang, H.; Hu, P., First-Principles Insight into the Degradation Mechanism of $CH_3NH_3PbI_3$ Perovskite: Light-Induced Defect Formation and Water Dissociation. *The Journal of Physical Chemistry C* **2018,** *122* (48), 27340-27349.
130. Wei, W.; Hu, Y. H., Catalytic role of H2O in degradation of inorganic–organic perovskite ($CH_3NH_3PbI_3$) in air. *International Journal of Energy Research* **2017,** *41* (7), 1063-1069.
131. Christians, J. A.; Miranda Herrera, P. A.; Kamat, P. V., Transformation of the Excited State and Photovoltaic Efficiency of $CH_3NH_3PbI_3$ Perovskite upon Controlled Exposure to Humidified Air. *Journal of the American Chemical Society* **2015,** *137* (4), 1530-1538.
132. Yang, J.; Siempelkamp, B. D.; Liu, D.; Kelly, T. L., Investigation of $CH_3NH_3PbI_3$ Degradation Rates and Mechanisms in Controlled Humidity Environments Using in Situ Techniques. *ACS Nano* **2015,** *9* (2), 1955-1963.
133. Lou, S.; Xuan, T.; Wang, J., (INVITED) Stability: A desiderated problem for the lead halide perovskites. *Optical Materials: X* **2019,** *1*, 100023.
134. Kim, Y.; Yassitepe, E.; Voznyy, O.; Comin, R.; Walters, G.; Gong, X.; Kanjanaboos, P.; Nogueira, A. F.; Sargent, E. H., Efficient Luminescence from Perovskite Quantum Dot Solids. *ACS Applied Materials & Interfaces* **2015,** *7* (45), 25007-25013.
135. Hamill, J. C., Jr.; Schwartz, J.; Loo, Y.-L., Influence of Solvent Coordination on Hybrid Organic–Inorganic Perovskite Formation. *ACS Energy Letters* **2018,** *3* (1), 92-97.

136. Liu, J.; Song, K.; Shin, Y.; Liu, X.; Chen, J.; Yao, K. X.; Pan, J.; Yang, C.; Yin, J.; Xu, L.-J., Light-induced self-assembly of cubic $CsPbBr_3$ perovskite nanocrystals into nanowires. *Chemistry of Materials* **2019,** *31* (17), 6642-6649.
137. Roy, M.; Vikram; Bhawna; Alam, A.; Aslam, M., Photoinduced quasi-2D to 3D phase transformation in hybrid halide perovskite nanoplatelets. *Physical Chemistry Chemical Physics* **2021,** *23* (48), 27355-27364.
138. Wu, R.; Gong, S.; Wu, L.; Yu, H.; Han, Q.; Wu, W., Laser-induced crystal growth observed in $CsPbBr_3$ perovskite nanoplatelets. *Physical Chemistry Chemical Physics* **2022,** *24* (14), 8303-8310.
139. Ruan, S.; Surmiak, M.-A.; Ruan, Y.; McMeekin, D. P.; Ebendorff-Heidepriem, H.; Cheng, Y.-B.; Lu, J.; McNeill, C. R., Light induced degradation in mixed-halide perovskites. *Journal of Materials Chemistry C* **2019,** *7* (30), 9326-9334.
140. Liu, L.; Deng, L.; Huang, S.; Zhang, P.; Linnros, J.; Zhong, H.; Sychugov, I., Photodegradation of organometal hybrid perovskite nanocrystals: Clarifying the role of oxygen by single-dot photoluminescence. *The journal of physical chemistry letters* **2019,** *10* (4), 864-869.
141. Kulbak, M.; Gupta, S.; Kedem, N.; Levine, I.; Bendikov, T.; Hodes, G.; Cahen, D., Cesium enhances long-term stability of lead bromide perovskite-based solar cells. *The journal of physical chemistry letters* **2016,** *7* (1), 167-172.
142. Dualeh, A.; Gao, P.; Seok, S. I.; Nazeeruddin, M. K.; Grätzel, M., Thermal behavior of methylammonium lead-trihalide perovskite photovoltaic light harvesters. *Chemistry of Materials* **2014,** *26* (21), 6160-6164.
143. Diroll, B. T.; Nedelcu, G.; Kovalenko, M. V.; Schaller, R. D., High-temperature photoluminescence of $CsPbX_3$ (X= Cl, Br, I) nanocrystals. *Advanced Functional Materials* **2017,** *27* (21), 1606750.

144. Sun, P.-P.; Li, Q.-S.; Yang, L.-N.; Li, Z.-S., Theoretical insights into a potential lead-free hybrid perovskite: substituting Pb^{2+} with Ge^{2+}. *Nanoscale* **2016,** *8* (3), 1503-1512.

145. Even, J.; Pedesseau, L.; Jancu, J.-M.; Katan, C., Importance of Spin–Orbit Coupling in Hybrid Organic/Inorganic Perovskites for Photovoltaic Applications. *The Journal of Physical Chemistry Letters* **2013,** *4* (17), 2999-3005.

146. Umebayashi, T.; Asai, K.; Kondo, T.; Nakao, A., Electronic structures of lead iodide based low-dimensional crystals. *Physical Review B* **2003,** *67* (15), 155405.

147. Yin, W.-J.; Yang, J.-H.; Kang, J.; Yan, Y.; Wei, S.-H., Halide perovskite materials for solar cells: a theoretical review. *Journal of Materials Chemistry A* **2015,** *3* (17), 8926-8942.

148. Slavney, A. H.; Hu, T.; Lindenberg, A. M.; Karunadasa, H. I., A Bismuth-Halide Double Perovskite with Long Carrier Recombination Lifetime for Photovoltaic Applications. *Journal of the American Chemical Society* **2016,** *138* (7), 2138-2141.

149. Reiss, P.; Carrière, M.; Lincheneau, C.; Vaure, L.; Tamang, S., Synthesis of Semiconductor Nanocrystals, Focusing on Nontoxic and Earth-Abundant Materials. *Chemical Reviews* **2016,** *116* (18), 10731-10819.

150. Fu, Z.; Xi, S., The effects of heavy metals on human metabolism. *Toxicology Mechanisms and Methods* **2020,** *30* (3), 167-176.

151. Needleman, H., Lead Poisoning. *Annual Review of Medicine* **2004,** *55* (1), 209-222.

152. Oh, J.-M.; Venters, C. C.; Di, C.; Pinto, A. M.; Wan, L.; Younis, I.; Cai, Z.; Arai, C.; So, B. R.; Duan, J.; Dreyfuss, G., U1 snRNP regulates cancer cell migration and invasion in vitro. *Nature Communications* **2020,** *11* (1), 1.

153. Jiang, Y.; Qiu, L.; Juarez-Perez, E. J.; Ono, L. K.; Hu, Z.; Liu, Z.; Wu, Z.; Meng, L.; Wang, Q.; Qi, Y., Reduction of lead leakage from damaged lead

halide perovskite solar modules using self-healing polymer-based encapsulation. *Nature Energy* **2019,** *4* (7), 585-593.

154. Zhou, Q.; Bai, Z.; Lu, W.-g.; Wang, Y.; Zou, B.; Zhong, H., In Situ Fabrication of Halide Perovskite Nanocrystal-Embedded Polymer Composite Films with Enhanced Photoluminescence for Display Backlights. *Advanced Materials* **2016,** *28* (41), 9163-9168.
155. Dirin, D. N.; Protesescu, L.; Trummer, D.; Kochetygov, I. V.; Yakunin, S.; Krumeich, F.; Stadie, N. P.; Kovalenko, M. V., Harnessing Defect-Tolerance at the Nanoscale: Highly Luminescent Lead Halide Perovskite Nanocrystals in Mesoporous Silica Matrixes. *Nano Letters* **2016,** *16* (9), 5866-5874.
156. Zhang, H.; Wang, X.; Liao, Q.; Xu, Z.; Li, H.; Zheng, L.; Fu, H., Embedding Perovskite Nanocrystals into a Polymer Matrix for Tunable Luminescence Probes in Cell Imaging. *Advanced Functional Materials* **2017,** *27* (7), 1604382.
157. Yoon, H. C.; Lee, H.; Kang, H.; Oh, J. H.; Do, Y. R., Highly efficient wide-color-gamut QD-emissive LCDs using red and green perovskite core/shell QDs. *Journal of Materials Chemistry C* **2018,** *6* (47), 13023-13033.
158. Wang, H.-C.; Lin, S.-Y.; Tang, A.-C.; Singh, B. P.; Tong, H.-C.; Chen, C.-Y.; Lee, Y.-C.; Tsai, T.-L.; Liu, R.-S., Mesoporous Silica Particles Integrated with All-Inorganic $CsPbBr_3$ Perovskite Quantum-Dot Nanocomposites (MP-PQDs) with High Stability and Wide Color Gamut Used for Backlight Display. *Angewandte Chemie International Edition* **2016,** *55* (28), 7924-7929.
159. Sun, C.; Zhang, Y.; Ruan, C.; Yin, C.; Wang, X.; Wang, Y.; Yu, W. W., Efficient and Stable White LEDs with Silica-Coated Inorganic Perovskite Quantum Dots. *Advanced Materials* **2016,** *28* (45), 10088-10094.
160. Li, Z.; Kong, L.; Huang, S.; Li, L., Highly Luminescent and Ultrastable $CsPbBr_3$ Perovskite Quantum Dots Incorporated into a Silica/Alumina Monolith. *Angewandte Chemie International Edition* **2017,** *56* (28), 8134-8138.

161. Chen, Y.; Liu, Y.; Hong, M., Cation-doping matters in caesium lead halide perovskite nanocrystals: from physicochemical fundamentals to optoelectronic applications. *Nanoscale* **2020,** *12* (23), 12228-12248.
162. Wang, H. C.; Wang, W.; Tang, A. C.; Tsai, H. Y.; Bao, Z.; Ihara, T.; Yarita, N.; Tahara, H.; Kanemitsu, Y.; Chen, S., High-performance $CsPb_{1-x}Sn_xBr_3$ perovskite quantum dots for light-emitting diodes. *Angewandte Chemie* **2017,** *129* (44), 13838-13842.
163. Liu, F.; Ding, C.; Zhang, Y.; Ripolles, T. S.; Kamisaka, T.; Toyoda, T.; Hayase, S.; Minemoto, T.; Yoshino, K.; Dai, S., Colloidal synthesis of air-stable alloyed $CsSn_{1-x}Pb_xI_3$ perovskite nanocrystals for use in solar cells. *Journal of the American Chemical Society* **2017,** *139* (46), 16708-16719.
164. Zhang, X.; Cao, W.; Wang, W.; Xu, B.; Liu, S.; Dai, H.; Chen, S.; Wang, K.; Sun, X. W., Efficient light-emitting diodes based on green perovskite nanocrystals with mixed-metal cations. *Nano Energy* **2016,** *30*, 511-516.
165. Zhang, X.; Wang, H.; Hu, Y.; Pei, Y.; Wang, S.; Shi, Z.; Colvin, V. L.; Wang, S.; Zhang, Y.; Yu, W. W., Strong blue emission from Sb3+-doped super small $CsPbBr_3$ nanocrystals. *The journal of physical chemistry letters* **2019,** *10* (8), 1750-1756.
166. Bera, S.; Ghosh, D.; Dutta, A.; Bhattacharyya, S.; Chakraborty, S.; Pradhan, N., Limiting heterovalent B-site doping in $CsPbI_3$ nanocrystals: Phase and optical stability. *ACS Energy Letters* **2019,** *4* (6), 1364-1369.
167. Yao, J.-S.; Ge, J.; Han, B.-N.; Wang, K.-H.; Yao, H.-B.; Yu, H.-L.; Li, J.-H.; Zhu, B.-S.; Song, J.-Z.; Chen, C., Ce3+-doping to modulate photoluminescence kinetics for efficient $CsPbBr_3$ nanocrystals based light-emitting diodes. *Journal of the American Chemical Society* **2018,** *140* (10), 3626-3634.
168. Shao, H.; Bai, X.; Cui, H.; Pan, G.; Jing, P.; Qu, S.; Zhu, J.; Zhai, Y.; Dong, B.; Song, H., White light emission in Bi 3+/Mn 2+ ion co-doped $CsPbCl_3$ perovskite nanocrystals. *Nanoscale* **2018,** *10* (3), 1023-1029.

169. Sa, R.; Zha, W.; Ma, Z.; Yuan, R.; Liu, D., Stable lead-free perovskite solar cells: A first-principles investigation. *Spectrochimica Acta Part A: Molecular and Biomolecular Spectroscopy* **2020,** *239*, 118493.
170. Shi, Z.; Guo, J.; Chen, Y.; Li, Q.; Pan, Y.; Zhang, H.; Xia, Y.; Huang, W., Lead-free organic–inorganic hybrid perovskites for photovoltaic applications: recent advances and perspectives. *Advanced Materials* **2017,** *29* (16), 1605005.
171. Gahlot, K.; de Graaf, S.; Duim, H.; Nedelcu, G.; Koushki, R. M.; Ahmadi, M.; Gavhane, D.; Lasorsa, A.; De Luca, O.; Rudolf, P., Structural Dynamics and Tunability for Colloidal Tin Halide Perovskite Nanostructures. *Advanced Materials* **2022**, 2201353.
172. Roknuzzaman, M.; Zhang, C.; Ostrikov, K. K.; Du, A.; Wang, H.; Wang, L.; Tesfamichael, T., Electronic and optical properties of lead-free hybrid double perovskites for photovoltaic and optoelectronic applications. *Scientific reports* **2019,** *9* (1), 1-7.
173. Hu, H.; Dong, B.; Zhang, W., Low-toxic metal halide perovskites: opportunities and future challenges. *Journal of materials chemistry A* **2017,** *5* (23), 11436-11449.
174. Sani, F.; Shafie, S.; Lim, H. N.; Musa, A. O., Advancement on lead-free organic-inorganic halide perovskite solar cells: a review. *Materials* **2018,** *11* (6), 1008.
175. Mahajan, P.; Datt, R.; Tsoi, W. C.; Gupta, V.; Tomar, A.; Arya, S., Recent progress, fabrication challenges and stability issues of lead-free tin-based perovskite thin films in the field of photovoltaics. *Coordination Chemistry Reviews* **2021,** *429*, 213633.
176. Yang, X.; Chen, Y.; Liu, P.; Xiang, H.; Wang, W.; Ran, R.; Zhou, W.; Shao, Z., Simultaneous power conversion efficiency and stability enhancement of Cs2AgBiBr6 lead-free inorganic perovskite solar cell through adopting a multifunctional dye interlayer. *Advanced Functional Materials* **2020,** *30* (23), 2001557.

177. Chatterjee, S.; Pal, A. J., Influence of metal substitution on hybrid halide perovskites: towards lead-free perovskite solar cells. *Journal of Materials Chemistry A* **2018,** *6* (9), 3793-3823.
178. Shen, Y.; Yin, J.; Cai, B.; Wang, Z.; Dong, Y.; Xu, X.; Zeng, H., Lead-free, stable, high-efficiency (52%) blue luminescent FA 3 Bi 2 Br 9 perovskite quantum dots. *Nanoscale Horizons* **2020,** *5* (3), 580-585.
179. Lou, Y.; Fang, M.; Chen, J.; Zhao, Y., Formation of highly luminescent cesium bismuth halide perovskite quantum dots tuned by anion exchange. *Chemical Communications* **2018,** *54* (30), 3779-3782.
180. Kwon, S. B.; Choi, S. H.; Yoo, J. H.; Kim, B. Y.; Kang, B. K.; Song, Y. H.; Yoon, D. H., Organic solvent-free lyophilization assisted recrystallization synthesis of high-purity green emissive Cs3MnX5 (X= I, Br). *Journal of Alloys and Compounds* **2020,** *845*, 156324.
181. Almutlaq, J.; Mir, W. J.; Gutiérrez-Arzaluz, L.; Yin, J.; Vasylevskyi, S.; Maity, P.; Liu, J.; Naphade, R.; Mohammed, O. F.; Bakr, O. M., CsMnBr3: Lead-Free Nanocrystals with High Photoluminescence Quantum Yield and Picosecond Radiative Lifetime. *ACS Materials Letters* **2021,** *3* (3), 290-297.
182. Bahmani Jalali, H.; Pianetti, A.; Zito, J.; Imran, M.; Campolucci, M.; Ivanov, Y. P.; Locardi, F.; Infante, I.; Divitini, G.; Brovelli, S.; Manna, L.; Di Stasio, F., Cesium Manganese Bromide Nanocrystal Sensitizers for Broadband Vis-to-NIR Downshifting. *ACS Energy Letters* **2022,** *7* (5), 1850-1858.
183. Lian, L.; Zheng, M.; Zhang, P.; Zheng, Z.; Du, K.; Lei, W.; Gao, J.; Niu, G.; Zhang, D.; Zhai, T.; Jin, S.; Tang, J.; Zhang, X.; Zhang, J., Photophysics in $Cs_3Cu_2X_5$ (X = Cl, Br, or I): Highly Luminescent Self-Trapped Excitons from Local Structure Symmetrization. *Chemistry of Materials* **2020,** *32* (8), 3462-3468.
184. Jun, T.; Sim, K.; Iimura, S.; Sasase, M.; Kamioka, H.; Kim, J.; Hosono, H., Lead-free highly efficient blue-emitting $Cs_3Cu_2I_5$ with 0D electronic structure. *Advanced Materials* **2018,** *30* (43), 1804547.

185. Zhang, Z.-X.; Li, C.; Lu, Y.; Tong, X.-W.; Liang, F.-X.; Zhao, X.-Y.; Wu, D.; Xie, C.; Luo, L.-B., Sensitive deep ultraviolet photodetector and image sensor composed of inorganic lead-free $Cs_3Cu_2I_5$ perovskite with wide bandgap. *The Journal of Physical Chemistry Letters* **2019,** *10* (18), 5343-5350.
186. Li, Y.; Shi, Z.; Liang, W.; Wang, L.; Li, S.; Zhang, F.; Ma, Z.; Wang, Y.; Tian, Y.; Wu, D., Highly stable and spectrum-selective ultraviolet photodetectors based on lead-free copper-based perovskites. *Materials Horizons* **2020,** *7* (2), 530-540.
187. Song, Y.; Liu, W.; Qin, Y.; Han, X.; Li, W.; Li, X.; Long, H.; Li, D.; Wang, K.; Wang, B. J. A. O. M., Photoinduced trap passivation for enhanced photoluminescence in 2D organic–inorganic hybrid perovskites. **2020,** *8* (7), 1901695.
188. Liu, X.; Yu, Y.; Yuan, F.; Zhao, C.; Dong, H.; Jiao, B.; Wu, Z., Vacuum dual-source thermal-deposited lead-free $Cs_3Cu_2I_5$ films with high photoluminescence quantum yield for deep-blue light-emitting diodes. *ACS Applied Materials & Interfaces* **2020,** *12* (47), 52967-52975.
189. Zhou, Y.; Wang, X.; He, T.; Yang, H.; Yang, C.; Shao, B.; Gutiérrez-Arzaluz, L.; Bakr, O. M.; Zhang, Y.; Mohammed, O. F., Large-Area Perovskite-Related Copper Halide Film for High-Resolution Flexible X-ray Imaging Scintillation Screens. *ACS Energy Letters* **2022,** *7* (2), 844-846.
190. Zhou, Y.; Chen, J.; Bakr, O. M.; Mohammed, O. F., Metal Halide Perovskites for X-ray Imaging Scintillators and Detectors. *ACS Energy Letters* **2021,** *6* (2), 739-768.
191. Wang, F.; Zhou, X.; Liang, X.; Duan, D.; Ge, C.-Y.; Lin, H.; Zhu, Q.; Li, L.; Hu, H., Solvent Engineering of Ionic Liquids for Stable and Efficient Perovskite Solar Cells. *Advanced Energy and Sustainability Research n/a* (n/a), 2200140.

192. Hoang, M. T.; Ünlü, F.; Martens, W.; Bell, J.; Mathur, S.; Wang, H., Towards the environmentally friendly solution processing of metal halide perovskite technology. *Green Chemistry* **2021,** *23* (15), 5302-5336.
193. Moore, D. T.; Tan, K. W.; Sai, H.; Barteau, K. P.; Wiesner, U.; Estroff, L. A., Direct Crystallization Route to Methylammonium Lead Iodide Perovskite from an Ionic Liquid. *Chemistry of Materials* **2015,** *27* (9), 3197-3199.
194. Bu, T.; Li, J.; Li, H.; Tian, C.; Su, J.; Tong, G.; Ono, L. K.; Wang, C.; Lin, Z.; Chai, N., Lead halide–templated crystallization of methylamine-free perovskite for efficient photovoltaic modules. *Science* **2021,** *372* (6548), 1327-1332.
195. Wang, Z.; Luo, M.; Liu, Y.; Li, M.; Pi, M.; Yang, J.; Chen, Y.; Zhang, Z.; Du, J.; Zhang, D., Air-Processed MAPbBr3 Perovskite Thin Film with Ultrastability and Enhanced Amplified Spontaneous Emission. *Small* **2021,** *17* (25), 2101107.
196. Li, D.; Chao, L.; Chen, C.; Ran, X.; Wang, Y.; Niu, T.; Lv, S.; Wu, H.; Xia, Y.; Ran, C., In situ interface engineering for highly efficient electron-transport-layer-free perovskite solar cells. *Nano Letters* **2020,** *20* (8), 5799-5806.
197. Hui, W.; Chao, L.; Lu, H.; Xia, F.; Wei, Q.; Su, Z.; Niu, T.; Tao, L.; Du, B.; Li, D., Stabilizing black-phase formamidinium perovskite formation at room temperature and high humidity. *Science* **2021,** *371* (6536), 1359-1364.
198. Niu, T.; Chao, L.; Gao, W.; Ran, C.; Song, L.; Chen, Y.; Fu, L.; Huang, W., Ionic Liquids-Enabled Efficient and Stable Perovskite Photovoltaics: Progress and Challenges. *ACS Energy Letters* **2021,** *6* (4), 1453-1479.
199. Hoang, M. T.; Pham, N. D.; Yang, Y.; Tiong, V. T.; Zhang, C.; Gui, K.; Chen, H.; Chang, J.; Wang, J.; Golberg, D., A facile, environmentally friendly synthesis of strong photo-emissive methylammonium lead bromide perovskite nanocrystals enabled by ionic liquids. *Green Chemistry* **2020,** *22* (11), 3433-3440.

This page is intentionally left blank

Chapter-2

Experimental Methods and Synthetic Procedures

This chapter covers the details of the experimental methods used in this thesis. I have explicitly written the detailed instrumentation and data analysis procedure for time-correlated single photon counting, femtosecond transient absorption spectroscopy and fluorescence correlation spectroscopy, and transmission electron microscopy used in my research work. A brief description of powder X-ray diffraction and X-ray photoelectron spectroscopic techniques were also discussed. All the syntheses related to this thesis are also described in detail.

2.1. Steady State Measurements

Shimadzu UV-2450 and JASCO V-670 spectrophotometers were used to record steady-state absorption spectra. Both instruments have halogen and deuterium lamps for light sources, and photomultiplier tubes for detectors. Steady-state emission spectra were recorded in Fluoromax-4, Horiba Jobin-Yvon spectrofluorimeter equipped with a 150W xenon arc lamp as the excitation source and a photomultiplier tube (190nm-850nm) as the detector.

2.2. Time-Correlated Single Photon Counting (TCSPC) Method

2.2.1. Basic principle

The fundamental principle of fluorescence lifetime measurement is to excite the sample with a delta function pulse and track the steady decline in fluorescence intensity over time. There are a few issues with the measurements, though. Most organic samples have very short fluorescence decay times, falling into the nanosecond time range. We therefore require a detector with a very quick response, which is challenging, in order to directly evaluate fluorescence lifespan. Second, in order to resolve any multi-exponential decays present in the sample, we must quantify the sample's fluorescence lifetime as well as the whole shape of the decay, or the well-known exponential waveform. Currently, the detector's response is the measurement of a single photon. Therefore, a picosecond order response from the detector would be required to resolve a nanosecond order lifetime component. This is impossible to accomplish, as the sample's faint emission after passing through all the optics might not be able to generate an electric signal even with an extremely fast photodiode and GHz oscilloscope. Therefore, it is impossible for an analogue measurement to capture the entire waveform of a sample's fluorescence decay. The time of the photon's arrival at the detector is determined in relation to the reference signal, which is the excitation pulse, using the time-correlated single photon counting method (TCSPC), which was initially introduced by Bollinger and Thomas

in 1961.[1, 2] A histogram of the waveform emerges after multiple cycles of this method being repeated. TCSPC's statistical methodology enables it to detect signals at very low levels. A high repetition rate laser source is utilised in TCSPC measurements, and the idea is that finding a single photon inside the pulse time is improbable, and finding two photons is quite improbable. So only the first photon detected within two consecutive excitation of the sample is considered. The first detected photon serves as the stop signal, while the excitation pulse serves as the start signal. A measurement and storage are made of the interval between the start and stop signals. If the single photon detection criterion is applied, then there may be several cycles where no photon is detected. This is acceptable because the occurrence of no photon per cycle or a single photon per cycle is completely arbitrary, and measurement over a large number of repeating cycles would statistically always produce the distribution. Every time a photon is detected in a cycle, a count 1 is made in the memory, along with the timing of the photon's arrival. The time to amplitude converter (TAC) is a crucial component of this sort of data collection. The TAC receives a synchronisation signal from the excitation pulse (also known as the "start" signal), and the capacitor inside it begins to charge. The charging of the capacitor halts when the emission photon or "stop" signal is acquired. During this window of time, the voltage inside the capacitor rises linearly, creating a voltage ramp. The magnitude of this voltage is stored in a specific channel according to time by a device known as a multichannel analyzer (MCA), an analog to digital converter. The entire histogram is recorded in the MCA across a number of iterations. The experimental stop rate should be kept at less than 2% of the start rate in order to maintain the one photon detection per cycle principle. When the "dead time" of the electronics is taken into account, this ratio is crucial. The electronics' minimum detection time between two consecutive photons is known as the "dead time." The first photon released may not be the first detected photon since it may fall within the dead period of electronics if the "stop" rate is high. As a result, many photons may arrive in a pulse cycle. As a result, there will be what is known

as a "pulse pile-up," which is essentially an over-representation of some spots in the histogram.[2, 3]

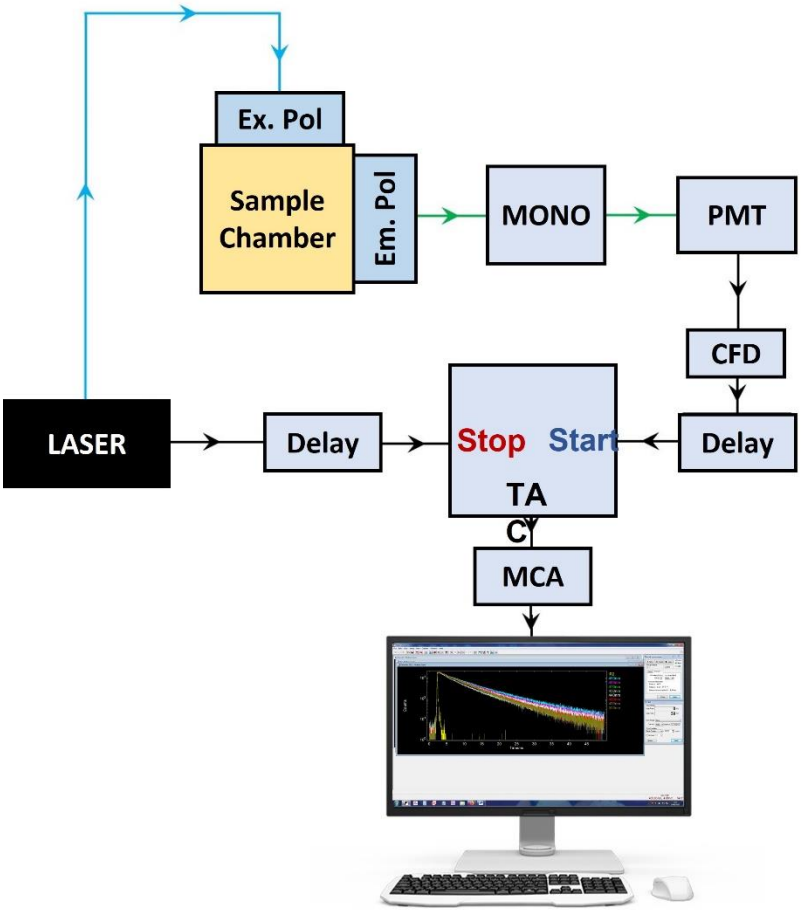

Figure 2.1. Schematic diagram of a standard TCSPC setup along with typical IRF and data

Multichannel plate photomultiplier tubes (MCP PMT) are the detector utilised in contemporary TCSPC configuration. The benefit of employing MCP PMT over simple PMT or single electron response detectors is due to the detector's transit time spread (TTS), which has a significant impact on the instrument's time resolution. A photoelectron is amplified in the dynodes after it is produced at the cathode of a PMT. A distribution of transit times, or TTS, is produced because this process of multiplication creates a group of electrons with a variety of velocities and the ability to travel in their own unique ways to the anode. TTS is less for MCP PMT compared to PMT and as TTS determines the instrument response, the use of MCP PMT is preferred. The rise and fall time of the electronics used in the TCSPC setup causes a

time jitter in the measurement. Moreover, random amplification optical signal by detector can cause a amplitude jitter in the electric signal. If a simple discriminator is used to send signal at TAC, then it can be triggered if the leading edge of the electric pulse crosses a certain threshold value. As a result, TCSPC employs a constant fraction discriminator (CFD). Basically, a CFD avoids the height difference-induced temporal jitters by sending a signal at TAC at a consistent fraction of a pulse. By monitoring the signal from a scattering process, a TCSPC instrument records its instrument response function (IRF), which is affected by the laser pulse width, TTS, and any other time fluctuations in the instrument. A schematic diagram depicting all the components of a TCSPC setup has been shown in figure 2.1.

I've utilised the TCSPC LifeSpec II instrument from Edinburgh Instruments in the UK for my experiments. This instrument has a Hamamatsu R3809-50 MCP PMT with an intrinsic detector response of <25 ps that is thermoelectrically cooled. Picosecond pulse diode lasers (EPL-series) from the same manufacturer serve as the excitation sources. I've utilised a 375 nm, and 405 nm diode laser with an 80 ps pulse width for my studies. This instrument's IRF was 120 ps when scattering from a Ludox suspension was measured. All data were taken at the Magic Angle polarisation to remove any influence from molecular rotational diffusion. The results from the instrument were evaluated using FAST software. Here is a brief explanation of the fitting procedure.

2.2.2. Data analysis procedure

The data processing process is not simple because the instrument's IRF has a finite width and the excitation pulse is not a delta function, having a finite width in time. These variables have an impact on the data, and the observed fluorescence decay actually merges the IRF and the real decline of fluorescence intensity.

$$I(t) = \int_0^t P(t)F(t - t')dt' \qquad (2.1)$$

Now, since the problem is poorly phrased, using this convolution to match the data is not simple. The precise IRF or prompt form, the fluorescence theoretical model, and the minimization of experimental random noise are all necessary for convolutions. As a result, to extract fluorescence lifetime, the majority of commercial software, including FAST, uses an iterative method, specifically the non-linear least square method. First, the weighted amplitudes of the lifetime components are added together to estimate the pure fluorescence intensity decay.[3-6]

$$F(t) = \sum_{i=1}^{n} a_i e^{-\frac{t}{\tau_i}} \quad (2.2)$$

$$\sum_{i=1}^{n} a_i = 1 \quad (2.3)$$

Here, τ_i are the lifetime components and a_i are the amplitudes. As previously mentioned, the IRF profile is recorded using a scatter, however it is measured at the excitation wavelength rather than the emission wavelength, which is inherently incorrect. However, the reconvolution requires IRF measurement using the same number of channels. Since this reconvolution is performed on a per-channel basis in a quantized way, a sum is employed in equation 2.1 in place of integration. The IRF is taken to be a collection of δ-functions in several channels, each with a different amplitude. The measurement results are presented as[3-6]

$$I(t) = \sum_{t_i=0}^{t} P(t)F(t - t_i)\Delta t \quad (2.4)$$

Δt is the time/channel in the equation above. The final fitting equation requires the addition of two more parameters. When there is a little discrepancy between the time zero location of the IRF and the intensity decay data, a shift parameter is used to account for it.(Δ). For fitting, we need a noise factor (A). Consequently, the whole form is

$$D(t) = A + I(t + \Delta) \quad (2.5)$$

The consistency of the assumed model is tested by the "goodness of the fit".[3-6]

$$\chi^2 = \sum_{j=1}^{n} \frac{[Y(j)-D(j)]^2}{\sigma_j^2} \quad (2.6)$$

In the above equation, $Y(j)$ is the fitted data,$D(j)$ is the experimental data and σ_j^2 is the standerd deviation. However, χ^2 is not the best choice for large number of datapoints. Instead, a quantity ${\chi^2}_R$ is defined as

$$\chi_R^2 = \frac{\chi^2}{n-p} \quad (2.7)$$

Here, n is the number of data points and p is the number of parameters. For TCSPC measurements, n is much larger than p. The value of χ^2 is estimated with different choice of fitting parameters and multiexponential model and the fitting is accepted comparing the value of χ^2 for different sets. However, as many distinct models might satisfy the fitting criteria, this iterative method suffers from an inherent difficulty of model selection based on intuition, making prior system knowledge crucial for TCSPC fitting.

2.2.3. Time resolved emission spectra (TRES)

The TCSPC records the fluorescence intensity degradation over time at a certain wavelength, which gives information about the excited state processes. However, analysing the time-resolved emission spectra of the photoexcited molecule is another effective method for observing the molecule's fate (TRES). Basically, a molecule's steady state emission spectrum is the time average of all its TRES, and studying TRES can reveal a wealth of knowledge about events that take place in the excited state, such as charge transfer and excited state reactions.[7-12] Additionally, it can shed light on how molecules in the excited state interact with the solvents around them.[7] TRES recordings from various times in the past have been made, but the instrument response distorts them.[17-21] In addition, simultaneous detection of numerous wavelengths is necessary for TRES recording. Fortunately, time resolved fluorescence decays captured at diverse wavelengths throughout the complete range

of emission spectra can be used to prepare TRES.[7-12] TRES can be mathematically represented as,

$$I(\lambda,t) = \frac{I_{ss}(\lambda)}{\sum_i a_i\tau_i}\sum_{i=0}^{n} a_i e^{-t/\tau_i} \quad (2.8)$$

Equation 2.8 states that we can observe the fluorescence intensity decay at a specific wavelength and generate the time-dependent intensity behaviour from the steady-state intensity. This method was used to acquire several points at various wavelengths, and each of the TRES was then fitted using a Maroncelli and Fleming-described lognormal function.[18,19]

$$L(\nu) = g_0 exp\left\{-\ln 2\left(\frac{\ln\left(1+\frac{2b(\nu-\nu_p)}{\Delta}\right)}{b}\right)^2\right\} \quad (2.9)$$

In the above equation, g_0, b, ν_p, Δ are peak height, asymmetry parameter, peak frequency, width parameter. The width parameter is related to full width half maxima (Γ) as follows[9, 10]

$$\Gamma = \Delta\left(\frac{\sinh(b)}{b}\right) \quad (2.10)$$

A lognormal function established by Maroncelli and Fleming was used to fit each of the TRES obtained using this approach to different wavelengths.

2.3. Femtosecond broadband transient absorption spectroscopy

2.3.1. Basic principle

Several methods are used to study femtosecond molecular dynamics, including the widely used pump-probe method known as broadband transient absorption spectroscopy. In typical pump-probe investigations, an ultrashort laser pulse known as the pump is used to produce a non-stationary molecular state, and a second suitably time-delayed laser pulse known as the probe is used to track the state's temporal evolution.[13-16] We employ resonant excitation in transient absorption spectroscopy, which means that, unlike Raman spectra, the excited electronic state population is prepared by the pump pulse and the population decrease is not

immediate. [13-16] Choosing the right probe pulse will affect how the dynamics of the excited state are studied. The probe can be used to investigate various photophysical properties of the molecule. It can be monochromatic or broadband in the UV-Visible or IR range.[13-16] Observing the pump's action also rely on the events the probe itself causes after the pump acts, or on the change in the probe's characteristics (such intensity). [13-16] The first instance of transient absorption spectroscopy is what we see.

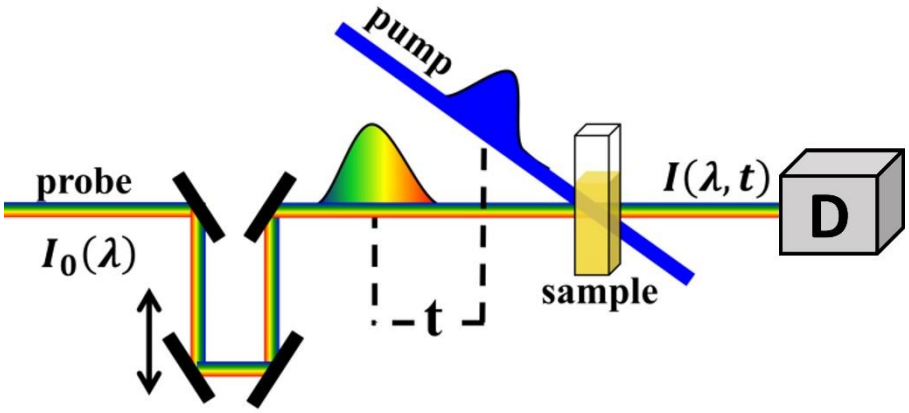

Figure 2.2. Schematic representation of transient absorption spectroscopy experiment

I employed 400 nm light as the pump light in our lab setting, which excite several molecules in the excited state (conduction band). While the pump is being dumped, a visible (450nm–750nm) white light continuum (WLC) probe is sent through the sample at various delay times managed by a mechanical delay stage, and the detector is watching the change in intensity of the probe light. Figure 2.2 illustrates the operation using a schematic diagram. To prevent the probe from exerting any multistep or multiphoton processes, the intensity of the probe is kept very low in comparison to the pump. Moment gated detection is effectively simultaneous detection across the entire range of the probe spectrum at a specific time, repeated over a number of time delays.[13-16] Since this is an absorption spectroscopy, the probe light can be subject to Lambert-Beer law.

$$I(\lambda, t) = I_0(\lambda) \times 10^{-\varepsilon(\lambda)N(t)l} \qquad (2.11)$$

Equation 2.11 states that the probe light's intensity before and after it passes the sample at a delay time t (($I_0(\lambda)$ and $I(\lambda,t)$), respectively, as seen in figure 2.2. It should be made clear that the time zero is marked at the precise point in the delay where the sample is simultaneously received by the pump and probe pulses. $\varepsilon(\lambda)$ is the molar extinction coefficient at wavelength λ, $N(t)$ is the population of a state after t time of the pump excitation and l is the path length of the sample. So according to figure 2.2 and equation 2.11, the absorbance $A(\lambda,t)$ is given by

$$A(\lambda,t) = log\frac{I_0(\lambda)}{I(\lambda,t)} = \varepsilon(\lambda)N(t)l \qquad (2.12)$$

The change in absorbance with and without the activity of the pump is the quantity that is measured in transient absorption technique and is mathematically stated as follows.

$$\Delta A(\lambda,t) = A(\lambda,t) - A(\lambda) \qquad (2.12)$$

$$\Delta A(\lambda,t) = log\frac{I_0(\lambda)}{I(\lambda,t)} - log\frac{I_0(\lambda)}{I(\lambda)} = log\frac{I(\lambda)}{I(\lambda,t)} \qquad (2.13)$$

Equation 2.13 suggests a scenario in which we will obtain the observable quantity by measuring probe intensity both with and without pump illumination of the sample. So, we can simply write

$$\Delta A(\lambda,t) = log\frac{I^{probe}}{I^{probe}_{pump}} \qquad (2.14)$$

It should be pointed out that in equation 2.14; the quantity I^{probe} is actually measured blocking the pump light completely with the use of a chopper. The population created or depleted by pump light will decay or grow with time i.e., as $N(t)$ changes with time, $\Delta A(\lambda,t)$ also changes with time and that provides us the photophysical dynamics of the system. Furthermore, as the observable $\Delta A(\lambda,t)$ does not contain any $I_0(\lambda)$ term, the intensity of probe before the sample need not to be measured which means a single beam spectrophotometer will work just fine.

However, a dual beam spectrophotometer is frequently used to remove the noise in the probe light. As an absorption spectroscopy, this particular pump probe approach can now track both radiative and non-radiative processes, depending on the spectrum of the probe.[13-16] A dual beam spectrophotometer is typically used to remove the noise in the probe light, though. Due to the fact that this particular pump probe approach uses absorption spectroscopy, it has the ability to track both radiative and non-radiative processes, depending on the probe's spectra.

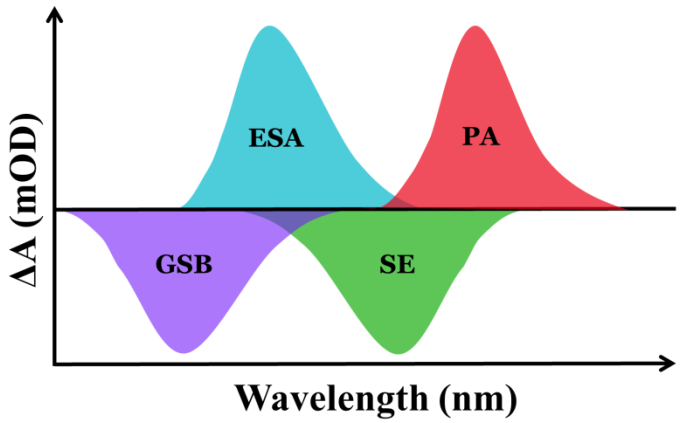

Figure 2.3. Contribution of different photophysical processes in transient absorption spectra.

Ground state bleaching: A part of molecules are aroused from their ground state by the pump pulse, and the population of molecules in their ground state declines. As a result, the ground state molecule now absorbs less probe light following pump excitation compared to before pump excitation, that is., $I^{probe} < I^{probe}_{pump}$. As a result, a negative ΔA spectrum is seen, which is smaller the longer the interval between the pump and the probe because molecules that have been stimulated to the ground state stop functioning. Ground state bleaching is the name given to this particular signal (GSB).

Stimulated Emission: Fluorescence occurs when an electronically stimulated molecule spontaneously emits light and then returns to its ground state. It is possible to stimulate the emission process from the excited to the ground state, or stimulated emission, if a resonant photon from external radiation travels through the excitation

volume. The stimulated photon's direction matches that of the photon from the stimulating radiation. Therefore, the probe can drive emission from the sample that has been excited by the pump if some or all of the frequencies included in the probe pulse resonate with the excited and ground states of the sample (including vibrational levels). Additionally, the probe's intensity at particular wavelengths will increase following the pump's activity because the emitted photons will travel with the probe and arrive at the detector. Therefore $I^{probe} < I^{probe}_{pump}$ will be satisfied and a negative spectrum will be observed in transient absorption. This signal is an example of stimulated emission (SE), and it resembles the molecule's spontaneous emission spectrum. Even if the SE signal is still Stokes-shifted in relation to the GSB signal, there can be a lot of early overlap. Under the supposition that the intensity of the probe light is so low that it has little effect on the population of the excited state, SE also deteriorates over time precisely as the excited state population declines as a result of various radiative and non-radiative molecular processes.

Excited State Absorption: Transient absorption signals' usefulness comes from their capacity to identify transitions that are invisible to fluorescence techniques. The observation of an excited state absorption (ESA) signal is one of them. A certain electronic excited state is produced in the sample by the pump beam. Now, some of the light wavelengths in the probe light may be in resonance with the energy difference between the populated excited state and other higher energy states, which causes the molecules in the excited state to absorb the light. This particular transition is not possible without the pump and therefore, in this case, $I^{probe} > I^{probe}_{pump}$ and we can observe a positive signal in the spectra.

Product Absorption: Another aspect of transient absorption spectroscopy that is challenging to measure using fluorescence methods is the product absorption (PA) signal. Once excited, the molecule can go through a variety of changes and excited state reactions, such as photoinduced electron and proton transfer, and the new transient species thereby created can absorb the probe light, leaving a positive

spectral signature known as, $I^{probe} > I^{probe}_{pump}$. in the transient absorption spectroscopy.

Transient absorption spectroscopy is an incredibly powerful technique for observing these four phenomena, but it is subject to a number of constraints, including the spectral spread of the probe and instrument response, which can limit the ability to observe one or more of the processes mentioned above.

2.3.2. Instrumental setup

I have used a commercially available femtosecond broadband transient absorption spectrometer (Femto-Frame-II, IB Photonics, Bulgaria) in our lab for my research. Figure 2.4 depicts the system's optical configuration. The 800 nm output of a Ti:Sapphire regenerative amplifier (SpitfirePro XP, Spectra-Physics, USA) pumped by a 20-W Q-switched Nd:YLF laser (Empower, Spectra-Physics, USA) and seeded by a Ti-Sapphire femtosecond oscillator (MaiTai SP, Spectra- Physics, USA) was used as the fundamental light for transient absorption experiments. Using a commercial autocorrelator, the repetition rate and pulse width of the output were measured to be 1 kHz and 80 fs, respectively. At beam splitter BS_1, this fundamental beam was divided into two pieces. The pump light was produced by one component, and the probe was created by the other. The same company's JANOS tripler, which produced the pump light, was used. The second harmonic 400 nm light was created by focusing the 800 nm light onto a BBO crystal. After passing through a waveplate and colliding with another BBO crystal to produce the third harmonic 266 nm light, the second harmonic and the remaining 800 nm light were produced. These three lights were separated using a set of dichroic mirrors and the 400 nm or the 266nm light was used for excitation light by using mirror M_6 or M_7. The other part of the fundamental beam after reflecting through mirror M_5 was passed through a retroreflector (RR) mounted on a mechanical delay stage using mirrors M_{B1}, M_{B2} & M_{B3}. This delay stage was used to generate maximum 2ns time delay between the

pump and the probe. A very small part of the 800 nm light was split in BS_2 and allowed to fall on a photodidode PD which controlled the chopper. The rest of the fundamental beam passed through a linear neutral density filter (ND_1), an iris and focused on a 0.3 mm sapphire crystal by lens L_4.

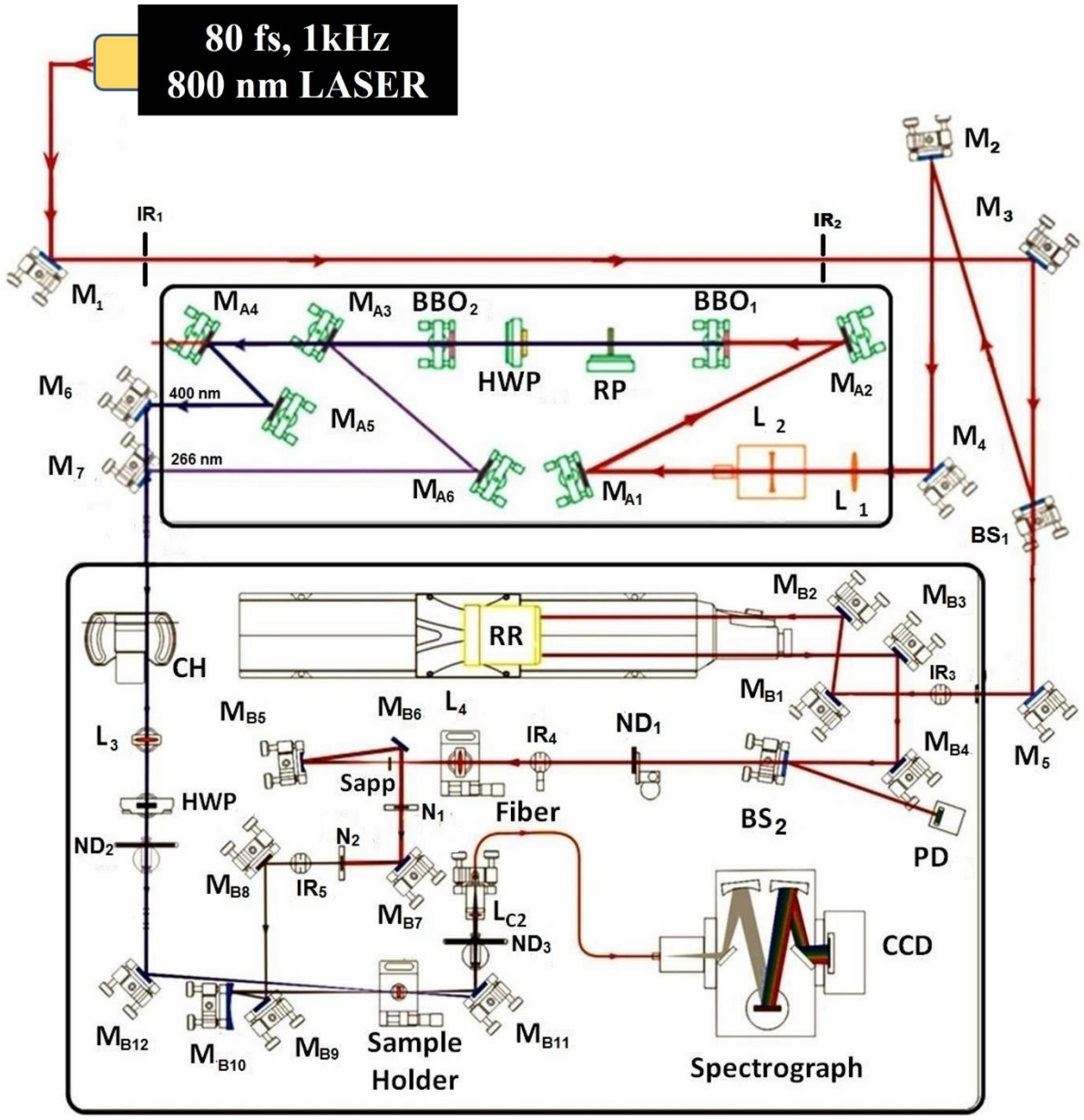

Figure 2.4. Optical layout of the femtosecond broadband transient absorption spectrometer

As a result, the sapphire crystal (Sapp) produced the white light continuum (WLC) probe, which has a wavelength range of 450 nm to 750 nm. However, the power and beam shape that the ND filter and the iris control greatly affect the character and shape of the probing light. The WLC then collected by a parabolic mirror M_{B5} and directed through the two Notch filters (N_1 and N_2) to cutoff residual fundamental radiation of 800nm using mirror M_{B6} and M_{B7}. The sample is then illuminated by the probe light utilising parabolic mirror MB_{10}. In the meantime, a half wave plate is used to modify the polarisation of the pump light relative to the probe while it is being steered through a chopper. A rotating ND filter (ND_2) controls the power of the pump and using lens L_3 and mirror M_{B12} the pump beam is focused into the same spot in the sample cuvette as the probe beam. A typical focal spot size is 100-200µm. As described in the preceding section, the purpose of the chopper is to temporarily turn off the pump light to enable measuring without a pump. The purpose of the chopper is to temporarily turn off the pump light to enable measuring without a pump, as described in the section above. The probe beam after passing through the sample is focused on the 200µm optical fiber cable by means of mirror M_{B11}. Another ND filter (ND_3) controls the amount of probe light that reaches the detector. The detector is a CCD spectrograph which detects the probe light scattered by a pair of diffraction gratings. The pump beam has slight inclination compared to the probe beam and therefore cannot reach the detector. The zero time is adjusted by observing the signal of a known sample (C152 in ethanol in my case) varying the delay time. The whole setup is controlled by software based on LABVIEW platform. The pump power is kept ~5-µW during measurements. Steady state absorption spectra were taken before and after the measurements to ensure no photo degradation of the sample.

2.4. Fluorescence Correlation Spectroscopy (FCS)

The fluorescence correlation spectroscopic (FCS) measurements were in a home-built instrument which is schematically shown in figure 2.5. I have used an Olympus

IX71 inverted microscope for this setup. A 60x water immersion objective with Numerical Apperture 1.2 was used to focus the 405 nm excitation light from a CW laser source (5mW, Optoelectronics Tech. Co. Ltd.) into the sample at a distance of 40 μm from the surface of the coverslip. The same objective is used to collect the emitted photons and focused on a multimode fiber patch chord of 25 μm diameter after passing through a dichroic mirror (ZT405rdc, Omega Optical Inc., USA) and an emission filter (FSQ-GG455, USA). Fluorescence signal was then directed towards a photon counting module (SPCM-AQRH-13-FC, Excelitas) through the fiber patch chord and then to the correlator card (FLEX990EM-12D, Correlator.com, USA) to generate the autocorrelation function G(τ). The autocorrelation function $G(\tau)$ that arises because of the temporal fluctuation of the fluorescence intensiy can be described as,[7]

$$G(\tau) = \frac{\langle \delta F(t) \delta F(t+\tau) \rangle}{\langle F(t) \rangle^2} \qquad (2.15)$$

The autocorrelation is the self-similarity of fluorescence intensity at different times. $\langle F(t) \rangle$ is the average fluorescence intensity, and $\delta F(\tau)$ and $\delta F(t+\tau)$ are the quantity of fluctuation in intensity around the mean value at time t and $(t+\tau)$;

$$\delta F(t+\tau) = F(t+\tau) - \langle F(t) \rangle \qquad (2.16)$$

For a single component system, the diffusion time (τ_D) can be obtained by fitting the autocorrelation function $G(\tau)$ using the following equation.[7]

$$G(\tau) = \frac{1}{N}\left(1 + \frac{\tau}{\tau_D}\right)^{-1}\left(1 + \frac{\tau}{\omega^2 \tau_D}\right)^{-1/2} \qquad (2.17)$$

Where, N is the number of particles in the observation volume and $\omega = l/r$ is the longitudinal to transverse radius ratio of the 3D Gaussian volume. By fitting the FCS autocorrelation curve we get two parameters, τ_D. From the diffusion time (τ_D) and transverse radius of the observation volume (r), the diffusion coefficient and hydrodynamic radius (r_H) of the molecule can be calculated using the following couple of equations.

$$D_t = \frac{r^2}{4\tau_D} \tag{2.18}$$

$$r_H = \frac{k_B T}{6\pi\eta D_t} \tag{2.19}$$

where, k_B is the Boltzmann constant, T is the temperature in Kelvin scale and η is the viscosity of the solution. I took several FCS data (of varying concentration) of rhodamine 6G (R6G) in water and globally fitted them to determine the value of ω. While calibrating the value of ω, the diffusion coefficient of R6G in water is taken to be D_t = 4.14 × 10^{-6} cm^2s^{-1}. For time dependent study, I have taken 10 µL of the sample from the mother diluted solution which is studied.

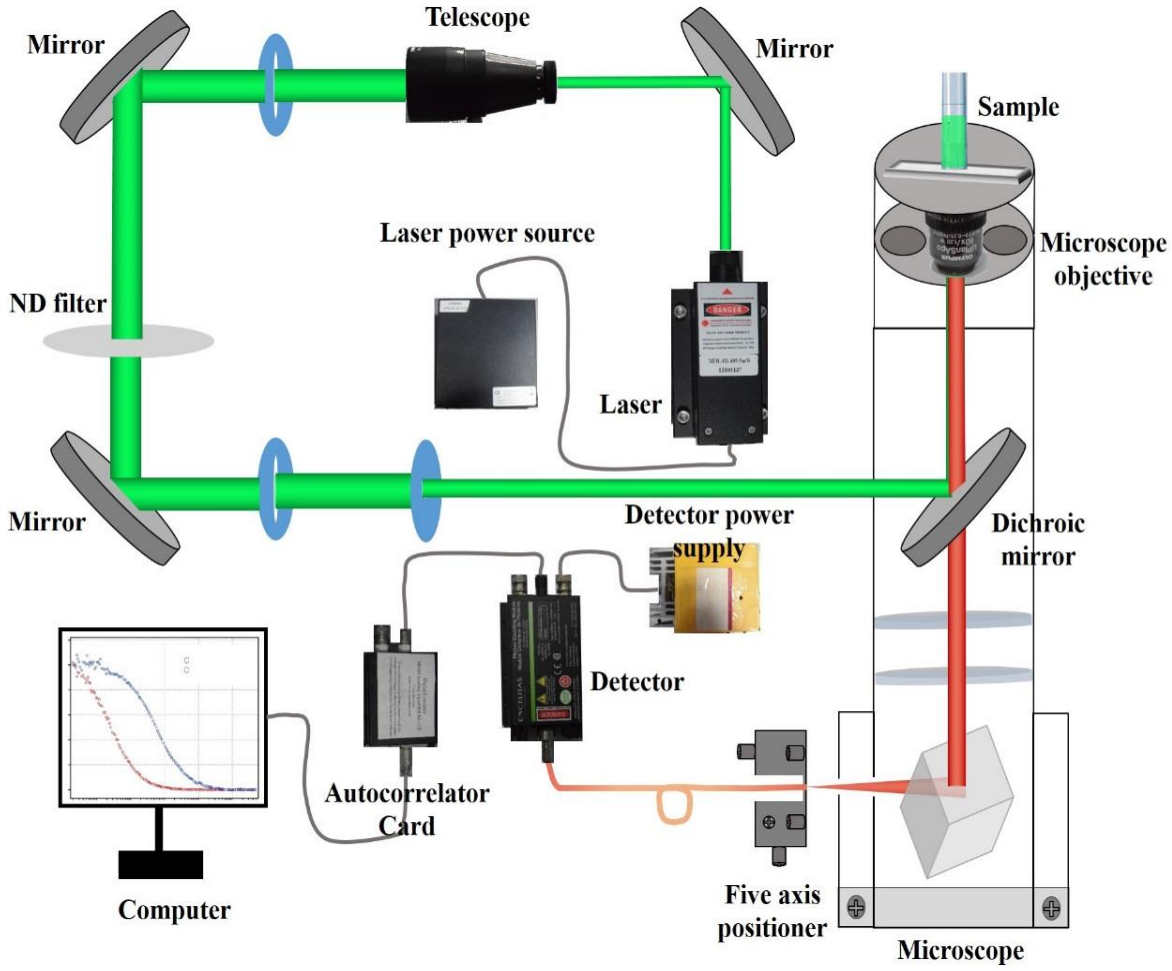

Figure 2.5. Schematic representation of home-built FCS setup.

2.5. Transmission electron microscopy (TEM)

2.5.1. Principle

The working principle of electron microscope is very similar to that optical microscope. Resolution is the reason of using electron in place of light. Resolution means the smallest distance between two points that can be separated. The smallest distance between two points that our eye can resolve is around 0.1-0.2 μm, which also depend on the condition of our eyes. The resolution of a system (δ) can be expressed by the classic Rayleigh criterion, which is used for optical microscope as,[17-19]

$$\delta = \frac{0.61\lambda}{\mu \sin \beta} \qquad (2.20)$$

In equation 2.20, λ is the wavelength of radiation, μ is the refractive index of the viewing medium, and β is the semi-angle o collection of the microscopic lens. In general, for a system $\mu \sin \beta$ is termed as numerical aperture and can be approximated to unity. So, the resolution of a microscope is directly proportional to the half of the wavelength of radiation. For optical microscope, the source of radiation is visible laser. Thus, the maximum resolution that can be achieved through blue laser light (~450 nm) is ~275 nm. The essence of electron microscope lies in this resolution limitation of optical microscopes. The low resolution of optical microscopes restricts the study of nanomaterials by it.

The famous physicist Louis de Broglie established that wavelength of the electrons is related to their energy, E. Ignoring the relativistic effects, we can approximately show that,[17, 19]

$$\lambda = \frac{1.22}{E^{\frac{1}{2}}} \qquad (2.21)$$

Where λ is in nm and *E* is expressed in eV.

So, if we use 100 keV electron energy as probe, then from equation 2.21, $\lambda = 0.004$ nm which is much smaller to the atomic dimension. So, using TEM we can have resolution to the atomic level. However, in reality this resolution depends on several instrumental factors. In recent time high resolution TEM (HRTEM) can have actual resolution to the atomic level.

2.5.2. Basic instrumentation

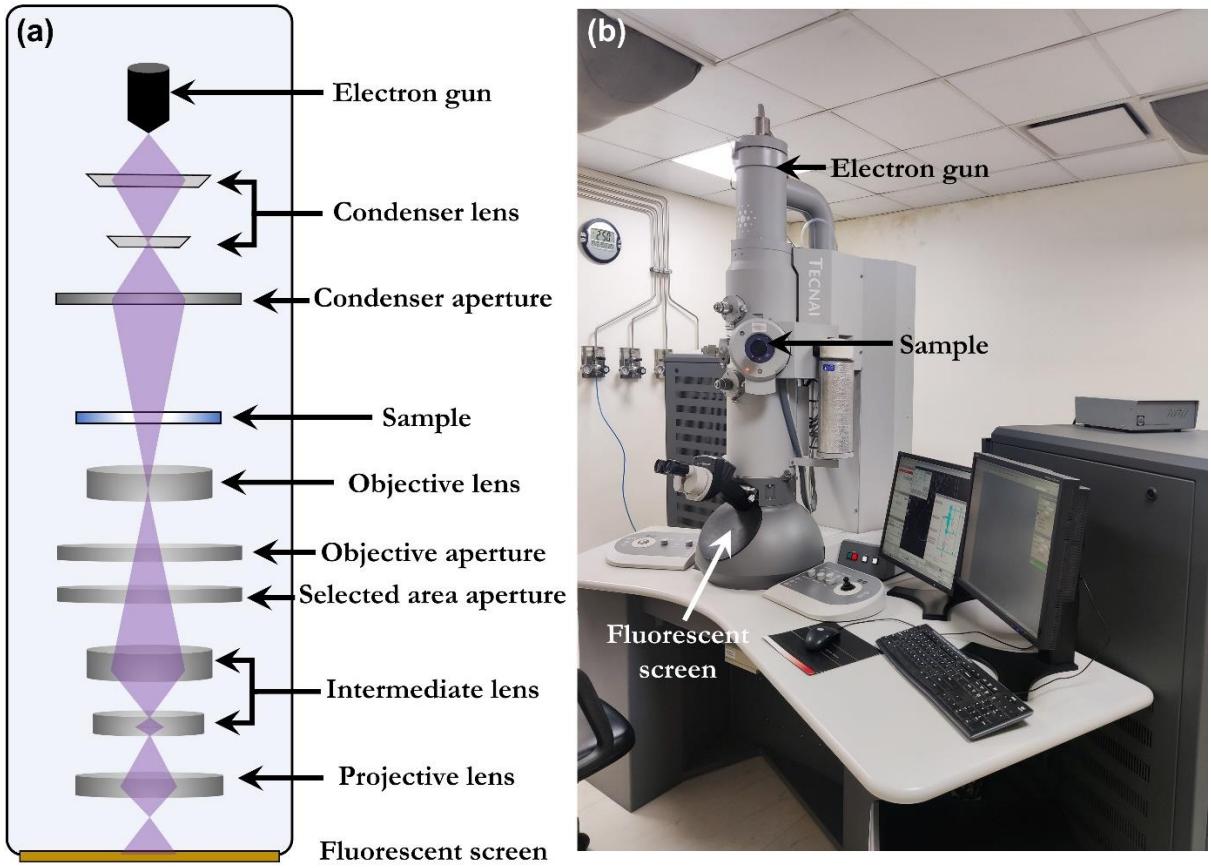

Figure 2.6. (a) Schematic representation of basic TEM instrument. (b) Real image of Technai G120 instrument in IIT Kanpur.

The basic TEM instrument consists of three main parts: electron gun, image producing system, and image recording system. The schematic representation of basic TEM setup is depicted in figure 2.6.[17, 19]

Electron gun: This part is responsible for producing electron beam in TEM. A cathode that is a tungsten filament generates electrons. The specimen is successfully

focused to produce a clearly defined image by the columnar aperture (hole), through which electrons are transmitted from the cathode to the anode at high voltage and constant energy. It also contains a condenser lens system that concentrates the electron beam on the specimen by using the electron gun's column hole and energy intensity. The TEM employs two condenser lenses to concentrate the electron beam on the specimen. The first lens, which has a high magnification, produces a smaller image of the specimen, which is then directed to the second condenser lens, which focuses the image on the objectives. Each of the two condenser lenses produces an image in this manner. Here, all of the lenses used to focus the electron beam are magnetic.[18, 20]

Image producing system: The objective lens, a portable stage for holding the specimen, intermediate lenses, and projection lenses are the components of the device. They work by magnifying the image produced by passing electrons through the specimen. The objective provides an intermediate image from the condenser that is sent to the projector lenses for magnification and has a small focal length of around 1 to 5 mm. There are two different kinds of projector lenses: an intermediate lens that greatly magnifies the image and a projector lens that generally magnifies more than an intermediate lens. The objectives and projector lenses require high power supplies with great stability for the highest grade of resolution in order to produce effective, high standard images.[20]

Image recording system: The fluorescent screen that is used to observe and focus on the image is part of it. It also has a digital camera that captures photographs that are then permanently stored after viewing. It has a vacuum system that prevents air molecules from being hit by or colliding with electrons, which would otherwise interfere with their movement and ability to focus. A vacuuming system makes it easier for electrons to travel directly to the image. The resulting grayscale or black and white image is referred to as a monochromatic image. Because the image must

be visible to the naked eye, electrons are permitted to pass through a fluorescent screen that is mounted to the bottom of the microscope.[18]

2.5.3. Sample preparation

The sample preparation in TEM analysis is one of the most crucial parts. For colloidal NCs, with band edge absorbance ~0.1 of colloidal suspension is used here as the parent solution. The NCs suspensions were sonicated about ~15 minutes before drop casting to the carbon-coated TEM grids. The TEM grids were then vacuum dried for overnight before placing to the TEM sample holder.

2.5.4. Image analysis

All the TEM image analysis has been done in ImageJ software. TEM generally produces three types of images: Normal TEM image which shows the morphology and particle size distribution, high resolution TEM image which is important to study the lattice fringes, and selected area electron diffraction (SAED) pattern from which the crystal phase analysis can be done by matching the crystal plane positions derived from powder X-ray crystallographic (PXRD) analysis.

Particle size distribution: Size of the NCs vastly controls their property. Therefore, particle size distribution analysis is very important in nanoscience. Through ImageJ, the average diagonal distance is calculated for each NC in an image, and this distribution of edge length is termed as particle size distribution.

HRTEM analysis and Fourier filtration: HRTEM analysis is done to study and identify the different phases in NCs through lattice fringes. In a raw HRTEM image, more than one lattice fringes may be observed which can hamper proper analysis. To overcome this issue, Fourier filtration of the image is needed.

Every image can be expressed as,[21]

$$F(x) = \sum_k G(k) \sin(kx) \qquad (2.22)$$

Where $F(x)$ is the real image in x axis, k is the frequency of the lattice planes. The lower order crystal planes have larger interplanar distance and thus lower frequency. $G(k)$ is the amplitude of the sine wave that construct the image.

Now, $F(x)$ is the real image in the x axis, and $G(k)$ is the collection of sine waves in the coordinate $k(x)$ that been used to construct the real image $F(x)$. This can be visualised as in figure 2.7.

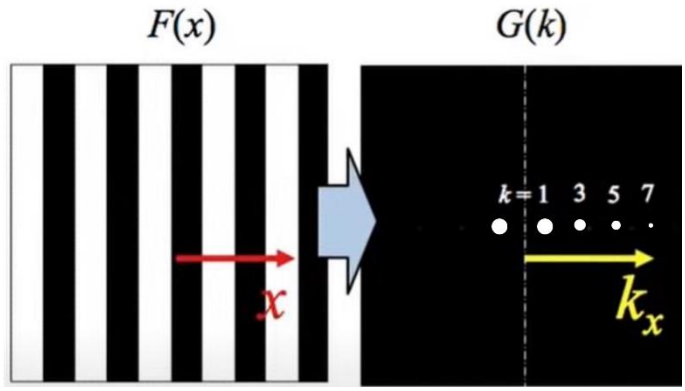

Figure 2.7. Representation of an image in real space *F(x)* and in Fourier space *G(k)*.

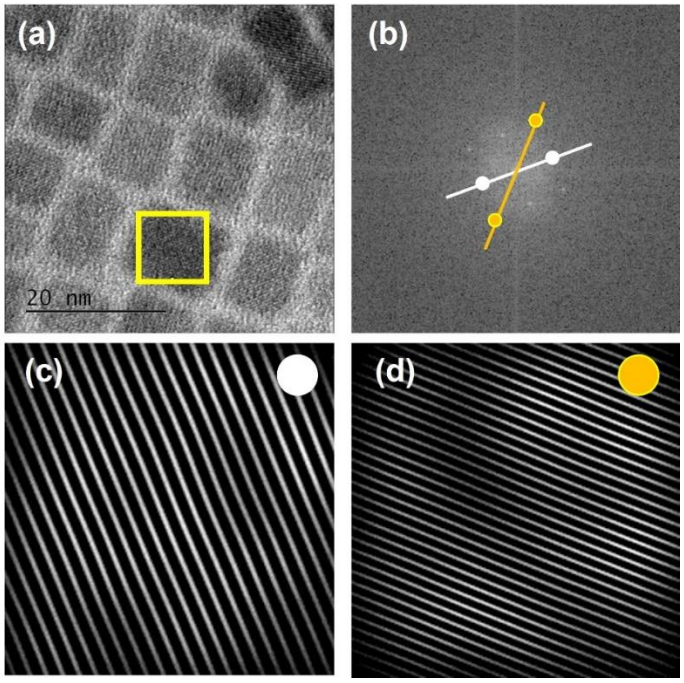

Figure 2.8. (a) HRTEM image of CsPbBr3 NCs. (b) Fourier transformed image of the selected area of figure 2.8a. (c) Fourier filtered image by selective choice of white *k* axis in figure 2.8b. (d) Fourier filtered image by selective choice of yellow *k* axis in figure 2.8b.

The *K(x)* points are always in perpendicular with the lattice planes. So, by Fourier transformation of a HRTEM image we get lots of *k* points in different direction, each of which set contains the details about a particular lattice plane. By selective choice of a particular *k* set then back Fourier transformed to visualize a particular crystal plane. This is depicted in figure 2.8 with a real HRTEM image of $CsPbBr_3$ NCs.

SAED analysis: SAED is another technique which is vastly used in TEM which contains the crystallographic information of the sample. In SAED the wave nature of the electrons is used. The relativistic wavelength of the electron is given by, [7, 22]

$$\lambda = \frac{hc}{\sqrt{eV(2m_0c^2+eV)}} \qquad (2.23)$$

Where *h* is plank's constant, m_0 is the rest mass of electron, *e* is the charge of electron, *c* is the speed of light, and *V* is the accelerating potential.

The electrons are diffracted on the crystal planes in a particular angle which acting as a diffraction grating. According to the Braggs' law if the diffracted electron beam angle is θ, then,[23]

$$n\lambda = 2d\sin\theta \qquad (2.24)$$

Where *n* is an integer and *d* is the interplanar distance. The diffraction pattern is created when each pair of initially parallel beams cross in the rear focus plane after being refracted by the magnetic lens of the microscope.

Whether the beam is diffracted by a single crystal or by a number of crystallites with various orientations, as in a polycrystalline material, determines the characteristics of the resulting diffraction image. Bright spots appear in a predictable way on the single-crystalline diffractogram. This is depicted with diffraction from a single $MAPbBr_3$ NC in figure 2.9a. This pattern can be viewed as a projection of a reciprocal crystal lattice in two dimensions. The diffraction image becomes a superposition of the diffraction patterns of individual crystals if there are more contributing crystallites. In the end, this superposition encompasses diffraction spots

from all possible orientation of crystallographic plane systems forms a ring pattern. This is shown in figure 2.9b with $CsPbBr_3$ NCs.

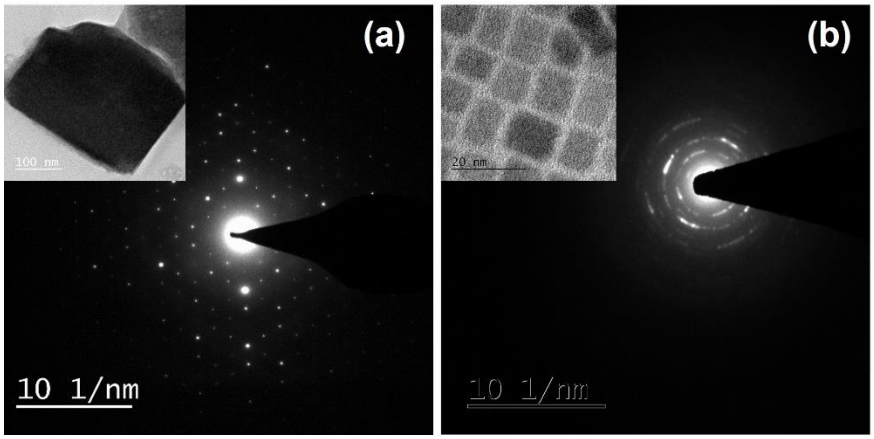

Figure 2.9. (a) Spot SAED pattern from a single $MAPbBr_3$ NC. The real image of $MAPbBr_3$ NC is in inset. (b) Ring SAED pattern from a large area containing many $CsPbBr_3$ NC. The real image of $CsPbBr_3$ NC is in inset.

Each bright in spot SAED pattern or each ring in ring SAED pattern arises from a particular crystal plane. The SAED image is in reciprocal space. The interplanar distance of a particular plane is calculated from the inverse of the distance of that particular spot or ring from the centre.

2.6. Powder X-ray diffraction (PXRD)

PXRD analysis of colloidal perovskite NCs were done to have the idea of the crystal phase of the NCs. X-rays are partially scattered by atoms when they strike the surface of a crystal. The X-ray that is not scattered passes through to the layer of atoms below, where it is again partially scattered and partially continues on to the next layer which is schematically shown in figure 2.10. The layer of atoms which generally called crystal planes act like the grating.[24, 25] The sample must be crystalline and the distance between atom layers must be close to the radiation wavelength for an X-ray to diffract.

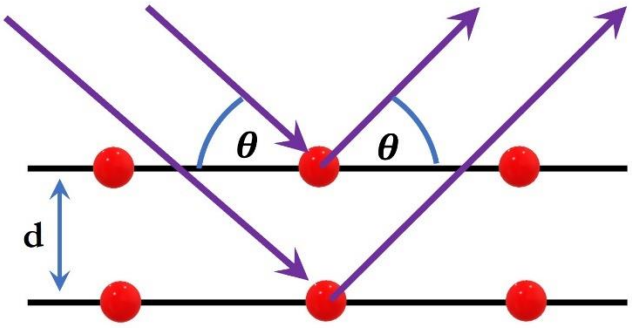

Figure 2.10. Schematic representation of X-ray diffraction from crystal planes.

The diffraction pattern exhibits a peak when beams diffracted by two separate layers are in phase; however, when they are out of phase, destructive interference appears and there is no peak. Diffraction peaks only occur if,[23]

$$\sin\theta = \frac{n\lambda}{2d} \qquad (2.25)$$

Where, θ is the angle of incident radiation, λ is the wavelength of radiation in nm, d is the spacing between atom layers or crystal planes, and n is an integer. This is known as famous Bragg's equation. This Bragg's equation is the working principle of XRD analysis.

PXRD patterns for my samples were collected in PANalytical XPert Powder diffractometer with Cu-Kα as incident radiation (λ = 0.154 nm) in the 2θ range between 5° to 60° with step size of 0.01°. For sample preparation I have used crude NC suspension in toluene/hexane and centrifuged it at 15000 rpm to precipitate out all NCs and dispersed this in 200 µL toluene/hexane. This NC dispersion was then drop casted on clean glass slide and kept this in open air to evaporate out all solvent molecules. This glass slide was then used then for PXRD experiment.

2.7. X-ray photoelectron spectroscopy (XPS)

XPS is used for the surface elemental analysis of materials. The working principle of XPS relied on the photoelectric effect. When sample is irradiated with X-ray, core

electrons from different elements of the sample are ejected with kinetic energy E_k. The kinetic energy of this ejected electrons is defined by,[26, 27]

$$E_k = h\nu - E_b - \phi \qquad (2.26)$$

Where, $h\nu$ is the energy of the incident X-ray beam, E_b is the binding energy of the electron, and ϕ is spectrometer work function. The E_k value is measured by the detector. For different elements, the E_b value is different for different core levels. Thus the E_k value is characteristics of a particular core level of a particular atoms. The XPS spectra is produced by plotting these E_k values with different intensities. The elemental percentage can also be done from this spectrum by integrating the respective peaks considering the relative sensitivity factor (RSF).[27]

The XPS data presented in this thesis were collected using PHI 5000 Versa Prob II model. Sample was prepared by drop casting respective NC suspension on a thin coverslip followed by vacuum drying.

2.8. Other instrumental techniques

FESEM: The field emission scanning electron microscopy (FESEM) images were collected by NOVA a NANOSEM 450 system in the secondary electron mode.

NMR: NMR spectra were recorded on a Bruker Avance 400 system (1H, 400 MHz; 13C, 100 MHz).

FTIR measurements: Fourier transform infrared (FTIR) measurements were carried out using Bruker Alpha-P FTIR with ATR accessory.

Thermogravimetric analysis (TGA): The thermal stabilities of the DESs were determined by thermogravimetric analysis (TGA) using a Mettler Toledo TGA/DSC 1 instrument. A dynamic mode at a temperature range from (17 to 250) ºC with a heating rate of 5ºC min-1 was used to determine the onset decomposition temperatures.

2.9. Synthetic procedures

2.9.1. Synthesis of methylammonium bromide (CH_3NH_3Br or MABr)

27.86 ml CH_3NH_2, 40% in methanol in 500 ml flask, was mixed with 100 ml of ethanol. Then, 8.5 ml of an HBr solution in 48%water was added dropwise while being continuously stirred at room temperature. To remove all solvents, the obtained solution was put in a rotary evaporator set at 60°C. MABr was dissolved in ethanol and twice precipitated with diethyl ether after being washed with diethyl ether many times.

2.9.2. Synthesis of methylammonium iodide (CH_3NH_3I or MAI)

100 ml of ethanol and 27.8 ml of CH_3NH_2, which is 40 percent methanol, were mixed in a 500 ml flask. After that, 30 ml of a 57% water solution of the HI was added at room temperature while being continuously stirred. To remove all solvents, the obtained solution was put in a rotary evaporator set at 60°C. Following multiple washes with diethyl ether, MAI was dissolved in ethanol and twice precipitated with the solvent. After that, 80 ml of hot ethanol was added to the MAI to dissolve it, and the mixture was then placed in a refrigerator set to -3°C for re-crystallization in order to produce extremely pure crystals.

2.9.3. Preparation of $CH_3NH_3Pb_{0.5}Bi_{0.33}I_3$ (MPBI) nanocrystals (NCs)

Methyl ammonium iodide (0.0159 g), lead iodide (0.0231g) and bismuth iodide (0.0195g) were dissolved together in DMF solvent. Then 200 µL oleic acid (OA) and 100 µL Olylamine (OAm) were added and shaken to get the precursor solution. Then 100 µL of this precursor was added to 3ml toluene and shaken vigorously and NC dispersion formed. Then this suspension was centrifuged at 7500 rpm to discard the large crystals. The yellow transparent NC solution then decants off and all the studies were done with this suspension. This centrifugation is a very important part

of this preparation as by this we can discard the large crystals formed and also discard the unreacted substances.

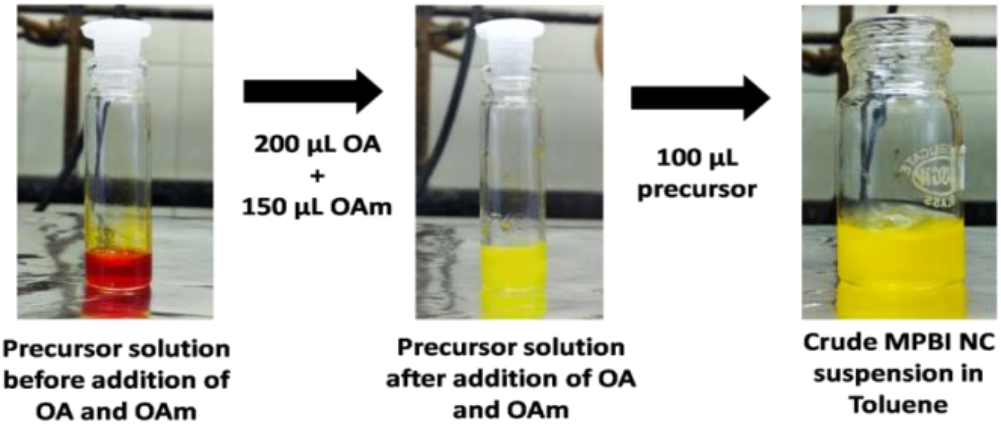

Figure 2.11. Preparation of MPBI NC.

2.9.4. Preparation of $CH_3NH_3PbI_3$ (MPI) NCs

Methyl ammonium iodide (MAI) (0.0159 g) and lead iodide (0.0462g) were dissolved together in DMF solvent. Then 200 µL oleic acid (OA) and 150 µL Olylamine (OAm) were added and shaken to get the precursor solution. Then 100 µL of this precursor was added to 3ml toluene and shaken vigorously and NC dispersion formed. Then this suspension was centrifuged at 7500 rpm to discard the large crystals. The yellow transparent NC solution then decants off and all the studies were done with this suspension.

2.9.5. Preparation of $CH_3NH_3PbBr_3$ (MPBr) NCs

I have prepared all the NCs by the antisolvent precipitation technique with slight modification.[1]Methyl ammonium bromide (0.0055 g) and lead bromide (0.0182 g) were dissolved together in 0.5 ml DMF solvent. Then 100 µL oleic acid (OA) and 125 µL oleyl amine (OAm) were added and shaken to get the precursor solution. Then 100 µL of this precursor was added to 3ml fresh $CHCl_3$ and shaken vigorously and NC dispersion formed. Then this suspension was centrifuged at 7500 rpm to

discard the large crystals. The pale-yellow transparent NC solution then decants off and all the studies were done with this suspension.

2.9.6. Preparation of $CH_3NH_3Pb_{1/2}Bi_{1/3}Br_3$ (MPBBr) NCs

Methyl ammonium bromide (0.0055 g), lead bromide (0.0091g) and bismuth bromide (0.0080g) were dissolved together in 0.5 ml DMF solvent. Then 100 µL oleic acid (OA) and 125 µL Oleylamine (OAm) were added and shaken to get the precursor solution. Then 100 µL of this precursor was added to 3ml $CHCl_3$ and shaken vigorously and NC dispersion formed. Then this suspension was centrifuged at 7500 rpm to discard the large crystals. The yellow transparent NC solution then decants off and all the studies were done with this suspension. For preparation of MPBBr with different OA and OAm ratio, the methods were same.

2.9.7. Preparation of MPBKBr and MPBBr-NaCl NCs

Methyl ammonium bromide (0.0055 g), lead bromide (0.0091g) and bismuth bromide (0.0080g) were dissolved together in 0.5 ml solution of KBr in DMF solvent. Then 100 µL oleic acid (OA) and 125 µL Oleylamine (OAm) were added and shaken to get the precursor solution. Then 100 µL of this precursor was added to 3ml $CHCl_3$ and shaken vigorously and NC dispersion formed. Then this suspension was centrifuged at 7500 rpm to discard the large crystals. The yellow transparent NC solution then decants off and all the studies were done with this suspension. For MPBBr-NaCl NCs, same procedure is followed and NaCl is used in place of KBr.

2.9.8. Synthesis of oleylammonium halide (OAmX) salts

OAmX salts were prepared by the reported procedure by Dutta *et al*.[28] In short, 10 ml of oleylamine (OAm) were taken along with required amount of hydrohalic acid (For OAmCl 1 mL of HCl, for OAmBr 1.28 mL of HBr and for OAmI 1.5 mL of HI) in a 25 mL two neck round bottomed flask. The resulting reaction mixture was

heated at 120 °C for 2 hours in nitrogen atmosphere. The reaction temperature then increased to 150 °C and further heated for 30 mins. The prepared OAmCl salt concentration was measured to be 0.85 mmol/mL, whereas the concentrations of OAmBr and OAmI salts were 0.51 mmol/mL and 0.34 mmol/mL, respectively. The synthesized OAmX salts were characterized by ^{1}H and ^{13}C NMR (see figure 2.12 to figure 2.14). The hexane diluted solutions (0.3 M OAmX) were then used for anion exchange reactions.

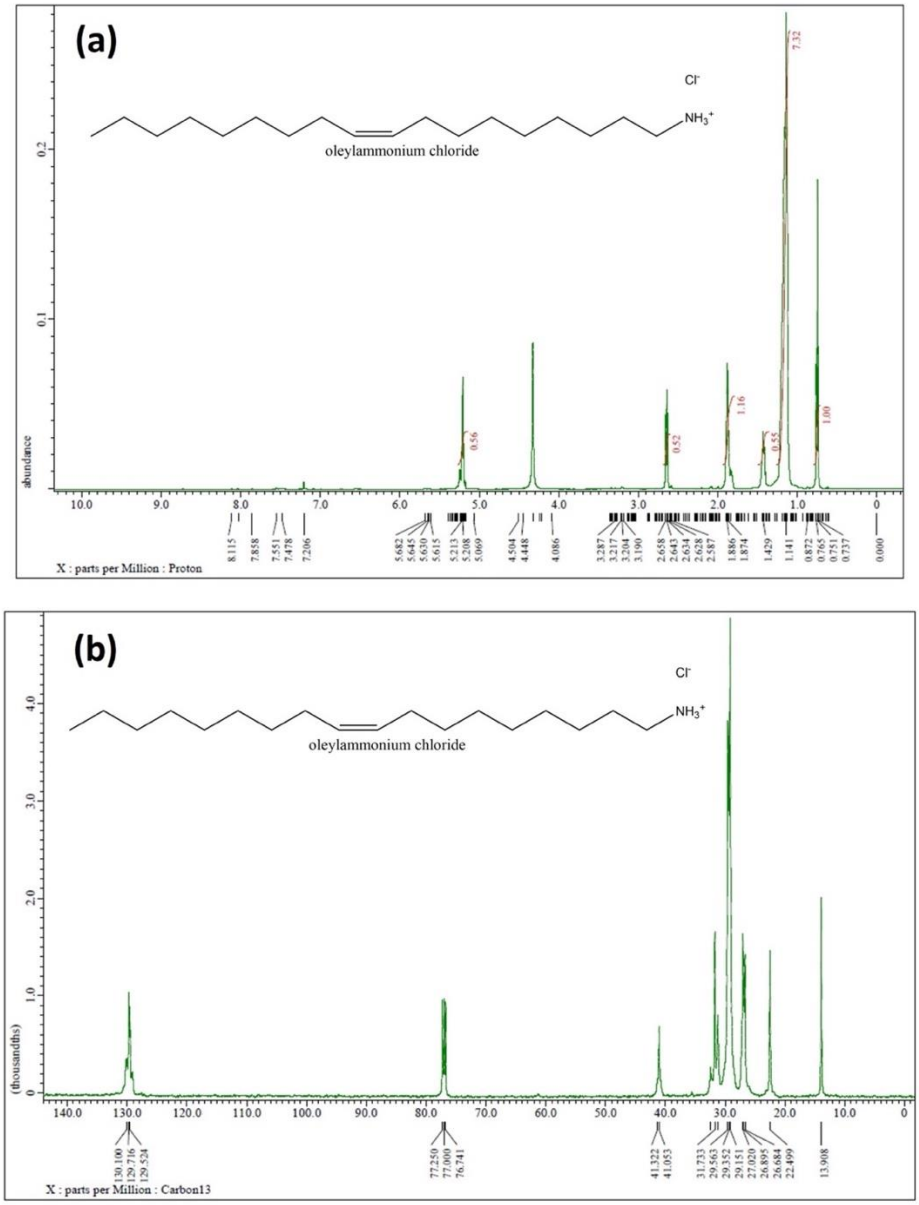

Figure 2.12. (a) ^{1}H NMR spectrum of OAmCl. (b) ^{13}C NMR spectrum of OAmCl.

OAmCl: ^{1}H NMR ($CDCl_3$, 500 MHz): δ 0.79 (t, 3H), 1.18 (m, 22H), 1.47 (m, 2H), 1.88-1.94 (m, 4H), 2.68 (t, 2H), 5.25 (m, 2H) (see figure S4a. Section S3 of the ESI). ^{13}C NMR ($CDCl_3$, 100 MHz): δ 14.1, 22.67, 26.87, 27.2, 29.35, 29.55, 29.75, 31.44, 31.92, 41.21, 76.94, 77.2, 77.45, 129.9 (see figure S4b. Section S3 of the ESI).

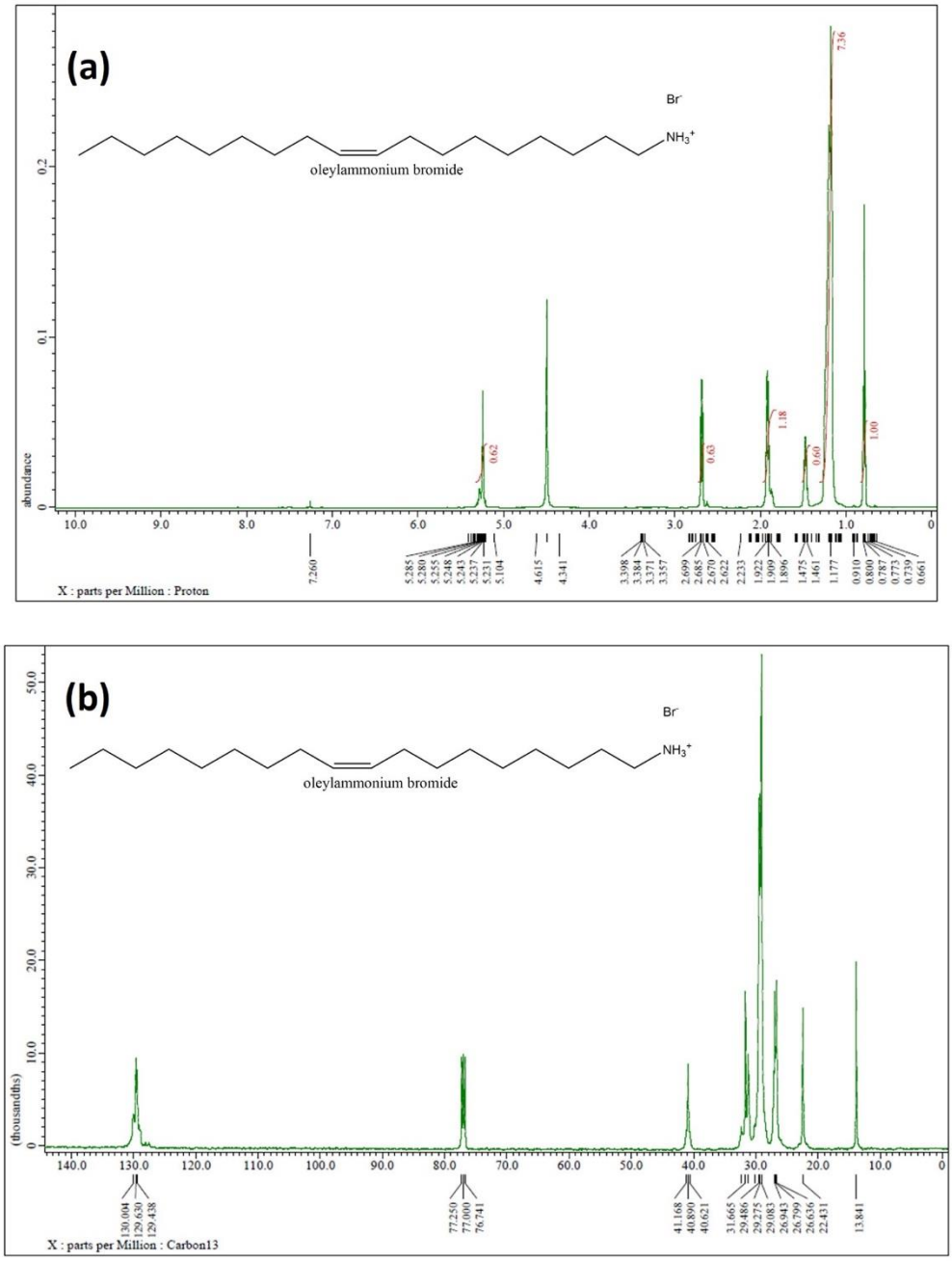

Figure 2.13. (a) ^{1}H NMR spectrum of OAmBr. (b) ^{13}C NMR spectrum of OAmBr.

OAmBr: ^{1}H NMR ($CDCl_3$, 500 MHz): δ 0.77 (t, 3H), 1.16 (m, 22H), 1.46 (m, 2H), 1.86-1.93 (m, 4H), 2.67 (t, 2H), 5.26 (m, 2H) (see figure S5a. Section S3 of the ESI). ^{13}C NMR ($CDCl_3$, 100 MHz): δ 13.8, 22.43, 26.67, 26.8, 29.01, 29.27, 29.49, 31.65, 40.89, 76.72, 77.0, 77.25, 129.7 (see figure S5b. Section S3 of the ESI).

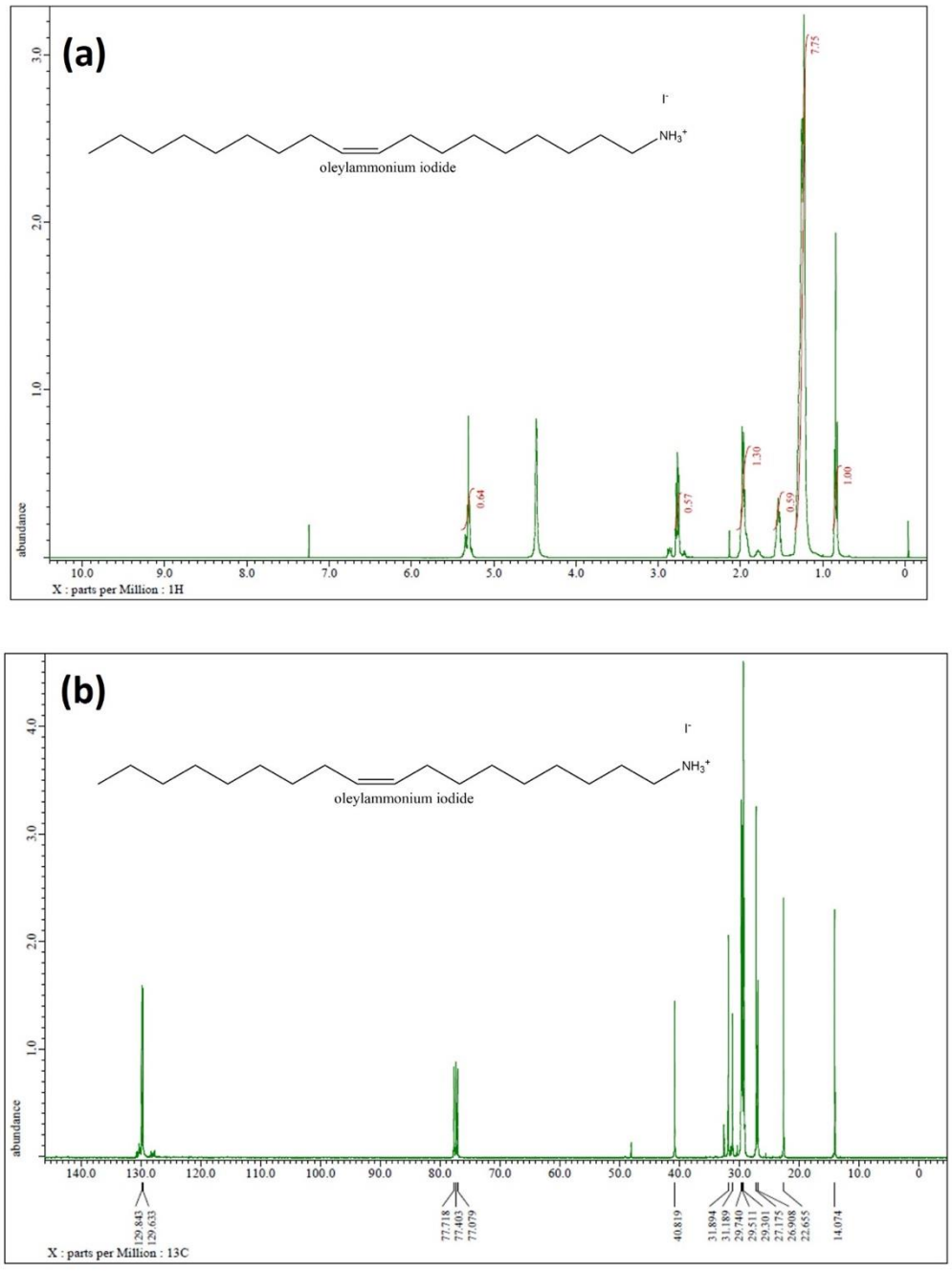

Figure 2.14. (a) ^{1}H NMR spectrum of OAmI. (b) ^{13}C NMR spectrum of OAmI.

OAmI: ^{1}H NMR ($CDCl_3$, 500 MHz): δ 0.84 (t, 3H), 1.23 (m, 22H), 1.44 (m, 2H), 1.92-2.01 (m, 4H), 2.77 (t, 2H), 5.31 (m, 2H) (see figure S6a. Section S3 of the ESI). ^{13}C NMR ($CDCl_3$, 100 MHz): δ 14.1, 22.64, 26.89, 27.2, 29.24, 29.51, 29.73, 31.21, 31.82, 40.77, 77.1, 77.4, 77.7, 130.2 (see figure S6b. Section S3 of the ESI).

2.9.9. Preparation of green medium for the synthesis of $MAPbX_3$ X= Cl, Br, I) NCs

The green reaction medium was prepared by adding 2 mL methylamine solution into 2 g lauric acid (LA) at 60 °C. The mixture was stirred for 30 minutes at the same condition. The high temperature is required to liquefy LA (melting point 43.2°C). This ionic liquid-like (IL) medium was then used to synthesize perovskite NCs. This ionic liquid like medium was characterized by ^{1}H NMR. The NMR spectrum of this medium is depicted in figure 2.15. All the detected protons can be assigned to the corresponding chemical shift of the cation and anion, which confirms the formation of an IL-like medium.

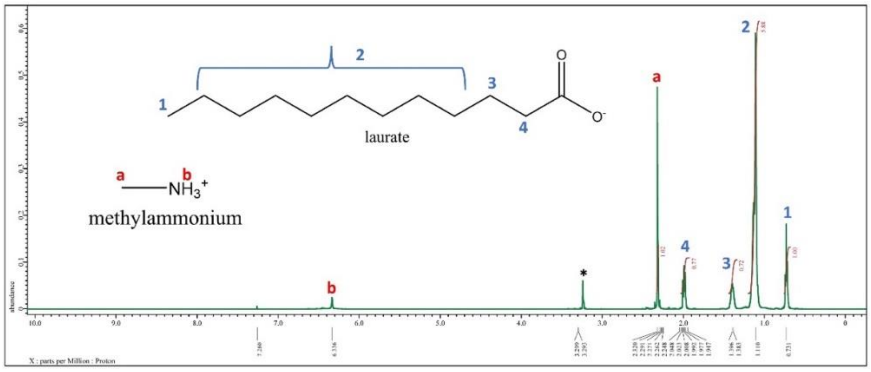

Figure 2.15. ^{1}H NMR spectrum of the ionic liquid like green solvent medium. (*) peak at 3.29 ppm originates from the residual methanol.

2.9.10. Synthesis of $CH_3NH_3PbBr_3$ NCs through green synthesis

I have prepared the $MAPbBr_3$ NCs by direct addition of 200 mg of $PbBr_2$ salt to 3 mL of the solvent medium at 60 ºC (see scheme 1). After the formation of bright green luminescent $MAPbBr_3$ NCs, I divided this into two parts (~1.5 mL each

containing $MAPbBr_3$ NC suspension in the solvent medium). Both the parts were centrifuged (40 ºC, 12577 g, 60 min), and the supernatants were discarded. Then, 1 mL of hexane was added to each part and sonicated (25 ºC, 53 MHz, 10 min) followed by centrifugation (40 ºC, 12577 g, 15 min). This process was repeated five times to discard the remaining medium. Then $MAPbBr_3$ residue from each part was redispersed in 5 mL of hexane (room temperature) and used for further studies. The synthetic procedure is schematically shown in figure 2.16.

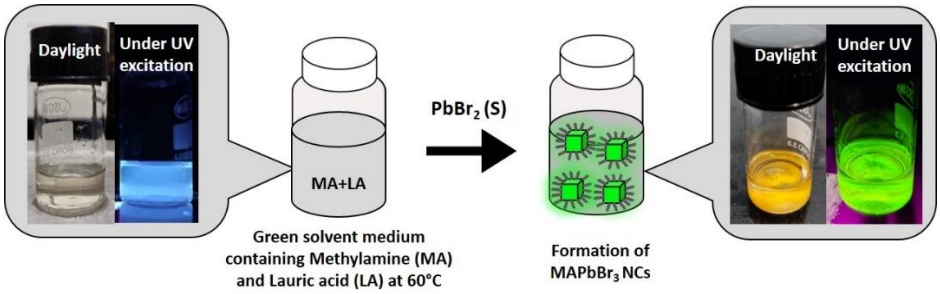

Figure 2.16. Schematic representation of the synthesis of $MAPbBr_3$ NCs. The solvent medium is composed of lauric acid (LA) and methylamine (MA). Real images of this medium in daylight and under UV (365 nm) are shown (leftmost image of the scheme). $MAPbBr_3$ NCs instantly formed by the addition of solid $PbBr_2$ to this medium. Real images of the synthesized $MAPbBr_3$ NCs in daylight and under UV (365 nm) are shown (rightmost image). A strong green PL of $MAPbBr_3$ NCs is observed under UV.

2.9.11. Synthesis of $MAPbBr_3$@lead laurate core-shell NCs

$MAPbBr_3$@lead laurate core-shell NC was prepared by direct addition of hexane dispersion of purified $MAPbBr_3$ NCs to the distilled water. A visible color change from deep yellow to white indicated the formation of lead laurate shell on the $MAPbBr_3$ NC core. The $MAPbBr_3$@lead laurate core/shell NPs were then extracted in hexane for further characterization.

2.9.12. Synthesis of $CH_3NH_3PbCl_3$ and $CH_3NH_3PbI_3$ NCs

$MAPbCl_3$ and $MAPbI_3$ NCs were prepared by direct addition of 200 mg of salts (lead chloride and lead iodide) to 3 ml of prepared solvent medium. Immediately after

addition of the salts, $MAPbCl_3$ (white) and $MAPbI_3$ (black) NCs were formed which were then purified by the similar procedure as $MAPbBr_3$ NCs.

2.9.13. Synthesis of menthol based deep eutectic solvents

The DESs were synthesized by heating acids in the right molar ratio with menthol. LA-menthol DES (LAMe) is synthesized by mixing LA with menthol in a 1:2 ratio. CA-Menthol (CAMe) and BA-Menthol DESs, on the other hand, were created in a 1:1 ratio using the same process. The DESs are transparent liquids at room temperature. These DESs were characterized using thermogravimetric studies (TGA), FTIR, and ^1H NMR.

H-bond doner (HBD)	H-bond acceptor (HBA)	Molar ratio	aspects
Lauric acid (LA)	Menthol	1:2	transparent liquid
Caprylic acid (CA)	Menthol	1:1	transparent liquid
Butyric acid (BA)	Menthol	1:1	transparent liquid

IR and NMR measurements were used to better characterize the DES media. Menthol has a broad O-H frequency centered at 3453 cm^{-1}, and all HBDs have a carbonyl frequency of ~1700 cm-1, both of which are modified following the synthesis of DES. The carboxylic C=O characteristic of pure BA is observed at 1708 cm^{-1}, whereas it is observed at 1710 cm^{-1} and 1701 cm^{-1} for CA and LA, respectively. These peaks shift to 1714cm^{-1}, 1719cm^{-1}, and 1717 cm^{-1} in BAMe, CAMe, and LAMe, respectively, after the synthesis of DESs (figure 2.17). The formation of an H-bonding network between menthol and different HBDs is indicated by these alterations in carboxylic carbonyl stretching frequency to higher values in corresponding DESs, which is consistent with prior observations. The shift is most noticeable in LAMe, implying the highest H-boning interaction among the three DESs.

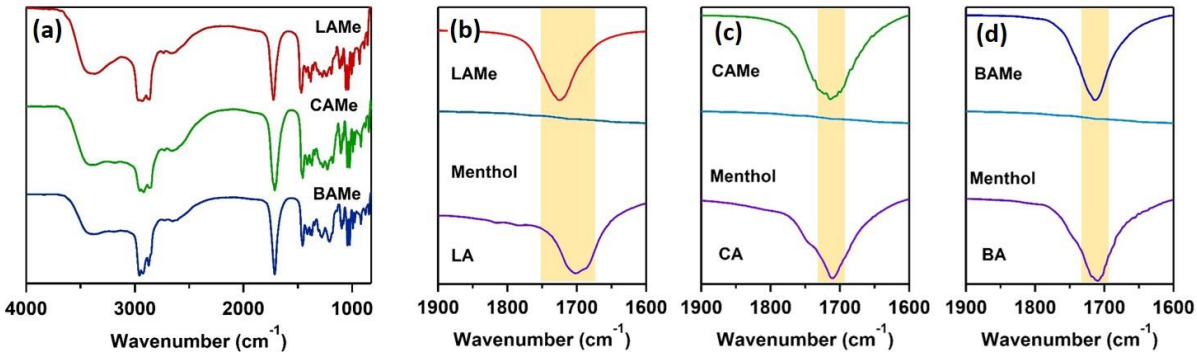

Figure 2.17. (a) IR analysis of the LAMe, CAMe and BAMe DES media. (b) IR spectra of LA, Menthol and LAMe in carbonyl region. (c) IR spectra of CA, Menthol and CAMe in carbonyl region. (d) IR spectra of BA, Menthol and BAMe in carbonyl region.

^{1H}NMR of the DES mediums also shows interesting feature regarding alcoholic hydrogen from menthol. In menthol the O-H proton was not observed due to its labile nature. But in all the DES mediums I have got a characteristic broad O-H hydrogen peak around 7-8 ppm range (figure 2.18 to figure 2.20). For BAMe and CAMe this peak came at 8.1 ppm (figure 2.19 and figure 2.20, respectively) but for LAMe it originates at 7.0 ppm (figure 2.18). This further indicates the formation of H-bonding interaction through the mentholic O-H. The structure of the DES media are complex and different types of interaction may be present. The indication of H-bonding through methanolic O-H arises a general question whether in this type of system a proper HBD or HBA can be assigned or not. This needs further studies.

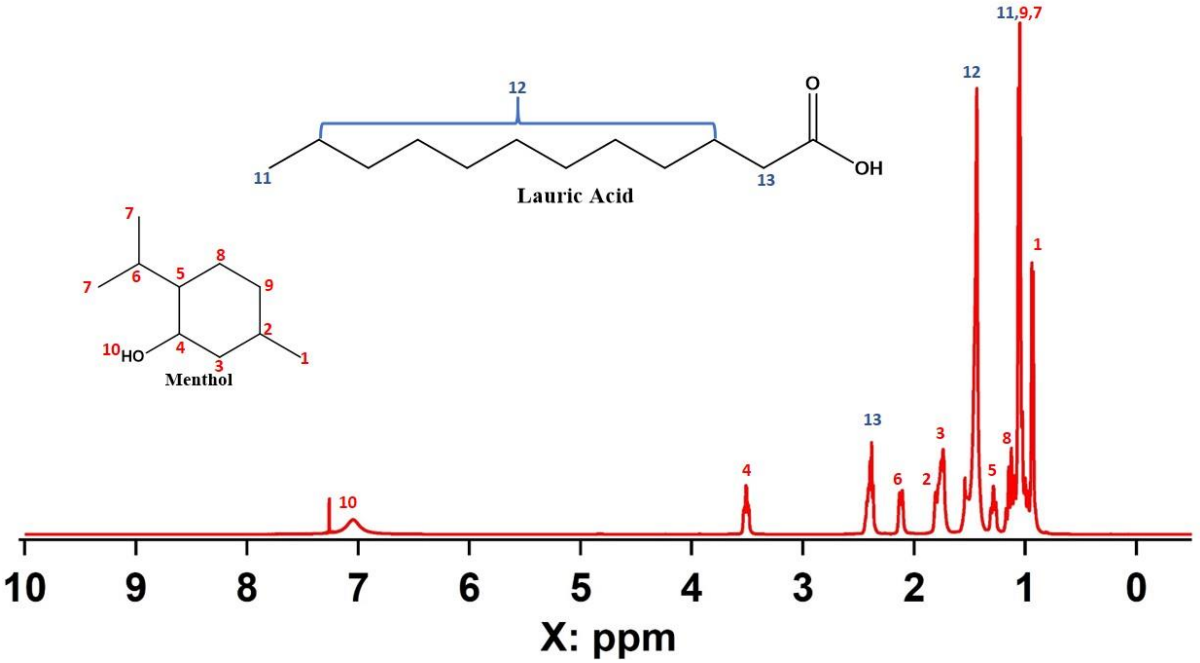

Figure 2.18. ^{1}H NMR spectrum of LAMe. All the corresponding NMR peaks have been assigned.

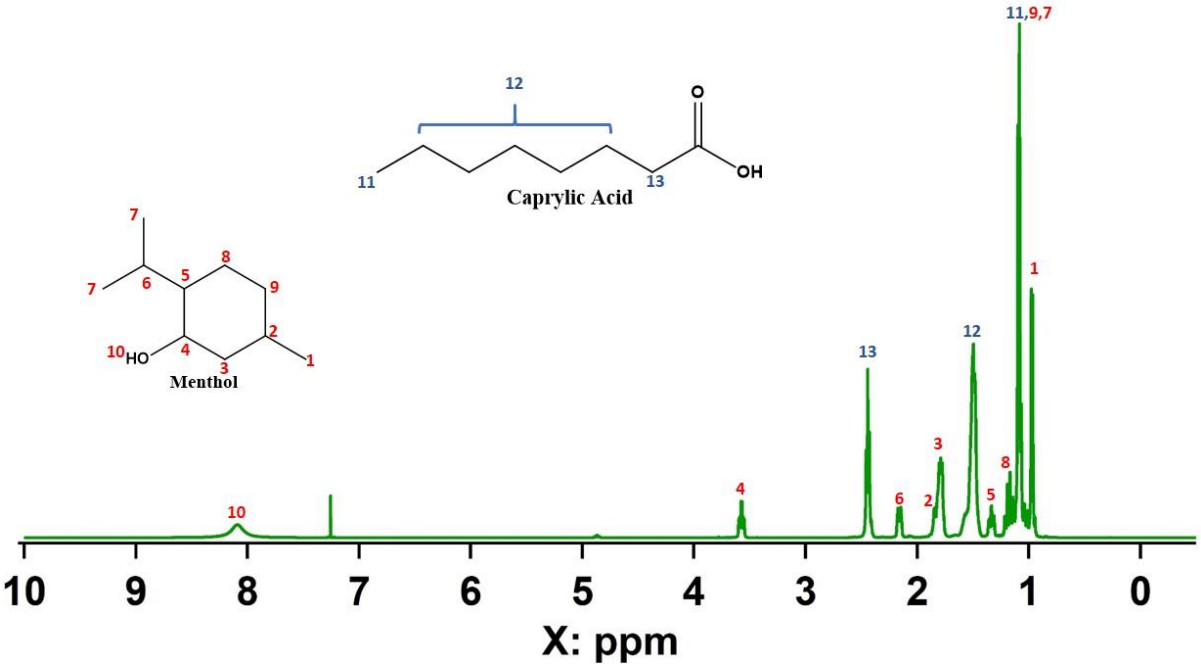

Figure 2.19. ^{1}H NMR spectrum of CAMe. All the corresponding NMR peaks have been assigned.

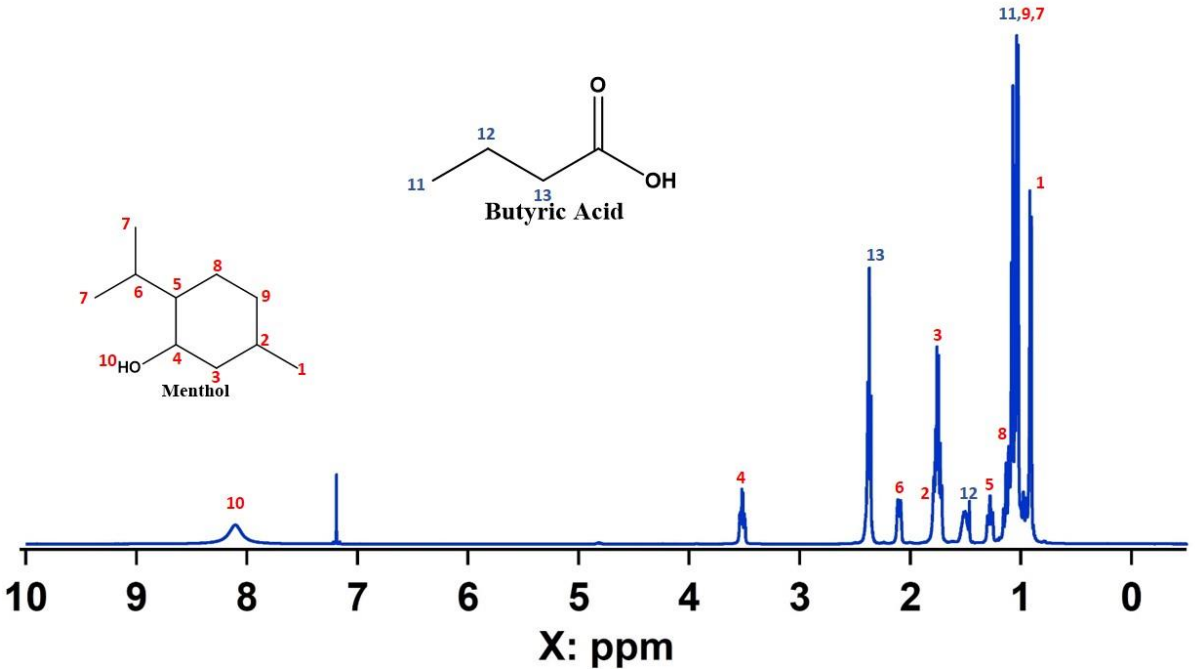

Figure 2.20. ^{1}H NMR spectrum of BAMe. All the corresponding NMR peaks have been assigned.

2.9.14. Synthesis of lead halide perovskite NCs and NPLs in DES medium

Synthesis of Cs-precursor in DES medium

65 mg of CsCO3 salt was added to 1 ml of DES (LAMe, CAMe or BAMe) and stirred for 100°C till it forms a clear colourless solution. This Cs-precursor was stored in normal atmospheric condition. At room temperature this Cs-precursor become solid. This was again re heated at different temperatures (depending upon the NC synthesizing temperature) before injecting.

Synthesis of $CsPbBr_3$ NCs in DES medium

7.2 mg of $PbBr_2$ salt was placed in a vial with 2ml DES (LAMe, CAMe or BAMe). Then 150 µL of OAm added to this mixture and stirred at 100°C till $PbBr_2$ fully solubilize. Cesium precursor was then heated at 100°C. 100 µL of this heated cesium precursor was then swiftly injected into the $PbBr_2$ precursor in DES. Instantly light yellow colored NCs formed which shows green photoluminescence under UV light. This NCs was then centrifuged at 15000 rpm for 1 hour. The supernatant DES was

discarded and the NCs were washed thoroughly with methyl acetate and then dissolved in hexane and centrifuged again at 10000 rpm for 10 mins. The supernatant contains the NCs of uniform size and used for further studies.

$CsPbBr_3$ NPLs with different width were synthesized using the same procedure, only by changing the temperature (100°C, 75°C, and 50°C) and the cesium precursor amount (25 µL, 50 µL, 75 µL and 100 µL) in LAMe.

Synthesis of other $CsPbX_3$ NCs (X=Cl, Cl/Br, Br/I, and I) in DES medium

The other halide perovskite NCs were also prepared by similar procedure except for $CsPbI_3$ NCs. For $CsPbCl_3$ NCs, 5.4 mg of $PbCl_2$ salt was dissolved in 2 ml LAMe DES in presence of OAm at 100°C. Then 100 µL of Cs-Precursor was injected into it. Immediately white colour $CsPbCl_3$ NC formed. This NCs was then centrifuged at 15000 rpm for 1 hour. The supernatant DES was discarded and the NCs were dissolved in hexane and centrifuged again at 10000 rpm for 10 mins. The supernatant contains the NCs of uniform size and used for further studies. For $CsPb(Cl/Br)_3$, a mixture of 2.7 mg of $PbCl_2$ and 3.6 mg of $PbBr_2$ were taken in DES whereas for $CsPb(Br/I)_3$ NCs 3.6 mg of $PbBr_2$ and PbI_2 were taken and respective NCs were prepared in a similar procedure. For $CsPbI_3$ NCs, 9 mg of PbI_2 was dissolved in 2 ml LAMe in presence of 200 µL OAmI and then prepared by similar procedure.

2.9.15. Synthesis of $CsPbBr_3$ NCs by hot injection procedure

The pristine $CsPbBr_3$ NCs were prepared by the reported procedure by Protesescu *et al.*[29] Briefly, 0.16 g of Cs_2CO_3, 6 mL of octadecene (ODE), and 0.5 mL of OA were combined in a 50 mL double-necked round-bottom flask (RB), which was then heated under vacuum at 120 °C for an hour and then under nitrogen atmosphere until all Cs_2CO_3 reacted with OA to generate Cs-oleate. In order to prevent precipitation, this solution was kept at this temperature. Another 50 mL double-necked RB was used to mix 0.069 g of $PbBr_2$, 5 mL of ODE, 0.5 mL of OA, and 0.5 mL of OAm before heating them at 110°C for an hour under vacuum. After raising the

temperature to 170 °C in a nitrogen environment, 0.45 mL of pre-heated Cs-oleate solution was fast injected. The solution was then quickly cooled in ice-cold water. The temperature was then raised to 170°C while being in nitrogen environment, and 0.45 mL of pre-heated Cs-oleate solution was quickly injected. The solution was then quickly cooled in ice-cold water.

2.9.16. Synthesis of lead free $Cs_3Cu_2I_5$ NCs in LAMe DES medium

Synthesis of Cs-precursor in LAMe

65 mg of CsCO3 salt was added to 1 ml of LAMe along with 0.2 ml of OA and stirred under nitrogen atmosphere at 80 °C. After fully solubilizing, a clear colourless solution is obtained which is kept at normal temperature and reheated before use.

Synthesis of $Cs_3Cu_2I_5$ NCs

29 mg of CuI salt was dissolved in 1ml LAMe in presence of 300 µL OAmI at 80 °C under high vacuum for 1 hour. After this the reaction temperature is reduced to room temperature and 1 ml of heated cesium precursor was added to this mixture under nitrogen atmosphere. Immediately the white $Cs_3Cu_2I_5$ NCs were precipitated, and reaction mixture was quenched in a ice bath to restrict further growth. The NCs were then centrifuged to discard the DES medium and washed with methyl acetate. The purified NCs were then redispersed in toluene medium and used for further studies.

2.10. Photoluminescence quantum yield (PLQY) measurement

PLQY of the NC suspensions were measured using reference method by using the following formula,

$$QY(sample) = QY(ref) \times \frac{I_{sample}}{I_{ref}} \times \frac{A_{ref}}{A_{sample}} \times \left(\frac{\eta_{sample}}{\eta_{ref}}\right)^2 \qquad (2.27)$$

In the above equation, I_{sample} is the integrated area under the PL spectrum of the sample, I_{ref} is the integrated area under the PL spectrum of the reference solution, A_{ref} is the absorbance of the refence solution at the PL excitation wavelength, A_{sample} is the absorbance of the sample at the sample wavelength and η_{sample} & η_{ref} are the refractive index of the sample and reference, respectively.

The reference dye solutions used for PLQY measurements for different NCs are tabulated in table 2.1.

Table 2.1. Dye solutions used for PLQY measurements for different NCs.

NCs	Dye (solvent)	QY (ref)
MPBI, MPI	Rhodamine B (ethanol)	96%
MPBr, CPB-2D	Coumarin-1 (ethanol)	73%
MPBBr, MPBKBr, $MAPbBr_3$, $CsPbBr_3$ (CPB)	Coumarin 152 (CAN)	19%
$Cs_3Cu_2I_5$	Quinine sulphate (0.05 M H_2SO_4 solution)	56.4%

References:

1. Bollinger, L.; Thomas, G. E., Measurement of the time dependence of scintillation intensity by a delayed-coincidence method. *Review of Scientific Instruments* **1961,** *32* (9), 1044-1050.
2. O'Connor, D., *Time-correlated single photon counting*. Academic Press, London, **1984**.
3. Lakowicz, J. R., *Topics in fluorescence spectroscopy: volume 1: Techniques*. Springer US: Boston, **2002**.
4. Becker, W., *Advanced time-correlated single photon counting techniques*. Springer Berlin Heidelberg: Berlin, Heidelberg, **2005**; Vol. 81.
5. Becker, W., Introduction to Multi-dimensional TCSPC. In *Advanced Time-Correlated Single Photon Counting Applications*, Springer, Switzerland, **2015**; pp 1-63.
6. Albrecht, C., Joseph R. Lakowicz: Principles of fluorescence spectroscopy. Springer US: Boston, MA: **2008**.
7. Lakowicz, J. R., *Principles of fluorescence spectroscopy*. Springer US: Boston, MA: **2006**.
8. Easter, J. H.; DeToma, R. P.; Brand, L., Nanosecond time-resolved emission spectroscopy of a fluorescence probe adsorbed to L-alpha-egg lecithin vesicles. *Biophysical journal* **1976,** *16* (6), 571-583.
9. Maroncelli, M.; Fleming, G. R., Picosecond solvation dynamics of coumarin 153: The importance of molecular aspects of solvation. *The Journal of chemical physics* **1987,** *86* (11), 6221-6239.
10. Underwood, D. F.; Blank, D. A., Ultrafast solvation dynamics: A view from the solvent's perspective using a novel resonant-pump, nonresonant-probe technique. *The Journal of Physical Chemistry A* **2003,** *107* (7), 956-961.
11. Fleming, G. R.; Gijzeman, O. L.; Freed, K. F.; Lin, S. H., Theory for time resolved emission spectra. *Journal of the Chemical Society, Faraday Transactions 2: Molecular and Chemical Physics* **1975,** *71*, 773-780.

12. Brearley, A. M.; Strandjord, A. J.; Flom, S. R.; Barbara, P. F., Picosecond time-resolved emission spectra: techniques and examples. *Chemical physics letters* **1985,** *113* (1), 43-48.
13. Rulliere, C., *Femtosecond laser pulses*. Springer New York: New York, NY, **2005**.
14. Gandolfi, M. T.; Moggi, L., Photochemical techniques. In *The Exploration of Supramolecular Systems and Nanostructures by Photochemical Techniques*, Springer Netherlands: Dordrecht, 2012; pp 67-95.
15. Ruckebusch, C.; Sliwa, M.; Pernot, P. d.; De Juan, A.; Tauler, R., Comprehensive data analysis of femtosecond transient absorption spectra: A review. *Journal of Photochemistry and Photobiology C: Photochemistry Reviews* **2012,** *13* (1), 1-27.
16. Berera, R.; van Grondelle, R.; Kennis, J., Ultrafast transient absorption spectroscopy: principles and application to photosynthetic systems. *Photosynthesis research* **2009,** *101* (2), 105-118.
17. Carter, C. B.; Williams, D. B., *Transmission electron microscopy: Diffraction, imaging, and spectrometry*. Springer New York: New York, NY: **2016**.
18. Hayat, M., *Basic techniques for transmission electron microscopy*. Elsevier, Netherlands: **2012**.
19. Zuo, J. M.; Spence, J. C., *Advanced transmission electron microscopy*. Springer New York: New York, NY: **2017**.
20. Reimer, L., *Transmission electron microscopy: physics of image formation and microanalysis*. Springer New York: New York, NY: **2013**; Vol. 36.
21. Buseck, P.; Epelboin, Y.; Rimsky, A., Signal processing of high-resolution transmission electron microscope images using Fourier transforms. *Acta Crystallographica Section A: Foundations of Crystallography* **1988,** *44* (6), 975-986.
22. Champness, P. E., *Electron diffraction in the transmission electron microscope*. Garland Science: 2020.

23. Jauncey, G., The scattering of x-rays and Bragg's law. *Proceedings of the national academy of sciences* **1924,** *10* (2), 57-60.
24. Holder, C. F.; Schaak, R. E., Tutorial on powder X-ray diffraction for characterizing nanoscale materials. ACS Publications: **2019**; Vol. 13, pp 7359-7365.
25. Swanson, H. E., *Standard X-ray diffraction powder patterns*. US Department of Commerce, National Bureau of Standards: **1970**.
26. Van der Heide, P., *X-ray photoelectron spectroscopy: an introduction to principles and practices*. John Wiley & Sons, Hoboken, New Jersey, U.S.: **2011**.
27. Watts, J. F., X-ray photoelectron spectroscopy. *Surface science techniques* **1994,** *45*, 5.
28. Dutta, A.; Behera, R. K.; Pal, P.; Baitalik, S.; Pradhan, N., Frontispiece: Near-Unity Photoluminescence Quantum Efficiency for All CsPbX3 (X=Cl, Br, and I) Perovskite Nanocrystals: A Generic Synthesis Approach. *Angewandte Chemie International Edition* **2019,** *58* (17).
29. Protesescu, L.; Yakunin, S.; Bodnarchuk, M. I.; Krieg, F.; Caputo, R.; Hendon, C. H.; Yang, R. X.; Walsh, A.; Kovalenko, M. V., Nanocrystals of Cesium Lead Halide Perovskites (CsPbX3, X = Cl, Br, and I): Novel Optoelectronic Materials Showing Bright Emission with Wide Color Gamut. *Nano Letters* **2015,** *15* (6), 3692-3696.

This page is intentionally left blank

Chapter-3

Reversible Ultra-Slow Crystal Growth of Mixed Lead Bismuth Perovskite Nanocrystal – Presence of Dynamic Capping

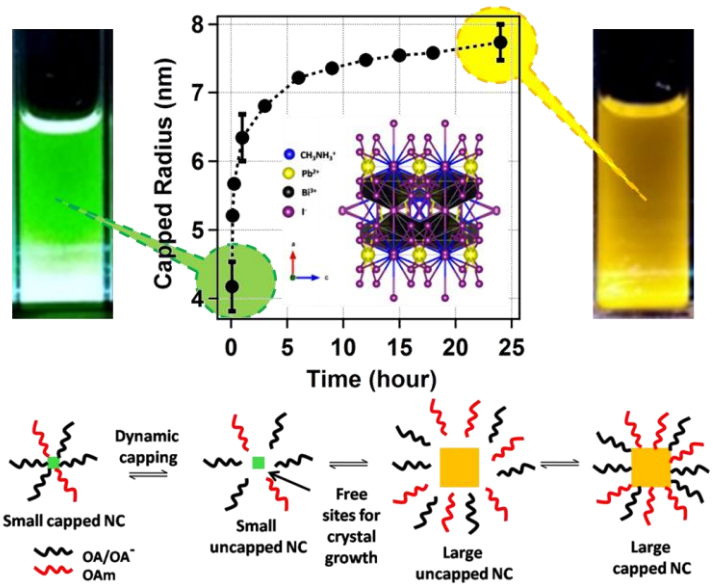

Chem. Eur. J. **2020**, *26*, 1506 –1510.

An ultra-slow crystal growth over a period of 24 hrs of a newly synthesized $CH_3NH_3Pb_{1/2}Bi_{1/3}I_3$ *perovskite (MPBI) nanocrystal in non-polar toluene medium is reported here. From several spectroscopic techniques as well as from TEM analysis we found that the size of nanocrystals changes continuously with time, in spite of being capped by the ligands. Using single molecular spectroscopic technique, we also found that this size change is not due to the stacking of nanocrystals but due to the crystal growth. The notable temperature dependence and reversible nature of nanocrystal growth is explained by the dynamic nature of the capping. The observed temperature-dependent ultra-slow growth is believed to be a pragmatic step towards controlling the size of perovskite NC in a systematic manner.*

3.1. Introduction

Organic-inorganic hybrid perovskite materials of ABX_3 type with A as organic cation, B as inorganic cation and X as halide ions rendered appreciable interest to the scientific community due to their unique properties suitable for the construction of photovoltaic cell with very high efficiency.[1-3] The nanocrystalline form of such perovskite materials showed a large fluorescence quantum yield with better photo stability and considered to be a good replacement of the traditional chromophores.[4] The compositional tuning of such nanocrystal (NC) provides a well-tuned emission characteristics of the material that makes it a potential candidate in the field of optoelectronics such as laser, nonlinear optics and light emitting diodes.[5, 6] Until now most of the reported perovskite NCs are lead (Pb) based with high emission quantum yield.[7] Keeping in mind the toxic nature of lead, it is desired to develop perovskite NCs with lower Pb content without compromising its interesting properties. Further, these Pb-based NCs exhibit poor moisture resistance, making these extremely vulnerable in the ambient condition.[8] Recently scientists have started to explore Pb-free perovskites with various cations at the B-site.[9] Among these, bismuth (Bi) based perovskites provide a better stability in the ambient condition, which is very much required for the application of these materials.[10] However, these Bi based perovskite NCs exhibit very low quantum yield.[11] So it is the primary concern to search for a system with high quantum yield without compromising the stability as much as possible. Keeping this in mind, we have synthesized organic-inorganic hybrid iodide perovskite NCs with appropriate ratio of Pb^{2+} and Bi^{3+} in order to maintain the formal charge balance i.e. (+2) in the B-site of these perovskites. Properties of Bi doped Pb halide NCs have been explored recently by some research groups.[12, 13] In our previous study we have also reported the potential of these charge balanced hybrid Pb-Bi perovskite thin films for solar cell application.[14]

Capping of NCs with long chain organic moieties is a key step for size control synthesis of the NCs as without capping the NCs stability is being compromised due

to the formation of non-fluorescent bulk perovskite materials.[15] Thus, capping is one of the most efficient ways to enhance the colloidal stability of perovskite NCs in the solution[16-18] Oleic acid (OA) and oleylamine (OAm) are popular capping agents reported in the literature for the synthesis of such perovskite NCs.[15, 16, 18, 19] OA has the less capping ability than OAm, but any of these two alone cannot provide a sufficient stability to Pb perovskite NCs because of their poor binding NC surface.[19] However, when these two ligands are used together, they form the oleate anion and olylammonium cation which are much more efficient as capping agents due to strong interaction with the surface of the NCs. [15, 19] For size and shape tunable synthesis of perovskite NCs, the proportion and the amount of OA and OAm play a crucial role. Akin to most of the nano-materials, the properties of perovskite NCs depend highly on their size and shape.[16] With the increase in the size of NCs the emission maximum shifts towards the lower energy, which can be controlled by the capping agents. Under a controlled condition, the spectral properties do not show any time dependence in most of the cases, rendering the formation of a stable NC.[5, 6, 15, 16] Interestingly in one report, Seth et al. have demonstrated the time-dependent shift of the emission maxima for $CsPbBr_3$ and $CsPbBr_2I$ perovskite NC suspensions under continuous light irradiation.[20] To explain this phenomenon, the authors hypothesized a change in average size of the NCs, though a detailed mechanism has not been put forward. Recently, Li et al. have reported a slow crystal growth of $CH_3NH_3PbBr_3$ perovskite NC on oil-water interface.[21] Kostopoulou et al. very recently reported a slow growth of $CsPbBr_3$ nanowire in toluene and a side-to-side coalescence of the nanocrystals is proposed as the mechanism.[22] However, to the best of our knowledge, such a slow crystal growth in normal antisolvent for hybrid perovskite NC is not observed yet.

In the present study, we have developed moderately moisture-stable NC having both Pb and Bi at the B-site of the ABX_3 structure with chemical composition $MAPb_{0.5}Bi_{0.33}I_3$ (MPBI). These NCs have shown greater stability compared to pure Pb-based perovskite NCs. We have performed X-ray diffraction (XRD) to find out

the crystalline nature, X-ray photoelectron spectroscopy (XPS) to verify the relative proportion of the individual components, and optical and microscopic characterizations. Furthermore, we have observed a time-dependent emission phenomenon in toluene, which has been explained in terms of dynamic capping-mediated crystal growth. To support our proposition, we have also carried out the temperature-dependent study to confirm the reversible nature of the dynamic capping process.

3.2. Characterization

3.2.1. Powder X-Ray Diffraction Study

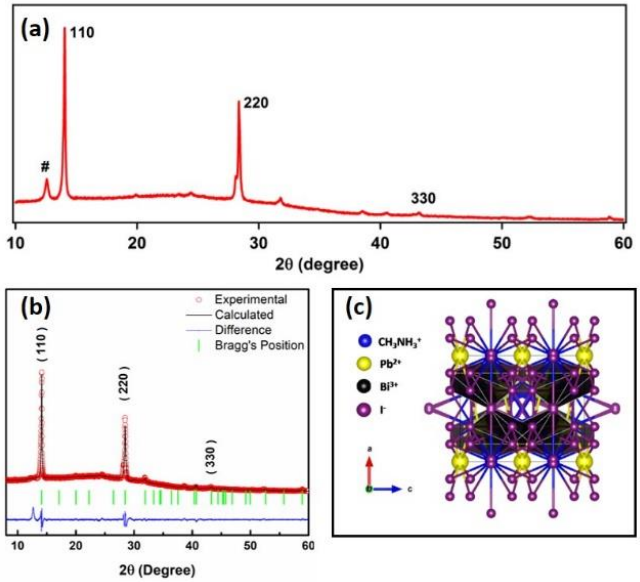

Figure 3.1. (a) Powder XRD raw data. The extra peak at 12.5º (#) came from partial degradation of MPBI to PbI_2. (b) Refined XRD data with Le-bail Analysis (c) Crystal model of MPBI.

MPBI NCs have been synthesized through single step reaction by ligand assisted method.[16] The detailed synthesis process is given in section 2.9.1 to section 2.9.4 of chapter-2 of this thesis. The crystal structure of as-synthesized MPBI NCs has been determined by corrected XRD, which have been fitted using Le-Bail method with constant scale factor in order to determine the lattice parameter and the space group

(see figure 1a). It is evident that MPBI NCs have crystallized in phase pure tetragonal structure. The fitted data has been found to be consistent with tetragonal crystal symmetry with I4/mcm space group as shown schematically in figure 1b. Refined structural parameters of MPBI composition obtained by Le-Bail refinement of XRD data are as follows; a=b=8.86Å; c=10.353Å.

3.2.2. X-ray Photoelectron Spectroscopic (XPS) Studies

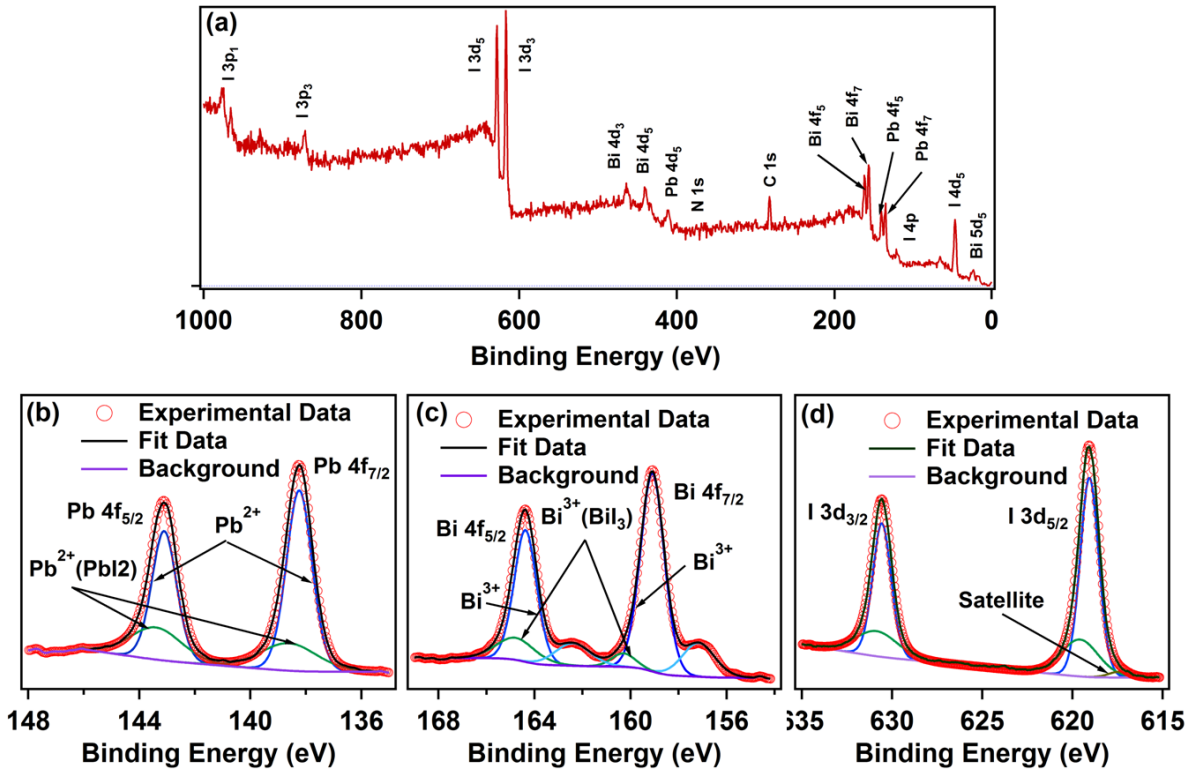

Figure 3.2. XPS data of MPBI NC. (a) Overall XPS data of MPBI NC. (b) XPS data of lead, (c) XPS data of bismuth, (d) XPS data of iodine.

XPS studies were performed to investigate the elemental composition of MPBI. The XPS spectrum was calibrated with respect to adventitious carbon binding energy at 284.8 eV. The XPS survey scan as shown in figure 3.2a, showed binding energy peaks at around 140 eV, 160 eV, 284 eV, 402 eV, and 625 eV which correspond to the photoelectron peaks of Pb 4f, Bi 4f, C 1s, N 1s and I 3d respectively.[23, 24] However, no signature of O 1s binding energy peak observed at around 530 eV,

unlike previous reports. Doublet peaks of Pb 4f, Bi 4f, and I 3d were observed as a result of their spin-orbit coupling. Moreover, we recorded high-resolution XPS spectra of all the constituents at around the above-mentioned binding energy. Concerned peaks in the high-resolution XPS spectra were fitted with the Lorentzian-Gaussian functions. The estimated binding energy of the concerned peaks with the corresponding area under the curves is presented in Table 3.1. All the estimated binding energy values of respective constituents of MPBI were found to be in good agreement with the previously reported literature. The Pb 6p valance shell electrons contribute to Pb–I framework to construct PbI_6^{4-} octahedral; whereas Bi 6p valance orbital electrons construct BiI_6^{3-} octahedra within the perovskite lattice. The Pb 4f spectrum exhibited doublet peaks at 138.24 eV and 143.1 eV which correspond to the spin-orbit splitting of the Pb $4f_{7/2}$ and $4f_{5/2}$ respectively. Broad FWHM in the Pb 4f spectrum allowed us to the fit two additional peaks around 138.62 eV and 143.4 eV which were attributed to the PbI_2 component. Bi 4f spectrum demonstrated doublet peaks at 159.09 eV and 164.38 eV which suggests Bi $4f_{7/2}$ and Bi $4f_{5/2}$ respectively. The deconvolution of Bi 4f peaks suggests the presence small amount of BiI_3 as well as metallic bismuth. The estimated binding energy peaks of Bi $4f_{7/2}$ and Bi $4f_{5/2}$ in BiI_3 are at 160.31 eV and 165.4 eV. Whereas the binding energies i.e., 157.16 eV and 162.43 eV represent the presence of metallic bismuth which suggests the reduction of some of the BiI_6^{3-} during the annealing process. The small amount of that PbI_2 and BiI_3 may have come from the unreacted residue of the perovskite NC solution. Small amount of degradation during annealing of the drop casted thin film of MPBI at the ambient atmosphere is expected to contribute to the fact that XPS spectra bear the signature of PbI_2, BiI_3, and metallic Bi. Figure 3.1a illustrates the presence of PbI_2 peak in our MPBI XRD pattern. Apparently, the absence of BiI_3 suggests that it is only present in a tiny amount which is lower than the detection limit of our XRD instrument. We anticipate that there are two reasons for the absence of metallic bismuth in the MPBI XRD pattern; apart from the presence in an undetectable amount, the amorphous nature of metallic bismuth may be the cause of

its absence in the MPBI XRD pattern. XPS spectrum of I 3d depicts two intense peaks at 619.05 eV and 630.56 eV which correspond to doublets $3d_{5/2}$ and $3d_{3/2}$ respectively. The shift to the higher binding energy of 619.58eV and 630.86 eV is associated with the iodide of both lead and bismuth. The binding energy 617.43 eV represents a satellite peak of I $3d_{5/2}$.

Table 3.1. Binding energy, FWHM, and area percentages from the deconvolution of XPS spectra of Pb 4f, Bi 4f, and I 3d in MPBI composition.

Elements	Spectral Region	Binding Energy (eV)	FWHM	Area %
Pb 4f	Pb^{2+} $4f_{7/2}$	138.24	1.09	42.06
	Pb^{2+} $4f_{7/2}$	138.62	2.37	13.92
	Pb^{2+} $4f_{5/2}$	143.10	1.05	29.03
	Pb^{2+} $4f_{5/2}$	143.40	2.18	14.99
Bi 4f	Bi $4f_{7/2}$	157.16	1.51	9.48
	Bi^{3+} $4f_{7/2}$	159.09	1.17	44.53
	Bi^{3+} $4f_{7/2}$	160.31	1.10	2.68
	Bi $4f_{5/2}$	162.43	1.76	7.60
	Bi^{3+} $4f_{5/2}$	164.38	1.15	32.49
	Bi^{3+} $4f_{5/2}$	165.40	1.48	3.22
I 3d	I^- $3d_{5/2}$satellite	617.43	1.34	1.30
	I^- $3d_{5/2}$	619.05	1.22	42.64
	I^- $3d_{5/2}$	619.58	2.42	15.67
	I^- $3d_{3/2}$	630.56	1.21	28.20
	I^- $3d_{3/2}$	630.86	2.77	12.19

3.3. Time-Dependent Optical Studies of MPBI NCs

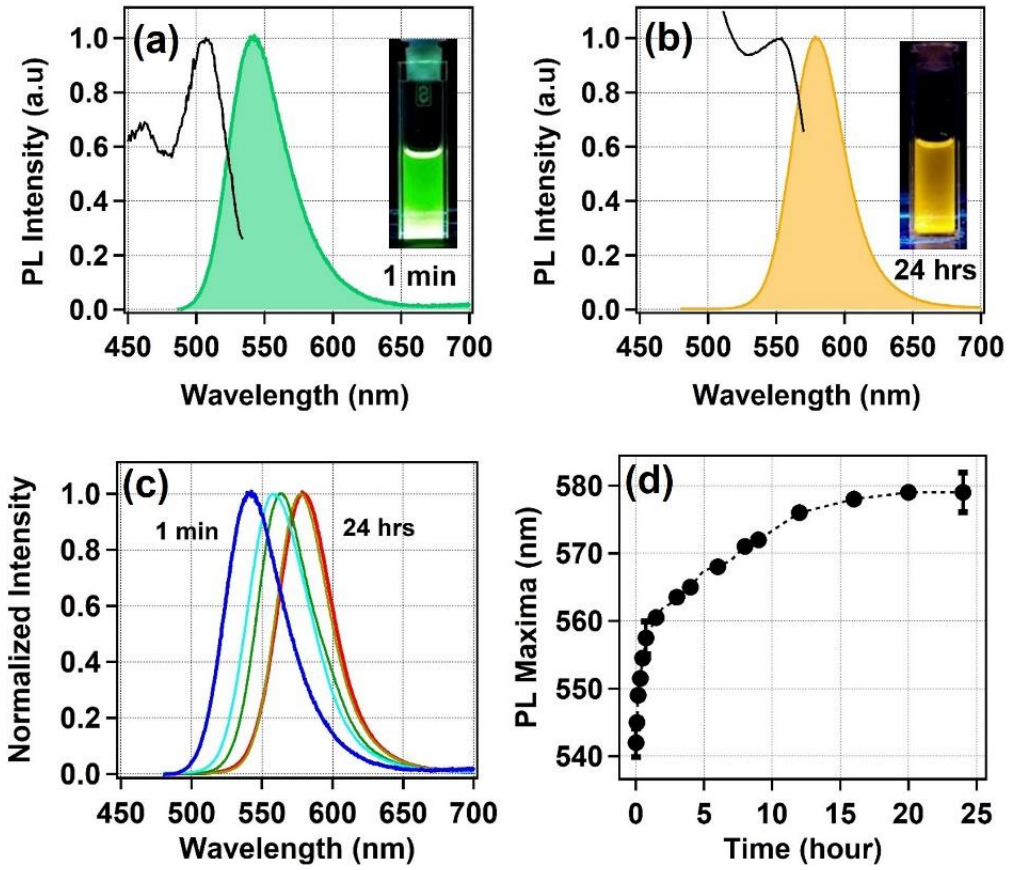

Figure 3.3. Time-dependent change in PL of MPBI NCs. (a) PL spectra of MPBI NCs immediately after preparation (1 min) and corresponding excitation spectra. In the inset, the corresponding optical image of MPBI NC suspension under 365 nm UV light is shown. (b) PL spectra of MPBI NCs after 24 h of its preparation and corresponding excitation spectra. In the inset, the corresponding optical image of MPBI NC suspension under 365 nm UV light is shown. (c) Time evolution of PL spectra of MPBI NCs from 1 min to 24 hours. (d) Gradual change in PL maxima with time of MPBI NCs. All the experiments were done at 25ºC.

MPBI NC suspension has shown a broad absorption spectrum and a strong yellow-green emission. The interesting feature of this study is the time-dependent variation in the PL spectrum, where one can see a huge redshift of 37 nm from the time zero spectrum ($\lambda_{em\text{-}max}$=542 nm at 25ºC). The MPBI NCs just after preparation show strong green PL centered at 542 nm (figure 3.3a) which evolves with time and

reaches 579 nm after 24 hours (figure 3.3b). The time evolution of PL spectra and PL maxima is represented in figure 3.3c and figure 3.3d respectively.

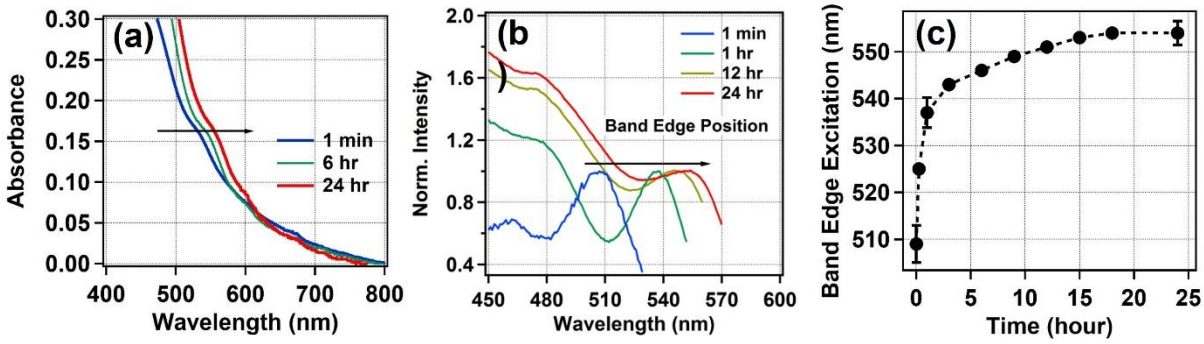

Figure 3.4. (a) Time-dependent change in absorption spectra of MPBI NCs. (b) Time-dependent change in excitation spectra of MPBI NCs. (Collected at corresponding PL maxima). (c) Gradual change in band edge position with progress in time.

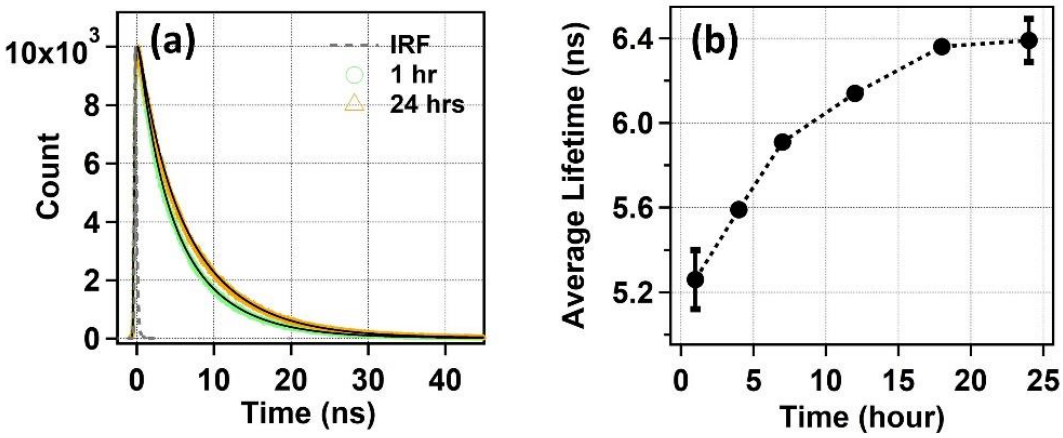

Figure 3.5. Time dependent change in lifetime of MPBI NCs. (a) PL transient of MPBI NCs after 1 hr and 24 hrs of preparation. (b) Gradual change in average lifetime of MPBI NCs from 1 hr to 24 hr.

The corresponding band edge is determined from the excitation spectra instead of absorption spectra because the absorption is very broad for such system (figure 3.4.a). The time dependent excitation spectra also portray a clear red shift of band edge position (see figure 3.4.b and figure 3.4.c). The red shift of the band edge as well as PL maxima may originate from the change in the size of the NC in the given time period. If so, this can be well explained by the quantum confinement.[25] In the

strong quantum confinement regime, i.e., when the size of the quantum dot is smaller than its excitonic Bohr radius then the effect of the size to the energy or band gap is much more pronounced.[25] In the strong confinement regime, a small increment in size attributes appreciably and results in a huge red shift in the emission maxima.

The lifetime is found to be 5.3 ns at 1 hr, which becomes 6.4 ns at 24 hrs and remain unaltered hence forth. Here, to note that it has not been possible to measure the excited state life-time of the nanocrystal at earlier time after its preparation, as the measurement of life-time takes about 20 mins. The general perception on the photophysical characteristics of metal/semiconductor nano-system is that the larger nanoparticles exhibit longer lifetime.[16, 26] The reason for this is not clear to us though. Nevertheless, in a similar line, we propose that the increase in the average lifetime is due to the increase in size of the MPBI NC with time. Fluorescence transients show a bi-exponential behaviour with components of 2.6 and ~7.0 ns for all the cases and interestingly, the contribution of the fast component decreases as a function of time until 24 h (see Table 3.2). The fast component is assigned to the bound exciton recombination process, which is formed immediately after the photoexcitation.[26] The longer component is attributed to trap-assisted recombination process.[27, 28] It has been found that, the contribution of the slow component increases (62 % at 1 h to 76 % at 24 h) as the NCs size increases with time.

Table 3.2. Lifetime component analysis of MPBI NC suspension at different time

Time of taking decay traces	Emission Maxima (nm)	a_1	τ_1 (ns)	a_2	τ_2 (ns)	τ_{av} (ns)
t = 1 hr	558	0.38	2.6	0.62	6.9	5.3
t = 4 hr	565	0.34	2.6	0.66	7.1	5.6
t = 7 hr	570	0.29	2.6	0.71	7.3	5.9
t = 12 hr	575	0.27	2.6	0.73	7.5	6.2
t = 24 hr	578	0.24	2.6	0.76	7.6	6.4

To quantify the time-dependent growth of the MPBI NCs, we have further carried out fluorescence correlation spectroscopic (FCS) measurements. FCS is a very sensitive technique based on the temporal fluctuation of fluorescence intensity in a very small observation volume and provides a diffusion timescale of the emissive species. Mathematically, we get the diffusion timescale after fitting the autocorrelation curve, generated in the FCS experiments, with a single diffusion component equation. Then using the Stokes–Einstein relationship, the size of the species can be calculated. The details of the experimental procedure, instrumentation and data fitting can be found in the section 2.4 of chapter-2. The single component fitting suggests narrow distribution of NC sizes (see figure 2g) and the calculated value of the radius of the NC is shown in Figure 2 h. It is to be noted that in this case the measured size of the NC is actually the size of the capped NC as the diffusion of the NC is accompanied by its capping agents. The capped radius value is found to increase from 4.2 nm at 1 min to 7.7 nm at 24 h.

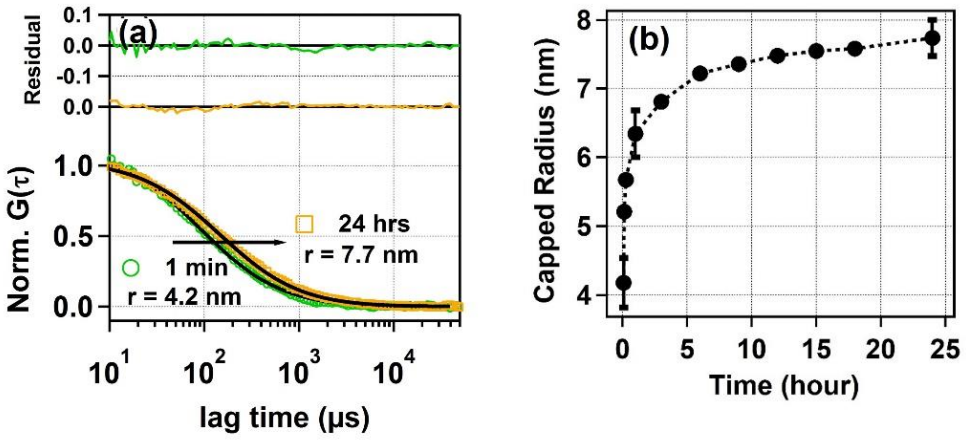

Figure 3.6. (a) FCS data of MPBI NCs immediately after preparation (1 min, green circles) and after 24 h (yellow squares) along with best-fit (black solid lines). (b) The change in capped radius value with time.

The trend of the increase in size is found to correlate well with the shift in excitation band edge, emission maxima, and average lifetime (figure 3.7). This clearly indicates that the size modulation is the reason behind the observed change in the

steady-state and time-resolved emission measurements. It suggests that the whole process is underway under the whole process is under quantum confinement regime.[25] A strong quantum confinement regime indicates that the NC size is smaller than Bohr excitonic diameter.[25]

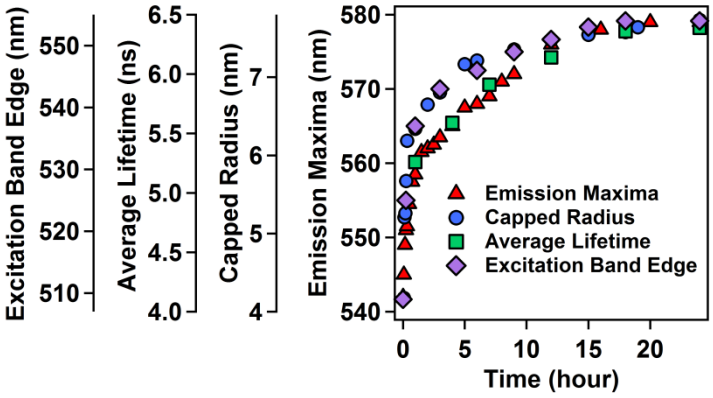

Figure 3.7. Comparison of the change in excitation band edge, emission maxima and average lifetime with capped radius at 25ºC.

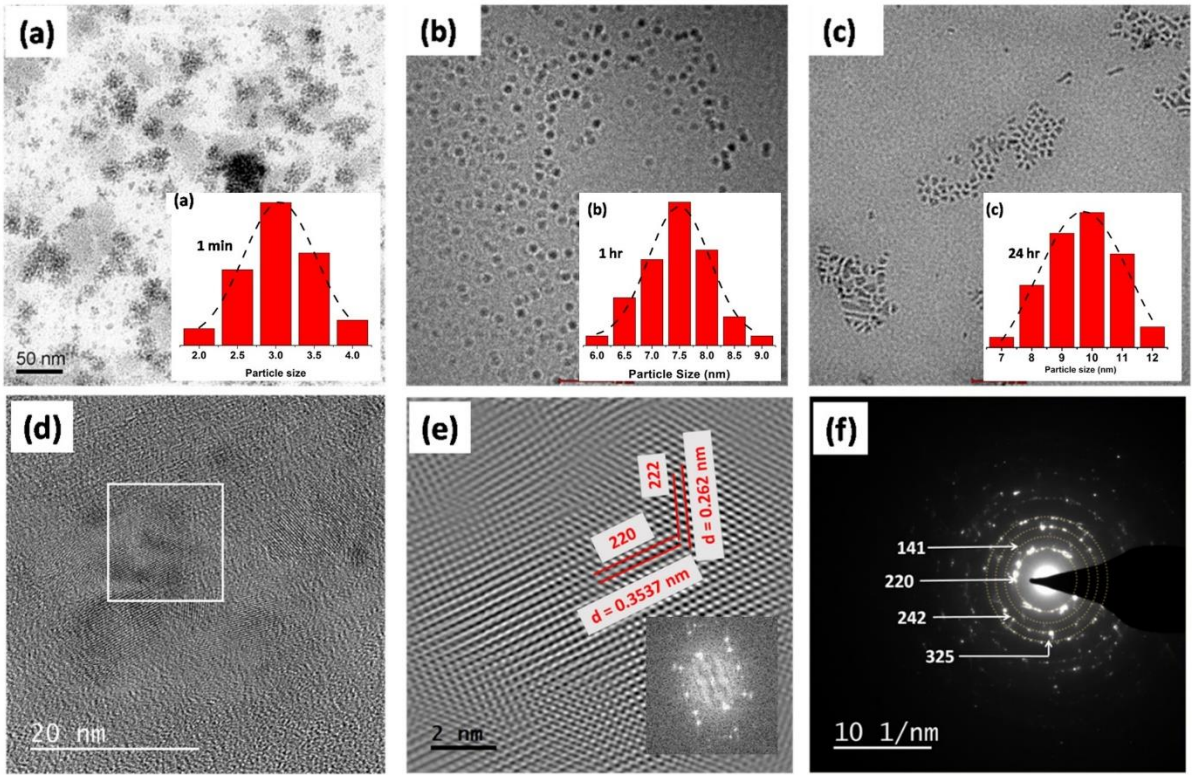

Figure 3.8. TEM images of MPBI NCs in toluene suspension (a) after 1 min of preparation, (b) after 1 h, and (c) after 24 h. (d) HRTEM image of MPBI NCs after 24 h. (e) Fourier filtered

image of the selected area from Figure 3 d. The inset shows the FFT of the selected area. (f) Diffraction pattern of the MPBI NCs showing pure tetragonal crystal phase.

To confirm the measured size of the NC by the FCS method, we have taken the TEM images (figure 3.8). Immediately after synthesis (1 min), after 1 h, and after 24 h, the diameters of the NCs are found to be 3, 7.5, and 9.5 nm, respectively (see figure 3.8a, figure 3.8b, and figure 3.8c, respectively), which corroborates quite well with the measured value through FCS, after considering the size of the capping agents. The almost spherical to somewhat irregular shapes of NCs in the TEM images also confirm the absence of any rod-shaped NCs, which can also induce a redshift to the emission maximum.

From the HRTEM image of MPBI NCs after 24 h (figure 3.8d), the crystal planes can be seen clearly. Figure 3.8e shows the Fourier filter image of the selected area from Figure 3.8d. As marked in the lattice image, two types of planes, (220) and (222) with d-spacing of 0.354 and 0.262 nm, respectively, are observed. From this high-resolution imaging, we confirmed that the increase in the size of the NCs is not due to agglomeration, but due to crystal growth. Figure 3.8f represents the diffraction pattern, which confirms the tetragonal crystal structure.

3.4. Comparison of growth kinetics of MPBI NCs with MPI NCs

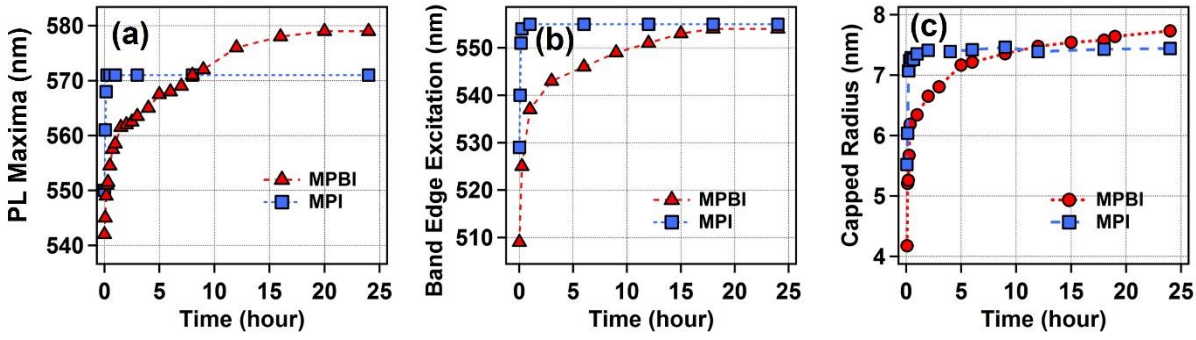

Figure 3.9. Comparison of growth kinetics of MPBI NCs and MPI NCs. (a) Time-dependent change in PL maxima after preparation of MPBI NCs (red) and MPI NCs (blue). (b) Time-dependent change in band edge excitation after preparation of MPBI NCs (red) and MPI NCs

(blue). (c) Time-dependent change in capped radius after preparation of MPBI NCs (red) and MPI NCs (blue).

To compare the growth kinetics of MPBI NCs with MPI NCs we monitored shift in PL maxima, shift in band edge excitation maxima, as well as time-dependent FCS measurement of MPI NCs. The FCS measurements render a very fast increment in capped radius from 5.5 to 7.3 nm within an hour and remain the same thereafter. So, for pure MPI NCs, the growth kinetics is way faster than MPBI NCs.

3.5. Proposed reason for crystal growth: Dynamic Capping

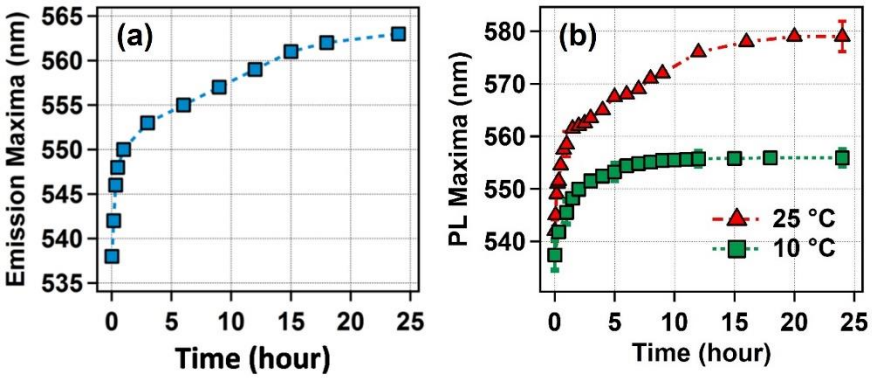

Figure 3.10. (a) Time-dependent change in PL maxima after preparation of MPBI NCs (MPBI NCs are prepared using 300 µL of OA and 250 µL of OAm. (b) Time-dependent change in PL maxima of MPBI NCs at 25ºC (red) and at 10ºC (green).

From all these investigations, we conclude that the size of the NC changes continuously with time and this increase in size originates through the crystal growth of individual NCs and not through the agglomeration of NCs. This is to note that the FCS studies are done in the nanomolar concentration and the possibility of agglomeration can be ruled out at this low concentration regime, which supports the HRTEM data. It is interesting to note here that even though the NCs are capped with OA and OAm, we could see continuous growth. In most of the cases of perovskite NCs the emission maximum was found to be unaltered with time, although the intensity generally decreases due to their stability issues.[10] The reason for the

observed crystal growth may be explained by the improper capping of the NCs. It is plausible that if a sufficient amount of OA and OAm are not available to cap every individual NC then some of the NCs may have bare sites.

To check this possibility, we have prepared the MPBI NCs using excess amounts of both OA and OAm, and also found a time-dependent redshift of the emission (figure 3.10a). However, in this case, the extent of the shift is found to be smaller. This controlled experiment also proves that the observed shift in emission maxima is not the mere consequence of improper capping. Another reason for having a bare site on the NC surface even after proper capping is the dynamic nature of the capping, that is, the capping agents are in equilibrium between the free and capped state. Understandably, such an equilibrium should be affected by the temperature. If the dynamic capping is the reason for the observed time-dependent change of the emission maximum of MPBI NCs, a decrease in the temperature should minimize the observed redshift with time. We have observed exactly the same as shown in figure 3.10b. The observed red shift in the emission maximum after 24 h has been found to be 19 nm at 10 °C, compared to what has been 37 nm at 25 °C. Moreover, the proposition of dynamic capping, that is, the existence of an equilibrium between the bound and free states of the capped agents, also suggests that even at the stable state of the NCs (e.g. after 24 h), a change in the temperature should also change the emission maximum of the NCs.

From figure 3.11, we can see that emission maxima of MPBI NCs exhibit high temperature dependence (553.5 nm at 5 °C to 581.2 nm at 30 °C) even after 24 h of its synthesis. The reversibility in temperature dependence also validates the presence of the equilibrium. FCS measurement also shows a decrease in size by lowering the temperature, which is reversible in nature (see figure 3.11c,d). This further proves that at a particular temperature, a particular size of NC is favoured and that is reversible with respect to temperature. This reversibility in size with temperature is

achieved through the dynamic capping nature of the ligand system. The schematic of the proposed equilibrium is shown in scheme 3.1.

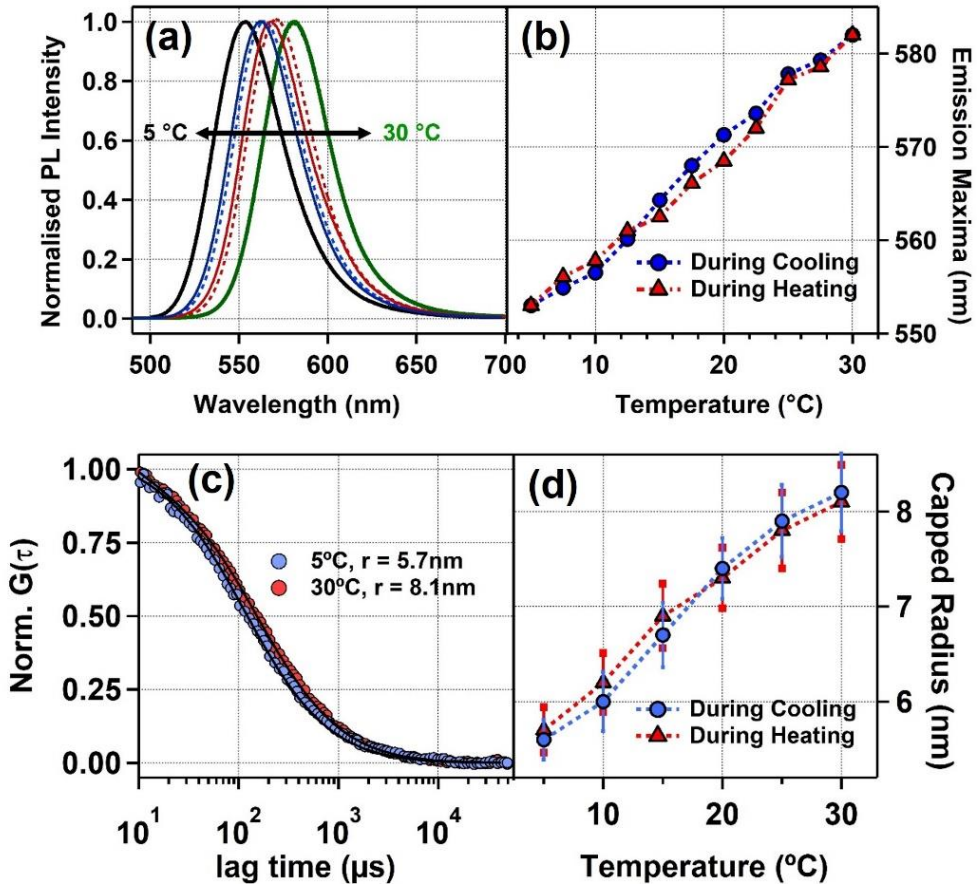

Figure 3.11. Temperature-dependent studies of MPBI NC after 24 hours from its preparation. (a) Reversible change of emission spectra with temperature. (b) The corresponding reversible change in emission maxima with temperature. (c) FCS data of MPBI NCs at 5 °C and at 30 °C. (d) Reversible change in capped radius with temperature.

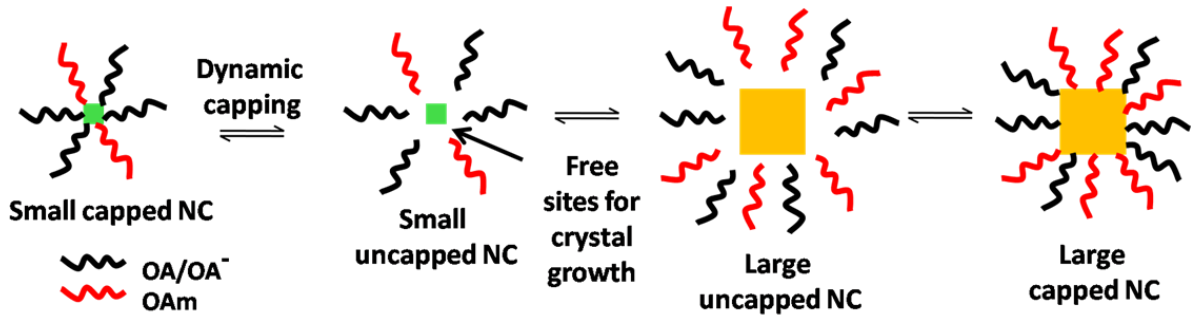

Scheme 3.1. Proposed mechanism of the crystal growth of MPBI NC in the toluene suspension mediated by dynamic capping.

3.6. Stability of MPBI NCs

Over a period of time a new peak at 12.5^{o} appears in the XRD pattern suggesting the formation of PbI_2, which is a marker of the degradation of MPBI NC (see figure 3.12). In spite of partial degradation, even on the 10th day, MPBI nanocrystal retains its tetragonal crystal structure.

The absorption spectra of the MPBI NC over the time is presented in figure 3.13a. It can be seen that with the progress in time, the absorbance in the band edge region is getting reduced, which also supports the partial degradation of MPBI. The spectrum of the 7th day show MPBI is still present in the medium but the amount is less.

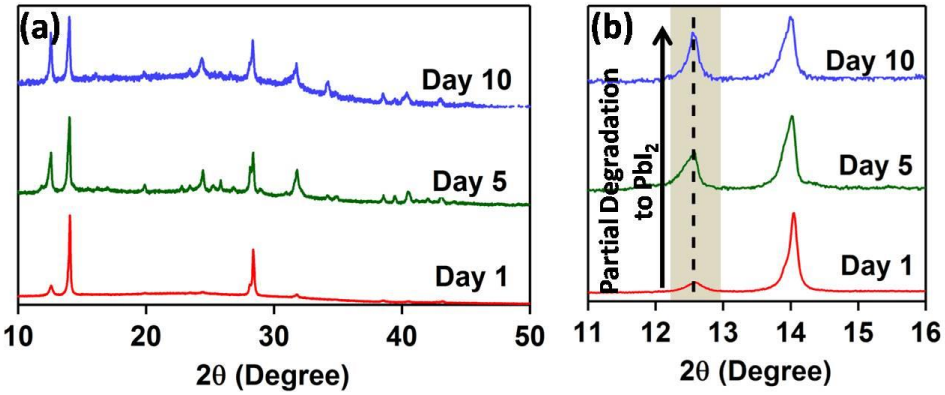

Figure 3.12. (a) PXRD data of MPBI NCs on day1, day5 and day10. (b) Relative increment of lead iodide peak, which indicates a partial degradation of the nanocrystal.

Interestingly, the emission quantum yield of MPBI NCs decreases continuously from day 1 (figure 3.12b). We propose that the decrease in quantum yield may be due to partial degradation of the nanocrystal along with the surface ligand desorption followed by the generation of surface trap states, which leads to the formation of observed non-emissive MPBI precipitate.

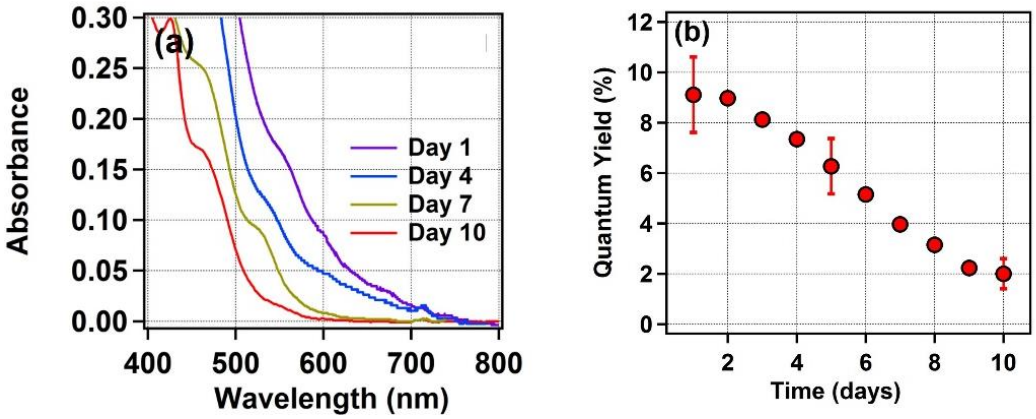

Figure 3.13. (a) Change in absorption spectrum of MPBI nanocrystals with progress in days. (b) Change in quantum yield of MPBI NC suspension in toluene with progress in days.

3.7. Correlation between estimated capped radius and actual average size of MPBI NCs at different time

In the suspension, NCs remains in capped form. Due to this in FCS technique we actually see the capped NCs passing through the observation volume. From the diffusion time constant we have measured the capped radius of the MPBI NC at different time. Now from literature the chain length of OA and OAm is about 2 nm.[29] So we should get approximately 4 nm extra size for capped NCs.

From the below table we can see that there is a difference in size of NCs calculated from the FCS measurements than TEM data even after considering the capping ligands. This contradiction can be answered if we consider the dynamic capping of the ligand molecules to the NC surface which is shown in the scheme 3.2. In the dynamic equilibrium some of the ligand molecules always remain detouched from the NCs surface and in the FCS measurement we actually see the NC movement along with capped and uncapped ligands, which eventually makes a size error. But any size change can be well understood by this technique.

Time	Size from TEM (nm)	Capped Diameter from FCS (nm)	Ligand length in both side (nm)	Extra size (nm)
t= 1 min	3.0	8.4	4	1.4
t= 1 hr	7.5	12.6	4	1.1
t= 24 hr	9.5	15.4	4	1.9

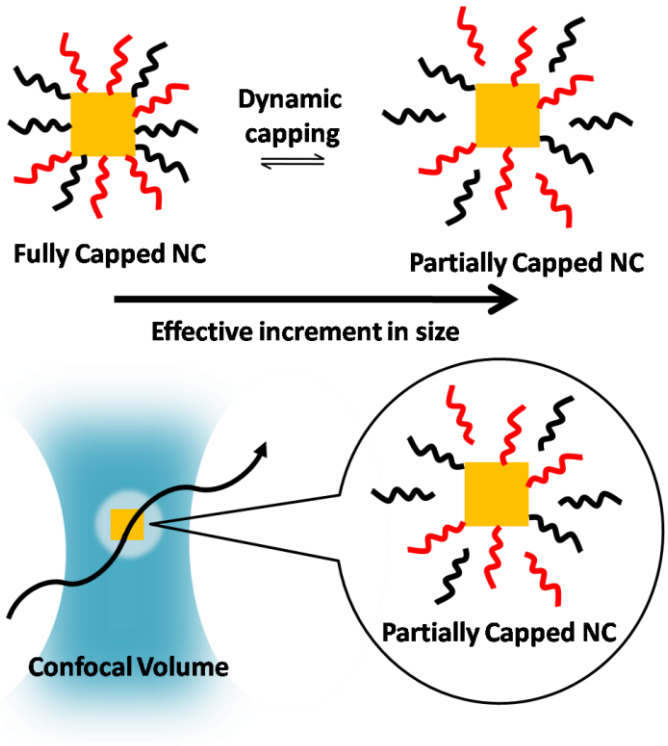

Scheme 3.2. Scheme of effective size increment of MPBI NC due to presence of dynamic capping.

3.8. Summary and Conclusions

In summary, we have synthesized a novel organic–inorganic hybrid lead-bismuth iodide perovskite NC, with charge balanced at the B-site of ABX_3 perovskite architecture, with a chemical composition of $CH_3NH_3Pb_{1/2}Bi_{1/3}I_3$ (MPBI). This NC

is found to be stable for more than 7 days under ambient conditions. MPBI NCs exhibit fairly strong emission characteristics with a maximum fluorescence quantum yield of 15 %, which depends on the condition. The MPBI NCs are found to undergo an ultra-slow crystal growth until 24 h of its preparation and size remains unaltered thereafter. Such an ultra-slow crystal growth of perovskite NCs is very rare and to the best of our knowledge this is the first report of hybrid perovskite NC growth in a normal anti-solvent medium. In addition, by controlling the temperature we can tune the extent of crystal growth. We believe that the present work is an important advancement towards controlling the perovskite NC size in a systematic manner. In future studies, we aim to arrest the crystal growth at any time point using external perturbation. We have also demonstrated that its spectral properties vary along with its size. Through the observed reversibility in the temperature-dependent emission and FCS measurement, the mechanism of the NC growth is explained in terms of dynamic capping. Just to emphasize here that in this report we have used FCS to measure the size of the NC for the very first time. MPBI NC is proposed to be a new category in the field of perovskite material, which can be a potential candidate for the replacement of pure lead-based perovskites.

References

1. Jeon, N. J.; Noh, J. H.; Yang, W. S.; Kim, Y. C.; Ryu, S.; Seo, J.; Seok, S. I., Compositional engineering of perovskite materials for high-performance solar cells. *Nature* **2015,** *517* (7535), 476-480.
2. Li, D.; Liao, P.; Shai, X.; Huang, W.; Liu, S.; Li, H.; Shen, Y.; Wang, M., Recent progress on stability issues of organic–inorganic hybrid lead perovskite-based solar cells. *RSC advances* **2016,** *6* (92), 89356-89366.
3. Fu, Q.; Tang, X.; Huang, B.; Hu, T.; Tan, L.; Chen, L.; Chen, Y., Recent progress on the long-term stability of perovskite solar cells. *Advanced Science* **2018,** *5* (5), 1700387.
4. Gao, M.; Zhang, C.; Lian, L.; Guo, J.; Xia, Y.; Pan, F.; Su, X.; Zhang, J.; Li, H.; Zhang, D., Controlled synthesis and photostability of blue emitting $Cs_3Bi_2Br_9$ perovskite nanocrystals by employing weak polar solvents at room temperature. *Journal of Materials Chemistry C* **2019,** *7* (12), 3688-3695.
5. Zhao, Y.; Zhu, K., Organic–inorganic hybrid lead halide perovskites for optoelectronic and electronic applications. *Chemical Society Reviews* **2016,** *45* (3), 655-689.
6. Fu, H., Colloidal metal halide perovskite nanocrystals: a promising juggernaut in photovoltaic applications. *Journal of Materials Chemistry A* **2019,** *7* (24), 14357-14379.
7. Shamsi, J.; Urban, A. S.; Imran, M.; De Trizio, L.; Manna, L., Metal halide perovskite nanocrystals: synthesis, post-synthesis modifications, and their optical properties. *Chemical reviews* **2019,** *119* (5), 3296-3348.
8. Dong, Y.; Zhao, Y.; Zhang, S.; Dai, Y.; Liu, L.; Li, Y.; Chen, Q., Recent advances toward practical use of halide perovskite nanocrystals. *Journal of Materials Chemistry A* **2018,** *6* (44), 21729-21746.
9. Sun, J.; Yang, J.; Lee, J. I.; Cho, J. H.; Kang, M. S., Lead-free perovskite nanocrystals for light-emitting devices. *The journal of physical chemistry letters* **2018,** *9* (7), 1573-1583.

10. Yang, B.; Chen, J.; Hong, F.; Mao, X.; Zheng, K.; Yang, S.; Li, Y.; Pullerits, T.; Deng, W.; Han, K., Lead-free, air-stable all-inorganic cesium bismuth halide perovskite nanocrystals. *Angewandte Chemie International Edition* **2017,** *56* (41), 12471-12475.
11. Leng, M.; Chen, Z.; Yang, Y.; Li, Z.; Zeng, K.; Li, K.; Niu, G.; He, Y.; Zhou, Q.; Tang, J., Lead-free, blue emitting bismuth halide perovskite quantum dots. *Angewandte Chemie International Edition* **2016,** *55* (48), 15012-15016.
12. Begum, R.; Parida, M. R.; Abdelhady, A. L.; Murali, B.; Alyami, N. M.; Ahmed, G. H.; Hedhili, M. N.; Bakr, O. M.; Mohammed, O. F., Engineering interfacial charge transfer in $CsPbBr_3$ perovskite nanocrystals by heterovalent doping. *Journal of the American Chemical Society* **2017,** *139* (2), 731-737.
13. Shao, H.; Bai, X.; Cui, H.; Pan, G.; Jing, P.; Qu, S.; Zhu, J.; Zhai, Y.; Dong, B.; Song, H., White light emission in Bi^{3+}/Mn^{2+} ion co-doped CsPbCl 3 perovskite nanocrystals. *Nanoscale* **2018,** *10* (3), 1023-1029.
14. Dey, P.; Khorwal, V.; Sen, P.; Biswas, K.; Maiti, T., Spectral Studies of Lead-Free Organic-Inorganic Hybrid Solid-State Perovskites $CH_3NH_3Bi_{2/3}I_3$ and $CH_3NH_3Pb_{1/2}Bi_{1/3}I_3$: Potential Photo Absorbers. *ChemistrySelect* **2018,** *3* (2), 794-800.
15. Seth, S.; Samanta, A., A facile methodology for engineering the morphology of $CsPbX_3$ perovskite nanocrystals under ambient condition. *Scientific reports* **2016,** *6* (1), 1-7.
16. Levchuk, I.; Herre, P.; Brandl, M.; Osvet, A.; Hock, R.; Peukert, W.; Schweizer, P.; Spiecker, E.; Batentschuk, M.; Brabec, C. J., Ligand-assisted thickness tailoring of highly luminescent colloidal $CH_3NH_3PbX_3$ (X= Br and I) perovskite nanoplatelets. *Chemical Communications* **2017,** *53* (1), 244-247.
17. Tan, Y.; Zou, Y.; Wu, L.; Huang, Q.; Yang, D.; Chen, M.; Ban, M.; Wu, C.; Wu, T.; Bai, S., Highly luminescent and stable perovskite nanocrystals with octylphosphonic acid as a ligand for efficient light-emitting diodes. *ACS applied materials & interfaces* **2018,** *10* (4), 3784-3792.

18. Xia, H.; Wu, S.; Li, L.; Zhang, S., High binding ability ligand controlled formation of $CsPbX_3$ (X= Cl/Br, Br, I) perovskite nanocrystals with high quantum yields and enhanced stability. *RSC advances* **2018,** *8* (63), 35973-35980.
19. Huang, H.; Raith, J.; Kershaw, S. V.; Kalytchuk, S.; Tomanec, O.; Jing, L.; Susha, A. S.; Zboril, R.; Rogach, A. L., Growth mechanism of strongly emitting $CH_3NH_3PbBr_3$ perovskite nanocrystals with a tunable bandgap. *Nature communications* **2017,** *8* (1), 1-8.
20. Seth, S.; Mondal, N.; Patra, S.; Samanta, A., Fluorescence blinking and photoactivation of all-inorganic perovskite nanocrystals $CsPbBr_3$ and $CsPbBr_2I$. *The journal of physical chemistry letters* **2016,** *7* (2), 266-271.
21. Li, F.; Cao, L.; Shi, S.; Gao, H.; Song, L.; Geng, C.; Bi, W.; Xu, S., Controlled Growth of $CH_3NH_3PbBr_3$ Perovskite Nanocrystals via a Water–Oil Interfacial Synthesis Method. *Angewandte Chemie* **2019,** *131* (49), 17795-17799.
22. Kostopoulou, A.; Sygletou, M.; Brintakis, K.; Lappas, A.; Stratakis, E., Low-temperature benchtop-synthesis of all-inorganic perovskite nanowires. *Nanoscale* **2017,** *9* (46), 18202-18207.
23. Zhidkov, I. S.; Poteryaev, A. I.; Kukharenko, A. I.; Finkelstein, L. D.; Cholakh, S. O.; Akbulatov, A. F.; Troshin, P. A.; Chueh, C.-C.; Kurmaev, E. Z., XPS evidence of degradation mechanism in $CH_3NH_3PbI_3$ hybrid perovskite. *Journal of Physics: Condensed Matter* **2019,** *32* (9), 095501.
24. Leng, M.; Yang, Y.; Zeng, K.; Chen, Z.; Tan, Z.; Li, S.; Li, J.; Xu, B.; Li, D.; Hautzinger, M. P.; Fu, Y.; Zhai, T.; Xu, L.; Niu, G.; Jin, S.; Tang, J., All-Inorganic Bismuth-Based Perovskite Quantum Dots with Bright Blue Photoluminescence and Excellent Stability. *Advanced Functional Materials* **2018,** *28* (1), 1704446.
25. Butkus, J.; Vashishtha, P.; Chen, K.; Gallaher, J. K.; Prasad, S. K.; Metin, D. Z.; Laufersky, G.; Gaston, N.; Halpert, J. E.; Hodgkiss, J. M., The

evolution of quantum confinement in $CsPbBr_3$ perovskite nanocrystals. *Chemistry of Materials* **2017,** *29* (8), 3644-3652.

26. Di Stasio, F.; Imran, M.; Akkerman, Q. A.; Prato, M.; Manna, L.; Krahne, R., Reversible concentration-dependent photoluminescence quenching and change of emission color in $CsPbBr_3$ nanowires and nanoplatelets. *The journal of physical chemistry letters* **2017,** *8* (12), 2725-2729.
27. Zhang, F.; Zhong, H.; Chen, C.; Wu, X.-g.; Hu, X.; Huang, H.; Han, J.; Zou, B.; Dong, Y., Brightly Luminescent and Color-Tunable Colloidal $CH_3NH_3PbX_3$ (X = Br, I, Cl) Quantum Dots: Potential Alternatives for Display Technology. *ACS Nano* **2015,** *9* (4), 4533-4542.
28. Hintermayr, V. A.; Richter, A. F.; Ehrat, F.; Döblinger, M.; Vanderlinden, W.; Sichert, J. A.; Tong, Y.; Polavarapu, L.; Feldmann, J.; Urban, A. S., Tuning the optical properties of perovskite nanoplatelets through composition and thickness by ligand-assisted exfoliation. *Advanced materials* **2016,** *28* (43), 9478-9485.
29. Wang, Z.; Wen, X.-D.; Hoffmann, R.; Son, J. S.; Li, R.; Fang, C.-C.; Smilgies, D.-M.; Hyeon, T., Reconstructing a solid-solid phase transformation pathway in CdSe nanosheets with associated soft ligands. *Proceedings of the National Academy of Sciences* **2010,** *107* (40), 17119-17124.

This page is intentionally left blank

Chapter-4

Potassium Induced Passivation of Deep Traps in Bismuth Doped Hybrid Lead Bromide Perovskite Nanocrystal: Massive Amplification of Photoluminescence Quantum Yield

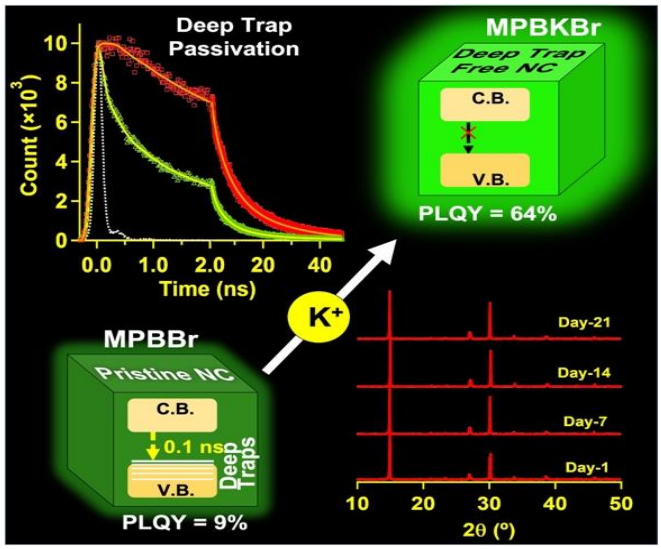

J. Phys. Chem. Lett. **2020,** *12*, 546-551.

The low photoluminescence quantum yield of Bi^{3+} doped lead halide perovskite nanocrystals (NCs) is a big challenge to the scientific community. This makes them a weak candidate in the optoelectronics field inspite of better stability than the pure lead analogue. Herein, the reason behind this reduction of quantum yield in hybrid mixed lead-bismuth bromide (MPBBr) NC is investigated and proposed to be due to ultrafast trapping transfer in the core of the NC, and not due to the surface trap states. Further, we have successfully boosted the quantum yield of MPBBr NC from 9% to 64% by passivating the deep traps within the crystal core by monovalent potassium ion doping. The stability of the developed Bi^{3+}/K^{+} doped lead halide perovskite NC was found to be extremely high in atmospheric condition and sustains it propertry upto 100 ^{o}C.

4.1. Introduction

In recent years the scientific community has noticed a rapidly growing interest in lead halide perovskite system due to its unique properties.[1-3] The efficiency of the solar cell is recorded as high as 24% using perovskite material.[4] On the other hand, the nano-crystalline (NC) version of these lead halide perovskite systems render high attention due to their promising optoelectronic properties with high photoluminescence (PL) quantum yield (QY).[5-7] Compositional and dimensional tuning of these materials give a way to adjust the band gap, which eventually provides a well-controlled emission characteristics ranging from violet to red. This makes lead halide perovskite NCs appropriate for laser, non-linear optics and in light emitting device applications.[8-9]

The toxic nature of the lead as well as vulnerability of lead halide perovskite in the atmospheric condition is a real hindrance to make these materials useful for commercial purposes.[10] This leads to the development of lead-free and B-site doped perovskite materials. Doping refers to the intentional insertion of a heteroatom to a target lattice, while keeping the basic host crystal structure intact, to modulate the fundamental optoelectronic properties of the material.[11-12] The heterovalant doped perovskites have shown better stability with respect to the pure lead analog with unique PL properties.[12-13] Charge carrier dynamics as well as the detail PL studies of such perovskite NCs are still not explored though. Few recent reports partly revealed the excitonic behavior of these kinds of materials.[14-15] Bi^{3+} is a common heterovalent dopant for B-site of the lead halide perovskite lattice as it does not affect the perovskite crystal architecture due to its similar ionic radius that of Pb^{2+} (Pb^{2+}: 119 pm and Bi^{3+}: 117 pm).[15] However, Bi^{3+} doping drastically drops the PLQY of lead halide perovskite NC and eventually makes it a bad choice in the field of optoelectronics, despite its greater stability in air.[13-15] According to the previous reports, the reason for the drop of PLQY is believed to be due to the activation of trap state induced quenching processes.[14,16] It is believed that Bi^{3+} induces trap states just below the conduction band.[14] Till date it is a common challenge to the perovskite

community to increase the quantum yield of the bismuth doped lead halide perovskite NC,[16-17] and we believe that the knowledge of the nature of the trap states is the key to this endeavor.

For lead halide as well as lead free perovskite NCs, surface passivation is a popular technique to increase the PL efficiency.[17-18] Long chain organic ligands are routinely used for this purpose.[13] Recently the use of extra halide and alkali metal ions have been reported as surface passivator that eventually boost the PLQY.[19-20] Alkali metals are introduced within the perovskite lattice to increase the emission properties and stability of the PNCs.[21] However, detailed study of charge carrier trapping in Bi^{3+} doped lead halide PNCs and way to boost its PL quantum yield is still a concern.

In this work, we synthesized $CH_3NH_3PbBr_3$ (MPBr) and $CH_3NH_3Pb_{1/2}Bi_{1/3}Br_3$ (MPBBr) NCs and performed material/optical characterization. We observed a huge red shift in the PL spectrum accompanied by a massive reduction in PLQY for MPBBr (509 nm, 9%) compared to MPBr (450 nm, 72%). The possible reason for this is presented as the direct transfer of the charged carriers from the conduction band to the trap states present in the core of the perovskite crystal structure. Detailed studies have also revealed that surface traps are not responsible for this trapping process. Further, we demonstrated the role of K^+ in boosting the PLQY of MPBBr from 9% to 64% and proposed a possible mechanism. K^+ insertion also improved the stability of the NC drastically.

4.2. Characterization of MPBr and MPBBr NCs

MPBr and MPBBr are synthesized by the well reported ligand assisted anti-solvent precipitation technique (see section 2.9.5 and 2.9.6 of chapter-2 for details).[13,22] Powder X-ray diffraction (PXRD) of MPBr and MPBBr are shown in figure 4.1, which indicate that

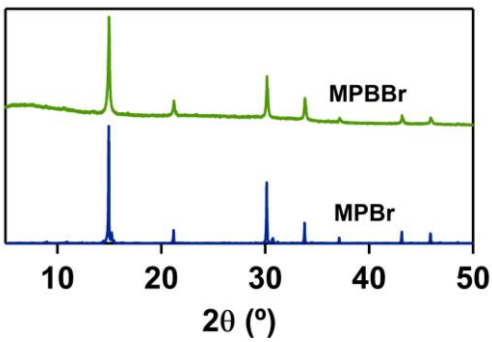

Figure 4.1. PXRD of MPBr, and MPBBr NCs.

bismuth incorporation does not deform the crystal structure and retains its cubic phase geometry. This is in line with the previous reports as well.[12,14]

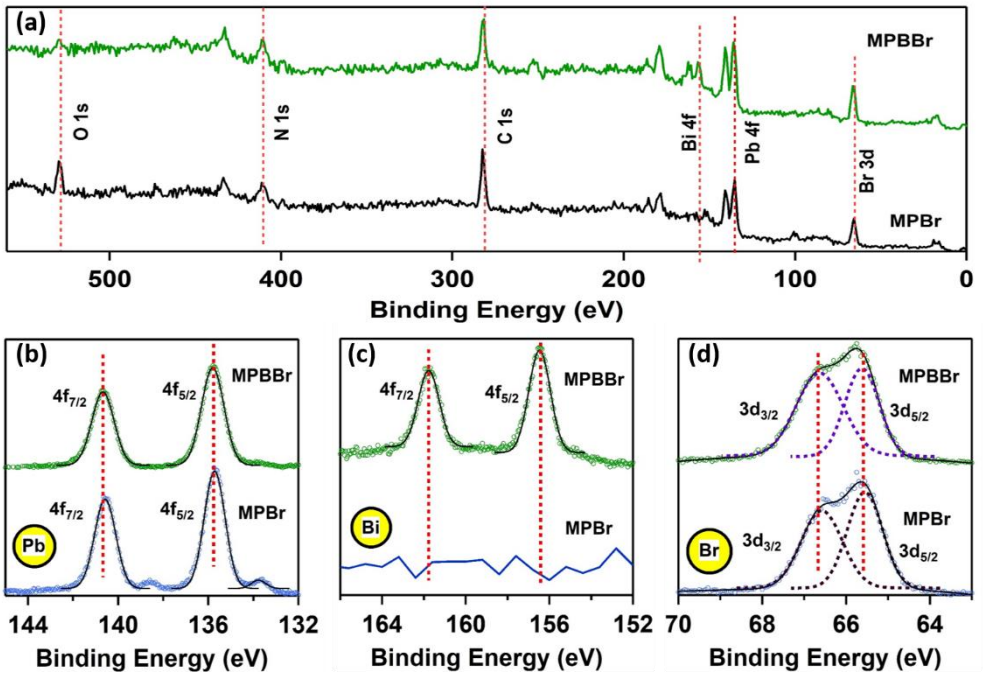

Figure 4.2. XPS analysis of MPBr and MPBBr NCs. (a) XPS survey spectra of MPBr and MPBBr NCs. (b) High Resolution XPS spectra for (a) Pb – 4f (c) Bi-4f and (d) Br-3d of MPBr and MPBBr NCs.

To explore the surface elemental composition of the constituent ions of the NCs, XPS of both MPBr and MPBBr were performed. The presence of every constituent ion in the respective NCs confirms the proper desired NCs formation. The XPS survey scan, as shown in figure 4.2a, showed binding energy peaks at around 65 eV, 140 eV, 160 eV, 284 eV, 410 eV and 530 eV which correspond to the photoelectron peaks of Br 3d, Pb 4f, Bi 4f, C 1s, N 1s and O 1s respectively.[5-7] Doublet peaks of Pb 4f (figure 4.2b), Bi 4f (figure 4.2c) and Br 3d (figure 4.2d) were observed as a result of their spin orbit coupling.[13] Moreover, we recorded high resolution XPS spectra of all the constituents at around above-mentioned binding energies. The Pb 6p valance shell electrons contribute to Pb–Br framework to construct $PbBr_6^{4-}$ octahedral[2]; whereas Bi 6p valance orbital electrons construct $BiBr_6^{3-}$ octahedra from

$Bi_2Br_9^{3-}$ cluster within the perovskite lattice. The Pb 4f spectrum of MPBBr NCs (figure 4.2b) exhibited doublet peaks at 135.72 eV and 140.68 eV which correspond to the spin orbit splitting of the Pb $4f_{7/2}$ and $4f_{5/2}$ respectively. The Gaussian fitting of Pb 6p doublet photoelectron peaks allowed us to say that it is actually consists of only single type of lead in the system, which means that the experimented MPBBr NCs are highly pure. The Bi 4f spectrum of MPBBr NCs (figure 4.2c) also exhibited doublet peaks at 156.49 eV and 161.69 eV which correspond to the spin orbit splitting of the Bi $4f_{7/2}$ and $4f_{5/2}$ respectively and the single Gaussian peak fitting eliminates the chance of presence of different type of Bi in the NCs. The Br 3d spectrum (figure 4.2d) deconvoluted to two Gaussian peaks (at 65.58 eV and at 66.68 eV) originating from spin orbit coupling. For MPBr NCs, the position of every fitted peaks is almost same but in the Pb 6p spectrum we can see presence of new small peaks at 135.8 eV and 138.6 eV which may be due to the presence of metallic Pb in the system which suggests the reduction of some of the $PbBr_6^{4-}$ during the annealing process.

TEM analysis of both MPBr and MPBBr shows very small NCs with a narrow size distribution (see figure 1a and figure S4-S5 of the SI). The average size of MPBr and MPBBr are estimated to be 2.0 and 2.2 nm, respectively. Figure 1b shows the selected area electron diffraction (SAED) pattern that confirms the cubic crystal phase of MPBBr. From the high-resolution transmission electron microscopy (HRTEM) image of MPBBr NCs (Figure 1c) the crystal planes can be seen clearly. Figure 1d shows the Fourier filter image of the selected area of figure 1c where we observed (210) crystal plane having d-spacing of 0.267 nm.

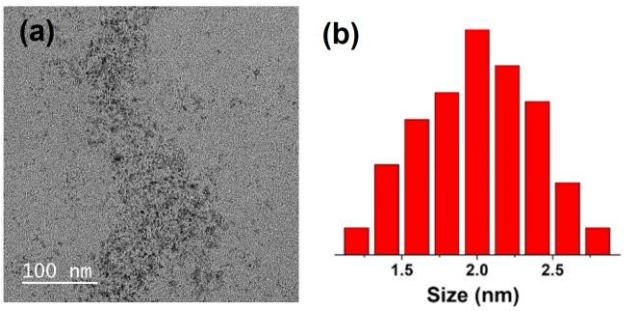

Figure 4.3. (a) TEM image of MPBr NCs. (b) Size distribution of MPBr NCs.

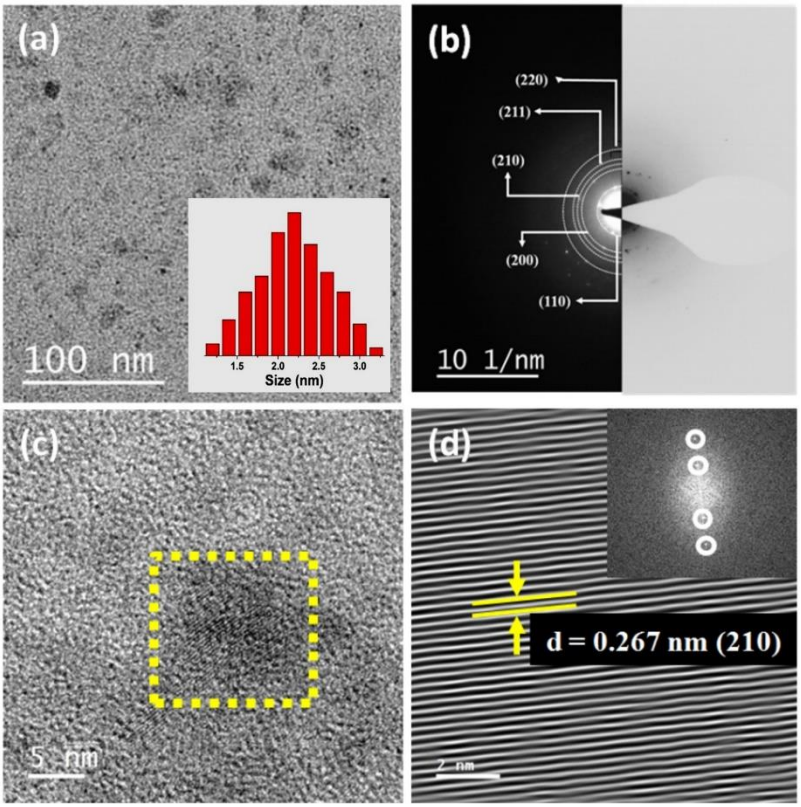

Figure 4.4. (a) Low magnification bright field TEM images MPBBr NCs (b) corresponding selected area electron diffraction (SAED) pattern, (c) high resolution of TEM image of MPBBr and (d) Fourier filter image of the selected area of yellow mark, right top inset shows the FFT of selected area.

4.3. Optical properties- Effect of Bi^{3+} insertion into MPBr NCs

MPBr shows a very sharp absorption with an excitonic peak at 445 nm and a strong emission centered at 451 nm with 72% PLQY (see figure 4.5a). The Introduction of Bi^{3+} in the lattice of pristine MPBr (MPBBr) results in the broadening of the absorption band with a long tail, probably originating from the transition into the sub-band gap energy levels or scattering.[12,23] We have noticed a 69 nm red shift in the emission maximum of MPBBr compared to MPBr with a drop in PLQY to 9% (see figure 4.5b). This large decrease in PLQY accompanied by a red shift in emission upon Bi^{3+} incorporation is in line with the previous reports.[12-15] The reduction of PLQY is believed to be due to Bi^{3+} induced strong perturbation to the density of states, in addition to the formation of a huge number of trap states in the

NC.[14-15] These trap states are responsible for the trapping of charged carrier and promote them to decay via the non-radiative pathway.

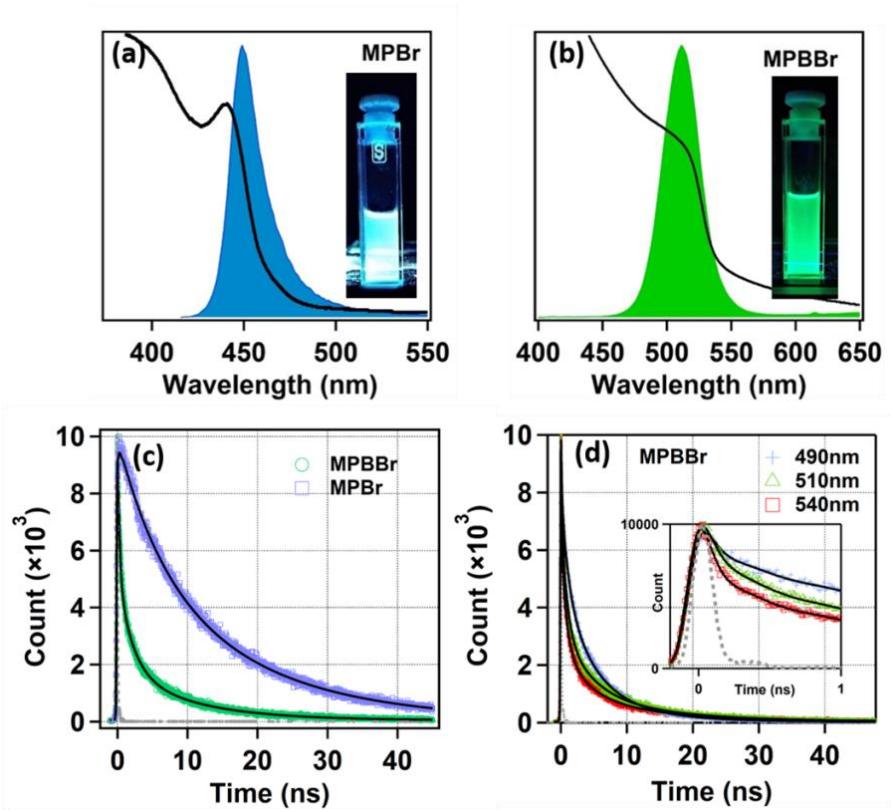

Figure 4.5. Optical characterization of MPBr and MPBBr NCs. Absorption and emission spectra of MPBr NCs. Photographic image of MPBr NCs under UV irradiation (365 nm excitation) is presented in the inset. (b) Absorption and emission spectra of MPBBr NCs. Photographic image of MPBBr NCs under UV irradiation (365 nm excitation) is given in the inset. (c) Transient photoluminescence of MPBr and MPBBr NCs (collected at their respective emission maxima at magic angle condition) upon 375 nm excitation. (d) Wavelength dependant photoluminescence transient of MPBBr NCs under same experimental condition as in (c).

To have a clear idea about the effect of Bi^{3+} insertion on the charge carrier dynamics and to explore the reason behind the PLQY reduction, we performed the time resolved PL studies at the respective emission maxima. The average PL lifetime of MPBr is found to be 8.8 ns that decreased to 1.8 ns in MPBBr (see figure 4.5c). This gives us a preliminary idea of the opening of new non-radiative channels in the MPBBr NCs. The PL transient of pristine MPBr is composed of two components,

2.3 ns (33%) and 12 ns (67%). The possible origin of the 2.3 ns component is excitonic recombination while the longer component of 12 ns is assigned to surface trap assisted recombination process.[13] For MPBBr, the PL transient was best fitted with a sum of four exponential function (see figure S11 and table S2 for fitting comparison). At 510 nm, the observed time components are– 90 ps (59%), 840 ps (22%), 4.5 ns (14%) and 13.4 ns (5%). The ultrafast component (~90 ps) is a quenching component and is assigned to the trapping transfer process according to the previous reports.[14,16] Trapping transfer process is the transfer of charged carriers to a trap state, which acts as a quenching center. When a carrier is transferred to a trap state, it can only relax via non-radiative pathway that eventually reduces the PLQY. The origin of ~800 ps lifetime component is presumably because of the transfer of excited charge carrier to free Bi^{3+} ions present in the system, which is suggested in theoretical studies.[15,24] These free interstitial Bi^{3+} can also act as a quenching center. The ~4 ns component is assigned to the radiative bound exciton recombination process and the 14 ns component is assigned to the surface trap assisted recombination process. To understand the nature of the trap states involved in the trapping transfer process, fluorescent transients at different wavelengths for MPBBr NCs were collected (figure 4.5d). The four component fitting parameters of every transient are documented in table 4.1.

Table 4.1. Wavelength dependent lifetime component analysis of MPBBr NCs prepared with OA=100 µL and OAm=125µL.

Wavelength (nm)	Component-1 (ns)	Component-2 (ns)	Component-3 (ns)	Component-4 (ns)
490	0.10 (49%)	0.89 (20%)	4.1 (25%)	10.9 (6%)
500	0.09 (53%)	0.78 (22%)	3.9 (18%)	11.3 (7%)
510	0.09 (59%)	0.84 (22%)	4.5 (14%)	13.4 (5%)
520	0.09 (63%)	0.79 (22%)	4.3 (9%)	13.8 (6%)
530	0.09 (68%)	0.75 (20%)	4.0 (8%)	14.1 (4%)
540	0.10 (70%)	0.73 (20%)	4.2 (5%)	14.2 (5%)

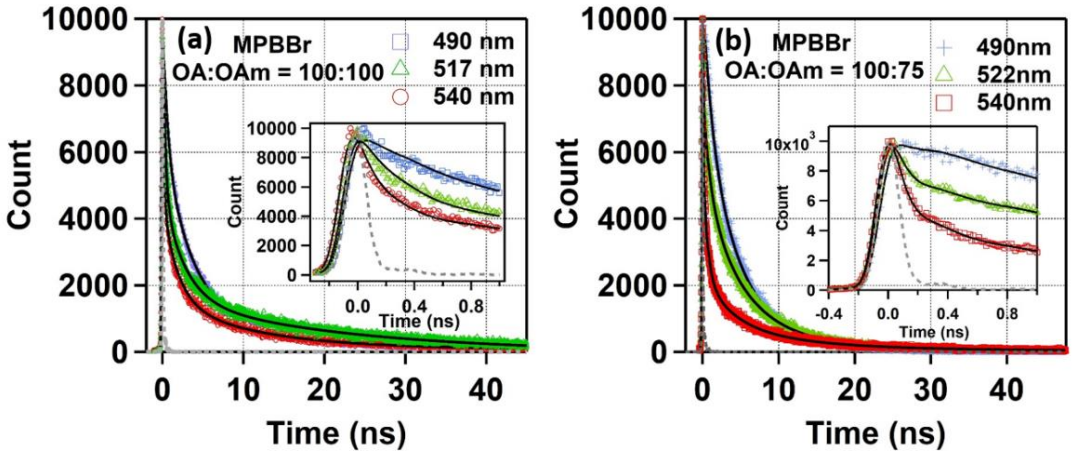

Figure 4.6. Time resolved emission spectra of MPBBr NCs prepared with different ratio of OA and OAm. (a) OA=100 µL and OAm=100µL, (b) OA=100 µL and OAm=75µL. Excitation wavelength is 375 nm.

The contributions of the 800 ps and >10 ns components are found to be almost constant, which indicate that these two processes are independent to the transients' energy. Here to mention that the emission in every NCs originates from the band edge position. The contribution of the ultrafast trapping transfer process (~90 ps component) is found to increase with the increase in the observation wavelength. The contribution of this process at 490 nm (blue end of the PL spectra of MPBBr) is found to be 48% whereas at 540 nm (red end of MPBBr PL spectra) the contribution becomes 70%. The contribution of the ~4 ns component (radiative bound exciton recombination process) follows exactly the reverse order to that of ~90 ps component (trapping transfer process); 27% at 490 nm and 5% at 540 nm. As a whole, we found that as we move to the lower energy transitions the contribution of the trapping transfer process is getting higher. This concludes that with the lower in energy of transitions, the density of the trap states associated with the trapping of charge carriers becomes higher. On the other hand, the long component contribution, which originated from the surface trap-assisted recombination of the charge carriers, remains unaltered with the energy of transition. This means that the trapping transfer process is surface trap independent. Here to mention that the surface trap-assisted recombination time component is found to depend on the observed wavelength,

which may be attributed to the NC size distribution.[13] To confirm more on this, MPBBr NC was prepared with different ratios of oleic acid (OA) and oleyl amine (OAm), which will have an effect on surface trap-assisted processes. Expectedly the results (see figure 4.6 and table 4.2 and table 4.3) are similar to that of original MPBBr NC and confirm the absence of surface trap involvement in the trapping transfer process.

Table 4.2. Wavelength-dependent lifetime component analysis of MPBBr NCs prepared with OA=100 µL and OAm=100µL.

Wavelength (nm)	Component-1 (ns)	Component-2 (ns)	Component-3 (ns)	Component-4 (ns)
490	0.06 (47%)	0.83 (18%)	4.1 (26%)	8.9 (9%)
500	0.06 (47%)	0.88 (16%)	4.4 (27%)	9.1 (10%)
510	0.04 (50%)	0.93 (17%)	4.6 (21%)	9.8 (12%)
517	0.07 (54%)	0.84 (18%)	4.3 (16%)	10.6 (12%)
540	0.08 (61%)	0.86 (18%)	4.6 (9%)	11.6 (12%)

Table 4.3. Wavelength dependent lifetime component analysis of MPBBr NCs prepared with OA=100 µL and OAm=75µL.

Wavelength(nm)	Component-1 (ns)	Component-2 (ns)	Component-3 (ns)	Component-4 (ns)
490	0.07(3%)	0.73 (14%)	3.9 (68%)	9.1 (15%)
500	0.07 (38%)	0.78 (16%)	4.1 (32%)	10.6 (14%)
510	0.07 (48%)	0.71 (13%)	4.0 (23%)	11.3 (16%)
522	0.08 (55%)	0.84 (14%)	4.3 (16%)	12.8 (15%)
530	0.07 (62%)	0.81 (15%)	4.2 (08%)	13.3 (15%)
540	0.08 (72%)	0.79 (12%)	4.3 (03%)	13.4 (13%)

4.4. Probable reason behind the formation of deep traps

Along with the surface trap states, cation vacancies may also originate within the core of the perovskite NCs upon Bi^{3+} incorporation to maintain the charge balance. Some recent reports suggest that Bi^{3+} induces deep traps within the lattice, when occupies the B-site of the perovskite structure.[15,25] These deep traps are formed due to the inertness of 6s of Bi, which has negligible interaction with the bromine 4p orbitals due to high spin-orbit coupling.[25] This leads to the lowering of valance band energy and the non-bonding 4p orbitals of bromine, just above the valance band, act as the deep trap states.[25] This is schematically represented in Scheme 1. This turns out as the quenching center within the crystal and is responsible for the trapping transfer process. As these dopant-induced deep traps are within the core of the NCs, these are surface-independent. From the wavelength-dependent PL transients of MPBBr NCs, we have already seen that in lower energy transients the contribution of the trapping transfer process becomes higher. This means that the trap states are located above the valance band, as the emission is originated from

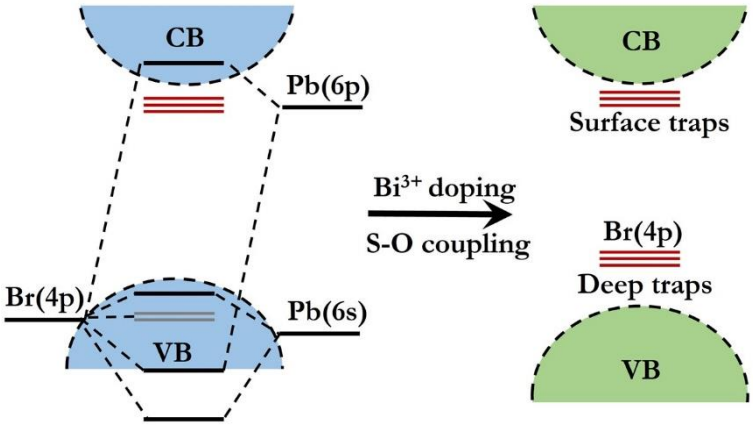

Scheme 4.1. Schematic representation of the formation of deep traps upon Bi^{3+} doping.

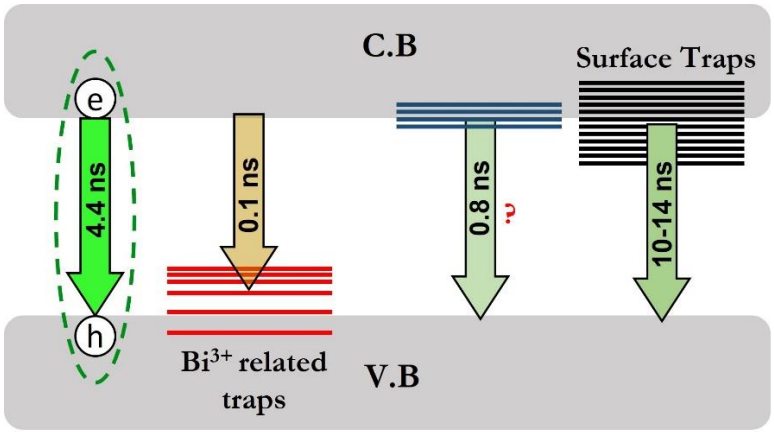

Scheme 4.2. Schematic representation of the photophysical processes in MPBBr NCs.

the band edge position. These bismuth-induced trapping sites mainly originate from the non-bonding bromine 4p orbitals and thus should act as hole trapping sites. The proposed energy diagram for the recombination of charge carriers in MPBBr NCs is shown in scheme 2.

4.5. Passivation of deep traps through K^+ co-doping

In MPBBr, as proposed, the crystal voids are in place to maintain the charge neutrality of the NC. We thought of filling up these voids and thus passivating the deep traps, with monovalent cations of suitable size so as to fulfill the charge balance criterion of the NC. In this case, the trapping of the charged carriers will not be operational and consequently, the PLQY should increase. Earlier, improved luminescent behavior of pristine lead halide perovskites has been noticed by alkali metal treatment and has been attributed to the restriction of halide migration and surface passivation.[21,26] To introduce a monovalent cation into the core, the size of that cation should match with the Pb^{2+} (radius = 119 pm) and Bi^{3+} (radius = 117 pm). This criterion can be roughly satisfied by both Na^+ (102 pm) and K^+ (139 pm). Here, we choose K^+ as a monovalent cation, as along with fulfilling the charge and size criteria its 4s orbital may interact efficiently with the non-bonding 4p orbitals of bromine to make this NC defect tolerant. The preparation of K^+ doped $CH_3NH_3Pb_{1/2}Bi_{1/3}Br_3$ (MPBKBr) NC is described in the section 2.9.7 of the chapter-2.

4.5.1. Characterization of MPBKBr NCs

The Introduction of K^+ in the lattice shifts the diffraction peaks to a lower angle (see figures 4.7b and 4.7c) indicating a lattice expansion. This signifies that K^+ occupies the interstitial vacant space in the host lattice.[21] The PXRD pattern clearly tells that perovskite NC retains its cubic phase with lattice parameter a = 5.95Å after K^+ insertion (see figure 4.7a). SAED pattern further confirms the retention of the cubic phase after K^+ insertion (figure 4.8b). From the TEM analysis, we can see that the size distribution of MPBKBr is broader than that of MPBr and MPBBr with an

average size of 5.6 nm (figure 4.8a). Figure 4.8c shows the HRTEM image of MPBKBr NCs. The Fourier filter image of the selected area of figure 3e clearly shows the (220) crystal plane having a d-spacing of 0.209 nm (see figure 4.8d).

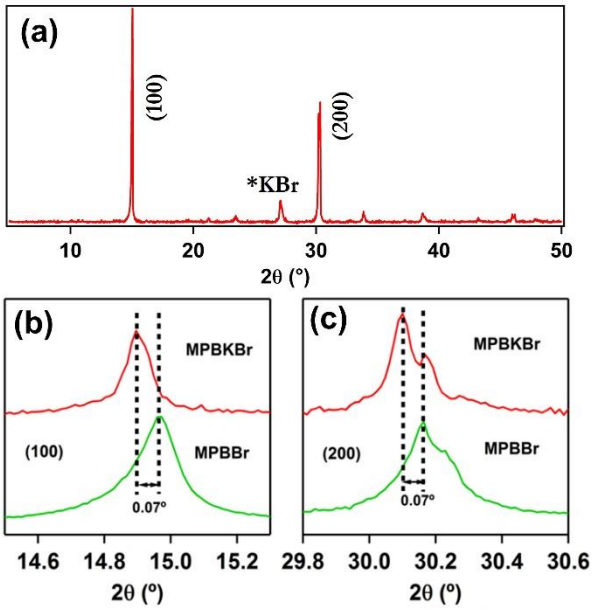

Figure 4.7. (a) PXRD pattern of MPBKBr NCs. (b) Shift of (100) diffraction peak of MPBBr NC after K^+ insertion, (c) Shift of (200) diffraction peak of MPBBr NC after K^+ insertion.

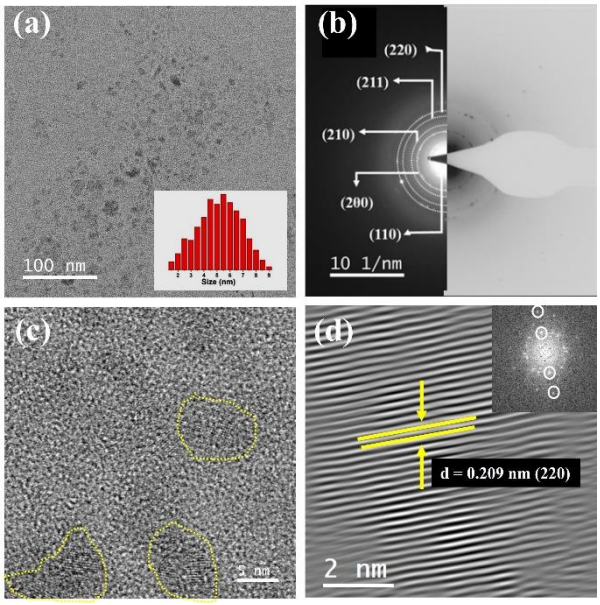

Figure 4.8. (a) TEM image of MPBKBr NC (b) corresponding selected are electron diffraction (SAED) pattern, (c) HRTEM image of MPBKBr NC and (d) Fourier filter image of the selected area of (c) showing (220) crystal plane having d-spacing of 0.209 nm.

To estimate the elemental composition of the prepared MPBKBr NCs, XPS analysis has been performed. The survey spectrum confirms the presence of C, N, O, Pb, Bi and Br in the sample (see figure 4.9a). The presence of potassium is confirmed from the high resolution XPS (Figure 4.9e). The low intensity of the potassium peaks is ascribed to the low sensitivity factor of potassium 2P orbital in XPS.[27] From XPS analysis, the Pb:Bi:K:Br ratio is calculated to be 1.00:0.34:0.25:3.46 for MPBKBr NCs.

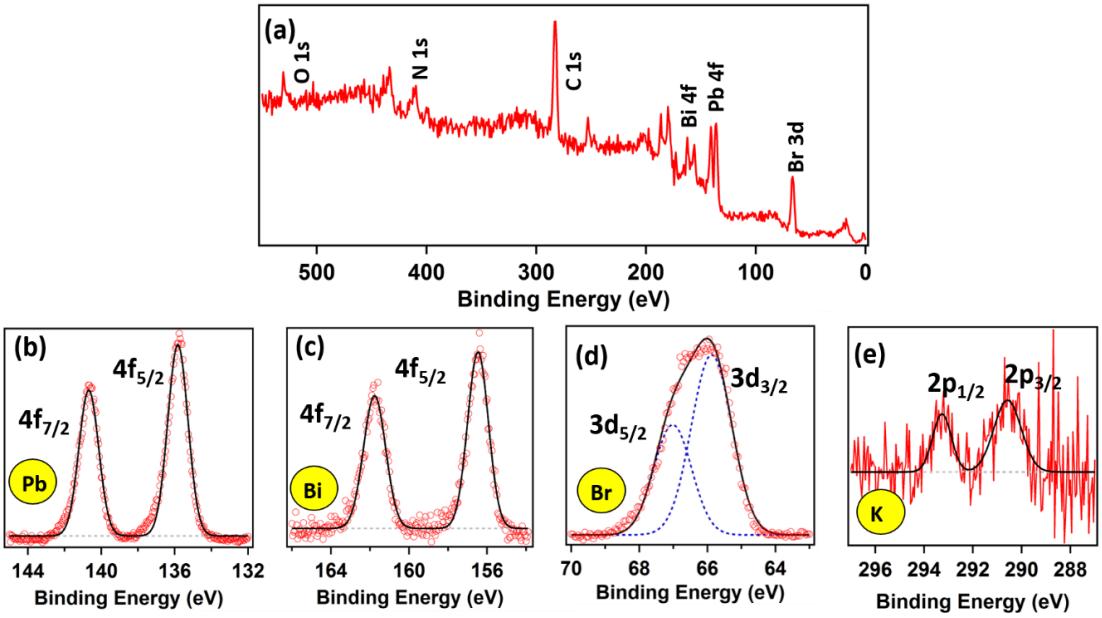

Figure 4.9. XPS analysis of MPBKBr NCs (a) Survey spectrum of MPBKBr NCs. High resolution XPS spectrum for (b) Pb–4f (c) Bi–4f, (d) Br–3d and (e) K-2p of MPBKBr NCs.

4.5.2. Passivation of deep trap- the absence of trapping transfer process

MPBKBr NCs shows a broad absorption spectrum and a highly intense emission spectrum centered at 516 nm (figure 4.10a). The broad absorption with a long tail is probably originating from the scattering from the suspension. The photograph of highly luminescent MPBKBr NCs under UV irradiation is shown in the inset of figure 4.10a. The PLQY was estimated to be 64%, which is seven times increment from MPBBr NCs (9%). To check the origin of this high PLQY we measured the PL transients of MPBKBr (figure 4.10b), which is best fitted with a sum of three exponential components – 1.5 ns (33%), 8 ns (43%) and 31 ns (24%). Interestingly, the ultrafast (100 ps) trapping transfer quenching component is totally absent in MPBKBr NCs, which is in agreement with our speculation. This confirms that K^+ directly passivates the deep traps within the crystal core and trapping of the charge carrier gets eliminated, resulting in a huge increment in the PLQY. The proposed mechanism is depicted in scheme 3. Stabilization of halide ion migration in the crystal imposed by K^+ doping has been predicted in an earlier study and this process

may also contribute in the enhancement of the PLQY in MPBKBr NC. The three other slower time components in MPBBr have been further retarded in MPBKBr. Passivation of the surface trapping sites by the free K^+ or Br^- ions could be one of the reasons for the increase in the average PL lifetime, as suggested in recent reports.[19,30]

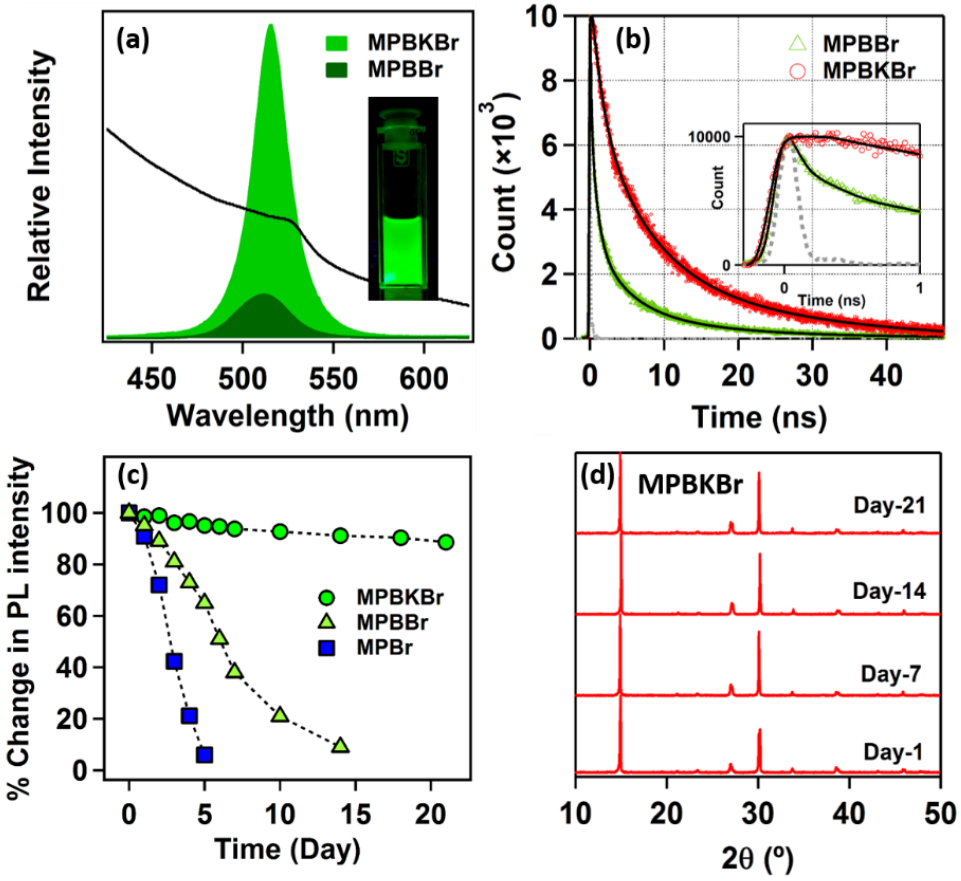

Figure 4.10. Optical characterization of MPBKBr NC. (a) Absorption and emission spectra, a comparison of emission with MPBBr is also shown. Photographic image of MPBr NCs under UV irradiation (365 nm excitation) is presented in the inset. (b) Transient photoluminescence of MPBKBr NC and comparison with that of MPBBr NC (collected at their respective emission maxima at magic angle condition upon 375 nm excitation). Early time decay characteristics are shown in the inset. (c) % change of PL intensity for MPBKBr, MPBBr and MPBr NCs in atmospheric condition until 21 days after its preparation. (d) PXRD analysis of MPBKBr film on a glass slide under atmospheric condition on four different days (day 1, day 7, day 14, day 21) after its preparation. The positions and intensities of the diffraction peaks remain unaltered and more importantly no extra impurity peaks have developed even after 21 days.

We also checked the stability of MPBKBr NCs as a function of time and temperature, and amazed to see that MPBKBr NCs are stable in atmospheric condition until 21 days with an only 10% reduction in the PL intensity (Figure 4.10c). A similar study with MPBr and MPBBr reveals that the PL intensity of these two perovskites NCs completely diminished on 5 and 15 days, respectively (see figure 4.10c). We also performed PXRD analysis of MPBKBr drop casted on a glass slide on four different days (day 1, day 7, day 14, day 21) after its preparation and found that the positions and intensities of the diffraction peaks remain unaltered. More importantly, no extra impurity peaks have developed even after 21 days (see figure 4.10d). This suggests a high stability of MPBKBr NCs in atmospheric condition. We also checked the thermal stability of MPBKBr NCs in the film mode (by drop casting the NCs solution over a glass slide) by measuring PXRD and taking photographic images. We found that MPBKBr NCs film is stable until 100 °C and upto this temperature the PXRD pattern remain unaltered (see figure 4.11).

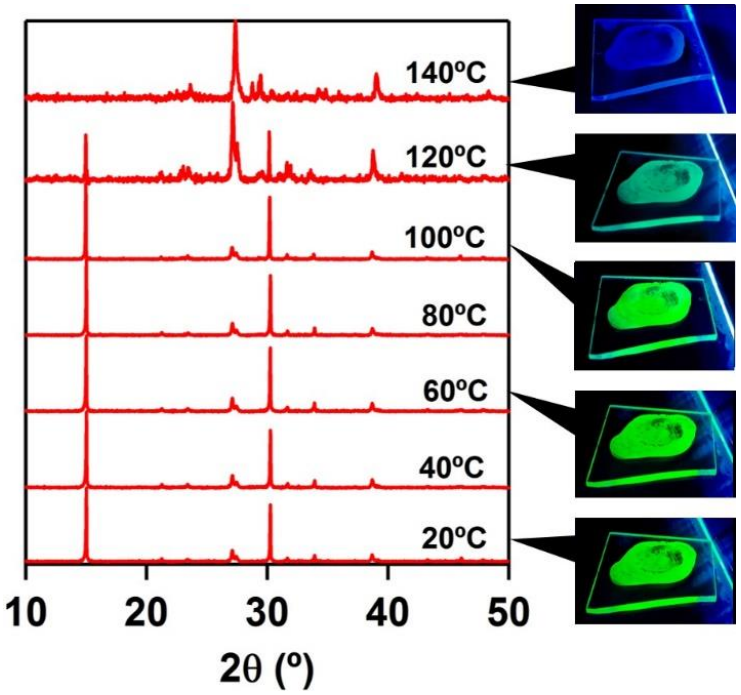

Figure 4.11. Thermal stability of MPBKBr film prepared by drop casting MPBKBr NCs on a glass slide monitored by PXRD data. The photographic images for few temperatures are also shown under UV illumination.

4.6. Passivation of deep traps through Na^+ co-doping

To support the fact of crystal void filling with monovalent cation and boosting the quantum yield, we have tried with Na^+ ion also as a supporting experiment. The

details of the synthesis procedure are mentioned in the section 2.9.7 of chapter-2. From the TEM analysis of this MPBBr-NaCl NCs (figure 4.12a), we can see that the shape is somewhat circular as previous ones and from the SAED pattern (figure 4.20c) we can see its crystalline nature. The average size is calculated to be 2 nm (figure 4.20b) and the size distribution is very sharp. Both Absorption and emission spectra is found to be broad in nature with emission maxima centered at 424 nm (figure 4.14d). The quantum yield shows a huge increment (62%) like in K^+ addition which reconfirm our speculations (figure 4.12d). Consequently, in the fluorescent transient also the ultrafast component is found to be missing (figure 4.12f). The fluorescent transient of MPBBr-NaCl shows a single exponential decay having value 3.2 ns which actually means the high-quality trap-free nature of the NCs. However further studies on charge carrier dynamics on MPBBr-NaCl have to be done.

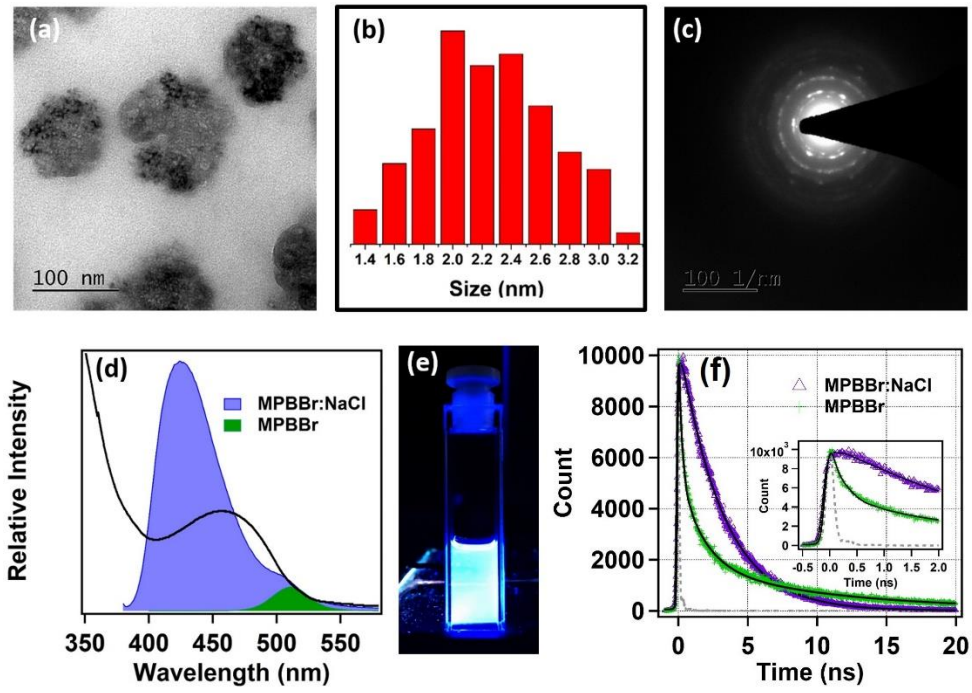

Figure 4.12. Microscopic and optical properties of MPBBr-NaCl NCs. (a) TEM image of MPBBr-NaCl NCs. (b) Size distribution of MPBBr-NaCl NCs. (c) SAED pattern of MPBBr-NaCl NCs. (d) Absorption and relative Emission spectra of MPBBr to MPBBr-NaCl NCs. (e) Optical image of MPBBr-NaCl under UV light. (f) Fluorescent transients of MPBBr-NaCl and MPBBr NCs. Inset shows the same in short time scale region. The

excitation wavelength was 375 nm. Transients were collected at the emission maxima of the respective NCs.

4.7. Conclusion

In conclusion, this work demonstrates the nature of the trap state involved in photoluminescence quenching in Bi^{3+} doped hybrid lead halide perovskite nanocrystals (MPBBr NCs). From the steady-state and time-resolved photoluminescence studies, we proposed that the deep traps in the crystal core of MPBBr NCs are responsible for the drastic drop of photoluminescence quantum yield and are totally surface trap independent. We also have shown how the passivation of deep traps can be achieved by the monovalent Na^{+} and K^{+} doping, leading to a massive amplification of photoluminescence quantum yield and its stability in open atmosphere.

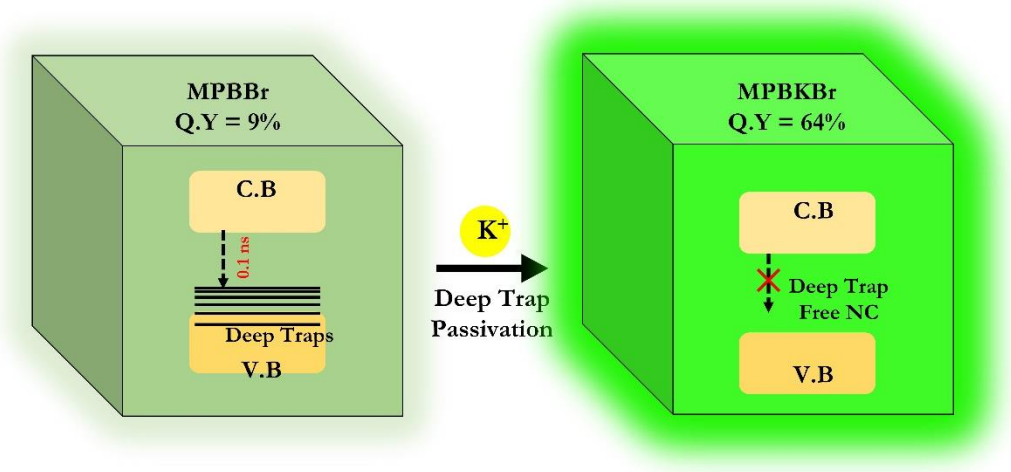

Scheme 4.3. Proposed photo physics of core trap passivation by K^{+} in MPBBr NCs.

References

1. Jeon, N. J.; J. Noh, H.; Yang, W. S.; Kim, Y. C.; Ryu, S.; Seo, J.; Seok, S. II. Compositional Engineering of Perovskite Materials for High-Performance Solar Cell. *Nature* **2014**, *517*, 476−480.
2. Li, D.; Liao, P.; Shai, X.; Huang, W.; Liu, S.; Li, H.; Shen, Y.; Wang, M. Recent Progress on Stability Issues of Organic–Inorganic Hybrid Lead Perovskite-Based Solar Cells. *RSC Adv.* **2016**, *6*, 89356−89366.
3. Fu, Q.; Tang, X.; Huang, B.; Hu, T.; Tan, L.; Chen, L.; Chen, Y. Recent Progress on the Long-Term Stability of Perovskite Solar Cells. *Adv. Sci.* **2018**, *5*, 1700387.
4. Jeon, N. J.; Na, H.; Jung, E. H.; Yang, T. -Y.; Lee, Y. G.; Kim, G.; Shin, H. -W.; Seok, S. II.; Lee, J.; Seo, J. A Fluorene-Terminated Hole-Transporting Material for Highly Efficient and Stable Perovskite Solar Cells. *Nat. Energy* **2018**, *3*, 682−689.
5. Paul, S.; Samanta, A. *N*-Bromosuccinimide as Bromide Precursor for Direct Synthesis of Stable and Highly Luminescent Green-Emitting Perovskite Nanocrystals. *ACS Energy Lett.* **2020**, *5*, 64−69.
6. Dutta, A.; Behera, R. K.; Pal, P.; Baitalik, S.; Pradhan, N. Near-Unity Photoluminescence Quantum Efficiency for All $CsPbX_3$ (X = Cl, Br, and I) Perovskite Nanocrystals: A Generic Synthesis Approach. *Angew. Chem., Int. Ed.* **2019**, 58, 5552−5556.
7. Bansal, P.; Khan, Y.; Nim, G. K.; Kar, P. Surface Modulation of Solution Processed Organolead Halide Perovskite Quantum Dots to Large Nanocrystals Integrated with Silica Gel G. *Chem. Commun*. **2018**, *54*, 3508−3511.
8. Akkerman, Q. A.; D'Innocenzo, V.; Accornero, S.; Scarpellini, A.; Petrozza, A.; Prato, M.; Manna, L. Tuning the Optical Properties of Cesium Lead Halide

Perovskite Nanocrystals by Anion Exchange Reactions. *J. Am. Chem. Soc.* **2015**, *137*, 10276−10281.

9. Zhang, F.; Zhong, H.; Chen, C.; Wu, X.; Hu, X.; Huang, H. Brightly Luminescent and Color-Tunable Colloidal $CH_3NH_3PbX_3$ (X = Br, I, Cl) Quantum Dots: Potential Alternatives for Display Technology. *ACS Nano* **2015**, *3*, 4533−4542**.**

10. Dong, Y; Zhao, Y.; Zhang, S.; Dai, Y.; Liu, L.; Li, Y. Recent Advances Toward Practical Use of Halide Perovskite Nanocrystals. *J. Mater. Chem. A* **2018**, *6*, 21729−21746.

11. Luo, B.; Li, F.; Xu, K.; Guo, Y.; Liu, Y.; Xia, Z.; Zhang, J. Z. B-Site Doped Lead Halide Perovskites: Synthesis, Band Engineering, Photophysics, and Light Emission Applications. *J. Mater. Chem. C* **2019**, *7*, 2781−2808.

12. Zhou, Y.; Chen, J.; Bakr, O. M.; Sun, H. -T. Metal-Doped Lead Halide Perovskites: Synthesis, Properties, and Optoelectronic Applications. *Chem. Mater.* **2018**, *30*, 6589−6613.

13. Chatterjee, S.; Dey, P.; Das, N.; Tiwari, K.; Maiti, T.; Sen, P. Reversible Ultra-Slow Crystal Growth of Mixed Lead Bismuth Perovskite Nanocrystals: The Presence of Dynamic Capping. *Chem. Euro. J.* **2020**, *26*, 1506−1510.

14. Begum, R.; Parida, M. R.; Abdelhady, A. L.; Murali, B.; Alyami, N. M.; Ahmed, G. H.; Hedhili, M. N.; Bakr, O. M.; Mohammed, O. F. Engineering Interfacial Charge Transfer in $CsPbBr_3$ Perovskite Nanocrystals by Heterovalent Doping. *J. Am. Chem. Soc.* **2017**, *139*, 731−737.

15. Yin, J.; Ahmed, G. H.; Bakr, O. M.; Bredas, J. -L.; Mohammed, O. F. Unlocking the Effect of Trivalent Metal Doping in All-Inorganic $CsPbBr_3$ Perovskite. *ACS Energy Lett.* **2019**, *4*, 789−795.

16. Yang, B.; Chen, J.; Hong, F.; Mao, X.; Zheng, K.; Yang, S.; li, Y.; Pullerits, T.; Deng, W.; Han, K. Lead-Free, Air-Stable All-Inorganic Cesium Bismuth

Halide Perovskite Nanocrystals. *Angew. Chem. Int. Ed.* **2017**, *56*, 12471−12475.

17. Leng, M.; Yang, Y.; Chen, Z.; Gao, W.; Zhang, J.; Niu, G.; Li, D.; Song, H.; Zhang, J.; Jin, S.; Tang, J. Surface Passivation of Bismuth-Based Perovskite Variant Quantum Dots To Achieve Efficient Blue Emission. *Nano Lett.* **2018**, *18*, 6076−6083.

18. Yang, D.; Li, X.; Zeng, H. Surface Chemistry of All Inorganic Halide Perovskite Nanocrystals: Passivation Mechanism and Stability. *Adv. Mater. Interfaces* **2018**, *5*, 1701662.

19. Yang, F.; Chen, H.; Zhang, R.; Liu, X.; Zhang, W.; Zhang, J.; Gao, F.; Wang, L. Efficient and Spectrally Stable Blue Perovskite Light-Emitting Diodes Based on Potassium Passivated Nanocrystals. *Adv. Funct. Mater* **2020**, *30*, 1908760.

20. Fang, Z.; He, H.; Gan, L.; Li, J.; Ye, Z. Understanding the Role of Lithium Doping in Reducing Nonradiative Loss in Lead Halide Perovskites. *Adv. Sci.* **2018**, *5*, 1800736.

21. Cao, J.; Tao, S. X.; Bobbert, P. A.; Wong, C. -P.; Zhao, N. Interstitial Occupancy by Extrinsic Alkali Cations in Perovskites and Its Impact on Ion Migration. *Adv. Mater*. **2018**, *30*, 1707350.

22. Levchuk, L.; Herre, P.; Brandl, M.; Osvet, A.; Hock, R.; Peukert, W.; Schweizer, P.; Spiecker, E.; Batentschuk, M.; Brabek, C. J. Ligand-Assisted Thickness Tailoring of Highly Luminescent Colloidal $CH_3NH_3PbX_3$ (X = Br and I) Perovskite Nanoplatelets. *Chem. Commun.* **2017**, *53*, 244−247.

23. Yang, B.; Mao, S.; Meng, W.; Tang, Y.; Xia, X.; Yang, S.; Deng, W.; Han, K. Lead-Free Direct Band Gap Double-Perovskite Nanocrystals with Bright Dual-Color Emission. *J. Am. Chem. Soc.* **2018**, *140*, 17001−17006.

24. Zhou, Y.; Yong, Z.-J.; Zhang, K.-C.; Liu, B.-M.; Wang, Z.-W.; Hou, J.-S.; Fang, Y.-Z.; Zhou, Y.; Sun, H.-T.; Song, B. Ultrabroad Photoluminescence and Electroluminescence at New Wavelengths from Doped Organometal Halide Perovskites. *J. Phys. Chem. Lett.* **2016**, *7*, 2735−2741.

25. Harikesh, P. C.; Wu, B.; Ghosh, B.; John, R. A.; Lie, S.; Thirumal, K.; Wong, L. H.; Sum, T. C.; Mhaisalkar, S.; Mathews, N. Doping and Switchable Photovoltaic Effect in Lead-Free Perovskites Enabled by Metal Cation Transmutation. *Adv. Mater.* **2018**, *30*, 1802080.

26. Zheng, F.; Chen, W.; Bu, T.; Ghiggino, K. P.; Huang, F.; Chen, Y.; Tapping, P.; Kee, T. W.; Jia, B.; Wen, X. Triggering the Passivation Effect of Potassium Doping in Mixed-Cation Mixed-Halide Perovskite by Light Illumination. *Adv. Energy Mater.* **2019**, *9*, 1901016.

27. Moulder, J. F.; Stickle, W. F.; Sobol, P. E.; Bomben, K. D. Handbook of X-ray Photoelectron Spectroscopy. *Physical Electronics,* **1992** *Minnesota, United States of America.*

28. Ulatowski, A. M.; Wright, A. D.; Wenger, B.; Buizza, L. R. V.; Motti, S. G.; Eggimann, H. J.; Savill, K. J.; Borchert, J.; Snaith, H. J.; Johnston, M. B.; Herz, L. M. Charge-Carrier Trapping Dynamics in Bismuth-Doped Thin Films of $MAPbBr_3$ Perovskite. *J. Phys. Chem. Lett.* **2020**, *11*, 3681−3688.

29. Saba, M.; Cadelano, M.; Marongui, D.; Chen, F.; Sarritzu, V.; Sestu, N.; Figus, C.; Aresti, M.; Piras, R.; Lehmann, A.G.; Cannas, C.; Musinu, A.; Quochi, F.; Mura, A.; Bongiovanni, G**.** Correlated Electron–Hole Plasma in Organometal Perovskites. *Nat. Commun.* **2014**, *5*, 5049−5058.

30. Yang, J. -N.; Song, J. -S.; Yao, Y.; Wang, K. -H.; Zhu, B. -S.; Yao, M. -M.; Rahman, S. U.; Lan, Y. -F.; Fan, F. -J.; Yao, H. -B. Potassium Bromide Surface Passivation on $CsPbI_{3-x}Br_x$ Nanocrystals for Efficient and Stable Pure Red Perovskite Light-Emitting Diodes. *J. Am. Chem. Soc.* **2020**, *142*, 2956−2967.

This page is intentionally left blank

Chapter-5

Massive Amplification of Photoluminescence and Exceptional Water Stability of $MAPbBr_3$ Nanocrystals through Core-Shell Nanostructure formation in a Self-Defense Mechanism

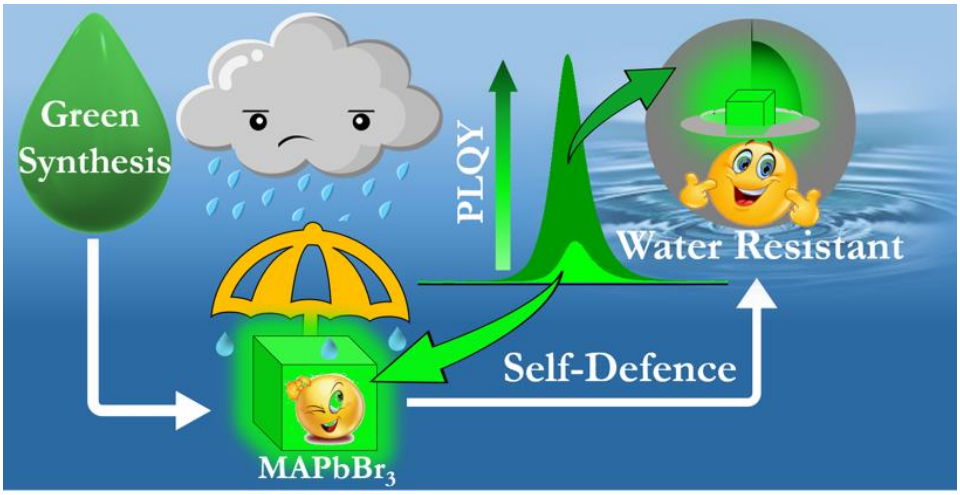

Mat. Adv. **2022**, *3*, 7360-7369.

Vulnerability to the atmospheric condition and associated toxicity limit perovskite's practical/industrial use despite of its tremendous promises in optoelectronics. This report plies an ionic liquid-like so-called green solvent to synthesize methylammonium lead bromide ($MAPbBr_3$) nanocrystals (NCs). The synthesized NC shows moderate photoluminescence quantum yield (PLQY) (~19%) and high environmental stability (at least six months). Further, the entire visible range was tuned through the anion exchange method. More interestingly, the synthesized NC forms a core-shell structure in a unique self-defense mechanism in presence of water, which is proposed to be $MAPbBr_3$@lead laurate. This core-shell structure is found to be beneficial in (a) preventing further degradation of the NC, and it becomes highly water stable (at least for two months), (b) surface modification to induce a massive five-fold amplification of PLQY, and (c) restricting the anion exchange reaction. Moreover, these unique properties are achieved without any special control. Also, the successful synthesis of other $MAPbX_3$ (X=Cl, I) demonstrates its potential universality as green medium for the first time. These remarkable observations are probably the first of their kind and should offer various new opportunities towards sustainable use and industrial production of perovskite nanocrystals in the future.

5.1. Introduction

Halide perovskites are considered as the potential game changer in the field of light-emitting diode, solar cell, photodetector and bioimaging because of their unique optical and electronic properties.[1-3] Despite the tremendous promises, the practical/industrial applicability is limited because of their vulnerability to the atmospheric condition, toxicity related to the perovskite material and its synthesis.[1, 4, 5] This report applies an ionic liquid like so-called green solvent that largely reduces the synthesis related toxicity, minimize the structural defects, and protects the perovskite nanocrystal from the degradation by water through a self-defense mechanism.

The most widely used precursor solvents for perovskite synthesis are hazardous and toxic dimethylformamide (DMF) along with its homologous dimethylacetamide (DMAC), N-methyl-2-pyrrolidone (NMP) and skin-penetrating dimethyl sulfoxide (DMSO). Another critical problem with these solvents is their high coordinating ability with the perovskite surface, which eventually facilitates the degradation of the perovskite structure and the formation of surface defects.[6-9] The use of less hazardous and non-coordinating organic solvent like acetonitrile (ACN) for this purpose has been attempted in recent times.[9, 10] A recent breakthrough was achieved using ionic liquids (ILs) (like carboxylic acid-methylamine, imidazole-based ionic liquid, and so on) as precursor medium.[11, 12] The first report came in 2015 by Moore *et al.* describing the synthesis of hybrid lead halide perovskite ($MAPbI_3$) thin film using methylammonium formate ionic liquid.[13] Consequent studies have proved the massive potential of such an approach.[11, 14-17] A few studies are also undertaken to venture the fundamental roles of the ILs in controlling perovskite nano crystal (NC)'s crystallization, nucleation, growth, interface modification and overall power conversion efficiency (PCE). [11, 12, 18, 19] The use of such solvents serves many purposes. (i) These can solubilize a vast series of materials.[11] (ii) By forming active intermediates, it provides an opportunity to control the crystal growth process.[11, 18,

[20] (iii) By interacting with uncoordinated lead, it might provide a much-needed enhancement in PLQY.[21] (iv) These liquids are considered environment-friendly. [11-14] (v) The synthesis of perovskite in a simple one-step reaction.[22] A recent perspective predicts ILs to be the next reformer in the field of perovskite research considering these facts.[22] Although the use of ILs in the synthesis process of the perovskite systems has emerged with its high potential, the research is still in its infancy, and a huge effort is necessary. The use of ILs in the synthesis of perovskite is still wandering around the improvement of solar cells. Surprisingly, the greener approach of synthesizing perovskite NCs got the minimum attention.

In this context, we prepared lead halide perovskite NC employing a lauric-acid based IL-like solvent system to address some of the issues related with perovskite NC's efficiency, stability and synthetic toxicity. We are inspired by few facts. (i) The only report on the synthesis of hybrid lead halide perovskite NCs with ILs was reported in 2020 by the Hoang *et al*., where they successfully synthesized highly luminescent $MAPbBr_3$ nanocrystals.[22] A systematic study involving the carboxylic acids of different carbon chain lengths from C1 to C4 suggests that the emissive property increases as the chain length of acid increases. They reached moderately high quantum yield (50%) and even shows a water stability of up to one hour. It can be assumed that further increment in the chain length of carboxylic acid might increase the emissive property along with the environmental stability due to an effective capping. But the ILs composed of long-chain carboxylic acids have never been employed in the perovskite synthesis. (ii) In previous reports, all the organic acids used are short-chain and consequently lack hydrophobic character. From our knowledge we know that lauric acid (LA) - based solvent shows a high hydrophobic character. Consequently, we expect that the capping with LA might introduce high moisture and environmental stability to the prepared NCs. (iii) Furthermore, LA can act as the surface capping ligand that provides stability to the NCs, and destructive consequences of solvent coordination will be nullified. (iv) LA induces confinement in contact with water, which may be a key to size tunability in the NC preparation

in the future.[23] (v) Most importantly, LA is a harmless natural fatty acid and the major component of coconut oil. Therefore, it should provide a green synthetic medium.

This report demonstrates a single-step synthesis of $MAPbBr_3$ NCs in an IL like green medium composed of methylamine and LA. In addition to showing a moderate photoluminescence quantum yield (PLQY ~19 %), the synthesized $MAPbBr_3$ NCs exhibit some remarkable properties that are probably the first of its kind and might pave the path for future exploration in this direction. The synthesized NCs exhibit a very high-water stability for up to three months. Core-shell structure formation by a unique self defence mechanism explains its tremendous water stability and five-fold amplification of PLQY. Further, successful synthesis of other $MAPbX_3$ (X=Cl, I) demonstrates its potential universality as green medium for the first time.

5.2. Results and Discussions

The green solvent medium for the synthesis of perovskite NCs was prepared through addition of methylamine and hydrophobic LA. Detailed synthesis is depicted in section 2.9.9 of chapter 2. The synthesized IL like medium shows good thermal stability and no weight loss is observed till 100 °C, confirmed from the thermogravimetric analysis (TGA) (see figure 5.1).

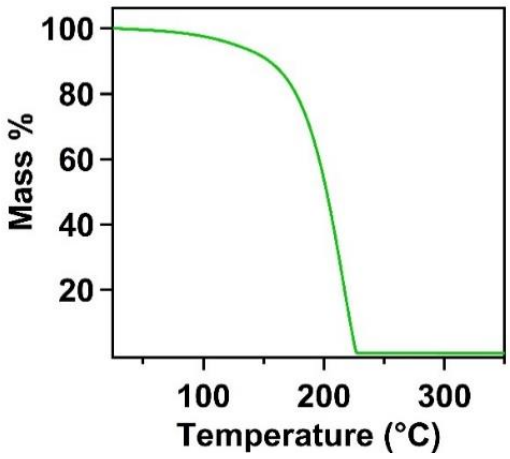

Figure 5.1. TGA data of the IL like green solvent medium

5.2.1. Characterisation of $MAPbBr_3$ NCs

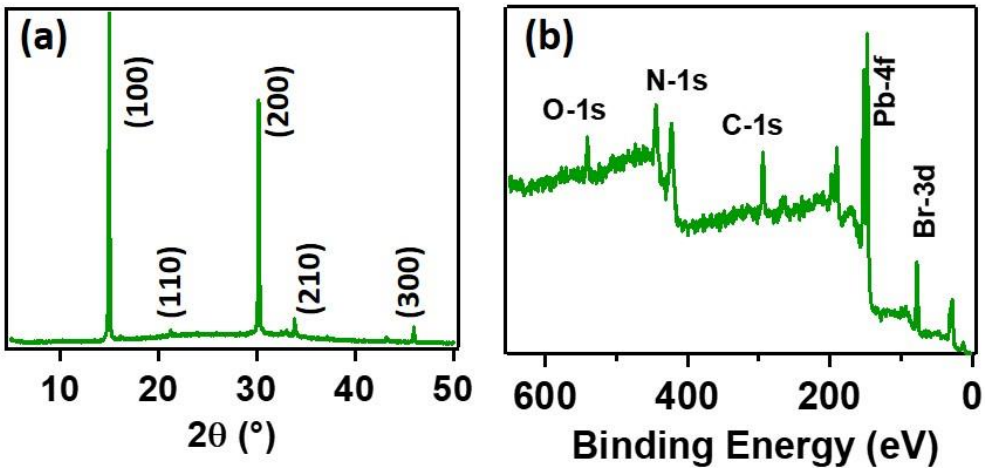

Figure 5.2. Powder X-ray diffraction (a) and XPS survey spectrum (b) of $MAPbBr_3$ NCs.

The $MAPbBr_3$ NCs was prepared by direct addition of $PbBr_2$ into the IL medium. Detail synthetic procedure is given in section 2.9.10 of chapter-2.The purified $MAPbBr_3$ NCs exhibit a pure cubic crystal structure evident from the PXRD pattern (see figure 5.2a).[5] X-ray photoelectron spectroscopy (XPS) confirms the presence of lead (Pb) and bromine (Br) on the surface of the NCs (see figure 5.2b). Further XPS analysis reveals that the synthesized NCs are having a bromine-rich surface with bromine to lead ratio of 3.13, which is very much in line with the previous reports.[2, 5]

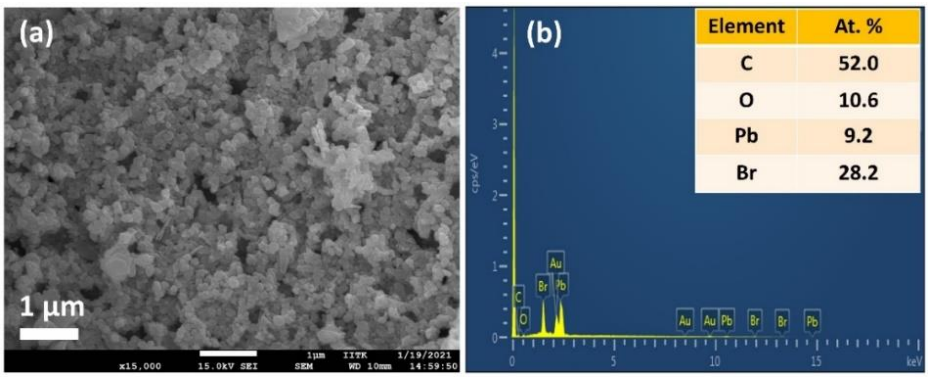

Figure 5.3. Scanning electron microscopic images of $MAPbBr_3$ NCs. (a) FESEM image of $MAPbBr_3$ NCs. (b) EDS elemental analysis of the $MAPbBr_3$ NCs from FESEM.

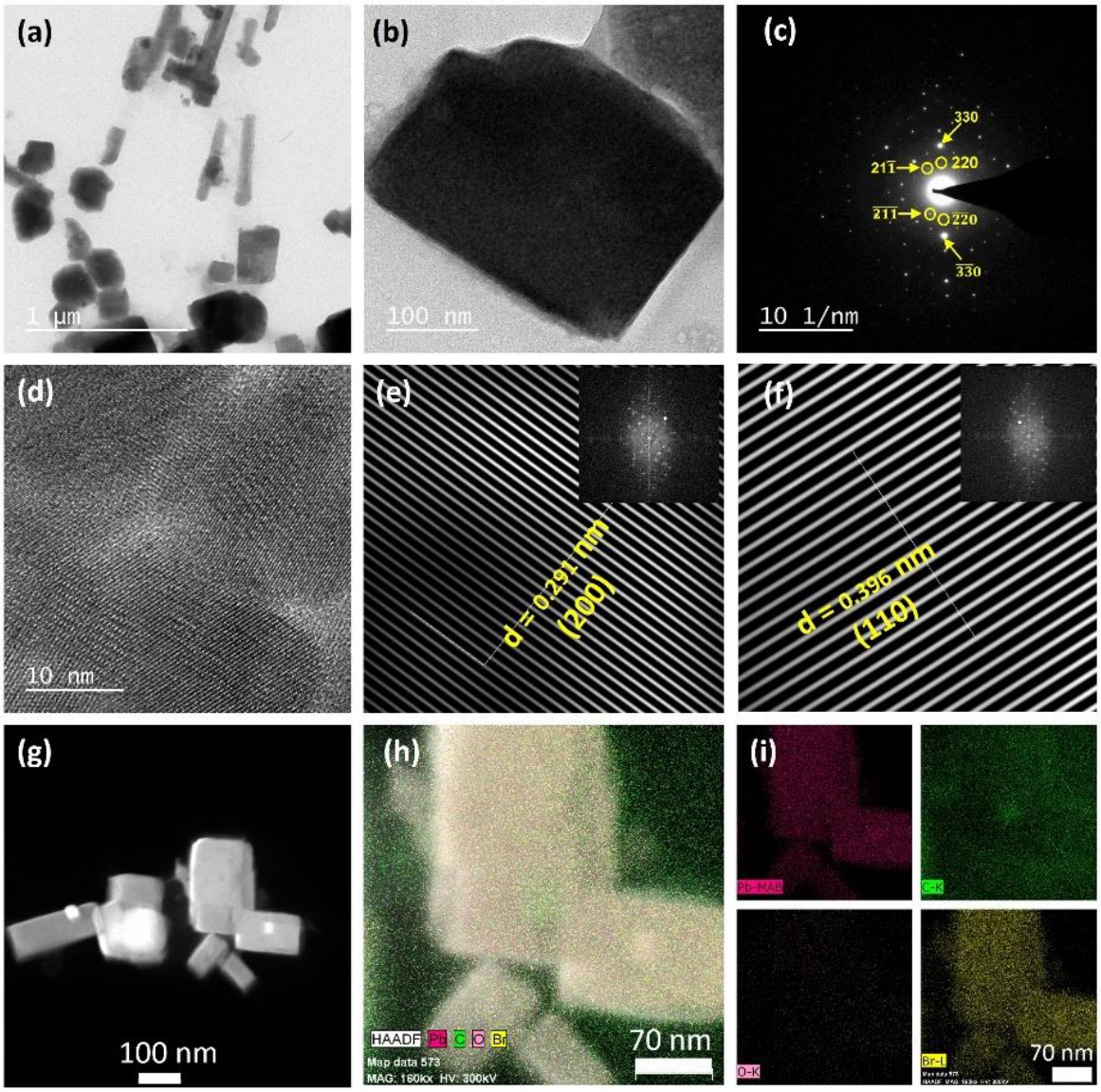

Figure 5.4. Microscopic characterization of the synthesized $MAPbBr_3$ NCs. (a) TEM image of synthesized $MAPbBr_3$ NCs. (b) TEM image of a single $MAPbBr_3$ nanocrystal. (c) Selected area electron diffraction (SAED) of the single $MAPbBr_3$ crystal. (d) High resolution TEM (HRTEM) image of synthesized $MAPbBr_3$ NCs. (e-f) Fourier filtered images showing (200) and (110) crystal planes. Inset contains the fast fourier transformed (FFT) pattern. (g) High-angle annular dark-field (HAADF) image of the $MAPbBr_3$ NCs. (h) EDS Elemental mapping of $MAPbBr_3$ NCs. (i) Mapping of induvial elements (Pb, C, O and Br).

Various microscopic characterizations have been done to have a clear idea about the microstructure of the synthesized $MAPbBr_3$ NCs. FESEM image shows that the purified NCs have a cubic morphology (see figure 5.3). Transmission electron microscopic (TEM) image of the NCs reveals that the NCs are mainly of square in shape, but some rod-like shapes are also observed (Figure 5.4a and figure 5.4b). The

TEM image also suggests the formation of large NCs, size > 100 nm. A bright-field image of a single NC (see figure 5.4b) along with selected area electron diffraction (SAED) further proves the formation of highly crystalline NC in the cubic phase[24] (figure 5.4c). From the high-resolution transmission electron microscopic (HRTEM) image of the synthesized NCs, the crystal planes can be seen clearly (see figure 5.4d). Fourier filtration of the selected area from figure 5.4d produces figure 5.4e and figure 5.4f, where we observe (200) and (110) crystal planes having d-spacing 0.283 nm and 0.391 nm respectively. High-angle annular dark-field (HAADF) image of the NCs further confirms the high crystallinity of the square shape NCs (see figure 5.4g). Figure 5.4h shows the energy-dispersive spectroscopy (EDS) elemental mapping of the $MAPbBr_3$ NCs from the TEM analysis, which shows high density of lead (Pb), bromine (Br) and carbon (C) on the surface. The EDS distribution mapping of every individual element is also included in figure 5.4i. The EDS analysis shows that the NCs exhibit a bromine-rich surface with a bromine to lead ratio of 3.41. Interestingly, EDS analysis also reveals that the NC surface has a very high density of carbon atoms, could be because of the presence of lauric acid as the capping ligand.

5.2.2. Optical Properties of $MAPbBr_3$ NCs

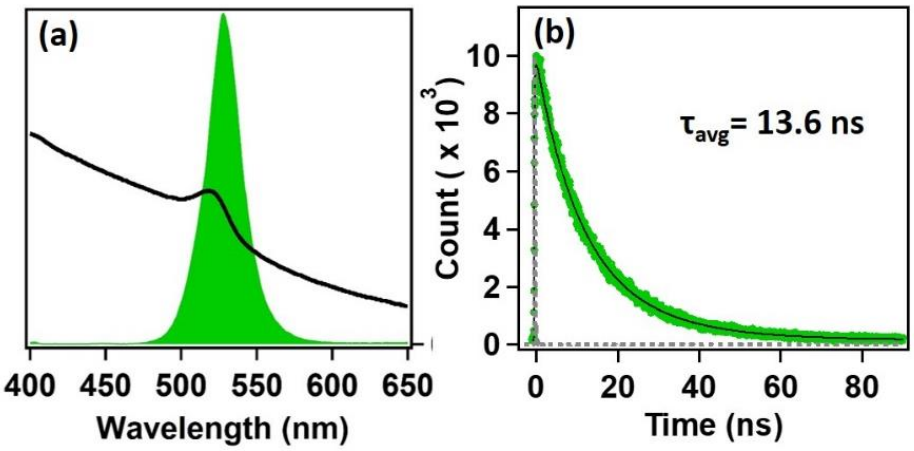

Figure 5.5. Optical properties of $MAPbBr_3$ NCs. (a) Steady state absorption (black) and emission spectra (green) of $MAPbBr_3$ NCs. (b) PL transient of $MAPbBr_3$ NCs upon exciting at 405 nm.

Steady-state and time-resolved PL studies were carried out to explore the optical properties of the synthesized $MAPbBr_3$ NCs. These $MAPbBr_3$ NCs show broad absorption spectra with an excitonic band centred at 521 nm and a very strong PL centred at 525 nm (see figure 5.5a). The PLQY is 19% and the average PL lifetime is 13.6 ns (61% 9.8 ns and 39% 18.9 ns) (see figure 5.5b). The 9.8 ns and 18.9 ns time components are assigned to the radiative excitonic recombination and surface assisted recombination process, respectively.[5, 25, 26]

5.2.3. Environmental stability of $MAPbBr_3$ NCs

These $MAPbBr_3$ NCs are highly stable in ambient condition up to at least six months. Although the PL intensity drops by 63% after six months (see figure 5.6a), the PXRD pattern remains almost unaffected (see figure 5.6b and figure 5.6c), indicating high stability of the crystalline phase with considerable retention of PL intensity.

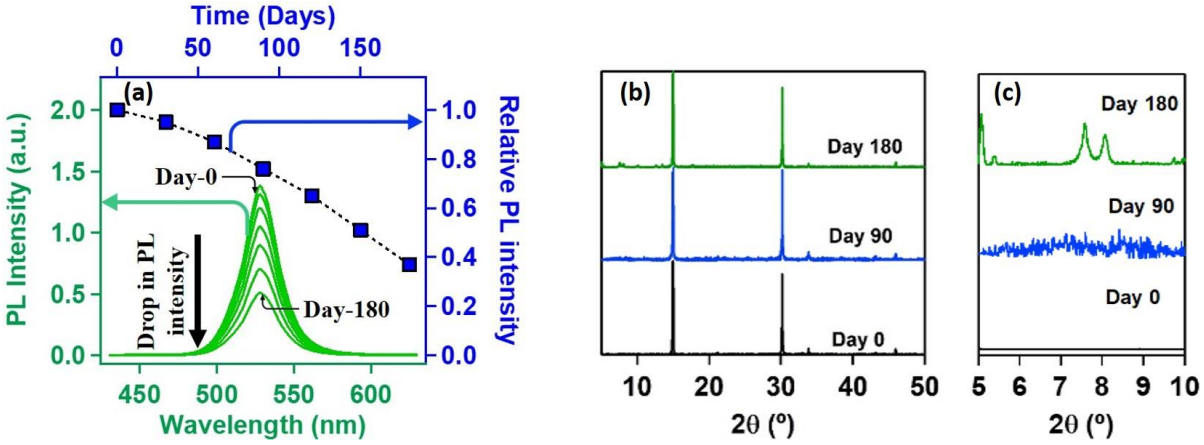

Figure 5.6. (a) PL Stability of $MAPbBr_3$ NCs. The green spectra denote the original PL spectra collected at different days after preparation (Excitation wavelength is 400 nm). The blue points denote the relative change in PL intensity of the green spectra. (b) PXRD pattern of $MAPbBr_3$ NCs in different days after preparation. (c) Magnified lower angle region from figure b.

5.2.4. Tuning of PL through anion exchange

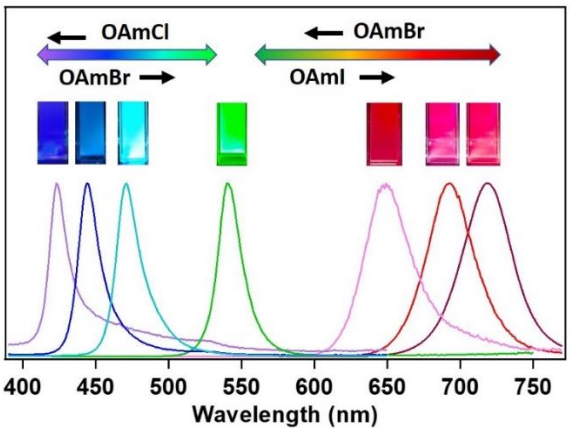

Figure 5.7. Tune of PL through anion exchange by oleylammonium halides (OAmX; X=Cl,Br,I).

Hybrid mixed lead halide perovskite NCs were synthesized from $MAPbBr_3$ through the anion exchange method to tune the PL over the entire visible region. We used 0.157 M hexane solution of oleylammoium halides (OAmX), as the halide source for this tuning. The detailed synthesis and characterizations of OAmX salts is described in the section 2.9.8 of chapter-2. The successive addition of OAmCl to the highly emissive $MAPbBr_3$ NCs gradually shifted the PL towards the blue region, indicating replacement of the bromide ions by the chloride ions in the perovskite lattice (see figure 5.7). The PL maximum reached to 421 nm at the saturation point (precisely, 210 µL of OAmCl to the 3 ml hexane suspension of purified $MAPbBr_3$ NCs obtained from addition of 100 mg of $PbBr_2$ salt to the green medium). This indicates the formation of $MAPbCl_3$ NCs by replacing almost all bromide ions of $MAPbBr_3$ NCs. The addition of OAmBr to $MAPbCl_3$ NCs again shifted the PL maxima towards the green region, indicating the reversibility of the process. The addition of OAmI to $MAPbBr_3$ showed a similar phenomenon and shifted the PL maximum up to 721 nm (precisely, 150 µL of OAmI to the 3 ml hexane suspension of purified $MAPbBr_3$ NCs obtained from addition of 100 mg of $PbBr_2$ salt to the green medium), indicating the formation of $MAPbI_3$ NCs (see figure 5.7). The change in halide composition is also monitored through XPS (see figure 5.8).

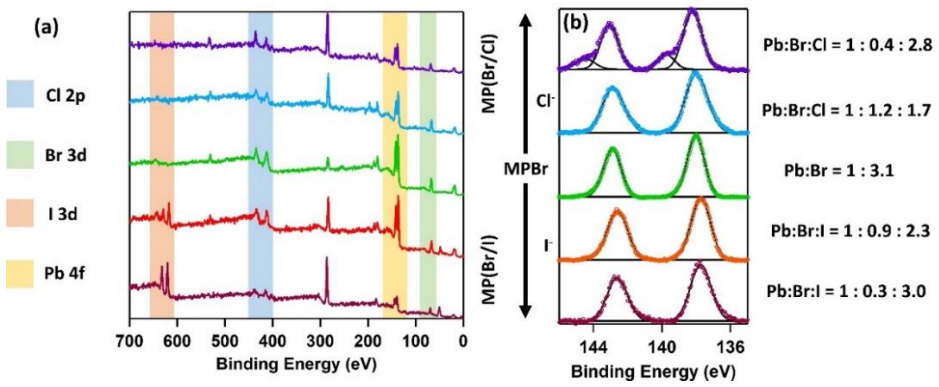

Figure 5.8. XPS of lead halide perovskites obtained from anion exchange reaction by OAmX (X=Cl, Br). (a) Survey spectra of lead halide perovskites obtained from anion exchange reaction by OAmX. The spectra corresponding to the lead halide perovskites having PL maxima 721 nm, 652 nm, 525 nm ($MAPbBr_3$), 458 nm and 424 nm (from down to up) respectively. (b) Corresponding binding energies of Pb-4f orbital. The calculated Pb:Br:X (X=Cl/I) is given.

5.2.5. Water stability of $MAPbBr_3$ NC through core-shell formation

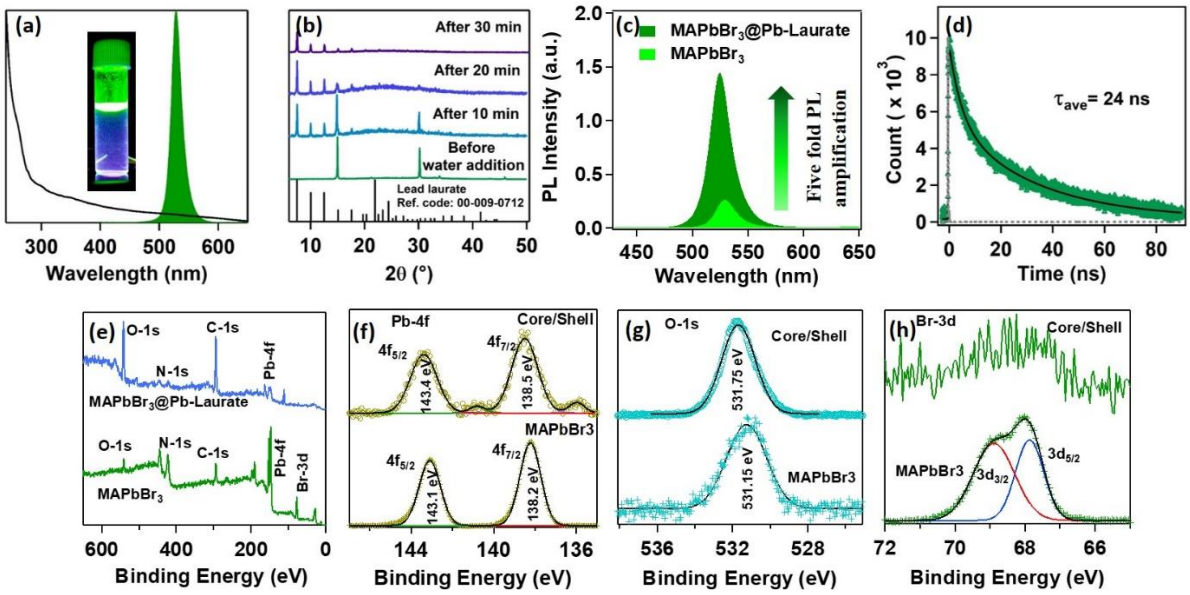

Figure 5.9. Characterization of $MAPbBr_3$@lead laurate core-shell NCs. (a) Steady state absorption (black) and emission (green) spectrum. (b) Time dependent change in PXRD pattern of lauric acid capped $MAPbBr_3$ NCs in water. Red stars denote the perovskite peaks. (c) Comparative PL intensities of $MAPbBr_3$ NCs and $MAPbBr_3$@lead laurate core/shell nanostructure. (d) PL transient of $MAPbBr_3$@lead laurate core-shell NCs upon exciting at 405 nm. (e) XPS survey spectrum of $MAPbBr_3$ NCs (lower part) and $MAPbBr_3$@lead laurate core/shell nanostructure (upper part). (f) High resolution XPS of Pb-4f of $MAPbBr_3$ NCs (lower part) and $MAPbBr_3$@lead laurate core/shell nanostructure (upper part). (g) High

resolution XPS of O-1s of $MAPbBr_3$ NCs (lower part) and $MAPbBr_3$@lead laurate core/shell nanostructure (upper part). (h) High resolution XPS of lead-4f of $MAPbBr_3$ NCs (lower part) and $MAPbBr_3$@lead laurate core/shell nanostructure (upper part).

Being highly water-immiscible, LA is expected to safeguard $MAPbBr_3$ NC from water while used as the capping ligand. The highly hydrophobic environment provided by the long alkyl chain of LA should not allow water molecules to go beyond the ligand environment and thus prevent the water molecules from interacting with the perovskite structure and increase the water stability. Keeping this in mind, we dispersed our synthesized $MAPbBr_3$ NCs into water. As expected, due to the hydrophobic character of the LA ligands, the NCs were unable to form suspension in the water, rather floats on the water surface even after vigorous shaking. The NCs show a very stable intense (see figure 5.9a) green photoluminescence in water, though the color of the NCs changes from deep yellow to white gradually. This flabbergasting observation motivates us to perform a time-dependent powder XRD study. The result shows an incremental decrease in the perovskite peaks with a concomitant appearance of new peaks in the low diffracting region (see figure 5.9b). Powder XRD of these new peaks shows high similarity with lead laurate (Ref. Code: 00-009-0712). The perovskite peaks fully disappear after 30 minutes (see figure 5.9b). However, the strong photoluminescence band at 528 nm remains persistent, confirming the presence of $MAPbBr_3$ perovskite NCs (see figure 5.9a). Interestingly, the PL intensity of the 528 nm band undergoes a 5-fold increase to reach near unity quantum yield (96%) (see figure 5.9c) in 30 min, while we observe a gradual increment in the lead laurate structure in powder XRD. We propose the formation of lead laurate shell over $MAPbBr_3$ NC as the possible mechanism for this observation. The masking of perovskite peaks in PXRD may be because of the lead laurate shell thickness. The time-resolved study of this core-shell type NCs shows an average lifetime of 24 ns that is almost twice of the parent $MAPbBr_3$ NCs (see figure 5.9d). The increment in average lifetime also signifies the sufficient attenuation of the non-radiative pathways in the core-shell type structure. XPS study of this sample reveals that the surface of the particles is mostly composed

of carbon and oxygen with a minimal amount of lead (79% C, 16% O and 5% Pb) (see figure 5.9e). The comparative XPS survey spectrum of both $MAPbBr_3$ NCs and $MAPbBr_3$@lead laurate further gives a clear picture of the carbon and oxygen rich surface in the core shell system, while for $MAPbBr_3$ NCs, the lead and bromine are sufficiently present on the surface. The high resolution XPS of Pb-4f of $MAPbBr_3$@lead laurate endure a shift of the binding energy by 0.3 eV (141.3 eV for $4f_{5/2}$ and 136.4 eV for $4f_{7/2}$) towards higher energy than the $MAPbBr_3$ NCs (141.0 eV for $4f_{5/2}$ and 136.1 eV for $4f_{7/2}$) (see figure 5.9f). This signifies the higher electronegative environment around the lead on the surface of the core-shell system. O-1s binding energy also shows a 0.6 eV shift, which can also be attributed to the same fact (see figure 5.9g). This observation confirms the formation of the Pb-O bond in the shell region. The very low concentration of bromine on the surface of the core-shell type structure further proves the formation of lead laurate shell (figure 5.9h).

TEM image of these core-shell type NCs is shown in figure 5.10a, which does not have a proper shape. A magnified image of this structure further reveals the formation of the lead laurate shell structure of thickness 5-8 nm (see figure 5.10b). The SAED pattern further confirms the presence of crystalline $MAPbBr_3$ NCs within the core of the structure (see figure 5.10c). The Fourier filtration from the selected area of the HRTEM image of $MAPbBr_3$@lead laurate (see figure 5.10d) produces figure 5.10e and figure 5.20f, where crystal planes (111) and (200) with d-spacing 0.37 nm and 0.30 nm, respectively, which are originating from the core are clearly visible. The bright field HAADF image (see figure 5.10g) further confirms the formation of the core-shell structure. The EDS elemental mapping of the core-shell structure clearly shows that the core is lead and bromine rich, whereas the shell is carbon rich which is a clear indication of lead laurate shell formation (see figure 5.10h). The EDS analysis from FESEM also conclude the same (see figure 5.11).

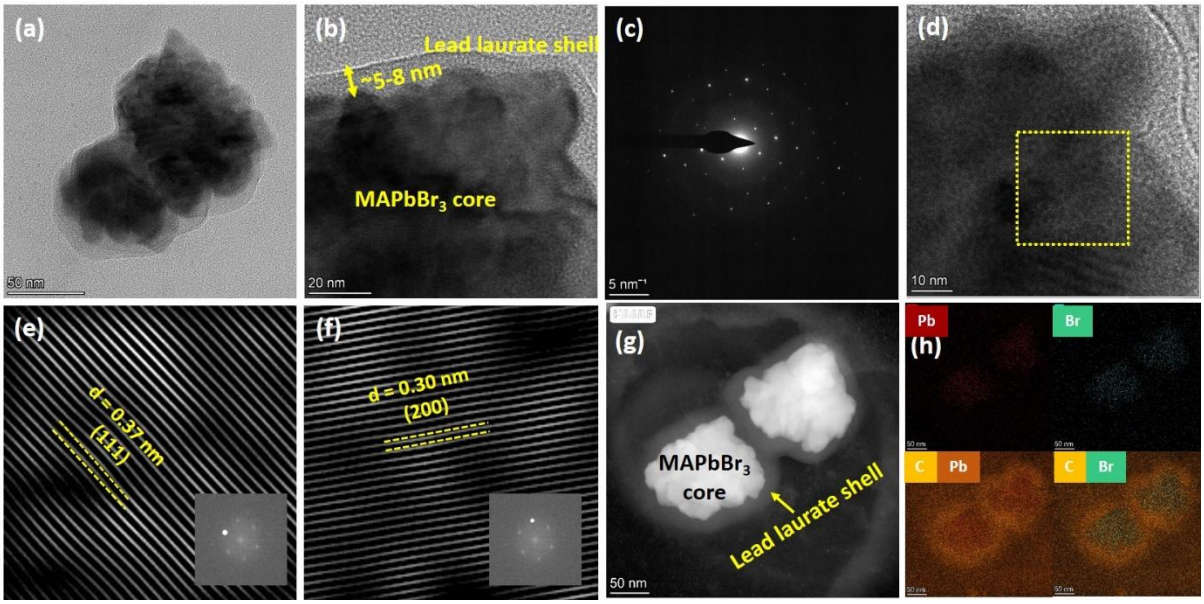

Figure 5.10. (a) TEM image of $MAPbBr_3$@lead laurate core-shell NCs. (b) Magnified TEM image of $MAPbBr_3$@lead laurate core-shell NCs. (c) SAED pattern of $MAPbBr_3$@lead laurate core-shell NCs. (d) HRTEM image of $MAPbBr_3$@lead laurate core-shell NCs. (e-f) Fourier filtration of the selected area showing (110) and (200) crystal planes. Inset containing the FFT pattern from the selected area of figure (g). (g) HAADF image of the $MAPbBr_3$@lead laurate core-shell NCs. (h) EDS elemental mapping of $MAPbBr_3$@lead laurate core-shell NCs (Pb, Br, C and Pb together, C and Br together).

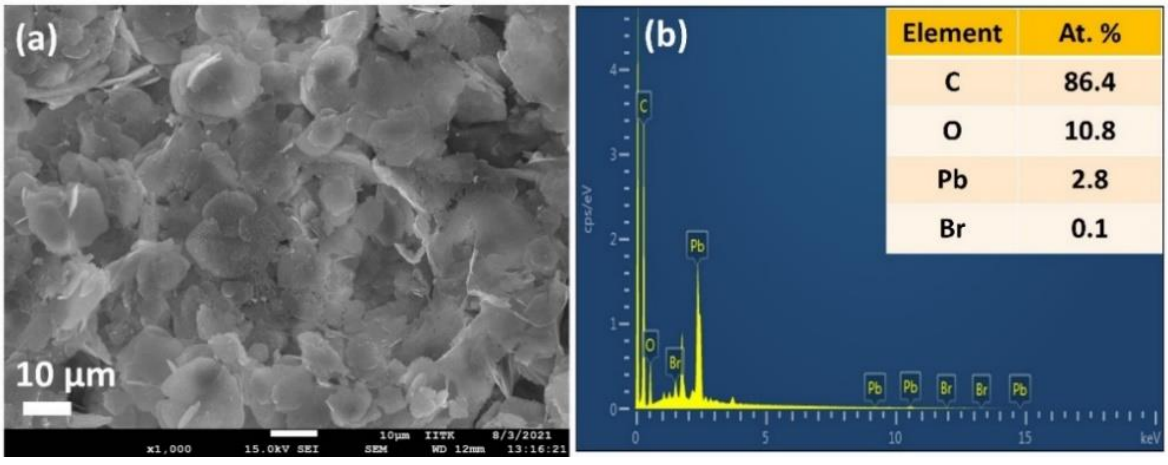

Figure 5.11. Scanning electron microscopic images of $MAPbBr_3$@lead laurate core/shell nanostructure. (a) FESEM image of $MAPbBr_3$@lead laurate core/shell nanostructure. EDS elemental analysis of the $MAPbBr_3$@lead laurate core/shell nanostructure from FESEM.

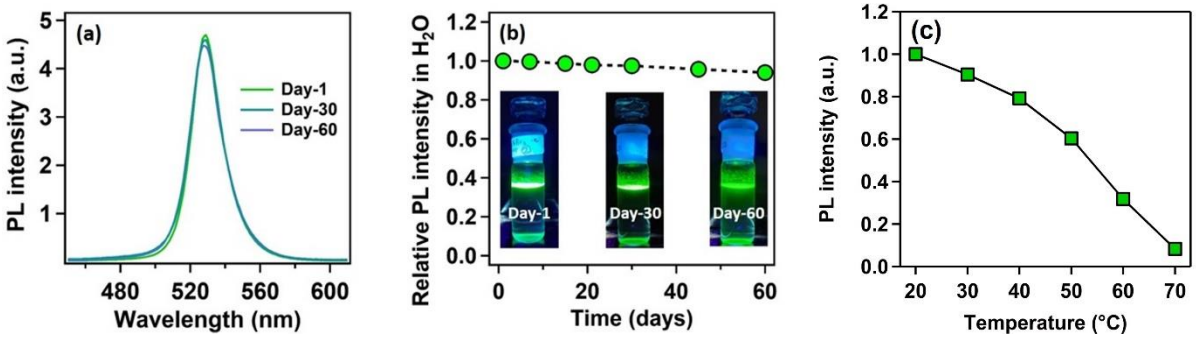

Figure 5.12. Water stability of the $MAPbBr_3$@lead laurate core-shell NC system. (a) Comparative PL spectra of the $MAPbBr_3$@lead laurate core-shell NC system in water, recorded on day-1, day-30, and day-60 upon exciting at 400 nm. (b) Relative change in PL intensity with the progress in days of the $MAPbBr_3$@lead laurate core-shell NC system in water. Real images of $MAPbBr_3$@lead laurate core-shell NC system in water under UV (365 nm) for day-1, day-30 and day-60 are given in inset. (c) Thermal stability of the MAPbBr3@lead laurate core-shell NCs.

After the self-growth of the lead laurate shell around the $MAPbBr_3$ NC core, the system shows extreme stability in the water as the formed lead laurate shell is itself hydrophobic. The PL intensity remains almost unaffected even after 60 days in the water (see figure 5.12a and figure 5.12b). The photographic images of the floating $MAPbBr_3$@lead laurate core-shell system in water under UV light show virtually unaffected PL intensity with the bare eye (see figure 5.12b). Such observations prove that the NCs have water stability. To note, the only available report of $MAPbBr_3$ NCs synthesized in green medium has much lower water stability (up to one hour).[22] The thermal stability was also checked for this core-shell system by monitoring its PL. With an increase in the temperature, the PL intensity decreases monotonously and becomes almost non-luminescent around 70 ºC, showing only moderate thermal stability (see figure 5.12c).

This $MAPbBr_3$@lead laurate core-shell structure did not respond to the anion exchange reaction (see figure 5.13). The thick 5-8 nm lead laurate shell completely inhibits the anion exchange process. This observation is important as the facile anion exchange process in the perovskite NCs might inhibit its use in white light-emitting diodes (WLEDs).[27-29] Earlier, Li *et al.* attempted to block the anion exchange process

by coating $CsPbBr_3$ NC by SiO_2 but failed.[30] However in the present case, the anion exchange reaction is ceased completely. This indicates that the shell thickness might acts as an effective shield for the anion exchange process. Recently Imran *et al.* reported a control over the anion exchange reaction in $CsPbX_3$ NC by using an amphiphilic polymer micelle and fabricated a stable WLED.[29] We believe that our green approach of synthesizing $MAPbBr_3$@lead laurate core-shell structure will play a crucial role in fabricating the stable WLED in the near future. Moreover, such water stability and suppression of the anion exchange ability of $MAPbBr_3$@lead laurate core-shell NC are achieved without any special control or extra perturbation generally needed to protect perovskite NC from water.[30, 31] This surprising and positive effect inspired us to have some insight into the mechanism of the process.

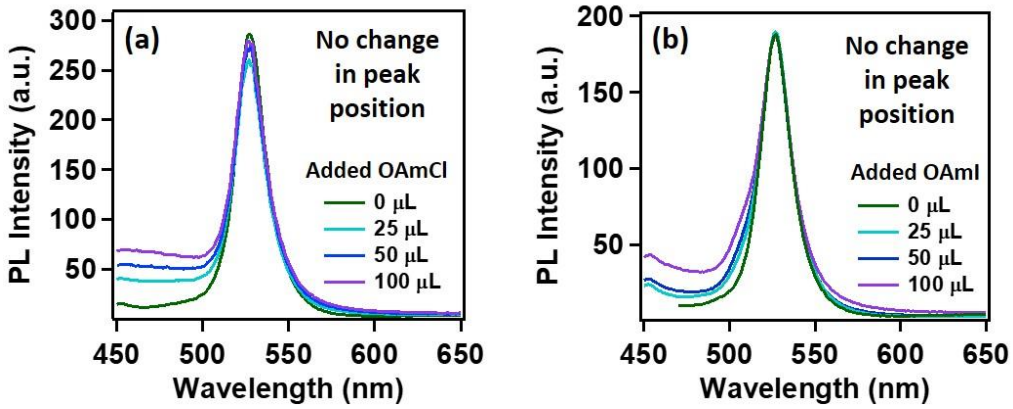

Figure 5.13. Response of the $MAPbBr_3$@lead laurate to the anion exchange reaction. (a) Response of the $MAPbBr_3$@lead laurate to the OAmCl. (b) Response of the $MAPbBr_3$@lead laurate to the OAmI. The concentrations of the added OAmCl and OAmI solutions were ~18 mmolar.

5.2.6. Mechanism of core shell formation through self-defense mechanism

To have an insight into the improved water stability and the formation of lead laurate shell on lauric acid capped $MAPbBr_3$ NCs, we propose a plausible mechanism involving the surface dissolution process of the NCs and the formation of lead laurate shell by the surface capping ligands in a self-defense mechanism. From the results it is evident that the lauric acid capped $MAPbBr_3$ NC forms the shell while in contact

with water. Recently, a very little amount of aqueous treatments have found to be beneficial to improve the surface properties of the hybrid lead halide perovskite NCs and its water stability through the formation of core-shell structures.[32, 33] Tiny amount of water degrades the surface of the NC on a small scale to produce the constituent cations and anions, which come into the water part.[33] However, LA being highly hydrophobic, the penetration of water molecules to the surface of the NCs is highly unlikely. But the formation of lead laurate shell indicates the removal of lead ion (Pb^{2+}) from the perovskite lattice site, which is the only source of the Pb^{2+} ion. It strongly suggests that water is somehow interacting with the $MAPbBr_3$ NC surface by overcoming the effectual barrier of the LA. We propose that, due to the dynamic nature of ligand binding,[34, 35] it is quite possible that a small fraction of dynamically bound lauric acid may slightly dislocated from the NC surface, leaving behind the NC surface becomes uncoordinated and allows very few water molecules to interact. This small fraction of water is ideal and sufficient to dissolve a limited surface layer of the $MAPbBr_3$ NC. Different constituent cations and anion like methylammonium ($CH_3NH_3^+$), divalent lead (Pb^{2+}) and bromide (Br^-) come into the water part and the divalent lead (Pb^{2+}) forms the lead laurate shell by reacting with laurate anion.

This small-scale water-assisted degradation of $MAPbBr_3$ NC becomes a boon and beneficial in three ways – (1) Within 30 minutes, an effective lead laurate shell has formed around the $MAPbBr_3$ NC core that protects the NC from any further degradation by the water. (2) The formation of the shell replenishes the surface of the $MAPbBr_3$ NC in a way that reduces the surface-related trap states and increases the radiative recombination rate. It ultimately increases the PLQY and average PL-lifetime of the core-shell perovskite NC and makes it highly water stable. (3) The hydrophobic nature of LA itself acts as the controller to optimize the interaction between water and perovskite surface. The reaction scheme on the surface of $MAPbBr_3$ NCs is proposed to be

$$CH_3NH_3PbBr_3\ (surface) \xrightarrow{H_2O} CH_3NH_3^+ + Pb^{2+} + 3Br^-$$

$$2RCOOH + Pb^{2+} = (RCOO)_2Pb + 2H^+$$

According to this reaction scheme, the medium should be acidic after the lead laurate shell formation and should also contain excess bromide ions. To confirm this, we measured the pH of the water after $MAPbBr_3$ NC treatment. The water become acidic (pH = 5.21) as expected after formation of the lead laurate shell, whereas the pH of the water that was used for the experiment was neutral (pH = 6.79). Further, we measured the bromide ion level of water as 200 PPM after the formation of the lead laurate shell by the ion chromatography (which was below detection limit before the $MAPbBr_3$ NC treatment). These two observations further established our proposed mechanism, which is depicted in scheme 1.

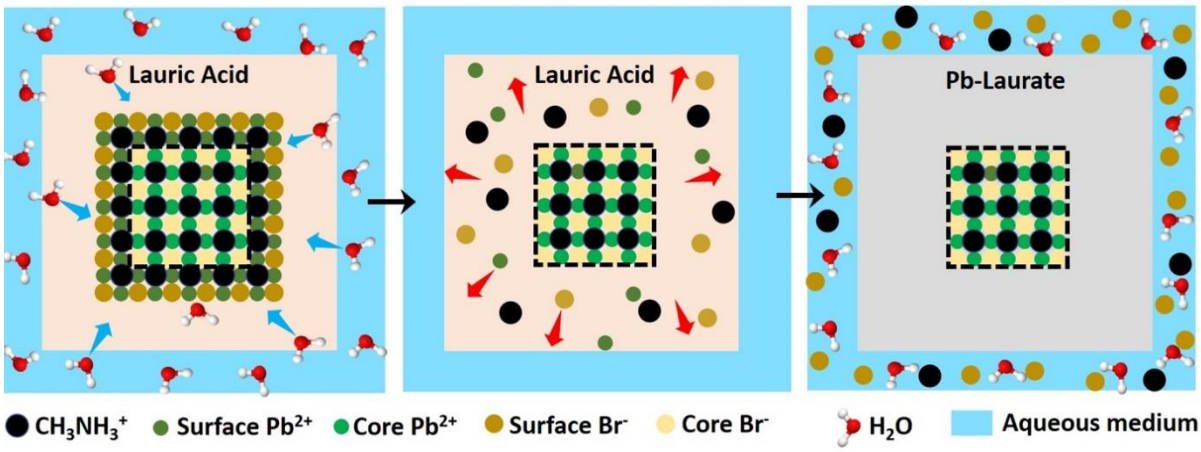

Scheme 1. Schematic representation of the proposed mechanism of lead laurate shell formation around the $MAPbBr_3$ NC in presence of water.

5.2.7. Synthesis of other $MAPbX_3$ (X=Cl, I) NCs – universality of the green solvent medium

To demonstrate the universality of the ionic liquid like medium, we synthesized other $MAPbX_3$ s (X=Cl, I). $MAPbCl_3$ and $MAPbI_3$ NCs were prepared by direct addition of $PbCl_2$ and PbI_2 salt to the green solvent medium (see section 2.9.12 of

chapter-2 for details). The purified $MAPbCl_3$ and $MAPbI_3$ NCs show pure cubic and tetragonal crystalline phase, respectively (see figure 5.14).[36] Along with $MAPbI_3$ phase, there also appears lower diffraction angle peaks. This may appear due to partial surface degradation to the lead laurate by the atmospheric moisture (see figure 5.14).

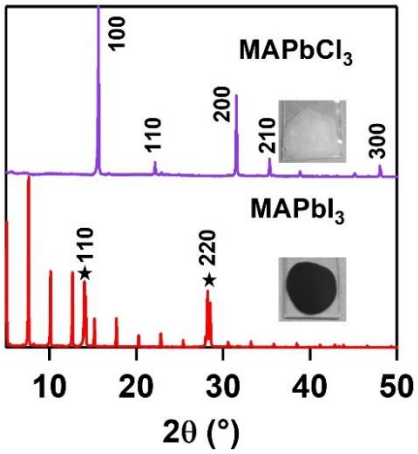

Figure 5.14. PXRD of $MAPbCl_3$ NCs (violet) and $MAPbI_3$ NCs (red). Both the NCs were prepared by direct addition of $PbCl_2$ salt and PbI_2 salt to the green solvent medium followed by extraction in hexane. The photographic image of the used NC films used for PXRD is given in inset.

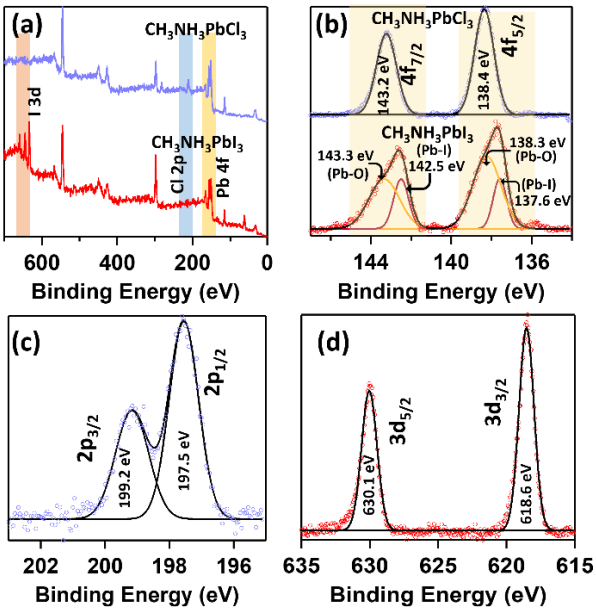

Figure 5.15. XPS analysis of $MAPbCl_3$ NCs and $MAPbI_3$ NCs. Both the NCs were prepared by direct addition of $PbCl_2$ salt and PbI_2 salt to the green solvent medium. (a) Survey spectra of $MAPbCl_3$ NCs (upper part, violet) and $MAPbI_3$ NCs (lower part, red). (b) High resolution

XPS of Pb-4f of $MAPbCl_3$ NCs (upper part, violet) and $MAPbI_3$ NCs (lower part, red). (c) High resolution XPS of Cl-2p of $MAPbCl_3$ NCs. (d) High resolution XPS of I-4d of $MAPbI_3$ NCs.

Detailed XPS analysis revealed a halide rich surface in both $MAPbCl_3$ (chlorine to lead ratio 3.1) and $MAPbI_3$ NCs (iodine to lead ratio 3.4) (see figure 5.15). However, high resolution XPS of lead shows that two types of lead are present in the $MAPbI_3$ NCs (see figure 5.15b). This may arise due to the partial surface degradation to lead laurate which is in line with the XRD analysis.

FESEM analysis shows the formation of cubic $MAPbCl_3$ NCs of size ~100-150 nm (see figure 5.16a). FESEM of $MAPbI_3$ NCs shows the formation of some irregular cubic particles of size ~100 nm (see figure 5.16b).

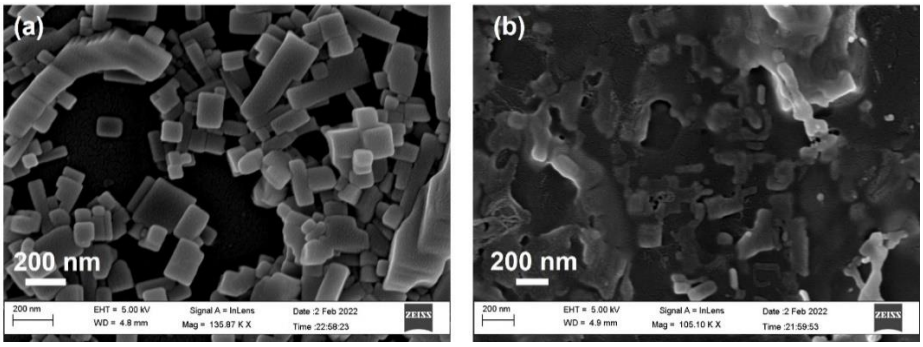

Figure 5.16. FESEM images of (a) $MAPbCl_3$ NCs and (b) $MAPbI_3$ NCs.

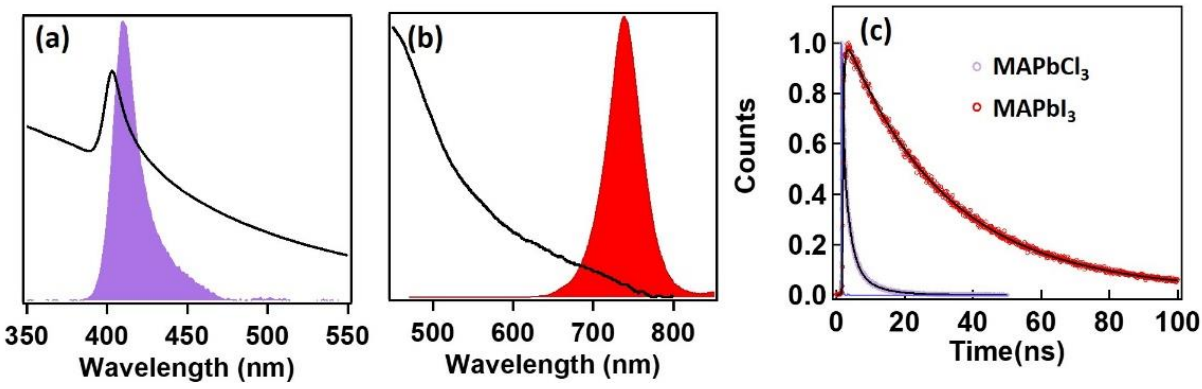

Figure 5.17. (a) Absorption (black) and PL spectra (violet) of $MAPbCl_3$ NCs. (b) Absorption (black) and PL spectra (red) $MAPbI_3$ NCs. (c) Time resolved PL of $MAPbCl_3$ NCs (violet) and $MAPbI_3$ NCs (red) having average lifetime 1.6 ns and 23.2 ns respectively. (d) PXRD of $MAPbCl_3$ NCs (violet) and $MAPbI_3$ NCs (red). Both the NCs were prepared by direct addition

of $PbCl_2$ salt and PbI_2 salt to the green solvent medium followed by extraction in hexane. The photographic image of the used NC films used for PXRD is given in inset.

The $MAPbCl_3$ NCs have a strong excitonic peak at 403 nm and a very weak PL at around 409 nm (see figure 5.17a). The $MAPbI_3$ NCs show a broad absorption and PL centered at 741 nm (see figure 5.17b). Time-resolved PL of $MAPbCl_3$ and $MAPbI_3$ NCs show an average lifetime of 1.6 ns and 23.2 ns, respectively (see figure 5.17c).

5.2.8. Reusability of the green solvent medium

The reusability of the solvent medium was checked for ten times. Primarily $PbBr_2$ (50 mg) salt was added to the medium (~3ml) to prepare $MAPbBr_3$ NCs. The NCs was then centrifuged at 40ºC and collected through redispersing in hexane. The green medium which remained in the supernatant was then again used for the synthesis of the NCs. This process was repeated for ten times and in each time the NCs were prepared with more or less same PL intensity (figure 5.18a and 5.18b) and in pure cubic crystalline phase (figure 5.18c).

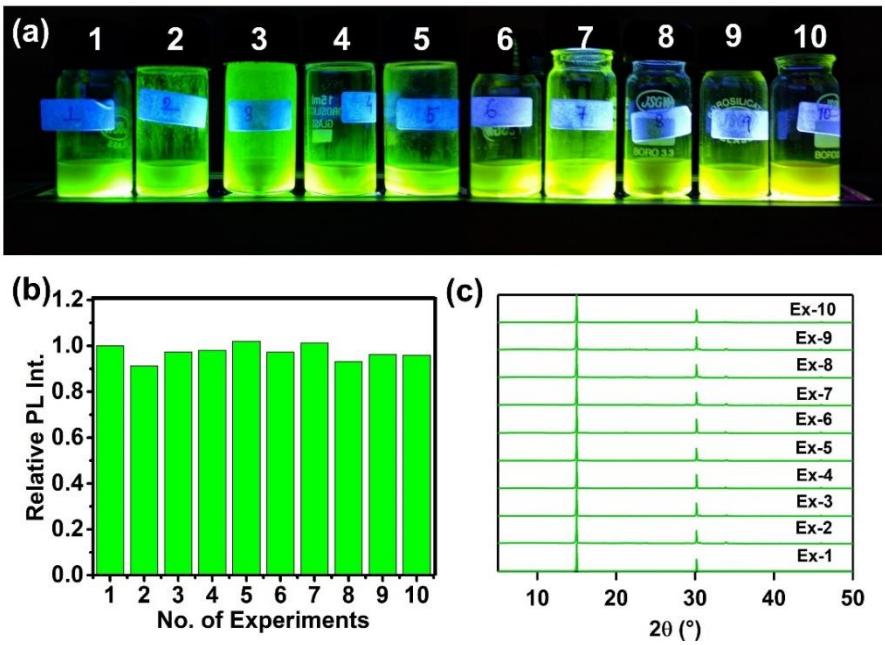

Figure 5.18. Reusability of the green solvent medium. (a) Optical images of the hexane extracted $MAPbBr_3$ NCs under UV light prepared by adding $PbBr_2$ to reused green medium

(1-10 denotes the n-th time that green medium being reused). (b) Relative PL intensity of the $MAPbBr_3$ NCs, prepared by reusing the green medium. (c) PXRD patterns of the $MAPbBr_3$ NCs, prepared by reusing the green medium.

5.3. Conclusions and Future Aspects

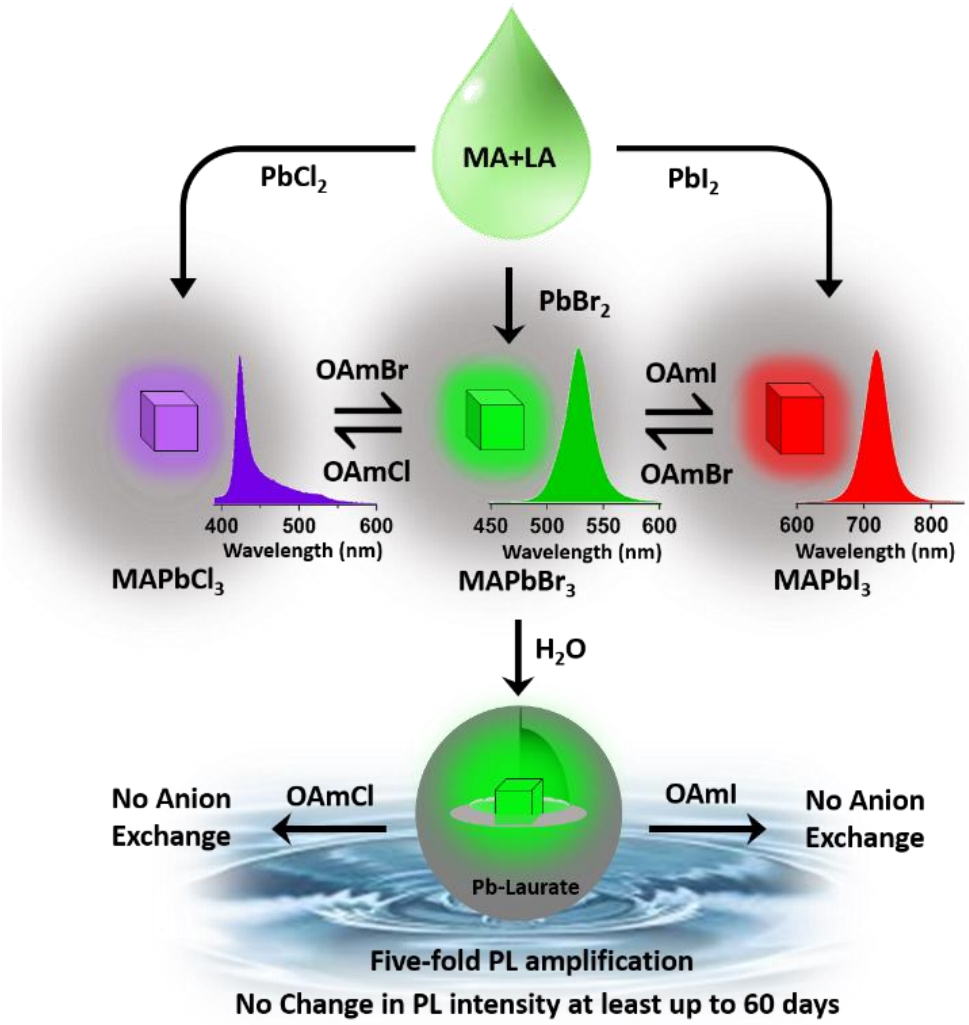

Scheme 2. Schematic representation of the main highlights of the work. Lauric acid and methyl amine (LA+MA) forms the green media, to which addition of $PbBr_2$ produces $MAPbBr_3$ NCs without the use of any hazardous solvent. The entire visible range was tuned through anion exchange. Addition of water to $MAPbBr_3$ NCs produces a core-shell in a unique self-defence mechanism that makes the NCs highly water stable (at least 60 days) with a five-fold increase in PLQY. The inhibition of anion exchange in the core-shell structure is also highlighted

In conclusion, this report demonstrates a single step green synthesis of $MAPbBr_3$ NCs embeded with lauric acid and the formation of $MAPbBr_3$@lead laurate core-

shell NC with exceptional water stability. The main highlights of this work are depicted in scheme 3 and also summarized as follows: (i) We have successfully synthesized green luminescent $MAPbBr_3$ NCs without using any hazardous organic solvents in a single-step green synthetic approach having a moderate PLQY of ~19%, and good environmental stability of up to 6 months. (ii) The PL over the entire visible range was tuned by synthesizing $MAPbX_3$ NCs (where X is Cl, Br, I, and a mixture of either Cl and Br or Br and I) through anion exchange method. (iii) The NC forms a core-shell structure ($MAPbBr_3$@lead laurate) in a unique self-defence mechanism when in contact with water, which proved to be hugely beneficial. Firstly, owing to its hydrophobic nature, the shell safeguards the perovskite from further degradation by water and makes it highly water stable (at least two months). Secondly, through surface modification, a five-fold increase of PLQY and two-fold increase of PL-lifetime is achieved. Thirdly, It prevents the anion exchange process. To our delight, all these positive effects are achieved without any special control or extra perturbation. Further, the universality is demonstrated by synthesizing the $MAPbCl_3$ and $MAPbI_3$ NCs in the medium following same procedure. To knowledge, such stability and PLQY enhancement in a self-defense mechanism is demonstrated for the first time, that too in a so called green medium and should be a reference point for accelerating the performance and stability of perovskite nanocrystals in the future.

References

1. Dong, Y.; Zhao, Y.; Zhang, S.; Dai, Y.; Liu, L.; Li, Y.; Chen, Q., Recent advances toward practical use of halide perovskite nanocrystals. *Journal of Materials Chemistry A* **2018,** *6* (44), 21729-21746.
2. Dey, A.; Ye, J.; De, A.; Debroye, E.; Ha, S. K.; Bladt, E.; Kshirsagar, A. S.; Wang, Z.; Yin, J.; Wang, Y., State of the art and prospects for halide perovskite nanocrystals. *ACS nano* **2021,** *15* (7), 10775-10981.
3. Tailor, N. K.; Abdi-Jalebi, M.; Gupta, V.; Hu, H.; Dar, M. I.; Li, G.; Satapathi, S., Recent progress in morphology optimization in perovskite solar cell. *Journal of Materials Chemistry A* **2020,** *8* (41), 21356-21386.
4. Vidal, R.; Alberola-Borràs, J.-A.; Habisreutinger, S. N.; Gimeno-Molina, J.-L.; Moore, D. T.; Schloemer, T. H.; Mora-Seró, I.; Berry, J. J.; Luther, J. M., Assessing health and environmental impacts of solvents for producing perovskite solar cells. *Nature Sustainability* **2021,** *4* (3), 277-285.
5. Chatterjee, S.; Ghosal, M.; Tiwari, K.; Sen, P., Potassium-Induced Passivation of Deep Traps in Bismuth-Doped Hybrid Lead Bromide Perovskite Nanocrystals: Massive Amplification of Photoluminescence Quantum Yield. *The Journal of Physical Chemistry Letters* **2020,** *12* (1), 546-551.
6. Zhang, F.; Huang, S.; Wang, P.; Chen, X.; Zhao, S.; Dong, Y.; Zhong, H., Colloidal synthesis of air-stable CH3NH3PbI3 quantum dots by gaining chemical insight into the solvent effects. *Chemistry of Materials* **2017,** *29* (8), 3793-3799.
7. Hamill, J. C., Jr.; Schwartz, J.; Loo, Y.-L., Influence of Solvent Coordination on Hybrid Organic–Inorganic Perovskite Formation. *ACS Energy Letters* **2018,** *3* (1), 92-97.
8. Stevenson, J.; Sorenson, B.; Subramaniam, V. H.; Raiford, J.; Khlyabich, P. P.; Loo, Y.-L.; Clancy, P., Mayer Bond Order as a Metric of Complexation Effectiveness in Lead Halide Perovskite Solutions. *Chemistry of Materials* **2017,** *29* (6), 2435-2444.

9. Gardner, K. L.; Tait, J. G.; Merckx, T.; Qiu, W.; Paetzold, U. W.; Kootstra, L.; Jaysankar, M.; Gehlhaar, R.; Cheyns, D.; Heremans, P., Nonhazardous solvent systems for processing perovskite photovoltaics. *Advanced Energy Materials* **2016,** *6* (14), 1600386.
10. Hassan, Y.; Ashton, O. J.; Park, J. H.; Li, G.; Sakai, N.; Wenger, B.; Haghighirad, A.-A.; Noel, N. K.; Song, M. H.; Lee, B. R.; Friend, R. H.; Snaith, H. J., Facile Synthesis of Stable and Highly Luminescent Methylammonium Lead Halide Nanocrystals for Efficient Light Emitting Devices. *Journal of the American Chemical Society* **2019,** *141* (3), 1269-1279.
11. Niu, T.; Chao, L.; Gao, W.; Ran, C.; Song, L.; Chen, Y.; Fu, L.; Huang, W., Ionic Liquids-Enabled Efficient and Stable Perovskite Photovoltaics: Progress and Challenges. *ACS Energy Letters* **2021,** *6* (4), 1453-1479.
12. Hoang, M. T.; Ünlü, F.; Martens, W.; Bell, J.; Mathur, S.; Wang, H., Towards the environmentally friendly solution processing of metal halide perovskite technology. *Green Chemistry* **2021,** *23* (15), 5302-5336.
13. Moore, D. T.; Tan, K. W.; Sai, H.; Barteau, K. P.; Wiesner, U.; Estroff, L. A., Direct Crystallization Route to Methylammonium Lead Iodide Perovskite from an Ionic Liquid. *Chemistry of Materials* **2015,** *27* (9), 3197-3199.
14. Oez, S.; Burschka, J.; Jung, E.; Bhattacharjee, R.; Fischer, T.; Mettenboerger, A.; Wang, H.; Mathur, S., Protic ionic liquid assisted solution processing of lead halide perovskites with water, alcohols and acetonitrile. *Nano Energy* **2018,** *51*, 632-638.
15. Li, D.; Chao, L.; Chen, C.; Ran, X.; Wang, Y.; Niu, T.; Lv, S.; Wu, H.; Xia, Y.; Ran, C., In situ interface engineering for highly efficient electron-transport-layer-free perovskite solar cells. *Nano Letters* **2020,** *20* (8), 5799-5806.
16. Liu, L.; Tang, Z.; Xin, C.; Zhu, S.; An, S.; Wang, N.; Fan, L.; Wei, C.; Huang, Q.; Hou, G., Acetate anion assisted crystal orientation reconstruction

in organic–inorganic lead halide perovskite. *ACS Applied Energy Materials* **2018,** *1* (6), 2730-2739.

17. Liu, D.; Shao, Z.; Gui, J.; Chen, M.; Liu, M.; Cui, G.; Pang, S.; Zhou, Y., A polar-hydrophobic ionic liquid induces grain growth and stabilization in halide perovskites. *Chemical Communications* **2019,** *55* (74), 11059-11062.
18. Seo, J. Y.; Matsui, T.; Luo, J.; Correa-Baena, J. P.; Giordano, F.; Saliba, M.; Schenk, K.; Ummadisingu, A.; Domanski, K.; Hadadian, M., Ionic liquid control crystal growth to enhance planar perovskite solar cells efficiency. *Advanced Energy Materials* **2016,** *6* (20), 1600767.
19. Li, M.; Zhao, C.; Wang, Z. K.; Zhang, C. C.; Lee, H. K.; Pockett, A.; Barbé, J.; Tsoi, W. C.; Yang, Y. G.; Carnie, M. J., Interface modification by ionic liquid: a promising candidate for indoor light harvesting and stability improvement of planar perovskite solar cells. *Advanced Energy Materials* **2018,** *8* (24), 1801509.
20. Xia, Y.; Ran, C.; Chen, Y.; Li, Q.; Jiang, N.; Li, C.; Pan, Y.; Li, T.; Wang, J.; Huang, W., Management of perovskite intermediates for highly efficient inverted planar heterojunction perovskite solar cells. *Journal of Materials Chemistry A* **2017,** *5* (7), 3193-3202.
21. Chakraborty, D.; Preeyanka, N.; Akhuli, A.; Sarkar, M., Enhancing the Stability and Photoluminescence Quantum Yield of CsPbX3 (X = Cl and Br) Perovskite Nanocrystals by Treatment with Imidazolium-Based Ionic Liquids through Surface Modification. *The Journal of Physical Chemistry C* **2021,** *125* (48), 26652-26660.
22. Hoang, M. T.; Pham, N. D.; Yang, Y.; Tiong, V. T.; Zhang, C.; Gui, K.; Chen, H.; Chang, J.; Wang, J.; Golberg, D.; Bell, J.; Wang, H., A facile, environmentally friendly synthesis of strong photo-emissive methylammonium lead bromide perovskite nanocrystals enabled by ionic liquids. *Green Chemistry* **2020,** *22* (11), 3433-3440.

23. Morrow, B. H.; Koenig, P. H.; Shen, J. K., Atomistic simulations of pH-dependent self-assembly of micelle and bilayer from fatty acids. *The Journal of Chemical Physics* **2012,** *137* (19), 194902.
24. Levchuk, I.; Herre, P.; Brandl, M.; Osvet, A.; Hock, R.; Peukert, W.; Schweizer, P.; Spiecker, E.; Batentschuk, M.; Brabec, C. J., Ligand-assisted thickness tailoring of highly luminescent colloidal CH 3 NH 3 PbX 3 (X= Br and I) perovskite nanoplatelets. *Chemical Communications* **2017,** *53* (1), 244-247.
25. Zhang, F.; Zhong, H.; Chen, C.; Wu, X.-g.; Hu, X.; Huang, H.; Han, J.; Zou, B.; Dong, Y., Brightly luminescent and color-tunable colloidal CH3NH3PbX3 (X= Br, I, Cl) quantum dots: potential alternatives for display technology. *ACS nano* **2015,** *9* (4), 4533-4542.
26. Paul, S.; Samanta, A., N-Bromosuccinimide as Bromide Precursor for Direct Synthesis of Stable and Highly Luminescent Green-Emitting Perovskite Nanocrystals. *ACS Energy Letters* **2019,** *5* (1), 64-69.
27. Imran, M.; Mai, B. T.; Goldoni, L.; Cirignano, M.; Jalali, H. B.; Di Stasio, F.; Pellegrino, T.; Manna, L., Switchable Anion Exchange in Polymer-Encapsulated APbX3 Nanocrystals Delivers Stable All-Perovskite White Emitters. *ACS Energy Letters* **2021,** *6* (8), 2844-2853.
28. Liu, X.-K.; Xu, W.; Bai, S.; Jin, Y.; Wang, J.; Friend, R. H.; Gao, F., Metal halide perovskites for light-emitting diodes. *Nature Materials* **2021,** *20* (1), 10-21.
29. Bidikoudi, M.; Fresta, E.; Costa, R. D., White perovskite based lighting devices. *Chemical Communications* **2018,** *54* (59), 8150-8169.
30. Li, M.; Zhang, X.; Yang, P., Controlling the growth of a SiO2 coating on hydrophobic CsPbBr3 nanocrystals towards aqueous transfer and high luminescence. *Nanoscale* **2021,** *13* (6), 3860-3867.

31. Ahmed, G. H.; Yin, J.; Bakr, O. M.; Mohammed, O. F., Successes and Challenges of Core/Shell Lead Halide Perovskite Nanocrystals. *ACS Energy Letters* **2021,** *6* (4), 1340-1357.
32. Yu, Z.; Sun, X., Acousto-optic modulation of photonic bound state in the continuum. *Light: Science & Applications* **2020,** *9* (1), 1.
33. Liu, Y.; Li, F.; Liu, Q.; Xia, Z., Synergetic Effect of Postsynthetic Water Treatment on the Enhanced Photoluminescence and Stability of CsPbX3 (X = Cl, Br, I) Perovskite Nanocrystals. *Chemistry of Materials* **2018,** *30* (19), 6922-6929.
34. De Roo, J.; Ibáñez, M.; Geiregat, P.; Nedelcu, G.; Walravens, W.; Maes, J.; Martins, J. C.; Van Driessche, I.; Kovalenko, M. V.; Hens, Z., Highly Dynamic Ligand Binding and Light Absorption Coefficient of Cesium Lead Bromide Perovskite Nanocrystals. *ACS Nano* **2016,** *10* (2), 2071-2081.
35. Chatterjee, S.; Dey, P.; Das, N.; Tiwari, K.; Maiti, T.; Sen, P., Reversible Ultra-Slow Crystal Growth of Mixed Lead Bismuth Perovskite Nanocrystals: The Presence of Dynamic Capping. *Chemistry – A European Journal* **2020,** *26* (7), 1506-1510.
36. Imran, M.; Caligiuri, V.; Wang, M.; Goldoni, L.; Prato, M.; Krahne, R.; De Trizio, L.; Manna, L., Benzoyl Halides as Alternative Precursors for the Colloidal Synthesis of Lead-Based Halide Perovskite Nanocrystals. *Journal of the American Chemical Society* **2018,** *140* (7), 2656-2664.

Chapter-6

Green Synthesis of 3D Cesium Lead Halide Perovskite Nanocrystals and 2D Ruddlesden-Popper Nanoplatelets in Menthol-based Deep Eutectic Solvents

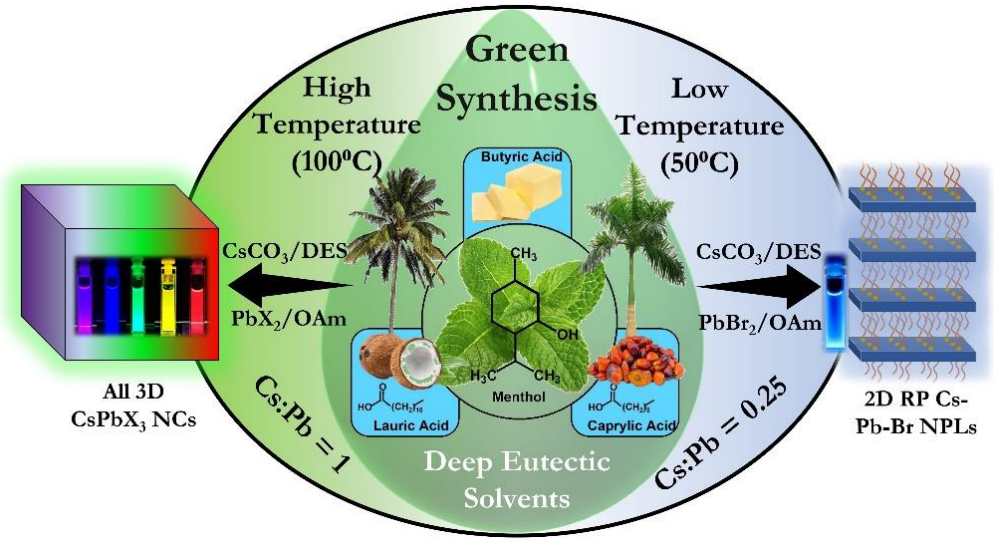

Shovon Chatterjee, Arghya Sen, and Pratik Sen. *Manuscript submitted*.

Organic solvent hazards are the most overlooked part of perovskite research. In this report, we employed menthol based deep eutectic solvents (DESs) as a green medium for the synthesis of cesium lead halide ($CsPbX_3$; X=Cl, Br, I, or either both) nanocrystals (NCs) and nanoplates (NPLs) with high PLQY (maximum of 78%) aiming to reduce the synthesis related toxicity. The reaction temperature and added precursor ratio in the DES medium were found to be the key factor in controlling the dimensionality of the NCs. The synthesized NCs and NPLs in the DES medium suffer from common halide vacancy-related defects, which were passivated by oleylammonium halide treatment to achieve near unity PLQY. With green DES as a synthesis medium, the present synthetic protocol lowered crystallization temperature, allow ambient condition synthesis, and yields high quality NCs/NPLs with almost uniform size distribution. This study presents a novel approach to the environmentally friendly synthesis of NCs and NPLs, which holds great potential for the practical large-scale synthesis of perovskites in industrial scale.

6.1. Introduction

Nature necessitates the environmental sustainability of all industrial productions. Among several factors, solvent is a substantial contributor to the overall toxicity profile of an industrial process.[1, 2] To tackle this issue, diverse green solvents are being introduced in lieu of conventional hazardous organic solvents in a variety of applications.[2-4] Midst all the alternate solvent media, deep eutectic solvents (DES) are quickly gaining interest among the researchers because of their uniqueness like easy preparation, fine tunability, cost-effectiveness, etc.[3-5] Although DESs have already been identified as alternate solvent for biochemical application,[4, 5] its use in material sciences has not been explored yet. Herein, we used menthol-based DESs as green solvent media to synthesize pure inorganic cesium lead halide nanocrystals (NC) ($CsPbX_3$ NCs, X=Cl, Br, I) which largely reduces the organic solvent-related hazards of perovskite NC synthesis. The photoluminescence tunability from violet to red has been achieved in DES media by tuning the halide compositions. The reaction temperature and cesium to lead precursor ratio in the DES medium were found to be the key factor in controlling the dimensionality and were further used to synthesize Ruddlesden-Popper $(OAm)_2Cs_2Pb_3Br_{10}$ nanoplatelets (NPLs) with blue photoluminescence.

Perovskite research has advanced at a breakneck speed in the last decade.[6, 7] Due to the defect-tolerant nature, high photoluminescence quantum yield (PLQY), and narrow PL bandwidth, the nanocrystalline form of lead halide perovskites have proved their immense potential in the field of optoelectronics.[6, 7] However, because of the low environmental and water stability, the practical application is still a long way off.[8, 9] Lead toxicity is still a key issue in perovskite, which is driving the development of lead-free perovskites.[10, 11] However, overcoming solvent-related toxicity during synthesis (typically due to toxic DMF, NMP, skin penetrating DMSO, skin irritant octadecene, etc.) is yet another crucial but overlooked aspect of this research field.[12] Another major worry is that these precursor solvents have a high propensity to coordinate with the perovskite surface, allowing the perovskite

structure to degrade.[13] Using ionic liquid (IL) as a precursor media, a few breakthroughs have been achieved in this direction. [12] Moore *et al.* reported the synthesis of methylammonium lead iodide thin film from methylamine/short chain carboxylic acid IL medium in 2015.[14] Following this, a number of studies have been published that indicate how IL additives can regulate crystal formation, stability, and surface modification in perovskite thin films.[12] [15]However, all of these reports revolve around the thin film/solar cell application of perovskite. For the first time Hoang *et al.* reported the green synthesis of methylammonium lead bromide NCs in 2020.[16] By combining methylamine with short-chain aliphatic carboxylic acids, they were able to synthesize an IL medium, which was used to synthesize $MAPbBr_3$ NCs with ~50% PLQY. Recently, we employed highly hydrophobic lauric acid to prepare methylammonium laurate IL medium, which finally leads to the formation of water stable $MAPbBr_3$@laed laurate core-shell nanostructure with near-unity PLQY.[17]

One major drawback of this IL-based alternate solvent media is the poor solubility of the precursor salts. The use of solid lead halide salts for synthesizing perovskite in IL media restricts the possibility of doping and synthesizing of mixed perovskite materials. [16, 17] The only solution is to increase the universality of the alternate solvent, where both hydrophobic and hydrophilic precursors are soluble. To tackle this issue, we have used menthol based DESs (Figure 1a-1d), c.a. 1:2 lauric acid/menthol (LAMe), 1:1 caprylic acid/menthol (CAMe), and 1:1 butyric acid/menthol (BAMe).[18, 19] The solubility of lead halide salts in these DES media are excellent in presence of oleyamine (OAm). Using this key solubility factor, we have synthesized highly luminescent $CsPbX_3$ NCs and 2D RP NPLs in this green DES medium.

6.2. Characterization of DESs

These DESs have excellent heat tolerance and remain colourless liquids at room temperature. TGA study shows no weight loss till 100°C for LAMe and CAMe (see

figure 6.1). However, the degradation of BAMe starts around 60°C (see figure 6.1). IR and NMR measurements were performed to characterize DES media as well which have been presented in section 2.9.13 of chapter 2.

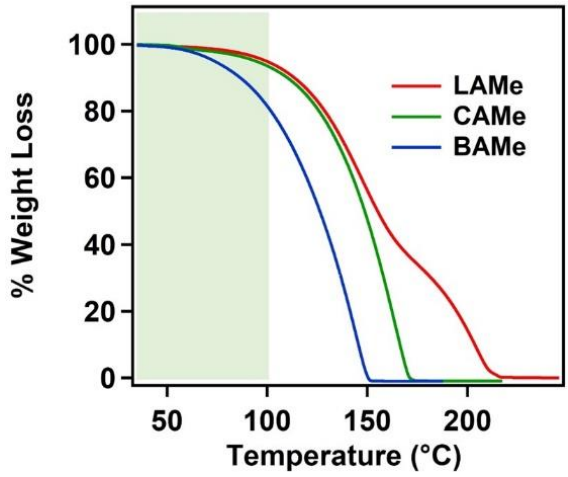

Figure 6.1. Thermogravimetric analysis of LAMe, CAMe, and BAMe DES media.

6.3. Characterization of CPB NCs prepared in DES media

Among pure inorganic perovskite NCs, green-emitting $CsPbBr_3$ is the most celebrated considering its structural stability and massive PLQY. The major synthetic protocol for the synthesis of this NC is the hot injection method, where temperature is raised to ~170 °C in inert atmospheric condition to initiate the crystallization. Also in the hot injection procedure, there is still no replacement of hazardous

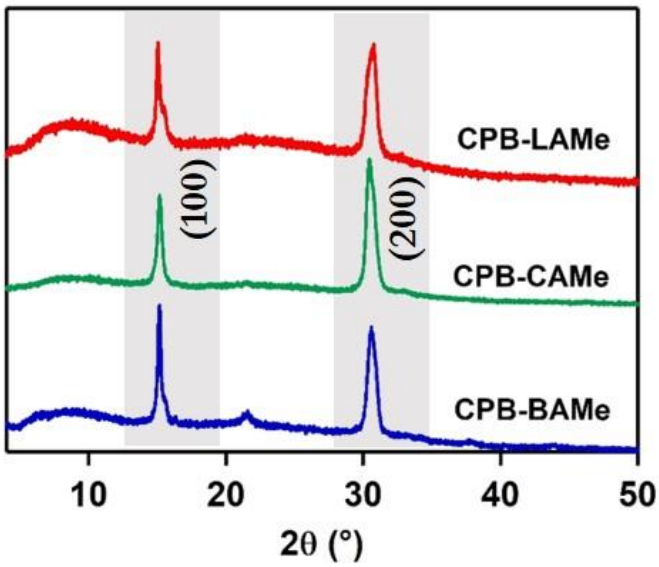

Figure 6.2. Powder X-ray diffraction (PXRD) pattern of CPB-LAMe (red), CPB-CAMe (green) and CPB-BAMe (blue).

and toxic octadecene solvent. By keeping these drawbacks in our mind, we planned to introduce a green solvent where a comparatively lower injection temperature is used for the crystallization of NC without any inert atmospheric condition. $CsPbBr_3$ NC was synthesized by a simple two-precursor approach at 100 °C in the open atmospheric condition by utilizing above mentioned DES media (see section 2.9.14 of chapter-2 for details). $CsPbBr_3$ NCs synthesized in LAMe, CAMe and BAMe are named as CPB-LAMe, CPB-CAMe, and CPB-BAMe, respectively. Powder XRD pattern confirms that the formed NCs are in a pure cubic crystalline phase (figure 6.2).

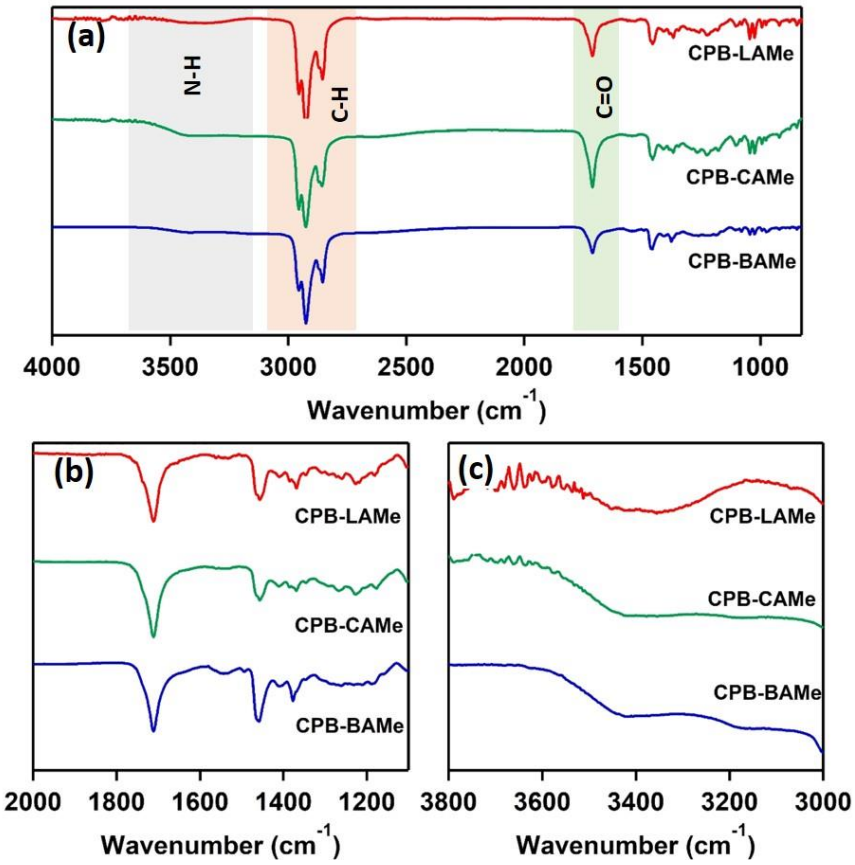

Figure 6.3. IR analysis of CPB NCs. (a) IR spectra of CPB-LAMe, CPB-CAMe and CPB-BAMe. (b) IR spectra of CPB-LAMe, CPB-CAMe and CPB-BAMe in carbonyl region. (c) IR spectra of CPB-LAMe, CPB-CAMe and CPB-BAMe in N-H stretching region.

FTIR spectra is utilized to probe capping ligand environments of purified dry CPB-LAMe, CPB-CAMe, and CPB-BAMe NCs are shown in figure 6.3. All of the NCs have a weak and broad absorption band near 3400 cm^{-1}, which originates from N-H stretching and absorption at ~2900 cm^{-1} and 1460 cm^{-1} is characteristic signature of the C-H stretching and bending mode respectively due to OAm capping ligand. The presence of corresponding aliphatic acids from DES as a capping ligand on the NC surface is indicated by another distinctive absorption band at 1700 cm^{-1} in all the cases. Energy dispersive X-ray (EDS) analysis of the NCs was carried out to have an idea about the elemental ratios of the NCs. CPB-LAMe shows bromine to lead ratio of 2.76:1, while for CPB-CAMe and CPB-BAMe it is 2.54:1 and 2.44:1, respectively, suggesting bromine deficient surface in all three NCs. This may originate from the bromine-deficient reaction condition as $PbBr_2$ salt was utilized as a dual source of bromine and lead in our synthesis. This problem is quite common in hot injection synthetic process.[20, 21] The X-ray photoelectron spectroscopy (XPS) of CPB-LAMe was carried out to have a better understanding on the surface composition of the NCs. The XPS analysis reveals that surface of CPB-LAMe has a bromine to lead ratio of 2.81 (figure 6.4). High resolution XPS spectra further reveal the formation of Pb^0 along with the CPB NCs (figure 6.4c). The appearance of Pb^0 may be because of mild reducing power of OAm.[22]

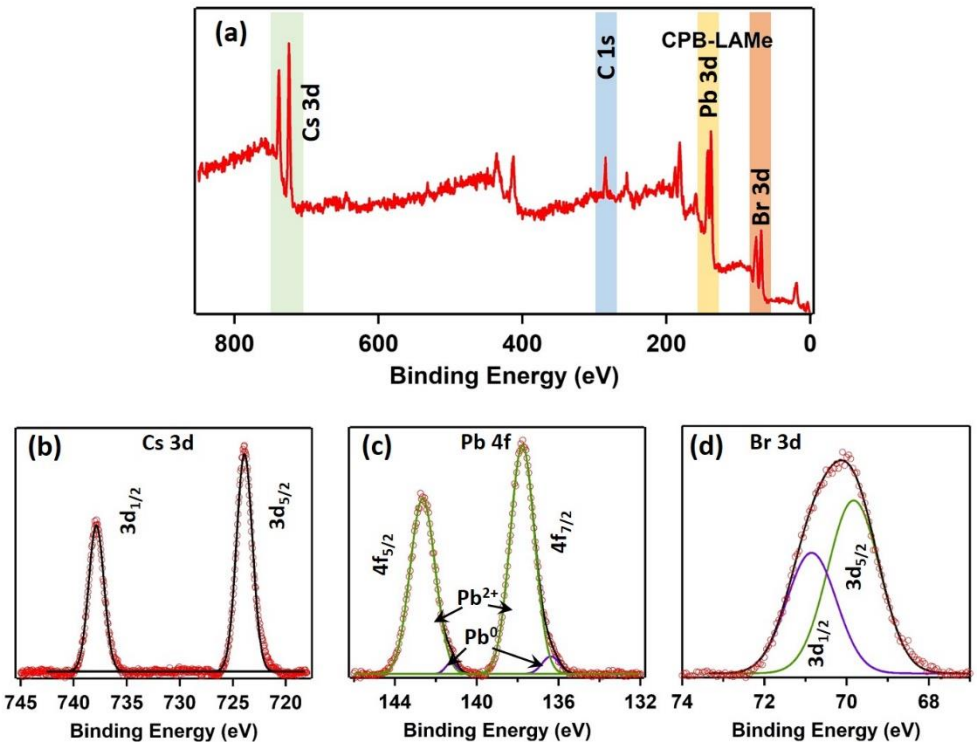

Figure 6.4. X-ray photoelectron spectroscopic (XPS) analysis of CPB LAMe. (a) Survey spectra of CPB LAMe. (b) High-resolution XPS of Cs 3d of CPB LAMe. (c) High-resolution XPS of Pb 4f of CPB LAMe. (d) High-resolution XPS of Br 3d of CPB LAMe.

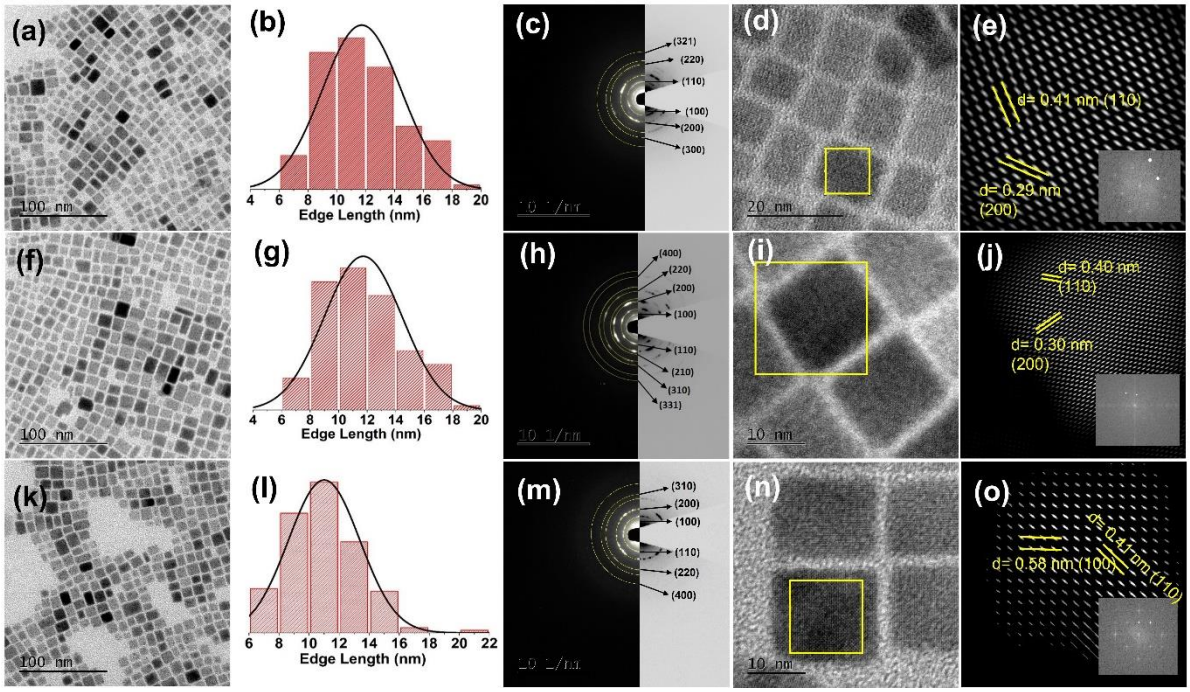

Figure 6.5. TEM characterization of CPB NCs. (a) TEM image of CPB-LAMe. (b) Size distribution of CPB-LAMe. (c) SAED pattern of CPB-LAMe. (d) HRTEM image of CPB-LAMe. (e) Fourier filtration of the selected area of figure 6.6b showing (110) and (200) crystal

planes. (f) TEM image of CPB-CAMe. (g) Size distribution of CPB-CAMe. (h) SAED pattern of CPB-LAMe. (i) HRTEM image of CPB-LAMe. (j) Fourier filtration of the selected area of figure 6.6i showing (110) and (200) crystal planes. (k) TEM image of CPB-BAMe. (l) Size distribution of CPB-BAMe. (m) SAED pattern of CPB-BAMe. (n) HRTEM image of CPB-BAMe. (o) Fourier filtration of the selected area of figure 6.6n showing (110) and (100) crystal planes.

Figures 6.5 show the transmission electron microscopic (TEM) images of CPB-LAMe, CPB-CAMe, and CPB-BAMe, respectively. In all the cases, we can see the formation of almost square-shaped NCs with uniform size distribution (figure 65a, figure 6.5f, and figure 6.5k). The average size of CPB-LAMe is found to be 12 ± 3.6 nm (figure 6.5b) whereas the average size of CPB-CAMe and CPB-BAMe are found to be 12 ± 4 nm and 11.2 ± 3.4 nm respectively (figure 6.5g and figure 6.5l, respectively). The ring pattern in the SAED confirm the cubic polycrystalline nature of the synthesized NCs (figure 6.5c, figure 6.5h, and figure 6.5m) for all the cases. Figure 6.6d shows the HRTEM image of the CPB-LAMe. Fourier filtration of the selected area from figure 6.6d clearly shows two crystal planes (110) and (200) corresponding to interplanar distances 0.41 nm and 0.29 nm respectively (figure 6.5e). Figure 6.6i and figure 6.5n shows the HRTEM images of CPB-CAMe and CPB-BAMe respectively. Two crystal planes (110) and (200) corresponding to interplanar distances 0.40 nm and 0.30 nm, respectively, can be seen from the Fourier filtration from the selected area of figure 6.5i (figure 6.5j). For CPB-BAMe similarly, two crystal planes (100) and (110) can be visualized from the Fourier filtered image as well (see figure 6.5o). Therefore, we conclude that our green solvent mediated lower temperature synthesis in open atmospheric condition is capable to produce good quality of CPB NC with uniform size distribution.

6.4. Optical properties of CPB NCs

The CPB NCs prepared in three different DES media at identical condition (100°C) shows almost identical optical properties. The NCs shows a broad absorption with

absorption edge at 510 nm and a sharp PL band centered at 513 nm in all cases (figure 6.6a). However, CPB-LAMe exhibited a high PLQY of 78%, whereas the NCs prepared in CAMe and BAMe shows relatively lower PLQY of 67% and 65%, respectively. The reason of high PLQY of $CsPbBr_3$ NCs prepared in LAMe may be because of effective passivation of CPB NC surface by both OAm and LA.

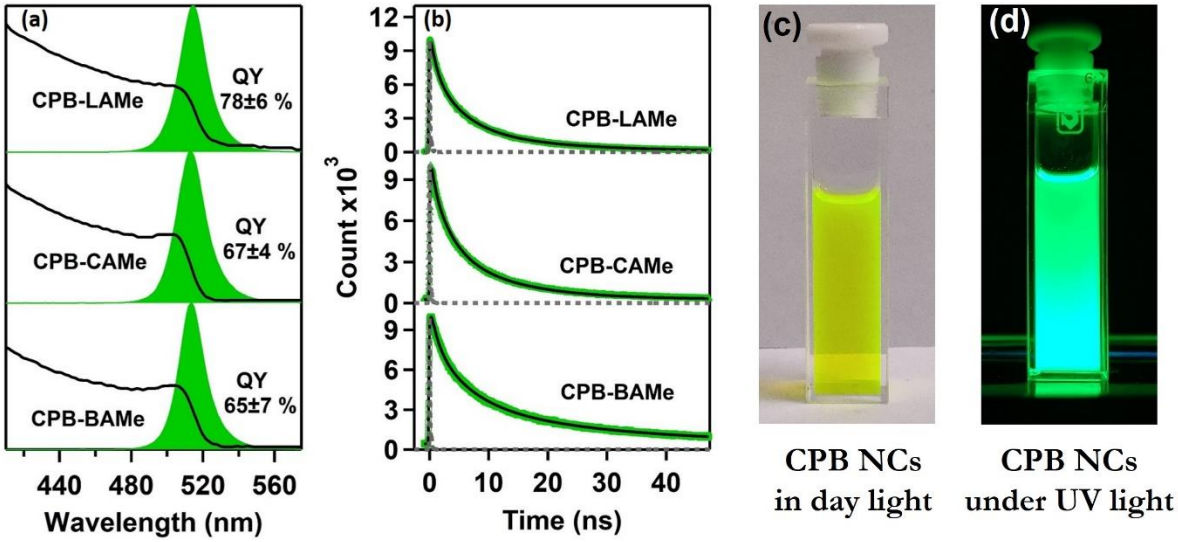

Figure 6.6. Optical properties of CPB NCs. (a) Steady state absorption (black spectrum) and PL (green solid spectrum) of hexane suspension of CPB-LAMe (top panel), CPB-CAMe (middle panel) and CPB-BAMe (lower panel). Corresponding PLQY values are given alongside. (b) Time resolved PL of hexane suspension of CPB-LAMe (top panel), CPB-CAMe (middle panel) and CPB-BAMe (lower panel). Excitation source 405 nm laser having IRF 120 ps. (c) Photographic image of hexane suspension of CPB NCs in normal day light. (d) Photographic image of hexane suspension of CPB NCs under UV light.

To have insight into the charge carrier dynamics, the time-resolved PL studies of all three purified CPB NCs have been done (figure 6.6b). All the time-resolved PL data have been fitted with a sum of three exponential fitting function, suggesting three different recombination sites present in the NCs. All the fitting parameters are tabulated in table 6.1.

Table 6.1: Time resolved PL fitting parameters of CPB-LAMe, CPB-CAMe and CPB-BAMe NCs.

Sample	τ_1 (relative %)	τ_2 (relative %)	τ_3 (relative %)	τ_{avg}
CPB-LAMe	1.4 ns (25%)	6.1 ns (52%)	19 ns (23%)	13.1 ns
CPB-CAMe	1.3 ns (27%)	5.9 ns (51%)	19 ns (22%)	13.0 ns
CPB-BAMe	1.3 ns (30%)	6.0 ns (50%)	24 ns (20%)	17.7 ns

The long lifetime component of ~20 ns originates from the recombination of charged carriers through the surface trap states.[22, 23] The lifetime component ~ 6 ns is the excitonic recombination process. [22-24] The origin of the shortest component ~ 1.4 ns is a little bit ambiguous. Literature says that this component indicates the presence of additional defect sites in the NCs that facilitate the non-radiative processes. [22] This means the CPB NCs can have trapping sites other than the trap states that originate from unsaturated surface dangling nonbonding orbitals. One possibility of such a trap state is the bromine vacancy in the NCs. To verify this, we treated the NC suspension with a hexane solution of OAmBr that act as a source of bromide ion. This post-synthetic treatment amplifies the PLQY of the system to near unity from 78% (figure 6.7a and figure 6.7b) and increases the average lifetime from 13.1 ns to 14.9 ns (figure 6.7c), suggesting a suppression of nonradiative decay channels in the system. Interestingly, the short lifetime component of 1.4 ns disappeared after OAmBr treatment (see table 6.2). This further suggests the origin of the short lifetime component is the recombination of the charged carrier through bromine-related trap states. This bromine vacancy repairing is shown schematically in figure 6.7d.

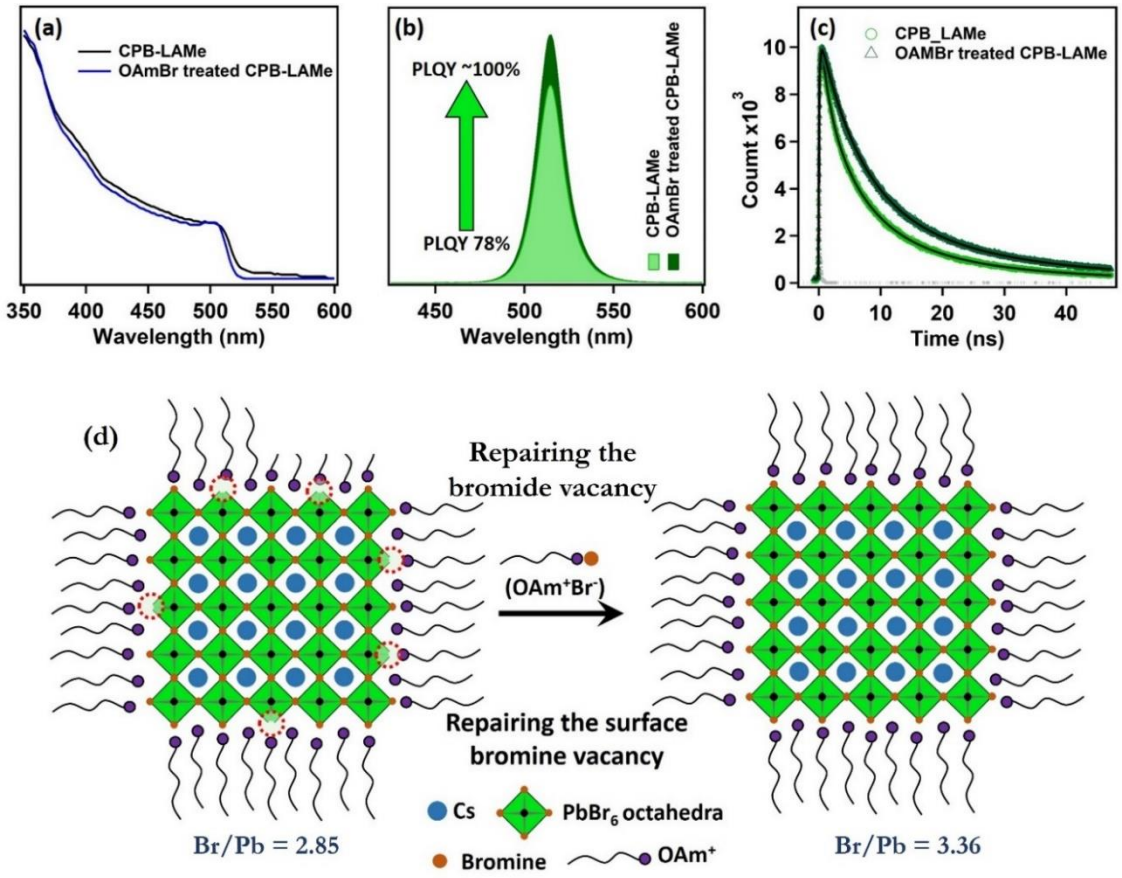

Figure 6.7. Effect of OAmBr treatment on optical properties of CPB-LAMe. (a) Comparative absorption spectra of CPB-LAMe and OAmBr treated CPB-LAMe. (b) Comparative PL spectra of CPB-LAMe and OAmBr treated CPB-LAMe. (c) Comparative PL transient at 510 nm of CPB-LAMe and OAmBr treated CPB-LAMe.

Table 6.2: Time resolved PL fitting parameters of CPB-LAMe and OAmBr treated CPB-LAMe NCs.

Sample	τ_1 (relative %)	τ_2 (relative %)	τ_3 (relative %)	τ_{avg}
CPB-LAMe	1.4 ns (25%)	6.1 ns (52%)	19 ns (23%)	13.1 ns
OAmBr treated CPB-LAMe		6.2 ns (63%)	20 ns (37%)	14.9 ns

The PL stability of these colloidal NCs was monitored for two months in ambient conditions. CPB-LAMe was found to retain ~84% of its original PL intensity after

two months. Whereas CPB-CAMe and CPB-BAMe retain ~60% of its PL intensity (see figure 6.8). This may be due to the better capping environment of CPB-LAMe, which restricts its PL intensity loss in ambient conditions.

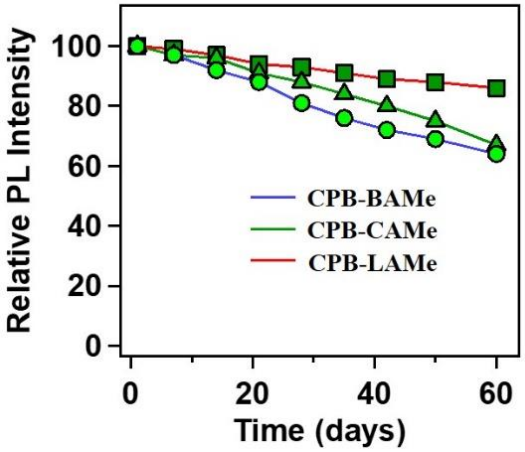

Figure 6.8. Ambient PL stability of colloidal CPB-LAMe, CPB-CAMe, and CPB-BAMe NCs.

6.5. Ultrafast charge carrier dynamics

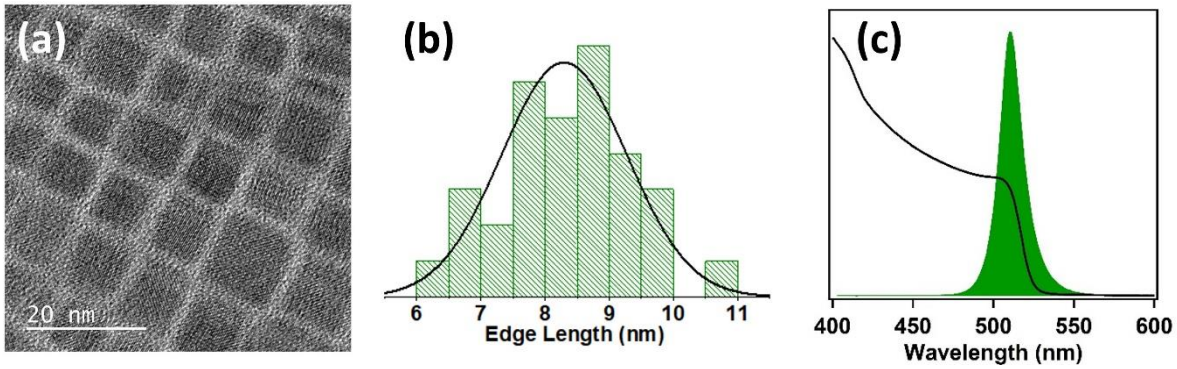

Figure 6.9. (a) TEM image of pristine CPB NCs. (b) Size distribution of pristine CPB NCs. (c) Steady state absorption (black spectrum) and PL (green) of pristine CPB.

To have a better insight on the charge carrier dynamics of the synthesized CPB-LAMe, femtosecond transient absorption spectroscopic measurements were performed, and the result is compared with the pristine $CsPbBr_3$ NCs prepared through frequently followed hot injection procedure (pristine CPB) (see figure 6.9 for TEM and optical characterizations, respectively) (synthesi is described in section

2.9.15 of chapter-2). The samples were excited above the band gap at 400 nm with femtosecond pulsed laser with same excitation power, and ttime-resolved difference absorption are measured. The results are shown in figure 6.10. CPB-LAMe and pristine CPB shows a strong photobleach signals (PB) at 512 nm and at 507 nm, respectively, which corresponds to their ground state bleaching (GSB) (figure 6.10b and figure 6.10e, respectively). At early time a strong excited state absorption (ESA) band around 530 nm is observed for both the NCs corresponding to the hot carrier (HC) absorption.[25] For both CPB-LAMe and pristine CPB NCs, the kinetics were fitted with a sum of three exponential function. The transient at PB maxima (512 nm) shows a rise component of 270 fs (figure 6.10c) that propose to corresponds to the HC cooling to the band edge.[25, 26] For pristine CPB, the HC cooling process shows a lifetime of 510 fs (figure 6.10f), which is in line with the previous studies.[25] The relaxation of hot carriers to the band edge depends on carrier-phonon coupling.[27, 28] The HC relaxation becomes faster when carrier-phonon interaction is higher. [27, 28] This carrier-phonon interaction in a particular NC is highly dependent on the size of the NCs and also on the ligand environment under the same excitation fluence.[27,29] Earlier study shows that the HC cooling rate becomes dramatically slower if the NC size is reduced.[29] The pristine CPB NCs have an average edge length of 8 nm, which is smaller than the CPB-LAMe NCs (average edge length of 12 nm). As, the ligand environment is similar for both CPB-LAMe and pristine CPB NCs, the smaller size of pristine CPB than CPB-LAMe may be the reason of slower HC cooling rate. Both CPB-LAMe and pristine CPB NCs show comparable two-component decay kinetics. The faster time constant of ~70 ps is assigned as biexciton lifetime and the longer component (>1 ns) is assigned as excitonic recombination process according to the literature. [25] The relative contribution of the biexcitonic species in CPB-LAMe and in pristine CPB remain almost similar in same experimental condition.

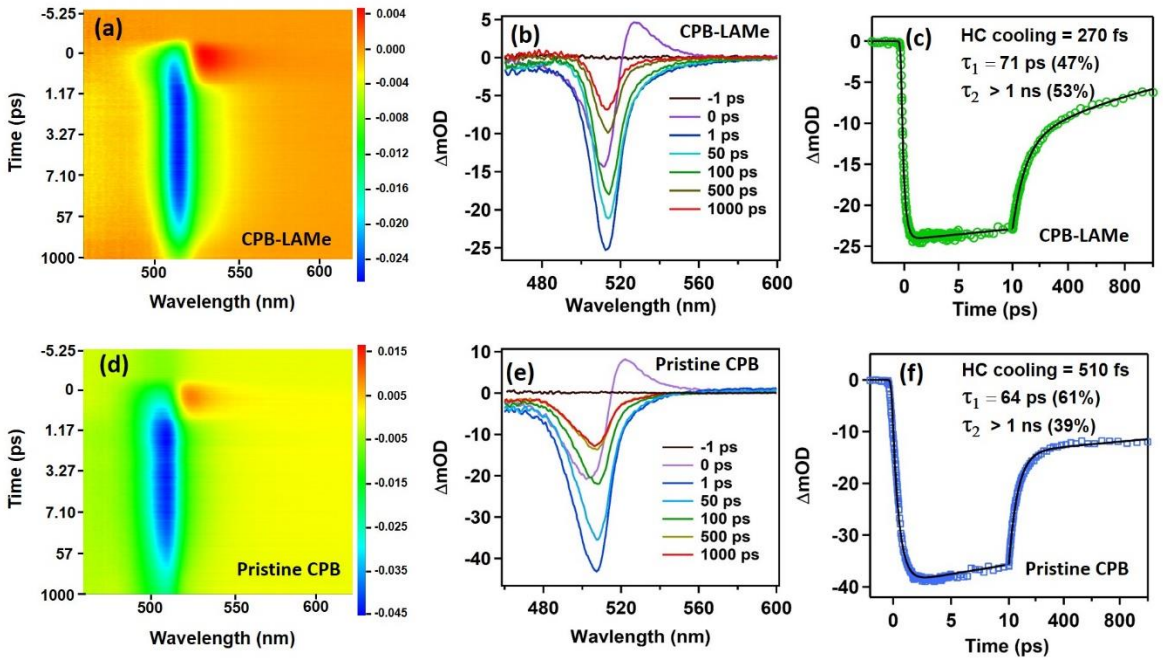

Figure 6.10. Ultrafast carrier dynamics of CPB-LAMe and pristine CPB. (a) Two-dimensional pseudo color mappings of the TA spectra of CPB-LAMe. (b) Representative TA spectra of CPB-LAMe at different times. (c) 512 nm transient of CPB-LAMe. (d) Two-dimensional pseudo color mappings of the TA spectra of pristine CPB. (b) Representative TA spectra of pristine CPB at different times. (c) 507 nm transient of pristine CPB.

6.6. Effect of reaction temperature and cesium to lead precursor ratio

Reaction temperature in perovskite NC synthesis typically plays a pivotal role to determine the size, morphology, and properties of the synthesized NCs.[30, 31] In the common hot injection process, tuning the reaction temperature is still a key to tune the size of the synthesized NCs. Apart from the temperature, the ratio of the reactant salts is also a paramount factor that can influence the NC properties to a certain extent.[32] To see the effect of these two important factors in the perovskite NC synthesis in DES media, we have studied the effect of reaction temperature and Cs:Pb precursor ratio on the prepared CPB NCs properties. Figures 6.11 a-c show the absorption and PL properties of the NCs prepared in LAMe DES at three different temperatures (100°C, 75°C, and 50°C) and four different precursor ratios. The ratio of precursors has no effect on the optical properties of the NCs if the reaction temperature is 100°C (figure 6.11a). In all the cases, the NCs show a strong

PL at 513 nm with a broad absorption, which resembles 3D NCs (n=∞). At 75°C reaction temperature, the PL properties of the NCs changes drastically on the precursor ratio (figure 6.11b). For all the cases a multipeak PL bands was observed. The absorption bands also show similar sharp excitonic features in accordance with the PL. This observation suggests the formation of lower-order perovskite NPLs. The PL shows sharp maxima at ~460 nm, ~470 nm, ~480 nm, and 513 nm, which are assigned to NPLs with n = 3,4,5 and ∞ respectively.[33] Here, n denotes the number of $PbBr_6^{4-}$ octahedral layers in the NPLs.[34, 35] The intensity ratios of the PL peaks vary with the cesium to lead ratio suggesting a change in the value of n.

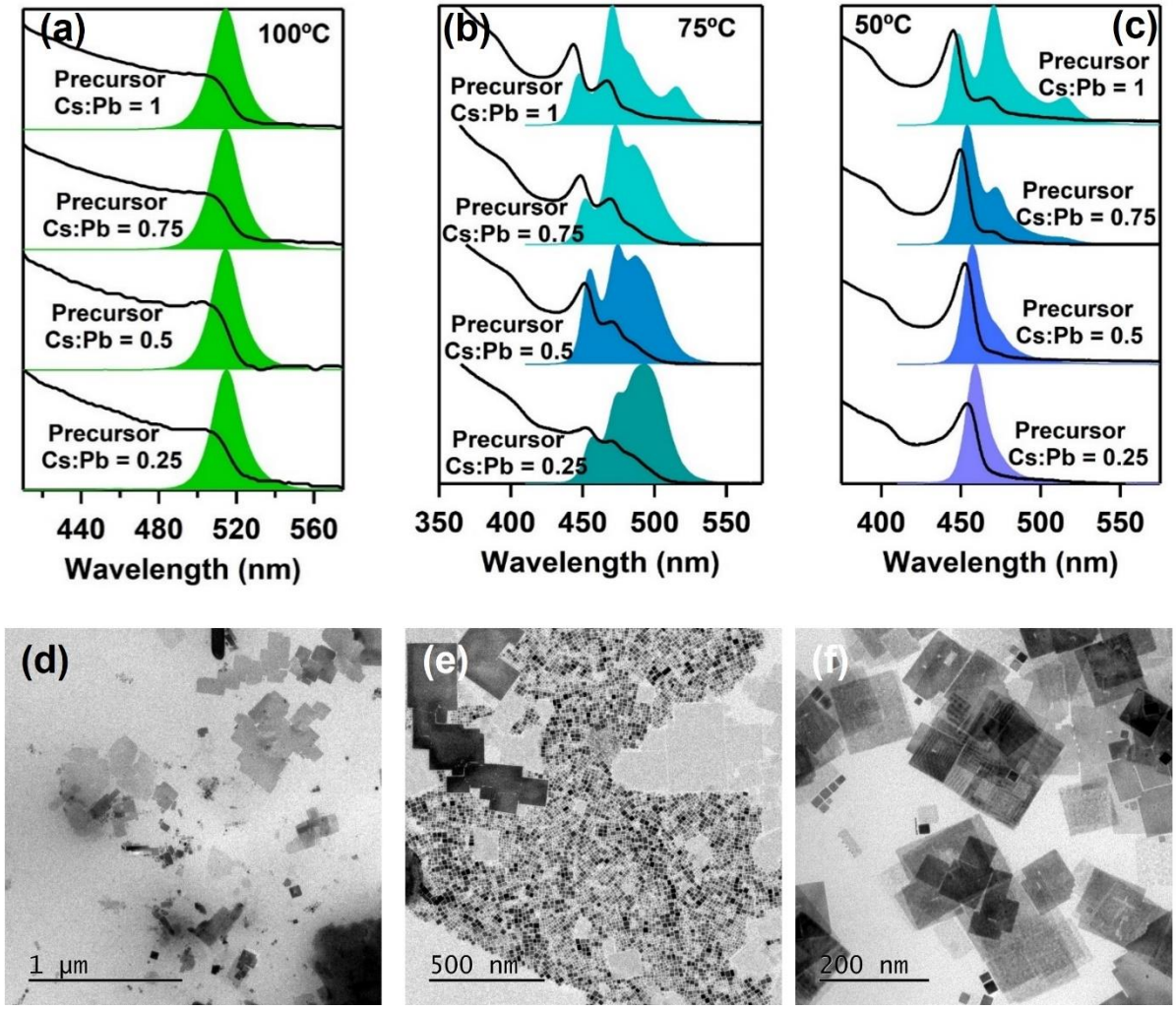

Figure 6.11. Effect of reaction temperature and cesium to precursor ratio on absorption and PL properties of CPB-LAMe NCs. (a) Absorption and PL of CPB-LAMe prepared at 100°C using different cesium to lead ratio (1 to 0.25 from top to bottom). (b) Absorption and PL of CPB-

LAMe prepared at 75°C using different cesium to lead ratio (1 to 0.25 from top to bottom). (c) Absorption and PL of CPB-LAMe prepared at 50°C using different cesium to lead ratio (1 to 0.25 from top to bottom). (d-f) TEM images of CPB-LAMe prepared at 75ºC keeping cesium to lead ratio unity.

The TEM images of the sample prepared at 75°C with unit cesium to lead ratio indicates the formation of different NPLs with 3D NCs (figures 6.11 d-f). Lowering the reaction temperature to 50°C and using cesium to lead ratio of 0.25 we were able to synthesize pure NPL (n=3) having a sharp excitonic absorption peak at 455 nm and PL band centered at 460 nm (figure 6.11c and figure 6.12a). For a better understanding of the structure and properties, we proceed with this pure NPL (n=3) for further characterization.

6.7. Properties of Ruddlesden-Popper CPB-2D (n=3) NPLs

NPLs were calculated to be 0.49 nm. Figures 6.12g-i show the TEM image of the synthesized CPB-2D NPLs. The formation of large 2D NPLs can be observed with lateral dimension in the order 200 nm. A careful analysis of TEM revels that along with these large nanosheets small ultrathin nanosheets of different shapes are also present. The different contrast in TEM images may be due to formation of RP type of structure, where different numbers of 2D nanosheets stacked together (figure 6.12g-i).

The composition of the NPLs were investigated through XPS study (figure 6.14). The RP quasi 2D NPLs have a general formula of $(A')_2A_{n-1}Pb_nX_{3n+1}$ where A′ is the long chain ammonium cation (here OAm^+), A is A-site cation (here Cs^+) and X is halide ion (here Br^-). For NPLs with n = 3, the structural formula of the system in the present case would be $(OAm)_2Cs_2Pb_3Br_{10}$. The XPS elemental study confirms that the lead to cesium ratio is 1.5, which further suggests the formation of CPB-2D where n=3. The ambient stability of the NPLs was found to be ~2 days through stead-

state PL measurement, after which it gradually transforms to bulk 3D perovskite structure (figures 6.15).

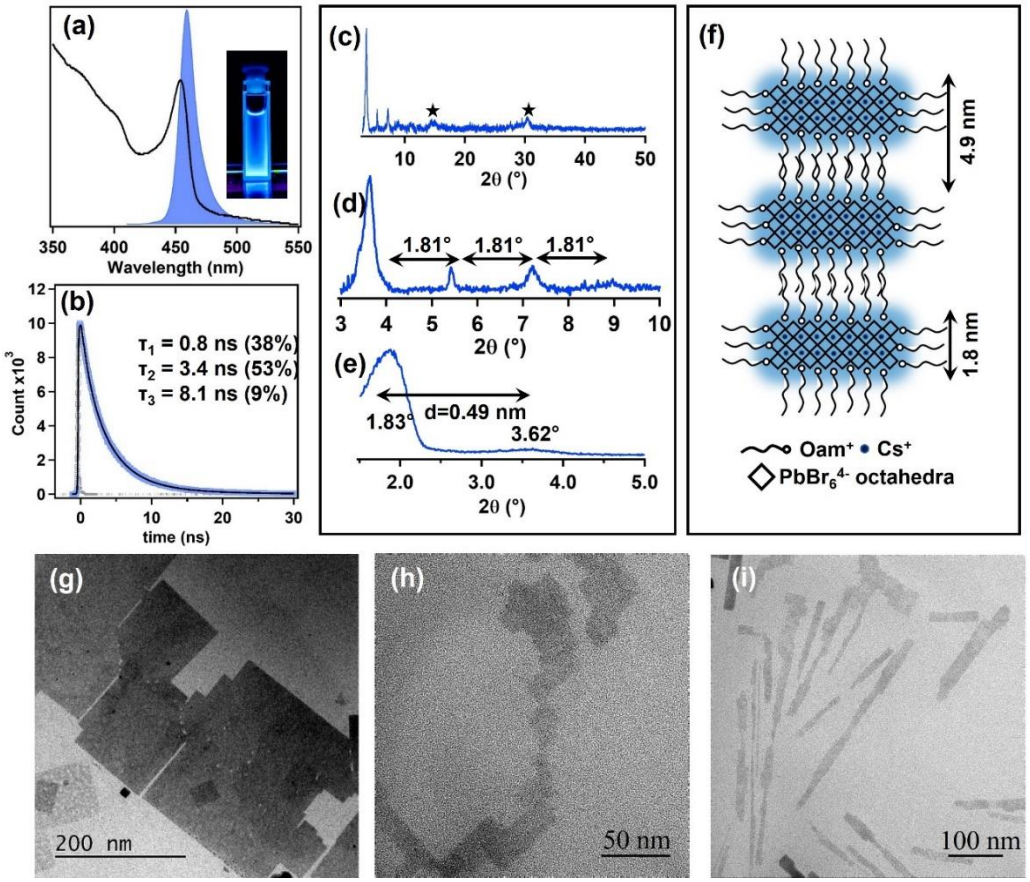

Figure 6.12. (a) absorption and PL of CPB-2D (n=3) (b) Time-resolved PL of hexane suspension of CPB-2D (n=3). The excitation source 405 nm. (c) PXRD pattern of CPB-2D (n=3). (d) Zoomed version of figure 4c in lower diffraction angle. (e) SAXS pattern of CPB-2D (n=3). (f) Pictorial representation of RP CPB-2D (n=3) structure. (g-i) TEM images of CPB-2D (n=3).

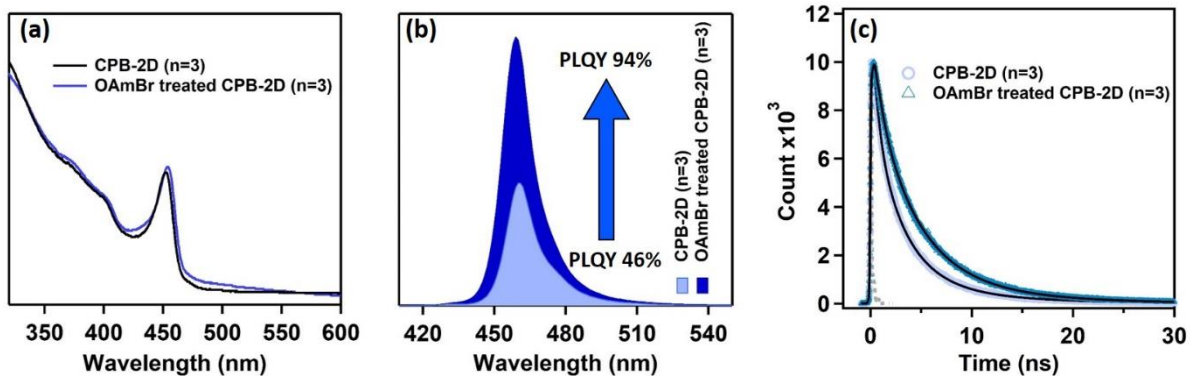

Figure 6.13. Effect of OAmBr treatment on optical properties of CPB-2D (n=3) NPLs. (a) Comparative absorption spectra of CPB-2D (n=3) NPLs and OAmBr treated CPB-2D (n=3) NPLs. (b) Comparative PL spectra of CPB-2D (n=3) NPLs and OAmBr treated CPB-2D (n=3) NPLs. (c) Comparative PL transient at 460 nm of CPB-2D (n=3) NPLs and OAmBr treated CPB-2D (n=3) NPLs.

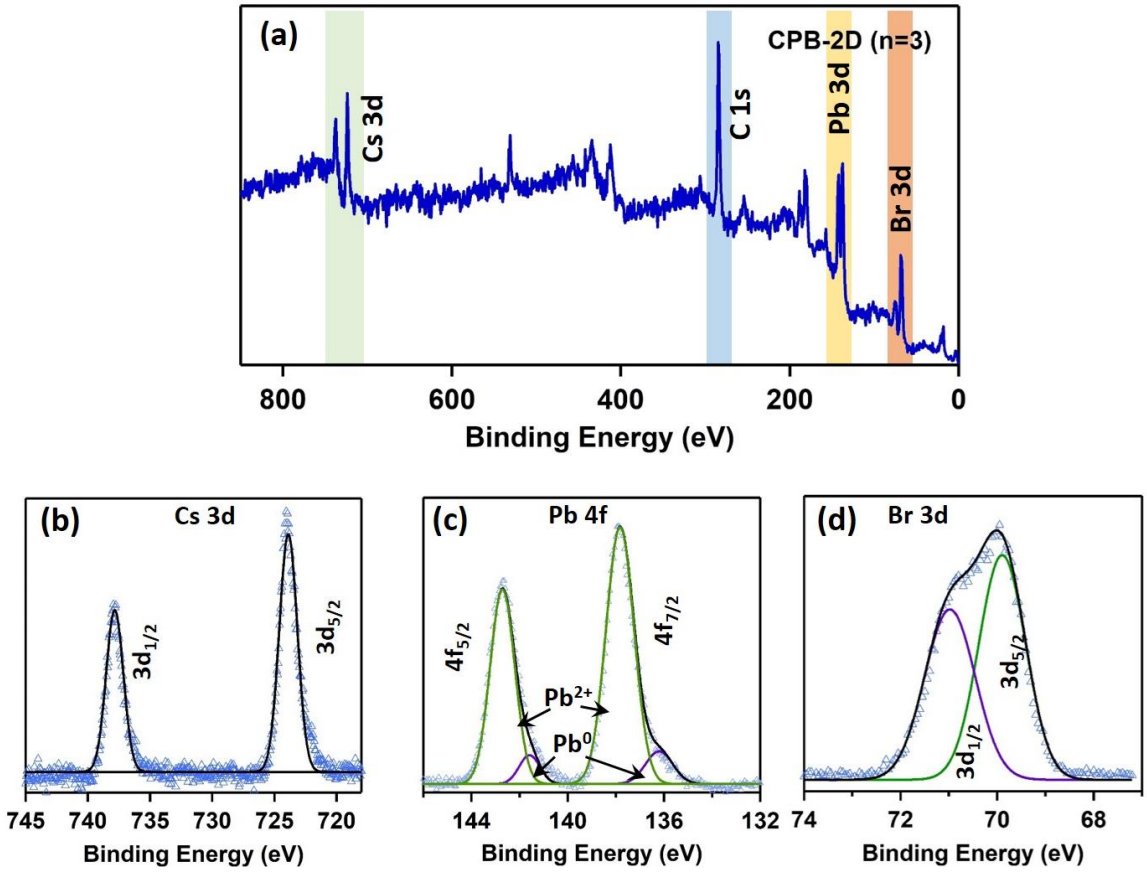

Figure 6.14. X-ray photoelectron spectroscopic (XPS) analysis of CPB-2D (n=3). (a) Survey spectra of CPB-2D (n=3). (b) High-resolution XPS of Cs 3d of CPB-2D (n=3). (c) High-resolution XPS of Pb 4f of CPB-2D (n=3). (d) High-resolution XPS of Br 3d of CPB-2D (n=3).

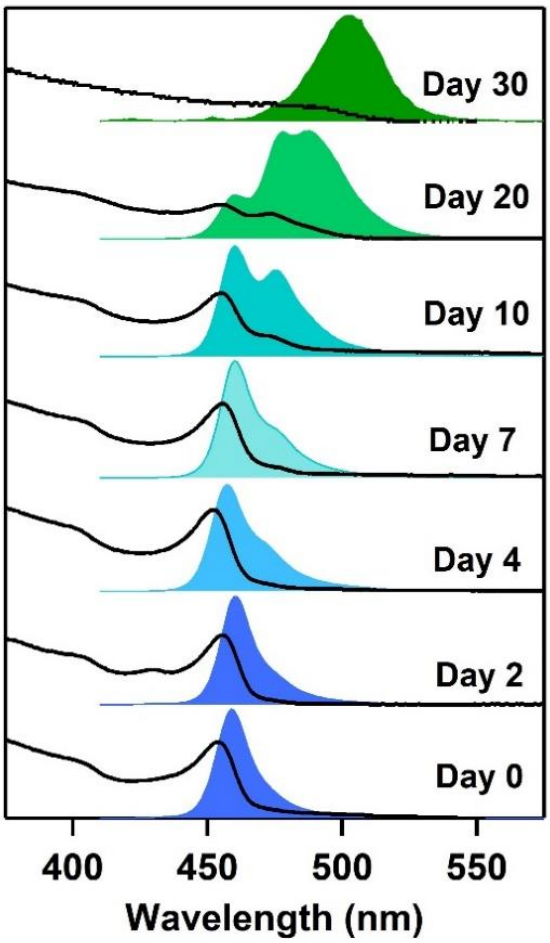

Figure 6.15. Ambient stability of CPB-2D (n=3).

6.8. Preparation of other halide perovskite NCs in DES medium

To check the universality of the DES media for perovskite NC synthesis, we have prepared the chlorine and iodine analogs as well (section 2.9.14 of chapter-2). The PXRD peaks move gradually to the lower diffraction angle from $CsPbCl_3$ to $CsPbI_3$ system due to the larger lattice parameter (figure 6.16), which is consistent with the previous studies.[36, 37] The band edge absorption shifted to longer wavelength from $CsPbCl_3$ to $CsPbI_3$ and the PL is also shifted from violet (pure NCs, PL maxima 413 nm) to red region (pure NCs, PL maxima 686 nm) (see figures 6.17 a-c). The PL transients of all the NCs show the presence of three distinct kinetics (figure 6.17d and table 6.3). The average lifetime gradually increases from 3.9 ns to 21.8 ns from

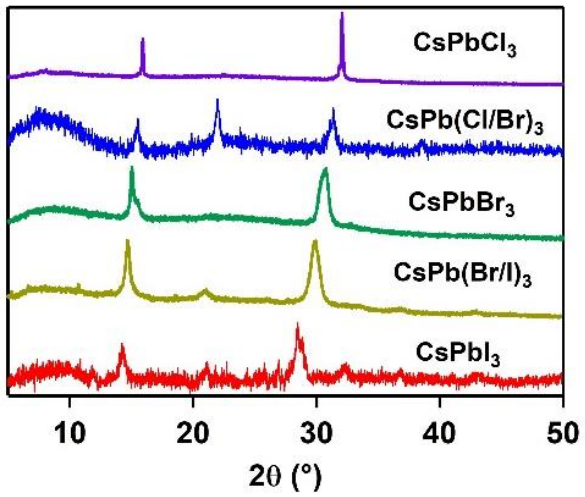

Figure 6.16. PXRD patterns of $CsPbCl_3$, $CsPb(Cl/Br)_3$, $CsPbBr_3$, $CsPb(Br/I)_3$, and $CsPbI_3$ NCs synthesized in LAMe.

$CsPbCl_3$ NCs to $CsPb(Br/I)_3$ NCs, which is in line with previous reports.[37] However, the average lifetime of $CsPbI_3$ NCs drops drastically may be due to the presence of large nonradiative decay channel through trapping sites. A closer look in the PL decay kinetics reveals that in $CsPbCl_3$ NCs the recombination of charge carriers through the chloride vacancy sites is maximum and also shows very fast decay kinetics (0.3 ns, 80%). The presence of chloride vacancy is also very common, which restricts its high PLQY in $CsPbCl_3$ NCs.[38] In the present study we estimated the PLQY of $CsPbCl_3$ NCs to be 23%. Going from $CsPbCl_3$ NCs to $CsPb(Br/I)_3$ NCs, the percentage of carrier recombination through halide vacancy sites decreases, and consequently the PLQY increases (PLQY estimated as 45% and 76% for $CsPb(Cl/Br)_3$ and $CsPb(Br/I)_3$ NCs, respectively). This study further suggests that the involvement of halide vacancies is one of the most important parameters to control the PLQY of the system.

Table 6.3. Time resolved PL fitting parameters of $CsPbCl_3$, $CsPb(Cl/Br)_3$, $CsPb(Br/I)_3$ and $CsPbI_3$ NCs.

Sample	τ_1 (relative %)	τ_2 (relative %)	τ_3 (relative %)	τ_{avg}
$CsPbCl_3$	0.3 ns (80%)	2.2 ns (11%)	12.6 ns (9%)	3.9 ns
$CsPb(Cl/Br)_3$	0.4 ns (49%)	3.2 ns (26%)	13.1 ns (25%)	10.6 ns
$CsPb(Br/I)_3$	0.9 ns (12%)	11.7 ns (28%)	24.2 ns (60%)	21.8 ns
$CsPbI_3$	0.6 ns (37%)	4.7 ns (26%)	24.4 ns (37%)	10.4 ns

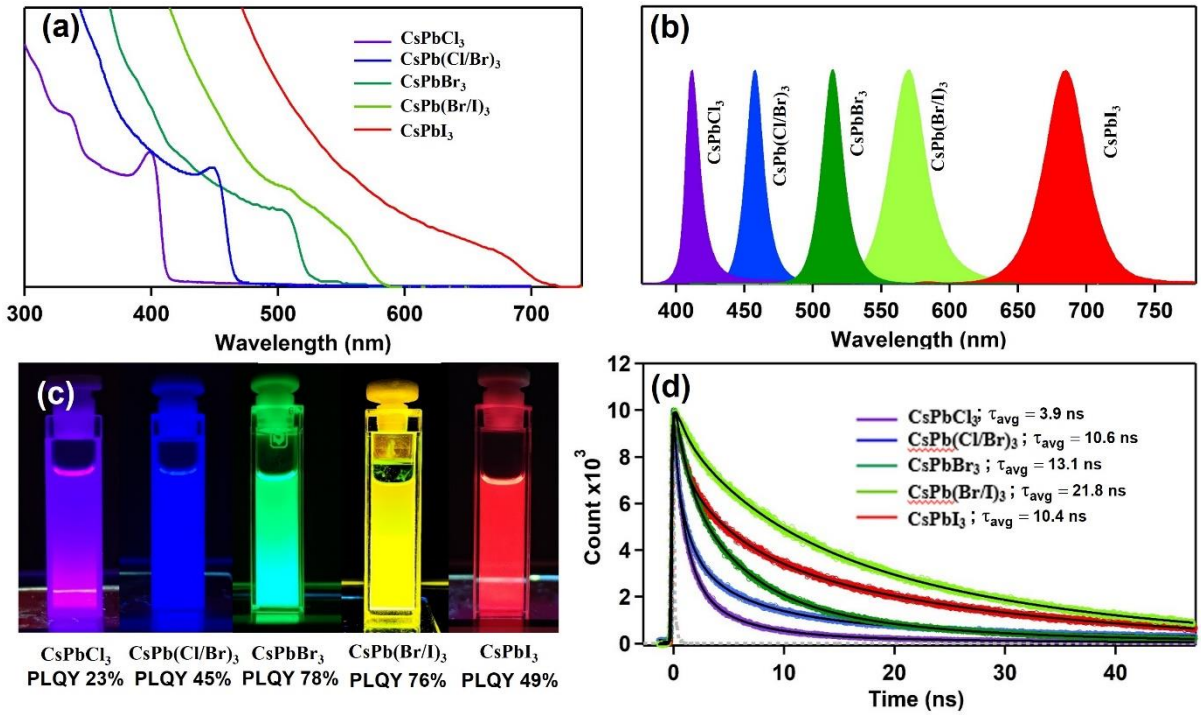

Figure 6.17. (a) Absorption spectra of $CsPbCl_3$, $CsPb(Cl/Br)_3$, $CsPbBr_3$, $CsPb(Br/I)_3$, and $CsPbI_3$ NCs synthesized in LAMe. (b) PL spectra of $CsPbCl_3$, $CsPb(Cl/Br)_3$, $CsPbBr_3$, $CsPb(Br/I)_3$, and $CsPbI_3$ NCs synthesized in LAMe. (c) Time-resolved PL spectra of $CsPbCl_3$, $CsPb(Cl/Br)_3$, $CsPbBr_3$, $CsPb(Br/I)_3$, and $CsPbI_3$ NCs synthesized in LAMe. (d) Photographic images of $CsPbCl_3$, $CsPb(Cl/Br)_3$, $CsPbBr_3$, $CsPb(Br/I)_3$, and $CsPbI_3$ NCs under UV light synthesized in LAMe.

The morphologies of the synthesized NCs were further investigated through TEM. TEM image of $CsPbCl_3$ suggests the formation of square-shaped NCs along with the formation of some long NPLs type of structures (figure 6.18a). square-shaped NCs show average size of 14 nm (figure 6.18b). Both $CsPb(Cl/Br)_3$ and $CsPb(Br/I)_3$ show square shaped NC morphology (figure 6.18c and figure 6.18e, respectively) with an average size of 15 nm (figure 6.18d) and 9 nm (figure 6.18f), respectively. The $CsPbI_3$ shows unique hexagonal morphology (figure 6.18g) of average corner distance around 50 nm (figure 6.18h) along few rod-like shapes. Understanding the mechanism of formation for this hexagonal morphology of $CsPbI_3$ in DES media needs further studies.

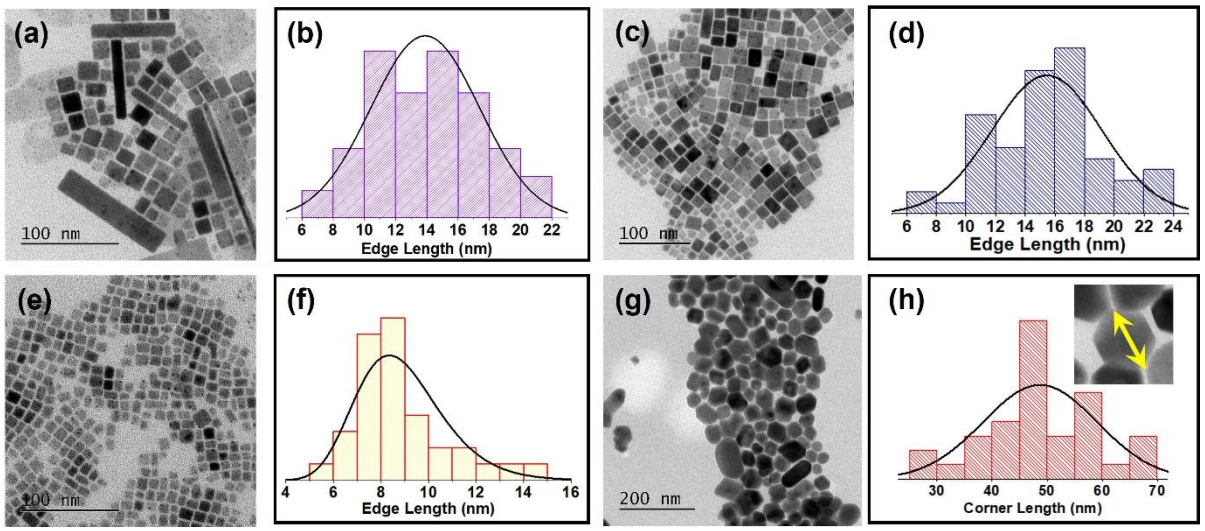

Figure 6.18. (a) TEM image of $CsPbCl_3$ NCs. (b) Size distribution of $CsPbCl_3$ NCs. (c) TEM image of $CsPb(Cl/Br)_3$ NCs. (d) Size distribution of $CsPb(Cl/Br)_3$ NCs. (e) TEM image of $CsPb(Br/I)_3$ NCs. (f) Size distribution of $CsPb(Br/I)_3$NCs. (g) TEM image of $CsPbI_3$ NCs. (h) Size distribution of $CsPbI_3$ NCs.

6.9. Conclusion

In conclusion, we have successfully synthesized and characterized all inorganic $CsPbX_3$ perovskite NCs as well as two-dimensional (2D) Ruddlesden-Popper perovskite NPLs (n=3) in environment-friendly DES for the first time. The reaction temperature and added precursor ratio have a significant impact on the formation of NC with controlled dimensionality. The common surface halide vacancy related defect lowers the PLQY of the synthesized NC and NPLs, which was restored by oleylammonium halide treatment. The charge carrier dynamics of the synthesized NCs in DES was similar to NC prepared by regular hot injection procedure. With green DES as a synthesizing medium, our synthesis protocol lowered crystallization temperature, took place in the open atmospheric condition, and produces good quality NC with almost uniform size distribution. Our findings indicate that precise control of the chemical environment of the perovskite precursor solution is crucial for producing highly reproducible and efficient NCs, and it open up a new route for accomplishing this employing DES medium.

References

1. Capello, C.; Fischer, U.; Hungerbühler, K., What is a green solvent? A comprehensive framework for the environmental assessment of solvents. *Green Chemistry* **2007,** *9* (9), 927-934.
2. Winterton, N., The green solvent: a critical perspective. *Clean Technologies and Environmental Policy* **2021,** *23* (9), 2499-2522.
3. Smith, E. L.; Abbott, A. P.; Ryder, K. S., Deep Eutectic Solvents (DESs) and Their Applications. *Chemical Reviews* **2014,** *114* (21), 11060-11082.
4. Zhang, Q.; De Oliveira Vigier, K.; Royer, S.; Jérôme, F., Deep eutectic solvents: syntheses, properties and applications. *Chemical Society Reviews* **2012,** *41* (21), 7108-7146.
5. Hansen, B. B.; Spittle, S.; Chen, B.; Poe, D.; Zhang, Y.; Klein, J. M.; Horton, A.; Adhikari, L.; Zelovich, T.; Doherty, B. W.; Gurkan, B.; Maginn, E. J.; Ragauskas, A.; Dadmun, M.; Zawodzinski, T. A.; Baker, G. A.; Tuckerman, M. E.; Savinell, R. F.; Sangoro, J. R., Deep Eutectic Solvents: A Review of Fundamentals and Applications. *Chemical Reviews* **2021,** *121* (3), 1232-1285.
6. Dey, A.; Ye, J.; De, A.; Debroye, E.; Ha, S. K.; Bladt, E.; Kshirsagar, A. S.; Wang, Z.; Yin, J.; Wang, Y.; Quan, L. N.; Yan, F.; Gao, M.; Li, X.; Shamsi, J.; Debnath, T.; Cao, M.; Scheel, M. A.; Kumar, S.; Steele, J. A.; Gerhard, M.; Chouhan, L.; Xu, K.; Wu, X.-g.; Li, Y.; Zhang, Y.; Dutta, A.; Han, C.; Vincon, I.; Rogach, A. L.; Nag, A.; Samanta, A.; Korgel, B. A.; Shih, C.-J.; Gamelin, D. R.; Son, D. H.; Zeng, H.; Zhong, H.; Sun, H.; Demir, H. V.; Scheblykin, I. G.; Mora-Seró, I.; Stolarczyk, J. K.; Zhang, J. Z.; Feldmann, J.; Hofkens, J.; Luther, J. M.; Pérez-Prieto, J.; Li, L.; Manna, L.; Bodnarchuk, M. I.; Kovalenko, M. V.; Roeffaers, M. B. J.; Pradhan, N.; Mohammed, O. F.; Bakr, O. M.; Yang, P.; Müller-Buschbaum, P.; Kamat, P. V.; Bao, Q.; Zhang, Q.; Krahne, R.; Galian, R. E.; Stranks, S. D.; Bals, S.; Biju, V.; Tisdale, W. A.; Yan, Y.; Hoye, R. L. Z.; Polavarapu, L., State

of the Art and Prospects for Halide Perovskite Nanocrystals. *ACS Nano* **2021,** *15* (7), 10775-10981.

7. Kovalenko, M. V.; Protesescu, L.; Bodnarchuk, M. I., Properties and potential optoelectronic applications of lead halide perovskite nanocrystals. **2017,** *358* (6364), 745-750.
8. Chen, S.; Zhang, Y.; Zhang, X.; Zhao, J.; Zhao, Z.; Su, X.; Hua, Z.; Zhang, J.; Cao, J.; Feng, J.; Wang, X.; Li, X.; Qi, J.; Li, J.; Gao, P., General Decomposition Pathway of Organic–Inorganic Hybrid Perovskites through an Intermediate Superstructure and its Suppression Mechanism. **2020,** *32* (29), 2001107.
9. Boyd, C. C.; Cheacharoen, R.; Leijtens, T.; McGehee, M. D., Understanding Degradation Mechanisms and Improving Stability of Perovskite Photovoltaics. *Chemical Reviews* **2019,** *119* (5), 3418-3451.
10. Xiao, Z.; Song, Z.; Yan, Y., From Lead Halide Perovskites to Lead-Free Metal Halide Perovskites and Perovskite Derivatives. **2019,** *31* (47), 1803792.
11. Fan, Q.; Biesold-McGee, G. V.; Ma, J.; Xu, Q.; Pan, S.; Peng, J.; Lin, Z., Lead-Free Halide Perovskite Nanocrystals: Crystal Structures, Synthesis, Stabilities, and Optical Properties. **2020,** *59* (3), 1030-1046.
12. Kim, H.-S.; An, Y.-J.; Kwak, J. I.; Kim, H. J.; Jung, H. S.; Park, N.-G., Sustainable Green Process for Environmentally Viable Perovskite Solar Cells. *ACS Energy Letters* **2022,** *7* (3), 1154-1177.
13. Zhang, F.; Huang, S.; Wang, P.; Chen, X.; Zhao, S.; Dong, Y.; Zhong, H., Colloidal Synthesis of Air-Stable $CH_3NH_3PbI_3$ Quantum Dots by Gaining Chemical Insight into the Solvent Effects. *Chemistry of Materials* **2017,** *29* (8), 3793-3799.
14. Moore, D. T.; Tan, K. W.; Sai, H.; Barteau, K. P.; Wiesner, U.; Estroff, L. A., Direct Crystallization Route to Methylammonium Lead Iodide Perovskite from an Ionic Liquid. *Chemistry of Materials* **2015,** *27* (9), 3197-3199.

15. Hoang, M. T.; Ünlü, F.; Martens, W.; Bell, J.; Mathur, S.; Wang, H., Towards the environmentally friendly solution processing of metal halide perovskite technology. *Green Chemistry* **2021,** *23* (15), 5302-5336.
16. Hoang, M. T.; Pham, N. D.; Yang, Y.; Tiong, V. T.; Zhang, C.; Gui, K.; Chen, H.; Chang, J.; Wang, J.; Golberg, D.; Bell, J.; Wang, H., A facile, environmentally friendly synthesis of strong photo-emissive methylammonium lead bromide perovskite nanocrystals enabled by ionic liquids. *Green Chemistry* **2020,** *22* (11), 3433-3440.
17. Chatterjee, S.; Khan, T.; Sen, A.; Das, N.; Sen, P., Massive amplification of photoluminescence and exceptional water stability of $MAPbBr_3$ nanocrystals through core–shell nanostructure formation in a self-defence mechanism. *Materials Advances* **2022,** *3* (19), 7360-7369.
18. Fan, T.; Yan, Z.; Yang, C.; Qiu, S.; Peng, X.; Zhang, J.; Hu, L.; Chen, L., Preparation of menthol-based hydrophobic deep eutectic solvents for the extraction of triphenylmethane dyes: quantitative properties and extraction mechanism. *Analyst* **2021,** *146* (6), 1996-2008.
19. Subba, N.; Das, N.; Sen, P., Partial Viscosity Decoupling of Solute Solvation, Rotation, and Translation Dynamics in Lauric Acid/Menthol Deep Eutectic Solvent: Modulation of Dynamic Heterogeneity with Length Scale. *The Journal of Physical Chemistry B* **2020,** *124* (31), 6875-6884.
20. Imran, M.; Caligiuri, V.; Wang, M.; Goldoni, L.; Prato, M.; Krahne, R.; De Trizio, L.; Manna, L., Benzoyl Halides as Alternative Precursors for the Colloidal Synthesis of Lead-Based Halide Perovskite Nanocrystals. *Journal of the American Chemical Society* **2018,** *140* (7), 2656-2664.
21. Paul, S.; Samanta, A., N-Bromosuccinimide as Bromide Precursor for Direct Synthesis of Stable and Highly Luminescent Green-Emitting Perovskite Nanocrystals. *ACS Energy Letters* **2020,** *5* (1), 64-69.
22. Ahmed, T.; Seth, S.; Samanta, A., Boosting the Photoluminescence of $CsPbX_3$ (X = Cl, Br, I) Perovskite Nanocrystals Covering a Wide Wavelength Range

by Postsynthetic Treatment with Tetrafluoroborate Salts. *Chemistry of Materials* **2018,** *30* (11), 3633-3637.

23. Chatterjee, S.; Ghosal, M.; Tiwari, K.; Sen, P., Potassium-Induced Passivation of Deep Traps in Bismuth-Doped Hybrid Lead Bromide Perovskite Nanocrystals: Massive Amplification of Photoluminescence Quantum Yield. *The Journal of Physical Chemistry Letters* **2021,** *12* (1), 546-551.
24. Chatterjee, S.; Dey, P.; Das, N.; Tiwari, K.; Maiti, T.; Sen, P., Reversible Ultra-Slow Crystal Growth of Mixed Lead Bismuth Perovskite Nanocrystals: The Presence of Dynamic Capping. **2020,** *26* (7), 1506-1510.
25. De, A.; Mondal, N.; Samanta, A., Hole Transfer Dynamics from Photoexcited Cesium Lead Halide Perovskite Nanocrystals: 1-Aminopyrene as Hole Acceptor. *The Journal of Physical Chemistry C* **2018,** *122* (25), 13617-13623.
26. Mondal, N.; Samanta, A., Complete ultrafast charge carrier dynamics in photo-excited all-inorganic perovskite nanocrystals ($CsPbX_3$). *Nanoscale* **2017,** *9* (5), 1878-1885.
27. Zeng, P.; Ren, X.; Wei, L.; Zhao, H.; Liu, X.; Zhang, X.; Xu, Y.; Yan, L.; Boldt, K.; Smith, T. A.; Liu, M., Control of Hot Carrier Relaxation in $CsPbBr_3$ Nanocrystals Using Damping Ligands. **2022,** *61* (15), e202111443.
28. Fu, J.; Xu, Q.; Han, G.; Wu, B.; Huan, C. H. A.; Leek, M. L.; Sum, T. C., Hot carrier cooling mechanisms in halide perovskites. *Nature Communications* **2017,** *8* (1), 1300.
29. Yu, B.; Chen, L.; Qu, Z.; Zhang, C.; Qin, Z.; Wang, X.; Xiao, M., Size-Dependent Hot Carrier Dynamics in Perovskite Nanocrystals Revealed by Two-Dimensional Electronic Spectroscopy. *The Journal of Physical Chemistry Letters* **2021,** *12* (1), 238-244.
30. Dutta, S. K.; Peng, L.; Hudait, B.; Xie, R.; Pradhan, N., Halide Perovskite Cluster Precursors: A Paradigm for Obtaining Structure- and Color-Tunable Light-Emitting Nanocrystals. *ACS Energy Letters* **2022,** *7* (9), 3177-3186.

31. Otero-Martínez, C.; García-Lojo, D.; Pastoriza-Santos, I.; Pérez-Juste, J.; Polavarapu, L. J. A. C., Dimensionality Control of Inorganic and Hybrid Perovskite Nanocrystals by Reaction Temperature: From No-Confinement to 3D and 1D Quantum Confinement. **2021,** *133* (51), 26881-26888.
32. Paul, S.; Ahmed, T.; Das, S.; Samanta, A., Effect of Lead:Halide Precursor Ratio on the Photoluminescence and Carrier Dynamics of Violet- and Blue-Emitting Lead Halide Perovskite Nanocrystals. *The Journal of Physical Chemistry C* **2021,** *125* (42), 23539-23547.
33. Otero-Martínez, C.; Ye, J.; Sung, J.; Pastoriza-Santos, I.; Pérez-Juste, J.; Xia, Z.; Rao, A.; Hoye, R. L. Z.; Polavarapu, L., Colloidal Metal-Halide Perovskite Nanoplatelets: Thickness-Controlled Synthesis, Properties, and Application in Light-Emitting Diodes. **2022,** *34* (10), 2107105.
34. Weidman, M. C.; Seitz, M.; Stranks, S. D.; Tisdale, W. A., Highly Tunable Colloidal Perovskite Nanoplatelets through Variable Cation, Metal, and Halide Composition. *ACS Nano* **2016,** *10* (8), 7830-7839.
35. Sen, A.; Chatterjee, S.; Sen, P., UV-Assisted Conversion of 2D Ruddlesden–Popper Iodide Perovskite Nanoplates into Stable 3D $MAPbI_3$ Nanorods. *The Journal of Physical Chemistry C* **2022**.
36. Bansal, P.; Khan, Y.; Kar, P., High luminescence color gradient by physical mixing of two perovskite nanocrystals. *New Journal of Chemistry* **2019,** *43* (10), 4116-4122.
37. Protesescu, L.; Yakunin, S.; Bodnarchuk, M. I.; Krieg, F.; Caputo, R.; Hendon, C. H.; Yang, R. X.; Walsh, A.; Kovalenko, M. V., Nanocrystals of Cesium Lead Halide Perovskites ($CsPbX_3$, X = Cl, Br, and I): Novel Optoelectronic Materials Showing Bright Emission with Wide Color Gamut. *Nano Letters* **2015,** *15* (6), 3692-3696.
38. Yong, Z.-J.; Guo, S.-Q.; Ma, J.-P.; Zhang, J.-Y.; Li, Z.-Y.; Chen, Y.-M.; Zhang, B.-B.; Zhou, Y.; Shu, J.; Gu, J.-L.; Zheng, L.-R.; Bakr, O. M.; Sun, H.-T., Doping-Enhanced Short-Range Order of Perovskite Nanocrystals for

Near-Unity Violet Luminescence Quantum Yield. *Journal of the American Chemical Society* **2018,** *140* (31), 9942-9951.

This page is intentionally left blank

Chapter-7

Evidence of Short-Lived High Energy Emissive State in Lead-Free $Cs_3Cu_2I_5$ Nanocrystals Synthesized in Lauric Acid- Menthol Deep Eutectic Solvent

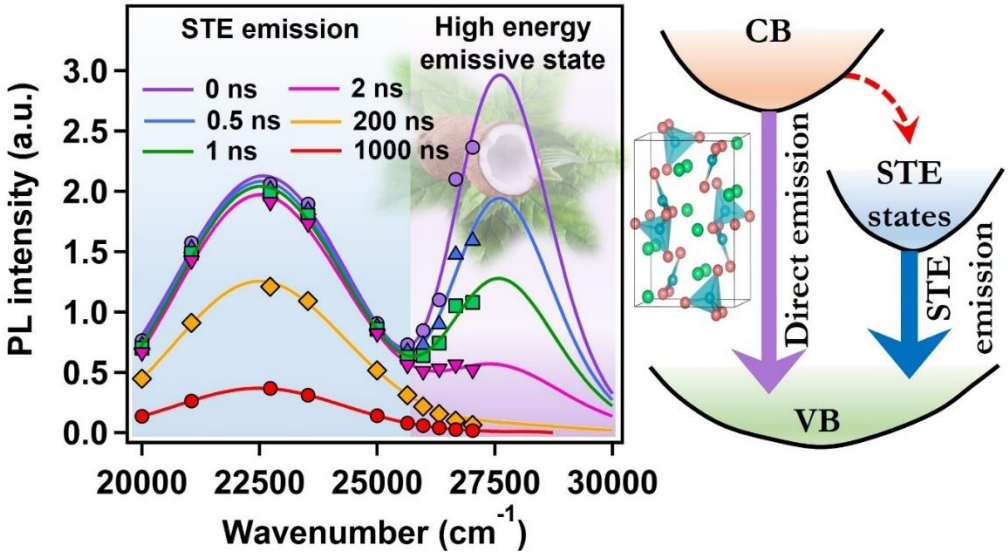

Shovon Chatterjee, and Pratik Sen *Manuscript under preparation*.

Lead toxicity as well as organic solvent related toxicity remained the key concerns in the practical use of lead halide perovskite NCs. In this report, a facile synthesis of lead-free $Cs_3Cu_2I_5$ NCs in a menthol based green deep eutectic medium is reported. The synthesized NCs showed uniform size distribution and a highly stoke-shifted photoluminescence band centered at 445 nm with PLQY of 74%. Time-resolved PL study reveals the presence of a short lifetime component. A detailed time resolved emission spectral analysis further reveals the presence of a short-lived high energy emissive state in the early time, which remained unobserved in steady-state photoluminescence spectrum. This evidence of short-lived high energy emissive state is unique proposed as band-to-band direct emission.

7.1. Introduction

Halide perovskite is one of the most flourishing scientific fields in the last decade due to its highly promising characteristics in optoelectronics, solar cell, photocatalysis, and so on.[1-3] Lead halide perovskites (LHP) in the halide perovskite family remain at the field's forefront because of their high PLQY, easy PL tunability, narrow PL bandwidth, and highly defect-tolerant nature.[4-5] Despite the significant advancements made in LHP materials, several technical and scientific barriers still prevent their widespread commercial use.[6-7] Among these, lead toxicity is one of the severe flaws.[7-8] Also, the inherent instability of the LHP structure in an open atmosphere restricts its commercialization.[9-10] Thus, it is essential to develop high-performance lead-free perovskites for optoelectronic applications. Concern to this, parallel research has been devoted to replacing lead in the B-site of the perovskite structure with other non-toxic metals, such as Sn, Mn, Cu, Ge, and Bi.[5, 11] Unfortunately, the low chemical stability of Sn-based perovskite is caused by the easy oxidation of Sn^{2+} to Sn^{4+} in the air.[11-12] Along with the environmental instability, the tin-based perovskite NCs shows very low PLQY due to intrinsic defect.[12] Due to the same problem germanium-based perovskites are also less explored.[11] On the other hand, the efficiency of bismuth-based perovskites is not sufficient until now to compete with pure lead analogs. Despite being of comparable size as Pb^{2+}, the bismuth (Bi^{3+}) trivalency causes the B sites to be occupied in a 2:1 ratio, creating a stoichiometric $A_3Bi_2X_9$.[11, 13] These perovskites often display low conductivity due to the high concentration of vacancies, which limits their use.[13]

In recent times, lead-free $Cs_3Cu_2I_5$, a zero-order perovskite structure has drawn research interest due to its strong blue photoluminescence.[14-15] High PLQY and very stable crystal structure make this perovskite structure ideal for next-generation optoelectronic applications.[15] $Cs_3Cu_2I_5$ along with its other halide analogs show broad, highly Stokes-shifted, and long lifetime photoluminescence originating from self-trapped excitons (STE) due to excited state Jahn-Teller effect.[14-16] Due to their

significant large Stoke shift, these materials exhibit self-absorption-free emission, which is extremely valuable in optoelectronics. [14-16] The Stoke shift is even larger in $Cs_3Cu_2Br_5$ and $Cs_3Cu_2Cl_5$ than in $Cs_3Cu_2I_5$ because of higher exciton phonon coupling.[16-17]

Free excitons are always in a competitive relation with STE.[18-19] So, it is abnormal that free exciton emission is not observed in steady-state PL spectra of $Cs_3Cu_2X_5$ perovskites.[14] To date, no evidence of such excitonic band-to-band emission is reported in $Cs_3Cu_2X_5$ perovskites and reasoned as very fast transition of charge carriers to the STE states after photoexcitation.[14]

Besides Photophysics, the synthetic control of $Cs_3Cu_2X_5$ perovskite also gained interest in recent times.[15, 20-21] Although, most of the synthesis methods produce bulk $Cs_3Cu_2X_5$, recently controlling the size and morphology of these materials have also come into focus.[21-23] However, the optical properties of both NCs and bulk crystals of these copper halide NCs are mostly similar.[15, 22]

The solvent-related toxicity is also one of the major concerns in perovskite NCs synthesis.[24] The copper-based halide perovskite NCs which eliminate lead-related toxicity, are also synthesized through conventional ligand-assisted reprecipitation (LARP) or hot injection procedures, which involve the use of hazardous organic solvents like dimethyl formamide (DMF), skin penetrating dimethyl sulfoxide (DMSO), or octadecene.[15] Apart from this, the coordinating ability of these organic precursor solvents is detrimental to the long-term colloidal stability of the NCs.[25-27] Addressing these solvent-related issues, ionic liquid (IL) mediums have already been used in lead halide perovskite NC synthesis by Hoang *et al.* in 2020.[28] We also have synthesized $MAPbBr_3$ NCs in an IL-type medium composed of hydrophobic lauric acid (LA) and methylamine that results in the formation of water-stable $MAPbBr_3$@lead laurate core-shell nanostructure with near-unity PLQY which has been discussed in chapter-5. However, the poor solubility of lead halide salts in these IL mediums, along with selectivity toward the preparation of methylammonium-

based perovskite NCs restrict its use in a broad aspect. In order to overcome these limitations, we used three menthol based deep eutectic solvent (DES) media in order to synthesize pure inorganic $CsPbX_3$ NCs (X=Cl, Br, and I) with high PLQY. However, to date, the synthesis of copper halide perovskite NCs in the green alternative medium is not yet been reported, which is necessary to discard both lead-related as well as solvent-related toxicity for large-scale industrial production.

Herein, we report a facile green synthesis of phase pure lead-free $Cs_3Cu_2I_5$ NCs with uniform size distribution and PLQY of 76% in lauric acid-menthol DES (LAMe) for the first time. The colloidal suspension shows a broad blue emission originating from the radiative recombination of STE. Time-resolved emission spectra (TRES) of the NCs reveal the presence of another short-lived higher energy emissive state, which is proposed to be band-to-band recombination in the NCs. The evidence of higher energy emissive state in copper-based perovskites is unique and will help to understand the photophysics of copper halide perovskites in a extensive way in near future.

7.2. Results and discussions

$Cs_3Cu_2I_5$ NCs are synthesized in LAMe DES medium through a modified hot injection procedure. In brief, CuI is dissolved in LAMe in the presence of oleylammonium iodide (OAmI) at 80 ºC under high vacuum. The cesium precursor was also prepared by dissolving $CsCO_3$ in LAMe in the presence of LA under an inert atmosphere. The cesium precursor was heated to 75 ºC before injecting to the copper iodide precursor. However, the CuI precursor cooled down to room temperature before the addition of the cesium precursor. After the addition of cesium precursor, the system was cooled down in an ice bath, and NCs were collected after purification. The detailed synthesis procedure is discussed in section 2.9.16 of chapter 2. All the studies were performed with the toluene suspension of the NCs.

7.2.1. Characterizations

The $Cs_3Cu_2I_5$ NCs crystallize in pure orthorhombic phase (*Pbnm*) evident from the PXRD pattern of the NCs depicted in figure 7.1. The phase purity of the NCs can be visualized from the reference pattern (Ref. code: 01-079-0333). The energy dispersive spectroscopic (EDS) analysis was done to check and confirm the actual atomic percentage of the respective atoms in the NCs. The result of the EDS analysis is tabulated in table 7.1.

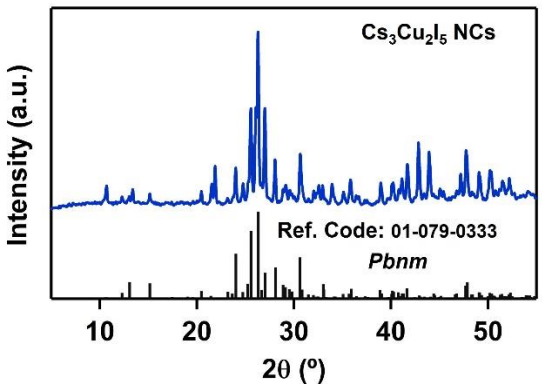

Figure 7.1. Powder X-ray diffraction (PXRD) pattern of the synthesized $Cs_3Cu_2I_5$ NCs.

Table 7.1. EDS analysis shows the relative atomic percentage of Cs, Cu, and I in $Cs_3Cu_2I_5$ NCs.

Element	Cs	Cu	I
Atomic percentage (%)	31%	10.5%	58.5%

Figure 7.2a and figure 7.2b depict the transmission electron microscopic (TEM) images of $Cs_3Cu_2I_5$ NCs in lower and higher magnification, respectively. These demonstrate the formation of spherical NCs with a fairly uniform size distribution with average size of 22 nm (figure 7.2c). The SAED pattern of the area presented in figure 7.2b shows the polycrystalline nature of the NCs (figure 7.2d). The high-resolution TEM (HRTEM) image of the NC is represented in figure 7.2d. The FFT

pattern is shown in the inset of figure 7.2e. The Fourier filtration of figure 7.2d produces figure 7.2e from which (122) lattice fringes with an interplanar distance of 0.37 nm is clearly observed.

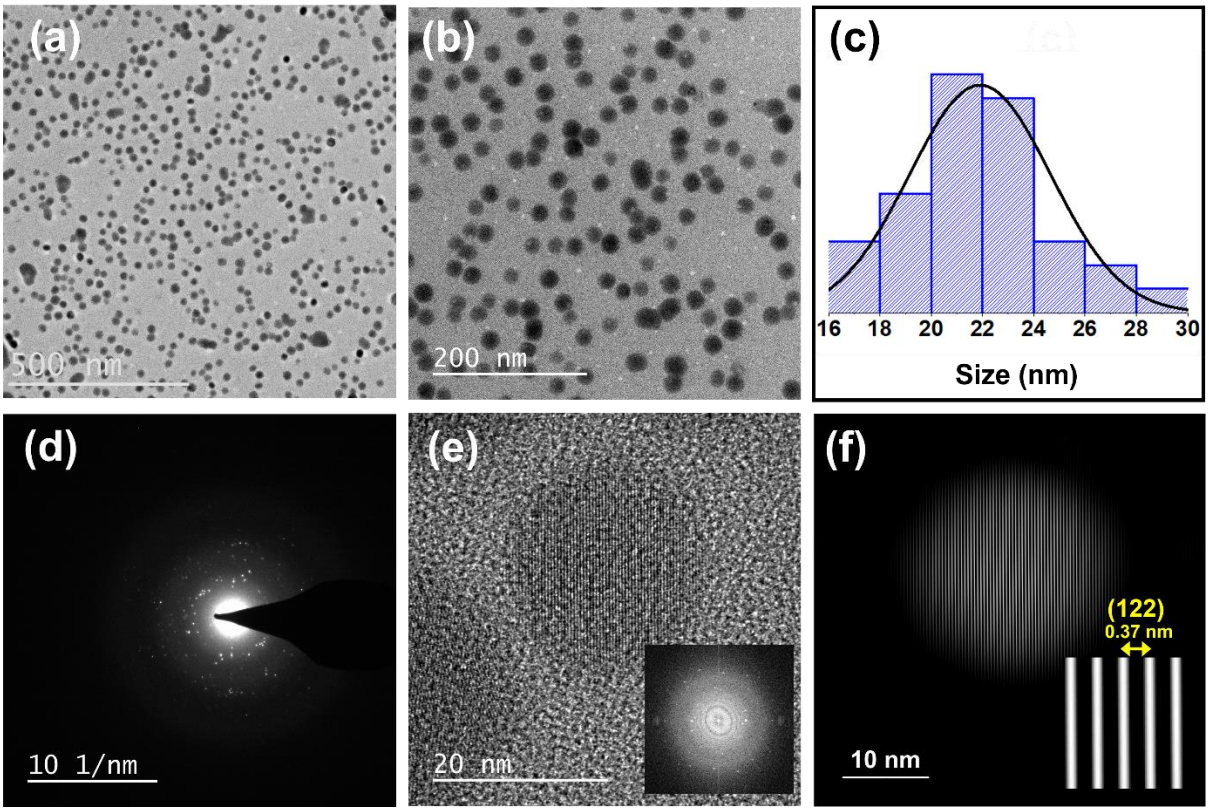

Figure 7.2. Transmission electron microscopic (TEM) analysis of $Cs_3Cu_2I_5$ NCs. (a) TEM image of $Cs_3Cu_2I_5$ NCs in lower magnification. (b) TEM image of $Cs_3Cu_2I_5$ NCs in higher magnification. (c) Size distribution of $Cs_3Cu_2I_5$ NCs. (d) SAED pattern of $Cs_3Cu_2I_5$ NCs. (e) HRTEM image of $Cs_3Cu_2I_5$ NCs. The FFT pattern is shown in the inset. (f) Fourier filtered image of figure 7.2e showing (122) lattice fringes.

7.2.2. Optical properties

The purified $Cs_3Cu_2I_5$ NC suspension shows an absorption peak cantered at 290 nm (black solid line in figure 7.3a) and a broad PL spectrum (blue solid line) with maximum at 445 nm. Inset of figure 7.3a shows the bright fluorescence photo of the NCs solution under UV illumination. The PLQY of the NCs is measured to be 76±4%. The PLE spectrum monitored at PL maxima shows a sharp band centered at

293 nm. The excitation wavelength-dependent PL spectrum of the NCs exciting at different wavelengths from 270 nm to 310 nm is depicted in figure 7.3b. The broadband PL spectra with PL maxima at 445 nm are exactly the same for the PL spectra excited at different wavelengths. As seen in figure 7.3c, the PLE spectra show the exact same shape and peak position when measured at various emission wavelengths between 380 to 540 nm. The aforementioned findings demonstrate that the PL emission of the $Cs_3Cu_2I_5$ NCs originates from the relaxation of the same excited state, which is in line with the previous reports.[14-15] This further proves the phase purity of the synthesized NCs.

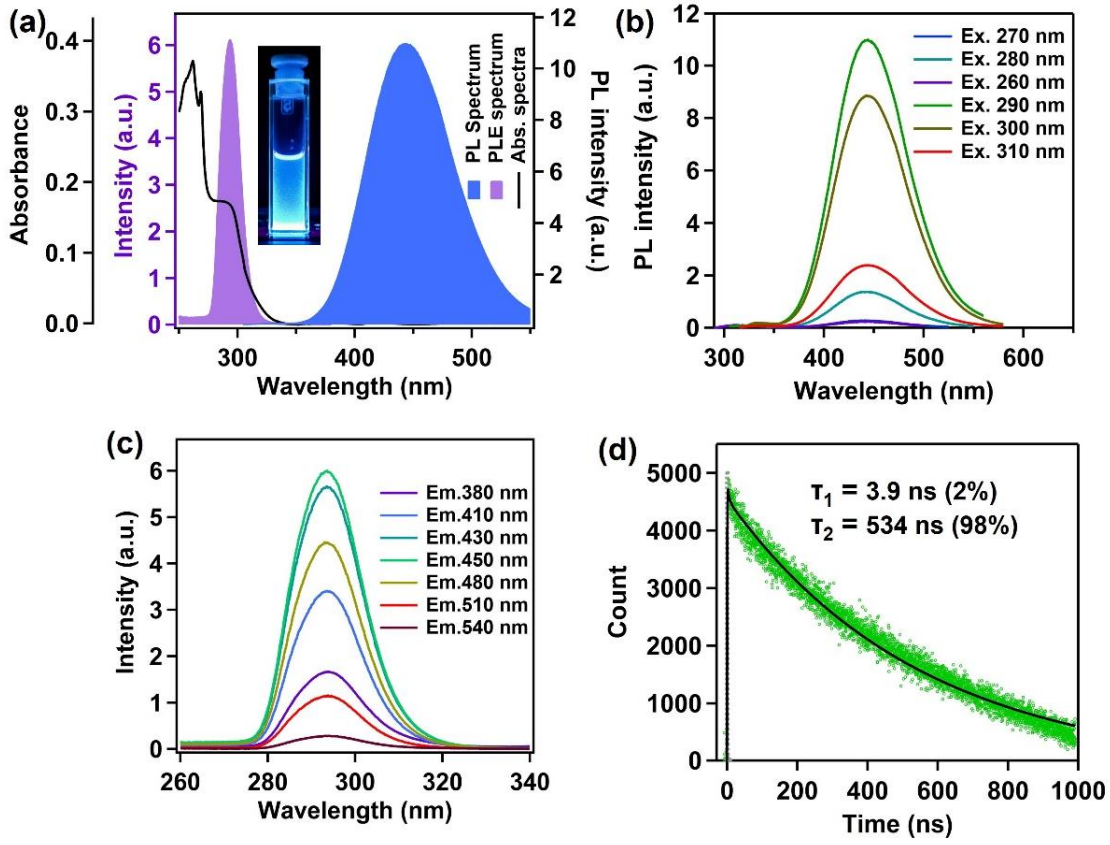

Figure 7.3. Optical properties of $Cs_3Cu_2I_5$ NCs. (a) Steady-state absorption spectrum (black spectrum), PL spectrum (solid blue spectrum), and PL excitation (PLE) spectrum (solid violet spectrum) of purified toluene suspension of $Cs_3Cu_2I_5$ NCs. The inset shows the photographic image of $Cs_3Cu_2I_5$ NCs suspension under 265 UV excitation. (b) Excitation wavelength-dependent PL spectrum of $Cs_3Cu_2I_5$ NCs. (c) PLE spectrum of $Cs_3Cu_2I_5$ NCs collected at

different PL wavelengths. (d) Time-resolved PL transient of $Cs_3Cu_2I_5$ NCs monitored at PL maxima.

The time-resolved PL transient of $Cs_3Cu_2I_5$ NCs shows a biexponential decay kinetics with a short lifetime component of 3.9 ns having a relative contribution of 3% and a long decay lifetime component of 534 ns with a relative contribution of 97%. The long decay component arises from the recombination of self-trapped excitons.[14, 29] However, the origin of the short decay component is a little ambiguous. Although most of the recent articles have reported the monoexponential PL decay kinetics of $Cs_3Cu_2I_5$ NCs, few reports have shown the multiexponential PL decay kinetics, which suggests that trap-assisted recombination is the origin of short-lifetime components.[30-32] But till now a detailed explanation of the origin of this short-lifetime component is absent.

7.2.3. Origin of short lifetime decay component

In $Cs_3Cu_2I_5$ perovskite, the photogenerated electron and hole get spatially separated and remain concentrated on copper and iodine atoms, respectively.[14] These spatially separated electrons and holes are then trapped because of the lattice distortion and remain confined, which explains the system's prolonged lifetime.[14] However, the presence of a short lifetime component in the PL decay kinetics ensures the availability of another recombination site other than STE in the system. To check, the energy distribution of these states, the PL decay kinetics of $Cs_3Cu_2I_5$ NCs were measured at various PL transients from the blue end to the red end of the PL spectrum (figure 7.4a and figure 7.4b). The relative contribution of these states to the overall steady-state PL intensity (f_i) was also calculated at various PL transient wavelengths using the formula,

$$f_i = \frac{a_i \tau_i}{\sum_i a_i \tau_i} \qquad (7.1)$$

Where a_i is the relative contribution of τ_i.

The results are tabulated in table 7.2.

Table 7.2. PL transient analysis at various PL wavelengths.

Transient wavelength (nm)	τ_1 (ns)	a_1 (%)	f_1 (%)	τ_2 (ns)	a_2 (%)	f_2 (%)
370	1.2	96%	5.3%	549	4%	94.7%
375	1.3	93%	3%	541	7%	97%
380	1.9	79%	1.3%	522	21%	98.7%
385	2	62%	0.5%	539	38%	99.5%
390	2.18	37%	0.2%	519	63%	99.8%
400	2.9	2%	0.1%	543	98%	99.9%
425	3.1	1%	0.04%	557	99%	99.96%
440	3.9	2%	0.08%	587	98%	99.92%
475	2.8	9%	0.06%	565	91%	99.94%
500	1.9	13%	0.1%	590	87%	99%
520	1.2	16%	0.1%	594	84%	99.8%

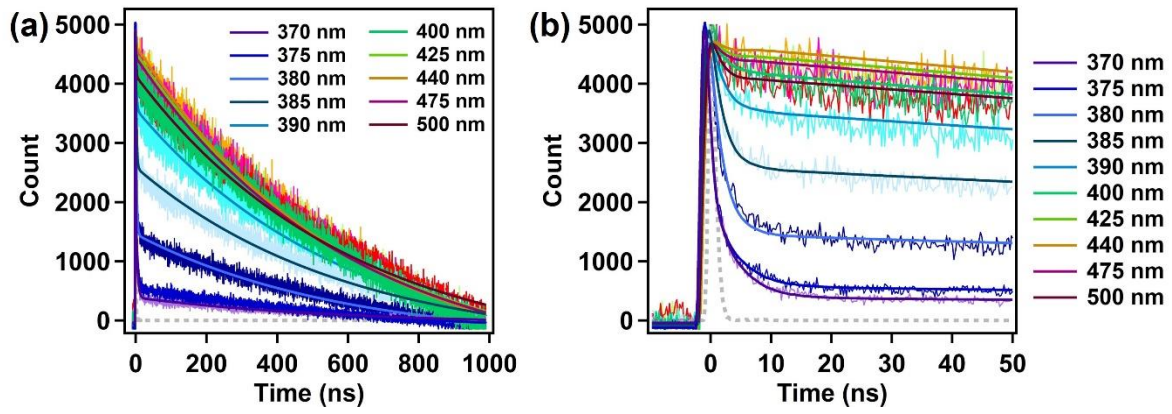

Figure 7.4. (a) PL transients of $Cs_3Cu_2I_5$ NCs at different PL wavelengths. (b) PL transients of $Cs_3Cu_2I_5$ NCs at different PL wavelengths in the early time region.

From the above analysis, we can see that one short-lifetime component is present in all PL transients. The relative contribution of this short-lifetime component was found to increase from 2% to 96% moving from PL maxima (~440 nm) to the blue end of the PL spectrum (370 nm). This signifies that the states corresponding to the short-lifetime component are situated in higher energy than the STE state. However,

the contribution of this high energy state in overall steady-state PL intensity is negligible because of the very long lifetime of the STE state. To see the evolution of this high energy state and STE emission over time, time resolved emission spectra (TRES) has been constructed. TRES analysis reveals that the emission intensity of the high energy emissive state is higher than STE emission in early time (<0.5 ns). The emission wavelength corresponding to this high energy emission is estimated to be ~360 nm (~27600 cm^{-1}) from the fitting of TRES analysis. However, this value may have been wrongly estimated as we could not take data points in higher energy region due to very low emission intensity. However, it is confirmed that the short lifetime decay corresponds to this higher energy emissive state. The fast decay of this emissive state may be because of the excited state reorganization through the excited state Jahn-Teller effect forming the STE emission band. However, we could not prove this statement due to the lower resolution of our instrument. The early-time high emission intensity of the high energy emissive state further proves that the origin of this higher energy emission band is not from the trap or defects, as trap-related emission intensity generally remains very low because of the non-radiative channels.

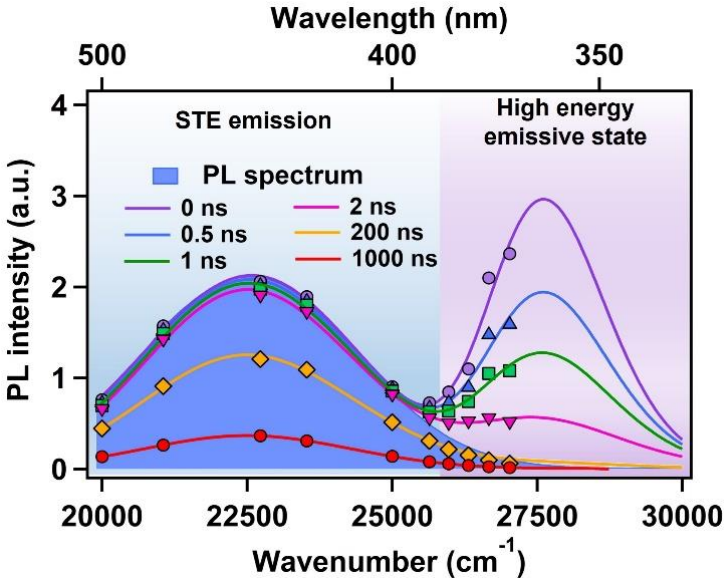

Figure 7.5. TRES of $Cs_3Cu_2I_5$ NCs. The contribution of high energy emissive state is in the violet background region and the contribution of STE state is in the blue region.

Another interesting fact from this wavelength dependent PL analysis is that the relative contribution of the short-lifetime component also increases towards the red end of the PL spectrum (2% at 440 nm, and 16% at 520 nm). We propose that the origin of this component is emission from the low-lying surface trap states which are energetically situated below the STE states. As these trap states' energy is just below the STE state, we can track the contribution of these trap states at the red edge of the PL spectra. So, we propose that the origin of short-lifetime components at the blue edge and at the red edge of the PL spectrum are different and are originating from high-energy band-to-band radiative recombination and from low-lying surface traps, respectively.

7.3. Conclusions

In conclusion, the phase pure lead-free $Cs_3Cu_2I_5$ NCs with the homogeneous size distribution of 22±4 nm have been successfully synthesized in LAMe DES green medium. The NCs show a strong broad steady-state PL band centered at 445 nm originating from the STE emission. The PL decay kinetics reveals the presence of a short-lived state in the higher energy. Further TRES analysis confirms that the high emissive energy state in the ~350 nm region is the origin of the short lifetime decay component. The high emission intensity in the early time of this ~350 nm emission band further nullifies the possible origin to be trap states and proposed to be originating from band-to-band free exciton recombination. The very short lifetime of this high-energy emissive state compared to the long-lived STE emission

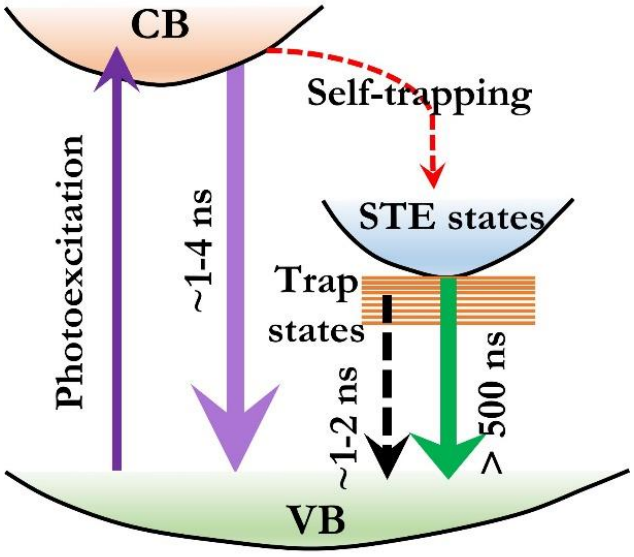

Scheme 7.1. Schematic representation of the recombination processes in $Cs_3Cu_2I_5$ NCs.

is the main reason behind its absence in the steady-state PL spectrum. The evidence of presence of a highly emissive energy state or free excitonic recombination is unique and will help to understand the photophysics of the copper-based perovskites from a new perspective.

References

1. Jena, A. K.; Kulkarni, A.; Miyasaka, T., Halide Perovskite Photovoltaics: Background, Status, and Future Prospects. *Chemical Reviews* **2019,** *119* (5), 3036-3103.
2. Zhang, Q.; Tavakoli, M. M.; Gu, L.; Zhang, D.; Tang, L.; Gao, Y.; Guo, J.; Lin, Y.; Leung, S.-F.; Poddar, S.; Fu, Y.; Fan, Z., Efficient metal halide perovskite light-emitting diodes with significantly improved light extraction on nanophotonic substrates. *Nature Communications* **2019,** *10* (1), 727.
3. Temerov, F.; Baghdadi, Y.; Rattner, E.; Eslava, S., A Review on Halide Perovskite-Based Photocatalysts: Key Factors and Challenges. *ACS Applied Energy Materials* **2022,** *5* (12), 14605-14637.
4. Dey, A.; Ye, J.; De, A.; Debroye, E.; Ha, S. K.; Bladt, E.; Kshirsagar, A. S.; Wang, Z.; Yin, J.; Wang, Y.; Quan, L. N.; Yan, F.; Gao, M.; Li, X.; Shamsi, J.; Debnath, T.; Cao, M.; Scheel, M. A.; Kumar, S.; Steele, J. A.; Gerhard, M.; Chouhan, L.; Xu, K.; Wu, X.-g.; Li, Y.; Zhang, Y.; Dutta, A.; Han, C.; Vincon, I.; Rogach, A. L.; Nag, A.; Samanta, A.; Korgel, B. A.; Shih, C.-J.; Gamelin, D. R.; Son, D. H.; Zeng, H.; Zhong, H.; Sun, H.; Demir, H. V.; Scheblykin, I. G.; Mora-Seró, I.; Stolarczyk, J. K.; Zhang, J. Z.; Feldmann, J.; Hofkens, J.; Luther, J. M.; Pérez-Prieto, J.; Li, L.; Manna, L.; Bodnarchuk, M. I.; Kovalenko, M. V.; Roeffaers, M. B. J.; Pradhan, N.; Mohammed, O. F.; Bakr, O. M.; Yang, P.; Müller-Buschbaum, P.; Kamat, P. V.; Bao, Q.; Zhang, Q.; Krahne, R.; Galian, R. E.; Stranks, S. D.; Bals, S.; Biju, V.; Tisdale, W. A.;

Yan, Y.; Hoye, R. L. Z.; Polavarapu, L., State of the Art and Prospects for Halide Perovskite Nanocrystals. *ACS Nano* **2021,** *15* (7), 10775-10981.

5. Cao, F.; Li, L., Progress of Lead-Free Halide Perovskites: From Material Synthesis to Photodetector Application. **2021,** *31* (11), 2008275.
6. Rosales, B. A.; Hanrahan, M. P.; Boote, B. W.; Rossini, A. J.; Smith, E. A.; Vela, J., Lead Halide Perovskites: Challenges and Opportunities in Advanced Synthesis and Spectroscopy. *ACS Energy Letters* **2017,** *2* (4), 906-914.
7. Schileo, G.; Grancini, G., Lead or no lead? Availability, toxicity, sustainability and environmental impact of lead-free perovskite solar cells. *Journal of Materials Chemistry C* **2021,** *9* (1), 67-76.
8. Li, J.; Cao, H.-L.; Jiao, W.-B.; Wang, Q.; Wei, M.; Cantone, I.; Lü, J.; Abate, A., Biological impact of lead from halide perovskites reveals the risk of introducing a safe threshold. *Nature Communications* **2020,** *11* (1), 310.
9. Davies, M. L. J. J., Addressing the stability of lead halide perovskites. **2020,** *4* (8), 1626-1627.
10. Xiang, W.; Liu, S. F.; Tress, W. J. E.; Science, E., A review on the stability of inorganic metal halide perovskites: challenges and opportunities for stable solar cells. **2021,** *14* (4), 2090-2113.
11. de Souza Carvalho, T. A.; Magalhaes, L. F.; do Livramento Santos, C. I.; de Freitas, T. A. Z.; Carvalho Vale, B. R.; Vale da Fonseca, A. F.; Schiavon, M. A., Lead-Free Metal Halide Perovskite Nanocrystals: From Fundamentals to Applications. *n/a* (n/a), e202202518.
12. Aftab, A.; Ahmad, M. I., A review of stability and progress in tin halide perovskite solar cell. *Solar Energy* **2021,** *216*, 26-47.
13. Cui, Y.; Yang, L.; Wu, X.; Deng, J.; Zhang, X.; Zhang, J., Recent progress of lead-free bismuth-based perovskite materials for solar cell applications. *Journal of Materials Chemistry C* **2022,** *10* (44), 16629-16656.
14. Hui, Y.; Chen, S.; Lin, R.; Zheng, W.; Huang, F., Photophysics in $Cs_3Cu_2I_5$ and $CsCu_2I_3$. *Materials Chemistry Frontiers* **2021,** *5* (19), 7088-7107.

15. Li, Y.; Zhou, Z.; Tewari, N.; Ng, M.; Geng, P.; Chen, D.; Ko, P. K.; Qammar, M.; Guo, L.; Halpert, J. E., Progress in copper metal halides for optoelectronic applications. *Materials Chemistry Frontiers* **2021,** *5* (13), 4796-4820.

16. Zhang, B.; Wu, X.; Zhou, S.; Liang, G.; Hu, Q., Self-trapped exciton emission in inorganic copper(I) metal halides. *Frontiers of Optoelectronics* **2021,** *14* (4), 459-472.

17. Xu, J.; Guo, S.; Qu, J.; Xu, S.; Wang, C.; Ban, D.; Cui, Y., Ultrasonically-prepared copper-doped cesium halide nanocrystals with bright and stable emission. *Nanoscale* **2021,** *13* (21), 9659-9667.

18. Liang, M.; Lin, W.; Zhao, Q.; Zou, X.; Lan, Z.; Meng, J.; Shi, Q.; Castelli, I. E.; Canton, S. E.; Pullerits, T.; Zheng, K., Free Carriers versus Self-Trapped Excitons at Different Facets of Ruddlesden–Popper Two-Dimensional Lead Halide Perovskite Single Crystals. *The Journal of Physical Chemistry Letters* **2021,** *12* (20), 4965-4971.

19. Li, J.; Wang, H.; Li, D., Self-trapped excitons in two-dimensional perovskites. *Frontiers of Optoelectronics* **2020,** *13* (3), 225-234.

20. Fang, S.; Wang, Y.; Li, H.; Fang, F.; Jiang, K.; Liu, Z.; Li, H.; Shi, Y., Rapid synthesis and mechanochemical reactions of cesium copper halides for convenient chromaticity tuning and efficient white light emission. *Journal of Materials Chemistry C* **2020,** *8* (14), 4895-4901.

21. Wang, L.; Shi, Z.; Ma, Z.; Yang, D.; Zhang, F.; Ji, X.; Wang, M.; Chen, X.; Na, G.; Chen, S.; Wu, D.; Zhang, Y.; Li, X.; Zhang, L.; Shan, C., Colloidal Synthesis of Ternary Copper Halide Nanocrystals for High-Efficiency Deep-Blue Light-Emitting Diodes with a Half-Lifetime above 100 h. *Nano Letters* **2020,** *20* (5), 3568-3576.

22. Gao, F.; Zhu, X.; Feng, Q.; Zhong, W.; Liu, W.; Xu, H.; Liu, Y., Deep-blue emissive $Cs_3Cu_2I_5$ perovskites nanocrystals with 96.6% quantum yield via InI3-assisted synthesis for light-emitting device and fluorescent ink applications. *Nano Energy* **2022,** *98*, 107270.

23. Hu, X.; Li, Y.; Wu, Y.; Chen, W.; Zeng, H.; Li, X., One-pot synthesis of Cs3Cu2I5 nanocrystals based on thermodynamic equilibrium. *Materials Chemistry Frontiers* **2021,** *5* (16), 6152-6159.
24. Lu, H.; Tan, X.; Huang, G.; Wu, S.; Zhou, Y.; Zhang, J.; Zheng, Q.; Chen, T.; Li, F.; Cai, Z.; Zeng, J.; Zhang, M., Green synthesis of highly stable CsPbBr3 perovskite nanocrystals using natural deep eutectic solvents as solvents and surface ligands. *Nanoscale* **2022,** *14* (46), 17222-17229.
25. Zhang, F.; Huang, S.; Wang, P.; Chen, X.; Zhao, S.; Dong, Y.; Zhong, H., Colloidal Synthesis of Air-Stable $CH_3NH_3PbI_3$ Quantum Dots by Gaining Chemical Insight into the Solvent Effects. *Chemistry of Materials* **2017,** *29* (8), 3793-3799.
26. Hamill, J. C., Jr.; Schwartz, J.; Loo, Y.-L., Influence of Solvent Coordination on Hybrid Organic–Inorganic Perovskite Formation. *ACS Energy Letters* **2018,** *3* (1), 92-97.
27. Stevenson, J.; Sorenson, B.; Subramaniam, V. H.; Raiford, J.; Khlyabich, P. P.; Loo, Y.-L.; Clancy, P., Mayer Bond Order as a Metric of Complexation Effectiveness in Lead Halide Perovskite Solutions. *Chemistry of Materials* **2017,** *29* (6), 2435-2444.
28. Hoang, M. T.; Pham, N. D.; Yang, Y.; Tiong, V. T.; Zhang, C.; Gui, K.; Chen, H.; Chang, J.; Wang, J.; Golberg, D.; Bell, J.; Wang, H., A facile, environmentally friendly synthesis of strong photo-emissive methylammonium lead bromide perovskite nanocrystals enabled by ionic liquids. *Green Chemistry* **2020,** *22* (11), 3433-3440.
29. Lian, L.; Zheng, M.; Zhang, P.; Zheng, Z.; Du, K.; Lei, W.; Gao, J.; Niu, G.; Zhang, D.; Zhai, T.; Jin, S.; Tang, J.; Zhang, X.; Zhang, J., Photophysics in $Cs_3Cu_2X_5$ (X = Cl, Br, or I): Highly Luminescent Self-Trapped Excitons from Local Structure Symmetrization. *Chemistry of Materials* **2020,** *32* (8), 3462-3468.

30. Ma, Z.; Shi, Z.; Yang, D.; Li, Y.; Zhang, F.; Wang, L.; Chen, X.; Wu, D.; Tian, Y.; Zhang, Y.; Zhang, L.; Li, X.; Shan, C., High Color-Rendering Index and Stable White Light-Emitting Diodes by Assembling Two Broadband Emissive Self-Trapped Excitons. **2021,** *33* (2), 2001367.
31. Liu, X.; Yu, Y.; Yuan, F.; Zhao, C.; Dong, H.; Jiao, B.; Wu, Z., Vacuum Dual-Source Thermal-Deposited Lead-Free Cs3Cu2I5 Films with High Photoluminescence Quantum Yield for Deep-Blue Light-Emitting Diodes. *ACS Applied Materials & Interfaces* **2020,** *12* (47), 52967-52975.
32. Cheng, S.; Beitlerova, A.; Kucerkova, R.; Nikl, M.; Ren, G.; Wu, Y., Zero-Dimensional $Cs_3Cu_2I_5$ Perovskite Single Crystal as Sensitive X-Ray and γ-Ray Scintillator. **2020,** *14* (11), 2000374.

This page is intentionally left blank

Chapter-8

General Conclusions and Future Aspects

This chapter provides a detailed conclusion of the research work presented in this thesis. Further, future aspects of the work presented in this thesis have also been discussed.

Even after almost a decade of research, the lead halide perovskite nanocrystals (LHP NCs) are still far from their practical use. The main problem still remains the same: stability and toxicity. Apart from the application-oriented research, the basic perovskite NC research around the globe can broadly be divided into three categories.

(i) **The research to prolong its environmental and colloidal stability:** This part of the research mostly concentrates on using new ligand systems and innovative core-shell structures to isolate the perovskite NCs from the outer perturbations.

(ii) **The research to maximize PLQY:** This category also works in a similar path to the previous one. The LHP NCs can have shallow surface defects which lower the PLQY of the system. These surface defects can be minimized by using proper surface passivation. Various innovative ligand systems have already been reported to achieve 100% PLQY of LHP NCs. Also, post-synthetic surface modifications by various ions also have been reported to amplify the PLQY of the system. Doping of metal ions in the LHP NCs also found to be beneficial to amplify its PLQY in many cases.

(iii) **The research to minimize the toxicity:** This part of the research mainly deals with lead-related toxicity, which results in various lead-free perovskite systems. However, these lead-free perovskite NCs are still far away to compete with the excellent properties of LHP NCs. In recent times, various lead-free perovskite NCs have been reported with high PLQY. In this respect, Cu (I) halide perovskite NCs, and Mn (II)- based perovskite NCs have shown very promising properties. However, in perovskite NCs synthesis we often use hazardous organic solvents. This solvent-related toxicity always remains underrated in perovskite research. The search for environment-friendly green solvents is necessary to overcome this important issue. Various ionic liquid mediums have recently been reported to synthesize LHP thin films, but the synthesis of NCs in the green alternative medium is still rare.

The overall research work presented has touched on almost every point mentioned above. This thesis mainly focused on to achieve sustainability of halide perovskite NCs. Technically this thesis can be divided into three subcategories.

1. **Effect of heterovalent Bi^{3+} doping on properties, stability, and on charge carrier dynamics of LHP NCs**

This part of the problem is covered in chapter-3 and in chapter-4. In chapter-3, reversible ultra-slow crystal growth is observed in Bi^{3+} doped $MAPbI_3$ NCs. Whereas, in chapter-4, the reason for photoluminescence quenching upon Bi^{3+} incorporation in $MAPbBr_3$ NCs is studied.

General conclusions: The Bi^{3+} doped LHP NCs are found to be superior in terms of stability to their pure lead analogs and Bi^{3+} doping in LHP NCs does not alter the crystal phase in the NCs. The dynamic ligand binding of oleic acid/oleylamine is the reason behind the ultra-slow crystal growth in Bi^{3+} doped $MAPbI_3$ NCs. A particular temperature stabilizes a particular size of the NCs and this temperature-dependent size change is reversible which is very unique. Bi^{3+} doping in LHP NCs quenches the PLQY to a large extent and the reason for this is further investigated in Bi^{3+} incorporated $MAPbBr_3$ NCs through charge carrier dynamics. It is seen that the formation of deep trap states upon Bi^{3+} incorporation in $MAPbBr_3$ NCs is the reason behind the PL quenching and these trapping sites are not related to the surface of NCs. The trapping transfer process quickly depopulates the excitonic state, resulting in quenching in the PL transient. The density of the deep trap states is found to be more associated with the lower energy PL transitions. The inertness of the bismuth 6s orbitals due to higher spin-orbit coupling leaves behind the bromine 6p orbitals as non-bonding which are proposed to form the deep trap states within the lattice. Further, these deep trap states have been passivated by co-doping K^+ into the lattice, which eventually amplifies the PLQY from 9% to 64%. This co-doping also boosted the stability of the system and the PL intensity and PXRD patterns remained unaffected for up to 21 days. So, the main conclusion of this work is by co-doping

K^+ in the lattice with heterovalent Bi^{3+}, higher stability can be achieved without hampering the PLQY of the system. Also, through doping with Bi^{3+} and K^+ the toxicity of the system gets reduced by lowering the lead percentage in the materials.

Future aspects: These two studies provide a general idea that how Bi^{3+} incorporation can change the stability, and photophysical properties of the LHP NCs. Further scope is there to study how in presence of bismuth, other metal ions other than K^+ and Na^+ can change the PL properties and stability of the system. Also, in iodide based NCs, if the growth can be stopped intentionally by any outer perturbation at a particular time, then NCs with desired PL can be easily synthesized.

2. **Reducing organic solvent-related toxicity by synthesizing perovskite NCs in environment-friendly solvent**

This part of the problem is covered mainly in chapter-5 and in chapter-6. In perovskite NC/thin film synthesis we generally use organic precursor solvents like dimethyl formamide (DMF), dimethyl sulfoxide (DMSO), N-Methyl-2-pyrrolidone (NMP), octadecene (ODE). Long-term exposure to certain organic solvents can have serious negative effects on human health. To minimize this solvent toxicity, in chapter-5, an innovative ionic liquid medium is introduced for $MAPbX_3$ NC synthesis (X= Cl, Br, I). In chapter-6, menthol-based deep eutectic solvents are introduced as a green medium for LHP NC synthesis.

General conclusions: Hoang et al. reported a facile synthetic approach for the synthesis of $MAPbBr_3$ NCs in the environment-friendly green solvent medium in 2020. This was the first report of LHP NC synthesis using an alternative green solvent. In this report, they have synthesized IL mediums composed of methylamine and short-chain carboxylic acids (C1-C4). Although, the PLQY of the synthesized NCs was decent (~50%), the water stability was not satisfactory. To overcome this water-stability issue, in chapter-5 a new IL medium is introduced composed of methylamine with hydrophobic lauric acid (LA). This creative application of LA in

the IL composition provided a variety of functions. The $MAPbBr_3$ NCs can easily be synthesized by the direct addition of $PbBr_2$ salt into the IL medium. Although the PLQY of the synthesized NCs is only 19% the hydrophobic LA in the ligand environment provides long-term stability for up to six months. The most intriguing aspect of this work is how the $MAPbBr_3$ NCs create a lead laurate shell over them as a novel type of self-defense when they come into contact with water. This core-shell structure is found to be beneficial in (a) preventing further degradation of the NC, and it becomes highly water stable (at least for two months), (b) surface modification to induce a massive five-fold amplification of PLQY (to near unity), and (c) restricting the anion exchange reaction. Also, this IL medium was further used to synthesize $MAPbCl_3$ and $MAPbI_3$ NCs.

Although the synthesized $MAPbBr_3$ NCs synthesized in IL medium composed of methylamine and lauric acid showed very interesting properties, this synthesis technique has some limitations.

(1) As the NCs are synthesized by the direct addition of lead halide salts, the size and morphology of the NCs cannot be tuned in a proper way.
(2) The mixed halide perovskite NCs cannot be prepared directly.
(3) Proper doping of any other metal ions is not possible.
(4) Also, most importantly as methylamine is a part of the IL medium which contribute as the A-site cation of the perovskite structure, all of these reported methylamine-based IL media are very much selective towards methylammonium-based LHP system. Pure inorganic LHP systems cannot be synthesized in these media.

To overcome these issues, we need a green medium with a high solubilizing ability of precursor salts that will remain inert in the synthesis process. Addressing these problems, in chapter-6 three different menthol-based deep eutectic solvents (DESs), c.a. 1:2 lauric acid/menthol (LAMe), 1:1 caprylic acid/menthol (CAMe), and 1:1 butyric acid/menthol (BAMe), were introduced for the synthesis of cesium lead

bromide perovskite NCs. In these DES solvents lead halide salts are highly soluble in presence of oleylamine. The reaction temperature and added precursor ratio have a significant impact on the formation of NC with controlled dimensionality. Further, all other halides/mix halide perovskite NCs were synthesized using the similar procedure in the DES medium. Also, this synthesis protocol used green DES as the synthesizing medium reduced the crystallization temperature, took place in an open atmosphere, and produced high-quality NC with nearly uniform size distribution and with high PLQY. This further concludes that these DES media can be a potential green alternative for any kind of perovskite NC synthesis.

Future aspects: This part of research is new and currently in its infancy. Various new green synthetic media can be used to synthesize the NCs. Also, the effect of various synthetic factors e.g., effect of temperature, precursor concentration, effect of different ligands in these media need to be studied in detail.

3. **Synthesizing lead-free $Cs_3Cu_2I_5$ NCs in LAMe DES medium: Discarding both solvent and lead toxicity**

This part of the thesis is covered in chapter-7. Here LAMe DES is used as a green solvent to synthesize $Cs_3Cu_2I_5$ NCs through which both lead toxicity and solvent toxicity can be discarded.

General conclusions: The synthesized NCs showed uniform size distribution of size ~22 nm. The NCs exhibit a strong, broad steady-state PL band with a center wavelength of 445 nm that results from self-trapped exciton (STE) emission. The main focus and interesting part of this work is the photophysics of the NCs. The presence of a transient state in the higher energy is revealed by the PL decay kinetics. Further time-resolved emission spectra (TRES) analysis reveals that the short lifetime decay component originates from the high emissive energy state at around 360 nm. The high emission intensity in the early time of this ~360 nm emission band further nullifies the possible origin to be trap states and proposed to be originating

from band-to-band free exciton recombination. The fundamental reason for its absence from the steady-state PL spectrum is the extremely short lifetime of this high-energy emissive state in comparison to the long-lived STE emission. The evidence of a highly emissive energy state or free excitonic recombination is novel and will provide fresh insight into the photophysics of copper-based perovskites.

Future aspects: Apart from green synthesis, this study provides a clear and unique insight into the Photophysics of copper-based perovskite NCs. The evidence of the presence of a high-energy emissive state in the system arises a clear question on the timescale of the excited state Jahn-Teller effect i.e., the excited state reorganization time. In general, it is believed that this excited state reorganization process is too fast for these copper-based perovskite systems that we cannot see any direct emission band. But the actual reason behind this is the very long lifetime of the STE state compared to the short-lived high energy emissive state. From this study, although the existence of the high-energy emissive state is confirmed the dynamics of this state still remain a mystery. The time limit of the instrument restricts us to its actual dynamics. However, a better and more detailed study is required to understand the actual Photophysics of this system.

List of Publications

14. Tuning of Photoluminescence of Graphene Oxide Based Nanomaterials in the UV-Visible Region: Formation of Aggregates by H-Bonding through Water Molecules

    Dinesh Kumar Pyne, **Shovon Chatterjee**, Soumalya Pramanik, Prosenjit Saha, Tuyan Biswas, Somnath Bali, Partha Dutta, Arnab Halder. *ChemistrySelect* **2022**, *7*, e202202707.

13. UV-Assisted Conversion of 2D Ruddlesden–Popper Iodide Perovskite Nanoplates into Stable 3D $MAPbI_3$ Nanorods

    Arghya Sen, **Shovon Chatterjee**, Pratik Sen. *J. Phys. Chem. C* **2022**, *126*, 18057.

12. Interaction of Aromatic Nitro Compounds and Fluoride Ions with Photoluminescent GO-Ce Nanoparticles: Understanding the Role of Local Environment of Cerium

    Dinesh K Pyne, Soumalya Pramanik, **Shovon Chatterjee**, Somnath Bali, Tuyan Biswas, Sohini Sengupta, Arnab Halder. *ChemistrySelect* **2022**, *7*, 202202095.

11. Red-emitting Polyaniline-Based Nanoparticle Probe for pH-sensitive Fluorescence Imaging

    Lokesh Yadav, Anjali Yadav, **Shovon Chatterjee**, Suhela Tyeb, Raju Kumar Gupta, Pratik Sen, Bushra Ateeq, Vivek Verma, Kanwar S Nalwa. *Biomaterials Advances* **2022**, *140*, 21308.

10. Green, Economical Synthesis of Nitrogen Enriched Carbon Nanoparticles from Seaweed Extract and their Application as Invisible Ink and Fluorescent Film

Vikram Singh, B Gorbel, **Shovon Chatterjee**, Pratik Sen, Vivek Verma. *Materials Letters* **2022**, *309*, 131446.

* 9. Massive Amplification of Photoluminescence and Exceptional Water Stability of $MAPbBr_3$ Nanocrystals through Core–Shell Nanostructure Formation in a Self-Defence Mechanism

Shovon Chatterjee, Tanmoy Khan, Arghya Sen, Nilimesh Das, Pratik Sen. ***Mater. Adv.*, 2022**, *3*, 7360-7369.

8. Photoluminescence Amplification of Cerium Incorporated Graphene Oxide Nanoparticles by Photoinduced Reduction: A Mechanistic Study Highlighting Structural Orderness

Dinesh kumar Pyne, **Shovon Chatterjee**, Tuyan Biswas, Prosenjit Saha, Partha Dutta, Arnab Halder. *J. Lumin.* **2021**, *235*, 118019.

7. Formamidinium Containing Tetra Cation Organic–Inorganic Hybrid Perovskite Solar Cell

Harish Singh, Pritam Dey, **Shovon Chatterjee**, Pratik Sen, Tanmoy Maiti. *SolarEnergy* **2021**, *220*, 258-268.

6. Chickpea Peel Waste as Sustainable Precursor for Synthesis of Fluorescent Carbon Nanotubes for Bioimaging Application

Vikram Singh, **Shovon Chatterjee**, Mahendra Palecha, Pratik Sen, Bushra Ateeq, Vivek Verma. *CarbonLetters*, **2021**, *31*, 117-123.

*5. Potassium-Induced Passivation of Deep Traps in Bismuth-Doped Hybrid Lead Bromide Perovskite Nanocrystals: Massive Amplification of Photoluminescence Quantum Yield

Shovon Chatterjee, Mainak Ghosal, Khushubo Tiwari, Pratik Sen. *Phys. Chem. Lett.* **2021**, *12*, 546-551.

*4. Reversible Ultra-Slow Crystal Growth of Mixed Lead Bismuth Perovskite Nanocrystals: The Presence of Dynamic Capping

Shovon Chatterjee, Pritam Dey, Nilimesh Das, Khushubo Tiwari, Tanmoy Maiti, Pratik Sen. *Chem. Eur. J.* **2020**, *26*, 1506–1510.

3. Thiazolothiazole-Based Fluorescence Probe towards Detection of Copper and Iron Ions through Formation of Radical Cations
Govindasamy Sathiyan, **Shovon Chatterjee**, Pratik Sen, Ashish Garg, Raju Kumar Gupta, Anand Singh. *ChemistrySelect* **2019**, *4*, 11718-11725.

2. A Novel Star Shaped Triazine-Triphenylamine Based Fluorescent Chemosensor for the Selective Detection of Picric Acid
Govindasamy Sathiyan, Bhuvaneshwari Balasubramaniam, Sudhir Ranjan, **Shovon Chatterjee**, Pratik Sen, Ashish Garg, Raju Kumar Gupta, and Anand Singh. *Materials Today Chem.* **2019**, *12*, 178–186.

1. Excitation Wavelength Dependent UV Fluorescence of Dispersed Modified Graphene Oxide: Effect of pH
Partha Dutta, Debabrata Nandi, Sudeshna Datta, Subhajit Chakraborty, Nilimesh Das, **Shovon Chatterjee**, Uday Chand Ghosh, Arnab Halder. *J. Lumin.* **2015**, *168*, 269-275.

List of Unpublished Works

*1. Green Synthesis of Pure Inorganic 3D and Ruddlesden-Popper Quasi 2D Cesium Lead Bromide Perovskite Nanocrystals in Menthol-Based Deep Eutectic Solvents
Shovon Chatterjee, Arghya Sen, Pratik Sen
(Manuscript submitted)

*2. Evidence of Short-Lived High Energy Emissive State in Lead-Free $Cs_3Cu_2I_5$ Nanocrystals
Shovon Chatterjee, Pratik Sen
(Manuscript under preparation)

3. Recovery of Colloidal Ruddlesden-Popper Perovskite Nanoplate: A Curious Case of Thiol
   Arghya Sen, **Shovon Chatterjee**, Pratik Sen
   (Manuscript submitted)

4. Effect of Hot and Cold Biexcitons in Early Time Band Gap Normalization in $CsPbBr_3$ Nanocrystals: A Complete Ultrafast Study
   Shovon Chatterjee, Pratik Sen
   (Manuscript under preparation)

5. Competitive Excited State Jahn-Teller Distortion and Electron-Hole Transfer Process in Lead-Free $Cs_3Cu_2I_5$ Nanocrystals
   Shovon Chatterjee, Pratik Sen
   (Manuscript under preparation)

Works in this thesis are based on the publications (or unpublished works) marked with an asterisk. The front pages of the three published articles are given in the following pages.

ChemPubSoc Europe

DOI: 10.1002/chem.201904905

CHEMISTRY A European Journal Communication

Nanotechnology

Reversible Ultra-Slow Crystal Growth of Mixed Lead Bismuth Perovskite Nanocrystals: The Presence of Dynamic Capping

Shovon Chatterjee,[a] Pritam Dey,[b] Nilimesh Das,[a] Khushubo Tiwari,[c] Tanmoy Maiti,[b] and Pratik Sen*[a]

Abstract: An ultra-slow crystal growth over a period of 24 h of a newly synthesized $CH_3NH_3Pb_{1/2}Bi_{1/3}I_3$ perovskite (MPBI) nanocrystal in non-polar toluene medium is reported here. From several spectroscopic techniques as well as from TEM analysis we found that the size of nanocrystals changes continuously with time, in spite of being capped by the ligands. Using a single molecular spectroscopic technique, we also found that this size change is not due to the stacking of nanocrystals but due to crystal growth. The notable temperature dependence and reversible nature of the nanocrystals growth is explained by the dynamic nature of the capping. The observed temperature-dependent ultra-slow growth is believed to be a pragmatic step towards controlling the size of perovskite NC in a systematic manner.

Organic–inorganic hybrid perovskite materials of ABX_3 type with A as the organic cation, B as the inorganic cation and X as halide ions rendered appreciable interest to the scientific community due to their unique properties suitable for the construction of a photovoltaic cell with very high efficiency.[1–3] The nanocrystalline form of such perovskite materials showed a large fluorescence quantum yield with better photostability and considered to be a good replacement of the traditional chromophores.[4] The compositional tuning of such a nanocrystal (NC) provides well-tuned emission characteristics of the material that makes it a potential candidate in the field of optoelectronics, such as in lasers, nonlinear optics, and light emitting diodes.[5,6] Until now most of the reported perovskite NCs are lead (Pb)-based with high emission quantum yield.[7] Keeping in mind the toxic nature of lead, it is desired to develop perovskite NCs with lower Pb content without compromising its interesting properties. Further, these Pb-based NCs exhibit poor moisture resistance, making these extremely vulnerable in the ambient conditions.[8] Recently scientists have started to explore Pb-free perovskites with various cations at the B-site.[9] Among these, bismuth (Bi) -based perovskites provide a better stability in the ambient condition, which is very much required for the application of these materials.[10] However, the quantum yield of these Bi-based perovskite NCs is very low.[11] Therefore, it is a primary concern to search for a system with high quantum yield without compromising stability. Keeping this in mind, we have synthesized organic–inorganic hybrid iodide perovskite NCs with an appropriate ratio of Pb^{2+} and Bi^{3+} in order to maintain the formal charge balance that is, (+2) in the B-site of these perovskites. Properties of Bi-doped Pb halide NCs have been explored recently by some research groups.[12,13] In our previous study, we have also reported the potential of these charge-balanced hybrid Pb–Bi perovskite thin films for solar cell applications.[14]

Capping of NCs with long-chain organic moieties is a key step for size control synthesis of the NCs as without capping, the NCs stability is being compromised due to the formation of non-fluorescent bulk perovskite materials.[15] Thus, capping is one of the most efficient ways to enhance the stability of perovskite NCs in the solution[16–18] Oleic acid (OA) and oleylamine (OAm) are popular capping agents reported in the literature for the synthesis of such perovskite NCs.[15,16,18,19] OA has less capping ability than OAm, but any of these two alone cannot provide a sufficient stability to Pb perovskite NCs because of their poor binding with Pb^{2+}.[19] However, when these two ligands are used together, they form the oleate anion and olylammonium cation, which are better capping agents due to the strong interaction with Pb^{2+} and X^-, respectively.[15,19] For size and shape tunable synthesis of perovskite NCs, the proportion and the amount of OA and OAm play a crucial role. Akin to most of the nanomaterials, the properties of perovskite NCs depend highly on their size and shape.[16] With increase in the size of NCs, the emission maximum shifts towards lower energy, which can be controlled by the capping agents. Under controlled conditions, the spectral properties do not show any time dependence in most of the cases, rendering the formation of a stable NC.[5,6,15,16] Interestingly in one report, Seth et al. have demonstrated the time-dependent shift of the emission maxima for $CsPbBr_3$ and $CsPbBr_2I$ perovskite NC suspensions under continuous light irradiation.[20] To explain this phenomenon, the authors hypothesized a change in average size

[a] S. Chatterjee, N. Das, Prof. P. Sen
Department of Chemistry, Indian Institute of Technology Kanpur
Kanpur 208 016, UP (India)
E-mail: psen@iitk.ac.in

[b] P. Dey, Dr. T. Maiti
Plasmonics and Perovskites Laboratory, Department of Materials Science and Engineering, Indian Institute of Technology Kanpur
Kanpur 208 016, UP (India)

[c] K. Tiwari
Department of Materials Science and Engineering; Indian Institute of Technology Kanpur, Kanpur 208 016, UP (India)

Supporting information and the ORCID identification number(s) for the author(s) of this article can be found under: https://doi.org/10.1002/chem.201904905.

THE JOURNAL OF PHYSICAL CHEMISTRY LETTERS
A JOURNAL OF THE AMERICAN CHEMICAL SOCIETY

pubs.acs.org/JPCL Letter

Potassium-Induced Passivation of Deep Traps in Bismuth-Doped Hybrid Lead Bromide Perovskite Nanocrystals: Massive Amplification of Photoluminescence Quantum Yield

Shovon Chatterjee, Mainak Ghosal, Khushubo Tiwari, and Pratik Sen*

Cite This: J. Phys. Chem. Lett. 2021, 12, 546−551 Read Online

ACCESS | Metrics & More | Article Recommendations | Supporting Information

ABSTRACT: The low photoluminescence quantum yield of Bi^{3+}-doped lead halide perovskite nanocrystals (NCs) is a big challenge to the scientific community. This makes them a weak candidate in the optoelectronics field in spite of their better stability than the pure lead analogue. Herein, the reason behind this reduction of quantum yield in hybrid mixed lead−bismuth bromide (MPBBr) NC is investigated and proposed to be due to ultrafast trapping transfer in the core of the NC, and not due to the surface trap states. Further, we have successfully boosted the quantum yield of MPBBr NC from 9% to 64% by passivating the deep traps within the crystal core by monovalent potassium ion doping. The stability of the developed Bi^{3+}/K^{+}-doped lead halide perovskite NC was found to be extremely high in atmospheric conditions, and this property is sustained up to 100 °C.

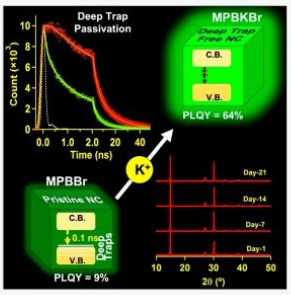

In recent years the scientific community has noticed a rapidly growing interest in lead halide perovskite systems due to their unique properties.[1−3] The efficiency of the solar cell is recorded as high as 24% using perovskite material.[4] On the other hand, the nanocrystalline (NC) version of these lead halide perovskite systems render high attention due to their promising optoelectronic properties with high photoluminescence (PL) quantum yield (QY).[5−7] Compositional and dimensional tuning of these materials provide a way to adjust the band gap, which eventually provides well-controlled emission characteristics ranging from violet to red. This makes lead halide perovskite NCs appropriate for laser, nonlinear optics, and light-emitting device applications.[8,9]

The toxic nature of the lead as well as vulnerability of lead halide perovskite in atmospheric conditions is a real hindrance to make these materials useful for commercial purposes.[10] This leads to the development of lead-free and B-site-doped perovskite materials. Doping refers to the intentional insertion of a heteroatom to a target lattice, while keeping the basic host crystal structure intact, to modulate the fundamental optoelectronic properties of the material.[11,12] The heterovalant-doped perovskites have shown better stability with respect to the pure lead analog with unique PL properties.[12,13] Charge carrier dynamics as well as detailed PL studies of such perovskite NCs have yet to be explored though. A few recent reports have partly revealed the excitonic behavior of these kinds of materials.[14,15] Bi^{3+} is a common heterovalent dopant for the B-site of the lead halide perovskite lattice as it does not affect the perovskite crystal architecture due to its similar ionic radius compared to that of Pb^{2+} (Pb^{2+}: 119 pm and Bi^{3+}: 117 pm).[15] However, Bi^{3+} doping drastically drops the PLQY of lead halide perovskite NC and eventually makes it a bad choice in the field of optoelectronics, despite its greater stability in air.[13−15] According to previous reports, the reason for the drop of PLQY is believed to be due to the activation of trap-state-induced quenching processes.[14,16] It is believed that Bi^{3+} induces trap states just below the conduction band.[14] To date, it is a common challenge to the perovskite community to increase the quantum yield of the bismuth-doped lead halide perovskite NC,[16,17] and we believe that the knowledge of the nature of the trap states is the key to this endeavor.

For lead halide as well as lead free perovskite NCs, surface passivation is a popular technique to increase the PL efficiency.[17,18] Long chain organic ligands are routinely used for this purpose.[13] Recently the use of extra halide and alkali metal ions have been reported as surface passivator that eventually boost the PLQY.[19,20] Alkali metals are introduced within the perovskite lattice to increase the emission properties and stability of the PNCs.[21] However, detailed study of charge carrier trapping in Bi^{3+}-doped lead halide PNCs and way to boost its PL quantum yield is still a concern.

Received: October 10, 2020
Accepted: December 23, 2020
Published: December 30, 2020

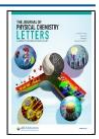

https://dx.doi.org/10.1021/acs.jpclett.0c03092
J. Phys. Chem. Lett. 2021, 12, 546−551

Materials Advances

ROYAL SOCIETY OF CHEMISTRY

PAPER

View Article Online
View Journal | View Issue

Cite this: *Mater. Adv.*, 2022, 3, 7360

Massive amplification of photoluminescence and exceptional water stability of $MAPbBr_3$ nanocrystals through core–shell nanostructure formation in a self-defence mechanism†

Shovon Chatterjee, Tanmoy Khan, Arghya Sen, Nilimesh Das * and Pratik Sen *

Received 14th June 2022,
Accepted 16th July 2022

DOI: 10.1039/d2ma00684g

rsc.li/materials-advances

Vulnerability to atmospheric conditions and their associated toxicity limit the practical/industrial use of perovskites despite their tremendous promise in optoelectronics. This study utilized an ionic liquid-like solvent to synthesize methylammonium lead bromide ($MAPbBr_3$) nanocrystals (NCs). The synthesized NCs showed a moderate photoluminescence quantum yield (PLQY) of ~19% and high environmental stability of at least six months. Further, the entire visible range was tuned through the anion-exchange method. More interestingly, the synthesized NCs formed a core–shell structure in a unique self-defence mechanism in the presence of water, which was proposed to be $MAPbBr_3$@lead laurate. This core–shell structure was found to be beneficial for (a) preventing further degradation of the NC, and making it water stable (at least for two months), (b) improving the PLQY by surface modification inducing a massive five-fold amplification, and (c) restricting the anion-exchange reaction. Moreover, these unique properties were achieved without any special control. Moreover, the successful synthesis of other $MAPbX_3$ (X = Cl, I) demonstrated its potential applicability.

1. Introduction

Halide perovskites are considered a potential game changer in the field of light-emitting diodes, solar cells, photodetectors, and bioimaging because of their unique optical and electronic properties.[1–3] Despite the tremendous promise, their practical/industrial applicability is limited because of their vulnerability to atmospheric conditions, and due to toxicity related to the perovskite materials and their synthesis.[1,4,5] This study utilized an ionic liquid-like solvent that could largely reduce synthesis-related toxicity, minimize structural defects, and protect the perovskite nanocrystal from degradation by water through a self-defence mechanism.

The most widely used precursor solvents for perovskite synthesis are hazardous and toxic dimethylformamide (DMF) along with its homologous dimethylacetamide (DMAC), *N*-methyl-2-pyrrolidone (NMP), and skin-penetrating dimethyl sulfoxide (DMSO). Another critical problem with these solvents is their high coordinating ability with the perovskite surface, which eventually facilitates the degradation of the perovskite structure and the formation of surface defects.[6–9] The use of less hazardous and non-coordinating organic solvents, like acetonitrile (ACN), for this purpose has been attempted in recent times.[9,10] A recent breakthrough was achieved using ionic liquids (ILs) (like carboxylic acid-methylamine, imidazole-based ionic liquid, and so on) as the precursor medium.[11,12] The first report came in 2015 by Moore *et al.* describing the synthesis of a hybrid lead halide perovskite ($MAPbI_3$) thin film using methylammonium formate ionic liquid.[13] Consequent studies have proved the massive potential of such an approach.[11,14–17] A few studies have also been undertaken to venture into the fundamental roles of the ILs in controlling the perovskite nanocrystals' (NCs) crystallization, nucleation, growth, interface modification, and overall power conversion efficiency (PCE).[11,12,18,19] The use of such solvents serves many purposes; including (i) these can solubilize a vast series of materials;[11] (ii) by forming active intermediates, it provides an opportunity to control the crystal-growth process;[11,18,20] (iii) by interacting with uncoordinated lead, it might provide a much-needed enhancement in the PLQY;[21] (iv) these liquids are considered environmentally friendly;[11–14] (v) the

Department of Chemistry, Indian Institute of Technology Kanpur, Kanpur – 208 016, UP, India. E-mail: psen@iitk.ac.in, nilimesh@iitk.ac.in; Fax: +91 51 2259 6806; Tel: +91 51 2259 6312

† Electronic supplementary information (ESI) available: PXRD pattern of $MAPbBr_3$ NCs, XPS data of $MAPbBr_3$ NCs and $MAPbBr_3$@lead laurate, FESEM data of $MAPbBr_3$ NCs and $MAPbBr_3$@lead laurate, the stability information of $MAPbBr_3$ NCs, the anion exchange related data of $MAPbBr_3$@lead laurate system and video of water stability of $MAPbBr_3$@lead laurate NC. See DOI: https://doi.org/10.1039/d2ma00684g